

Plasmons in nanostructures with applications to metamaterial science

Zur Erlangung des akademischen Grades eines
DOKTORS DER NATURWISSENSCHAFTEN
(Dr. rer. nat.)

Fakultät für Chemie und Biowissenschaften
Karlsruher Institut für Technologie (KIT) - Universitätsbereich
genehmigte
DISSERTATION

von
Dipl-Chem. Dipl-Phys. Stephan Bernadotte
aus
Konstanz

Dekan: Prof. Dr. S. Bräse

Referent: Prof. Dr. W. Klopper

Korreferent: Prof. Dr. F. Evers

Tag der mündlichen Prüfung: 21. Okt. 2011

Contents

1	Introduction	7
2	Introduction to metamaterial science	9
2.1	Metamaterials	9
2.2	Negative refraction	9
2.3	The building blocks	11
2.4	How to measure the response parameters?	13
2.5	How to calculate the response parameters?	16
I	Response of single nanostructures to external electromagnetic fields	17
3	Circuit models for SRRs	19
3.1	The resonance structure	19
3.2	Resonance frequency	22
3.3	Calculation of response properties	22
3.4	Index of refraction	24
4	Basic linear response theory	25
4.1	General response theory	25
4.2	Density response and RPA	29
4.2.1	Response functions	29
4.2.2	Meaning of the poles	30
4.2.3	Random Phase Approximation	31
4.2.4	Beyond the Random Phase Approximation	33
4.3	Dynamical conductivity	34
4.4	Damping	38
4.5	Eigenmode expansion	39

5	Discretized Model	41
5.1	Definition of the model	41
5.2	Electronic structure	42
5.2.1	Hartree theory	42
5.2.2	Hartree-Fock theory	43
5.3	Response functions and calculation of the induced density	44
5.3.1	Hartree theory	44
5.3.2	Hartree-Fock theory	44
5.3.3	Response equations in particle-hole space	45
5.4	Implementation	46
6	Continuum model	51
6.1	The model	51
6.2	Comparison between continuum and discretized model	53
7	Longitudinal plasmons in simple geometries	55
7.1	Introduction	55
7.2	Identification of plasmons	55
7.3	Cuboid geometry in 3D	59
7.3.1	Parabolic dispersion	59
7.3.2	Tight-binding cubes : cos-dispersion	62
7.3.3	Comparison between continuum model and numerics	65
7.4	Rectangular geometry in 2D	66
7.4.1	Parabolic electronic dispersion	66
7.4.2	Half-filled tight-binding rectangles	68
7.4.3	Comparison of analytics with numerics	70
7.5	One dimensional systems	72
7.5.1	General dispersion	72
7.5.2	Comparison of continuum theory to numerics	76
7.6	Generalization and summary	77
8	The Split Ring Resonator	79
8.1	Introduction	79
8.2	Definition of the model systems	80
8.2.1	Geometry the SRR	80
8.2.2	External fields	81
8.3	Plasmonic excitations	82
8.3.1	Density profiles	82

8.3.2	Symmetry considerations	83
8.3.3	Plasmon dispersion on SRRs	85
8.4	Polarizabilities	96
8.4.1	Definition and general properties	96
8.4.2	Symmetry considerations	96
8.4.3	Expressions for the oscillator strengths from continuum theory	97
8.4.4	Obtaining oscillator strengths with the discretized model	98
8.4.5	Comparison between discretized and continuum model	99
8.5	Tuning the electromagnetic response	103
8.5.1	Resonance frequency	103
8.5.2	Oscillator strengths	104
8.5.3	How to obtain strong magnetic resonances?	105
9	Quantum chemical calculations	107
9.1	Polyene chains	108
9.2	Influence of exact exchange	112
9.3	Rings	117
9.4	Summary	119
II	From a single resonator to the medium: The metamaterial	121
10	Outline	123
11	Plasmon hybridization	125
11.1	Two resonators	125
11.1.1	Two electric dipoles	125
11.1.2	Two SRRs	130
11.2	Plasmonic bands in one dimension	133
11.2.1	Electric dipole coupling	133
11.2.2	Coupling of SRRs	134
11.3	Three dimensional materials	136
12	Macroscopic medium theory	139
12.1	Maxwell equations in the presence of media	139
12.2	From microscopic to macroscopic Maxwell equations	144
12.3	Averaging procedure	145
12.4	Polarization and magnetization	147
12.5	Macroscopic fields	148

12.6	Macroscopic response functions	152
12.7	Environmental form factors	152
12.8	Macroscopic response functions of simple metamaterials	154
12.8.1	Parallel SRRs	154
12.8.2	Anti-parallel geometry	154
12.8.3	SRRs in plane with random slit position	155
12.8.4	Random SRR medium with completely arbitrary direction of slits .	156
12.8.5	Two-component medium	156
13	Index of refraction	159
13.1	Index of refraction	159
13.2	Extinction theorem	160
13.3	Index of refraction of an SRR medium	161
13.3.1	Geometry of the molecular crystal	161
13.3.2	Calculation of refractive index	161
13.3.3	Condition for negative permeability	163
13.3.4	Designing optical metamaterials	165
14	Summary and Outlook	167
A	Coupling of the SRR to the light field	181
A.1	Dependence on the origin	181
A.2	The coupling Hamiltonian	182
A.3	Choice of origin	183
A.4	External potentials	184
B	Calculation of the polarizabilities	187
B.1	Calculation of the electromagnetic moments	187
B.2	Explicit expressions for the polarizabilities	188
C	Basics of (TD)DFT	189
C.1	DFT	189
C.2	TDDFT	190
D	Identification of plasmonic modes	191
E	Extinction theorem	195

Chapter 1

Introduction

In 1968 Veselago made a theoretical analysis of media where both the electric permittivity and magnetic permeability were negative [1]. He found that media exhibit negative refraction. While negative electric permittivities were known in 1968, it took more than 20 years to find materials where the magnetic permeability becomes also negative in a certain frequency window [2]. In order to highlight that such a behavior does not appear in known natural materials, the term *metamaterial* is used. The first suggestion for the geometry of a building block of a metamaterial was a split ring resonator (SRR), where an external magnetic field perpendicular to the ring plane excites a plasmonic resonance that is accompanied by a current which in turn leads to a huge magnetic moment. The basic physics of these resonators is traditionally analyzed by employing circuit models, where the inductance and the capacity are solely determined by the geometry of the resonator and the resistance is obtained from Drude theory. In addition to SRRs, cut wire pairs [3] and fishnet structures [4] are also used as building blocks for metamaterials.

One main focus of the active research in metamaterial sciences is the construction of materials that exhibit a negative index of refraction in the optical frequency regime, as such materials are proposed to be applicable to perfect lensing [5, 6] or to the construction of cloaking devices [7, 8, 9, 10]. In recent years, a considerable effort has been made in order to achieve this goal [11, 12, 13]. However, there are still problems tracing back to the experimental techniques that are used for the construction of the materials [12]: (i) One has not yet achieved to fabricate building blocks of sizes that are smaller than a few nanometers. As the resonance frequency roughly drops with the reciprocal system size, smaller building blocks are highly desirable in order to obtain resonances in higher frequency regimes. (ii) The fabrication of a three-dimensional metamaterial is really demanding.

In addition to the need of improvement in experimental setups, the circuit based theoretic-

cal approaches had to be extended by taking into account the acceleration of the electrons due to their moments of inertia [14, 15] as well as quantum effects [16, 17], if one goes to smaller system sizes.

Recently, the attention of the metamaterial community has been drawn to studying the coupling effects of individual resonators. The concept of plasmon hybridization was introduced, allowing to interpret the coupling in the same manner as the linear combination of atomic orbitals, forming molecular orbitals [18, 19, 20, 21]. However, the calculation of the effective material parameters is still actively discussed in recent literature [22, 23, 24, 25] and seems to be a topic with a long history [26, 27, 28, 29].

In the light of the developments in metamaterial sciences in the last 10 years, the important question arises, if there exist alternative routes for the construction of building blocks and media thereof. In this thesis, a new bottom up pathway for the development of these building blocks is investigated theoretically: Organic molecules with delocalized electronic π -systems are proposed as candidates for possible building blocks of metamaterials. This choice seems suitable because of the structural flexibility and the possibility to build molecular crystals. The central theme of this work will be the analysis of the response of such molecular crystals to electromagnetic fields based on a microscopic theory. The results of this analysis will then be used to suggest guide-lines for the construction of molecular crystals with desired properties.

In this work the following strategy will be followed: First, a formalism has to be developed that is capable of describing plasmonic resonances in nanostructures (Chapter 4). Based on that formalism, a numerical model (Chapter 5) and a continuum model (Chapter 6) will be developed. Both models will be tested by reproducing known results of plasmonic excitations (Chapter 7). The models will then be applied to the calculation of the microscopic response properties of isolated split ring resonators (Chapter 8). By performing quantum chemical calculations for molecules the analytical model will be tested against density functional theory calculations and differences will be analyzed (Chapter 9). Having understood the response behavior of isolated molecules, an effective medium theory will be developed: The coupling of the individual resonators will be calculated (Chapter 11) and an averaging procedure yields the macroscopic material parameters (Chapter 12). Finally, the index of refraction will be determined and guide-lines for the construction of metamaterials with desired properties will be suggested (Chapter 13).

Chapter 2

Introduction to metamaterial science

2.1 Metamaterials

The recent developments in nanotechnology have opened a pathway to the construction of material classes with outstanding optical properties that have not been found in nature so far. In order to distinguish these artificially tailored materials from structures that are known in nature, the term *metamaterial* has been introduced. One major focus of the research in metamaterial sciences is the fabrication of materials with desired optical properties. The research in this field, however, is not only restricted to electromagnetic waves, but also ranges to acoustic [30] and seismic waves [31].

2.2 Negative refraction

In cases of ordinary refraction, i.e., when the refractive index is positive, a light ray traveling from one medium with refractive index n_1 into another medium with refractive index n_2 is refracted at the boundary according to Snell's law:

$$\frac{\sin \theta_1}{\sin \theta_2} = \frac{n_2}{n_1}, \quad (2.1)$$

where the angles are measured with respect to the normal of the boundary between the two media as depicted in Figure 2.1. Looking at equation (2.1), it is obvious, that the sign of the refracted light ray changes its sign when n becomes negative. This is also shown in Figure 2.1.

In order to understand how the index of refraction may become negative, we have a closer look at the quantities that determine the index of refraction: the *electric permittivity* ϵ and the *magnetic permeability* μ . Both quantities are complex, depend on the frequency

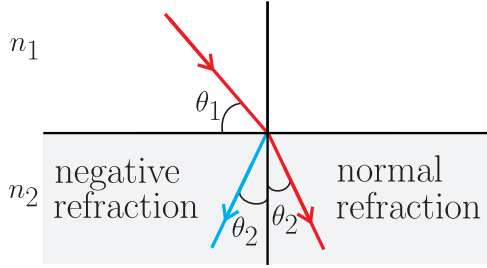


Figure 2.1: Snell's law of refraction at the boundary of two media with refractive indices n_1 and n_2 . The red line shows the ray path in the case of normal refraction and the blue line shows the ray path in the case of negative refraction.

of the light field, and are related to the index of refraction via

$$n = \sqrt{\varepsilon \mu}, \quad (2.2)$$

where one has to take the principal value of the square root. In many materials μ has only a weak dependency on the frequency and is close to one. In this case the index of refraction is solely determined by the electric permittivity. A typical parameterization for ε is obtained by utilizing the Lorentz oscillator model. Within this model one treats the bound electrons of the material under consideration in a harmonic approximation. Each oscillator has a resonance frequency ω_j as well as a damping constant γ_j and is driven by the electric field. The oscillating electrons give rise to oscillating dipole moments, so one obtains for ε

$$\varepsilon(\omega) = 1 + \frac{4\pi e^2 N}{m} \sum_j \frac{f_j}{\omega_j^2 - \omega^2 - i\omega\gamma_j}, \quad (2.3)$$

where e is the electron charge, N the number density of electrons and f_j the oscillator strength. The prefactor in front of the sum is just the square of the usual plasma frequency in three dimensions. As the imaginary part of ε must be positive in dissipative media, one knows that the polar angle ϕ of ε lies between 0 and π when ε is considered in the complex plane. If one now takes the principal value of the square root of ε in order to obtain n , one sees that the polar angle of n lies between 0 and π , so the real part of n must be positive. The situation can change, if μ can differ from unity. We now consider the case that μ has a resonance in the vicinity of the resonance of ε such that there is a frequency window in which the real part of both ε and μ is negative. We have depicted such a situation in Figure 2.2 Now the polar angle of n^2 is greater than π , so the polar angle of n lies between $\pi/2$ and π and the real part of n is therefore negative.

Finally, we present the results of the povray simulation of a negative index material [32] that is depicted in Figure 2.3.

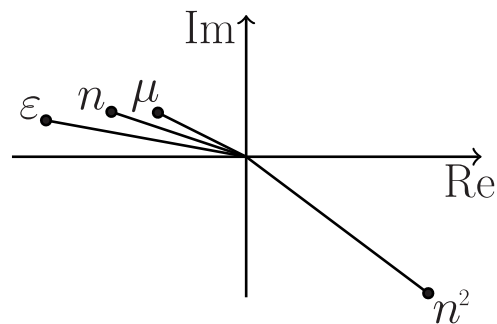


Figure 2.2: Example of material parameters ε and μ that lead to negative index of refraction.



Figure 2.3: The difference in the optical density of air and 'normal' water (left) causes a straw in a glass of water to seem to be shifted at the interface and slightly enlarged inside the liquid. In 'negative-index water' (right), the straw would seem to continue in 'the wrong direction'. This is the principle that applies to negative index materials [32].

2.3 The building blocks

Knowing that one needs a negative real part of both ε and μ in order to obtain negative refraction and that the real part of ε becomes easily negative in the vicinity of resonances, the most natural idea is to look for structures exhibiting strong magnetic resonances. The first suggestion for such a structure was the split ring resonator (SRR) whose structure is shown on the right side in Figure 2.4. In the presence of a time-dependent external magnetic field that is perpendicular to the ring plane there is a voltage drop at the ends of the SRR. According to Ohm's law the voltage drop induces a current. As a result charges with different signs are accumulated at the ends, so the ends act like a plate condenser. Time-dependent current gives also rise to an induced voltage, so the SRR behaves like a coil. Combining now both results suggests that the SRR behaves like an \mathcal{LC} -circuit

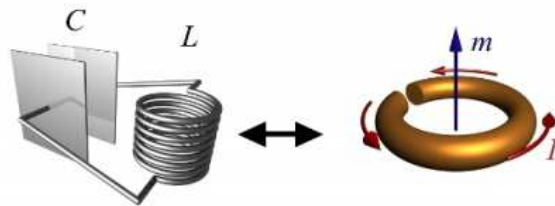


Figure 2.4: On the right side the structure of an SRR is shown. On resonance, a huge current I is excited accompanied by a huge magnetic moment m . The interpretation of the resonances in terms of a circuit model is depicted on the left side.

with inductance \mathcal{L} and capacitance \mathcal{C} . Such circuits are known to exhibit a resonance for frequencies ω_0 that are given by

$$\omega_0 = \frac{1}{\sqrt{\mathcal{L}\mathcal{C}}}. \quad (2.4)$$

The circuit parameter are obtained by using the usual expression from classical electrodynamics. We will give explicit calculations in Chapter 8.

If one now fabricates a material that consists of SRRs and building blocks that exhibit a negative real part of the permittivity at the resonance frequency of the SRRs, one has constructed a negative index material. The first experimental verification of the negative refractive index of such a material has been given in 2000 [33], where the electric resonances come from wires. The structure of the material is depicted in Figure 2.5.

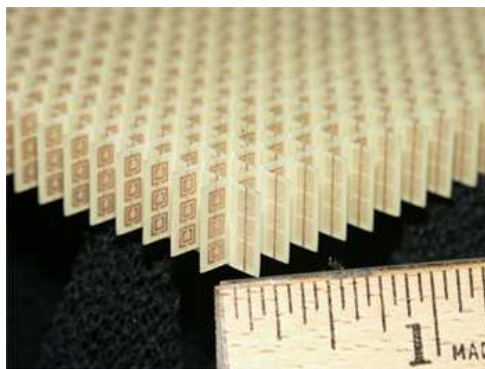


Figure 2.5: Structure of a metamaterial that consists of SRRs and wires [33].

Comparing now the size of the SRRs and the wires, one may wonder what the additional building blocks are good for, as one would expect that SRRs should by themselves already have electric and magnetic resonances in the same frequency window as the wires.

Such common resonances indeed exist, but it has been shown that *bianisotropy* makes it impossible for media consisting solely of SRRs in a parallel alignment to achieve negative refraction [34], making bianisotropy a parasitic effect [35, 36]. Bianisotropy takes into account that electric fields may excite magnetic moments and that magnetic fields may excite electric moments. The corresponding material parameters are denoted as ξ and ζ . The constitutive equations for such materials then read

$$\begin{pmatrix} \mathbf{D} \\ \mathbf{B} \end{pmatrix} = \begin{pmatrix} \varepsilon & \xi \\ \zeta & \mu \end{pmatrix} \begin{pmatrix} \mathbf{E} \\ \mathbf{H} \end{pmatrix}, \quad (2.5)$$

and the corresponding index of refraction is given by

$$n = \sqrt{\varepsilon\mu - \xi\zeta}, \quad (2.6)$$

where we have assumed that the medium is isotropic. We will demonstrate in Chapter 3 that ξ and ζ lead to a cancellation of the terms that are necessary in order to achieve negative refraction.

2.4 How to measure the response parameters?

The typical experimental approach in order to obtain the response parameters of a given metamaterial comprises two steps:

- i) The transmission and reflection spectra of the material under consideration are measured. As an example for experimental spectra we show the spectra obtained in [37] in Figure 2.6.
- ii) One then solves the Maxwell equations numerically using finite element methods. The parameters that enter these calculations are the geometries of the building blocks, the lattice constants and effective bulk permittivities and conductivities. The transmission and reflection spectra are calculated and compared with experimental spectra. If they agree, a *retrieval procedure* [38, 39, 40] is applied in order to extract the effective response parameters. We show the theoretical spectra from [37] in Figure 2.7 and the effective material parameters obtained with a retrieval procedure in Figure 2.8. Some retrieval procedures are based on transfer matrix methods allowing to calculate the transmission and reflection spectra, while others use the Fresnel equations for the calculation of the spectra. The theoretically expected spectra are then fitted to the experimental yielding the material parameters as fit parameters. It has been highlighted that the reliability of the retrieval procedure depends on the inclusion of bianisotropy [38].

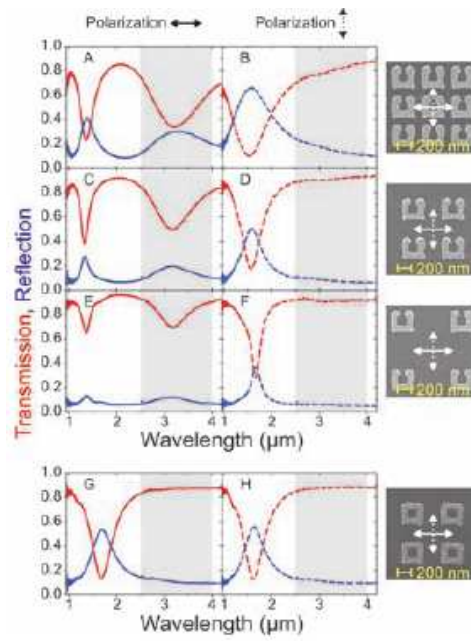


Figure 2.6: Experimental transmission and reflection spectra from [37].

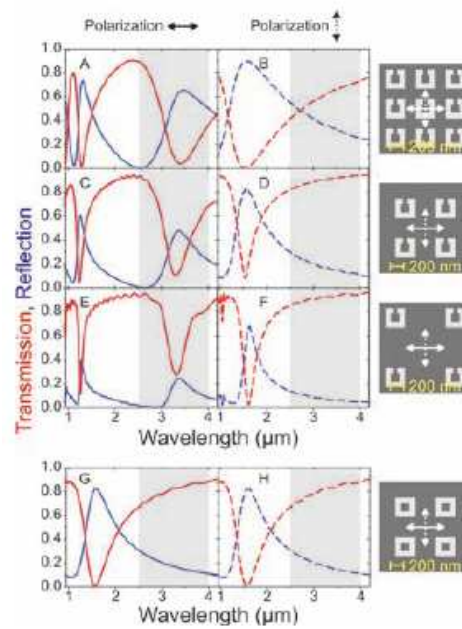


Figure 2.7: Theoretical transmission and reflection spectra from [37].

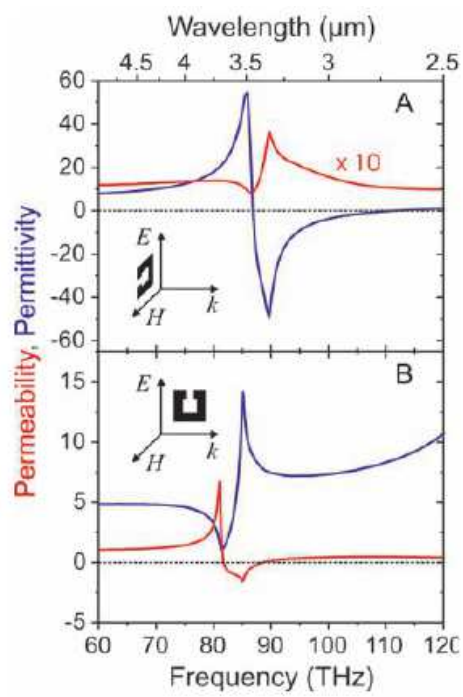


Figure 2.8: Results of a retrieval procedure for ϵ and μ from [37].

2.5 How to calculate the response parameters?

If one attacks the problem of determining the response parameters purely from the theoretical side, one could solve the Maxwell equations using finite element methods. Another possibility is to understand the response of an isolated building block and then to calculate the response of the material. It was shown in Section 2.3 that circuit models provide an easy way in order to understand the resonances of these blocks. It has been suggested that the coupling of the resonators can be treated by employing circuit models, too. The most common approach, however, is the homogenization of the electromagnetic fields. Homogenization means that one averages the induced dipole moments and the induced electromagnetic fields in order to obtain (hydrodynamic) smooth response properties. Roughly 100 papers on the homogenization of metamaterials have been published since 2003, indicating that the calculation of the macroscopic response properties is a topic of great scientific interest.

Part I

Response of single nanostructures to external electromagnetic fields

Chapter 3

Circuit models for SRRs

The conventional approach to understand the resonance structure of the magnetic permeability of a metamaterial built from split ring resonators is based on circuit models. These simple models determine the inductance \mathcal{L} and the capacity \mathcal{C} solely from the geometric parameters of the slit ring resonator of interest plus bulk material parameters, typically on the level of static Drude theory. We will also show that one can improve on the simple models by employing the *dynamic* conductivity from Drude theory, leading to the appearance of the kinetic inductance term. The scaling of the resonance frequency is analyzed with respect to the system size. The polarizabilities are calculated so as to determine the index of refraction of a medium built up from the SRRs. Finally, we conclude that SRRs by themselves cannot constitute a medium with negative refraction.

3.1 The resonance structure

The objective of this section is to show how the response of a single resonator to the light field relates to parameters derived from circuit theory, very commonly used in the literature for describing the resonance behavior of individual resonators [14, 34, 41, 42, 43]. The geometry of a single slit ring resonator is depicted in Figure 3.1.

First, one must understand how a resonance structure arises and which parameters control the resonances. A frequency dependent external voltage U_{ext} is applied at both arm ends of the resonator. Within the linear regime, the induced current I oscillates with the same frequency as the external voltage. This current is the source of an internal magnetic field, giving rise to an induced voltage U_{ind} in accordance with the Law of Induction. Via the inductance \mathcal{L} , one obtains a simple relationship between U_{ind} and the time derivative of I , denoted by a dot, such that

$$U_{\text{ind}} = -\mathcal{L}\dot{I}. \tag{3.1}$$

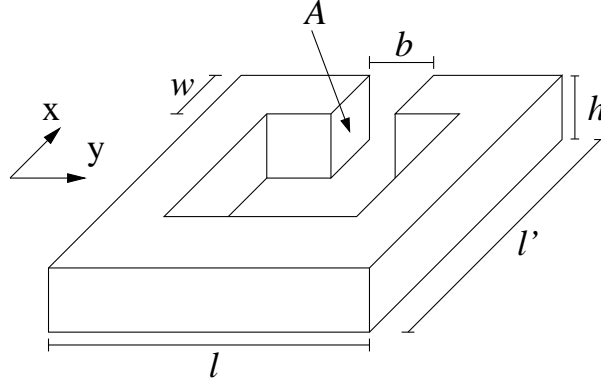


Figure 3.1: Split ring resonator geometry

A reasonable initial guess for \mathcal{L} is obtained by approximating the SRR with a circular loop with radius r_{eff} . Its circular cross section radius is denoted as r_{cs} . The radii are given by,

$$r_{\text{eff}} = \frac{L_{\text{eff}}}{2\pi} \quad (3.2)$$

and

$$r_{\text{cs}} = \sqrt{\frac{A}{\pi}}, \quad (3.3)$$

where we have introduced the effective length of the wire,

$$L_{\text{eff}} = 2l + 2l' - b \quad (3.4)$$

The explicit expression for the inductance reads [44]

$$\mathcal{L} = \frac{4\pi}{c^2} r_{\text{eff}} \ln \left(\frac{8r_{\text{eff}}}{r_{\text{cs}}} \right). \quad (3.5)$$

The oscillating current is accompanied by the accumulation of charges Q with different signs at the ends of both arms corresponding to a plate capacitor. The resulting voltage drop U_{cap} between the two plates is determined by the capacity \mathcal{C} ,

$$U_{\text{cap}} = \frac{1}{\mathcal{C}} Q. \quad (3.6)$$

For the geometry considered here, the capacity is approximately

$$\mathcal{C} = \frac{A}{4\pi b}. \quad (3.7)$$

We include Ohmic losses via the resistance \mathcal{R} ,

$$\mathcal{R} = \frac{L_{\text{eff}}}{\sigma(\omega) A}, \quad (3.8)$$

which is obtained by using the Drude conductivity $\sigma(\omega)$ from Drude theory,

$$\sigma(\omega) = \frac{\frac{e^2 n_{3\text{D}} \tau}{m}}{1 - i\omega\tau} \quad (3.9)$$

where e is the elementary charge, $n_{3\text{D}}$ the concentration of the conducting electrons, and m denotes the electron mass. The relaxation time scale is denoted by τ . The first calculations of the resonance frequency utilizing circuit theory have been performed neglecting the frequency dependency of the conductivity. However, it has turned out that the inclusion of the frequency dependency of the conductivity is necessary in order to obtain quantitative results. The frequency dependency takes the inertia of the electrons into account and is a direct consequence of Newton's equation [45],

$$m \left(\frac{dv}{dt} + \frac{v}{\tau} \right) = eE_{\text{ext}}, \quad (3.10)$$

where v is the electron velocity.

If one plugs equation (3.9) into equation (3.8), the contribution from the electrons' inertia can be recast into the form of an inductance. In the literature this term is referred to as kinetic inductance [46] or electron self-inductance [14, 15],

$$\mathcal{L}_{\text{kin}} = \frac{L m}{e^2 n_{3\text{D}} A}. \quad (3.11)$$

It is also known from the literature that the kinetic inductance is more important than the regular inductance describing the magnetic restoring forces, when the system size is decreased. The total inductance is then the sum of both inductances, $\mathcal{L}_{\text{tot}} = \mathcal{L} + \mathcal{L}_{\text{kin}}$.

One finally arrives at

$$\mathcal{L}_{\text{tot}} \dot{I} + \mathcal{R} I + \frac{1}{\mathcal{C}} Q = U_{\text{ext}}. \quad (3.12)$$

Introducing the frequency dependent impedance $Z(\omega)$,

$$Z(\omega) = -i\omega \mathcal{L}_{\text{tot}} + \mathcal{R} + \frac{1}{-i\omega \mathcal{C}}, \quad (3.13)$$

equation (3.12) can be recast into the following form

$$I = \frac{1}{Z} U_{\text{ext}}, \quad (3.14)$$

which is simply a generalization of Ohm's Law. The resonance condition for the circuit dictates that $Z(\omega)$ vanishes,

$$z_{\mathcal{LRC}} = \sqrt{\frac{1}{\mathcal{L}_{\text{tot}}\mathcal{C}} - \frac{\mathcal{R}^2}{4\mathcal{L}_{\text{tot}}^2}} - i\frac{\mathcal{R}}{2\mathcal{L}_{\text{tot}}}. \quad (3.15)$$

The real part of $z_{\mathcal{LRC}}$ is the resonance frequency, which for small Ohmic losses depends only on \mathcal{L}_{tot} and \mathcal{C} ,

$$\omega = \frac{1}{\sqrt{\mathcal{L}_{\text{tot}}\mathcal{C}}}. \quad (3.16)$$

The imaginary part describes the damping of the excitation.

3.2 Resonance frequency

We now attempt to address the following question: How does the resonance frequency scale as a function of the system size? In order to answer this query, the resonance frequency is initially calculated from the circuit parameters in the limit of small damping, by employing equation (3.16) and utilizing the expressions from the two previous sections, namely,

$$\omega^2 = \frac{1}{\frac{m}{4\pi e^2 n_{3D}} \left(\frac{L}{b}\right) + \frac{1}{c^2} A \left(\frac{r_{\text{eff}}}{b}\right) \ln \left(8 \frac{r_{\text{eff}}}{r_{\text{cs}}}\right)}. \quad (3.17)$$

For practical applications, one is interested in the dependence of the resonance frequency on the system size. For this purpose one introduces a dimensionless scaling factor s for all lengths. The first term in the denominator is independent of s and the second term scales as s^2 . For small system sizes, corresponding to the limit $s \rightarrow 0$, the resonance frequency is independent of the system size and saturates [15, 46]. We will show in Chapter 5 that this is the typical behavior of 3D plasmons. The second term dominates, if one increases the system size, $s \rightarrow \infty$. In this limit the resonance frequency drops off with the reciprocal system size. The scaling behavior shows that it is not possible to go beyond the saturation threshold. However, when quantum corrections are included, the scaling behavior changes significantly in the limit $s \rightarrow 0$.

3.3 Calculation of response properties

Having obtained an expression for the current as a response to an external voltage, we can now calculate all electromagnetic dipole moments that are necessary for determining the

polarizabilities. The polarizabilities are defined by expanding the induced dipole moments p_y and m_z in terms of the applied electric and magnetic fields,

$$\begin{pmatrix} p_y \\ m_z \end{pmatrix} = \begin{pmatrix} \alpha_{yy} & \beta_{\text{EM},yz} \\ \beta_{\text{ME},zy} & \gamma_{zz} \end{pmatrix} \begin{pmatrix} E_{\text{ext},y} \\ B_{\text{ext},z} \end{pmatrix}. \quad (3.18)$$

The external electric field $E_{\text{ext},y}$ pointing into the y -direction will lead to an external voltage drop $U_{\text{ext}} = E_{\text{ext}}b$ at the condenser plates. If one assumes that the separated charges are mainly located at the condenser plates, one has $p_y = Qb$ and arrives at

$$\alpha_{yy} = \frac{\frac{b^2}{\mathcal{L}_{\text{tot}}}}{-\omega^2 - i\omega\frac{\mathcal{R}}{\mathcal{L}_{\text{tot}}} + \frac{1}{\mathcal{L}_{\text{tot}}\mathcal{C}}}. \quad (3.19)$$

In addition to the electric dipole moment, there is also a magnetic dipole moment associated with the transverse current. The area of the coil is approximated by $A_{\text{coil}} = L^2/(4\pi)$ and one obtains a magnetic dipole moment of $m_3 = IA_{\text{coil}} = \frac{1}{c}L^2I/(4\pi)$. Thus, the polarizability that describes the magnetic dipole moment induced by an external electric field is given by

$$\beta_{\text{ME},yz} = \frac{\frac{i\omega b L^2}{4\pi c \mathcal{L}_{\text{tot}}}}{-\omega^2 - i\omega\frac{\mathcal{R}}{\mathcal{L}_{\text{tot}}} + \frac{1}{\mathcal{L}_{\text{tot}}\mathcal{C}}}. \quad (3.20)$$

For the calculation of the response to the external magnetic field B_z , one uses the Law of Induction, $U_{\text{ext}} = i\omega B_z A_{\text{coil}}$, in order to determine the induced voltage $U_{\text{ext}} = i\omega(l + l')^2 B_z/(4\pi)$. From the induced dipole moments, one finally obtains the following expression:

$$\beta_{\text{EM},zy} = \frac{-\frac{i\omega b L^2}{4\pi c \mathcal{L}}}{-\omega^2 - i\omega\frac{\mathcal{R}}{\mathcal{L}_{\text{tot}}} + \frac{1}{\mathcal{L}_{\text{tot}}\mathcal{C}}}, \quad (3.21)$$

$$\gamma_{zz} = \frac{\frac{\omega^2 L^4}{16\pi^2 c^2 \mathcal{L}_{\text{tot}}}}{-\omega^2 - i\omega\frac{\mathcal{R}}{\mathcal{L}_{\text{tot}}} + \frac{1}{\mathcal{L}_{\text{tot}}\mathcal{C}}}. \quad (3.22)$$

All polarizabilities have in common that they exhibit a resonance at the same frequency. If one neglects any interaction between the resonators, the macroscopic response functions read

$$\varepsilon_{yy} = 1 + 4\pi n_{\text{SRR}} \alpha_{yy}, \quad (3.23)$$

$$\xi_{yz} = 4\pi n_{\text{SRR}} \beta_{\text{EM},yz}, \quad (3.24)$$

$$\zeta_{zy} = 4\pi n_{\text{SRR}} \beta_{\text{ME},zy}, \quad (3.25)$$

$$\mu_{zz} = 1 + 4\pi n_{\text{SRR}} \gamma_{zz}. \quad (3.26)$$

This equation will be derived later in Chapter 12.

3.4 Index of refraction

If one considers electromagnetic waves with a wave vector that is parallel to the x -axis, and with an electric field vector that is parallel to the y -axis, the corresponding index of refraction can be expressed as

$$n^2 = \epsilon_{yy}\mu_{zz} - \xi_{yz}\zeta_{zy}, \quad (3.27)$$

or

$$n^2 = 1 + 4\pi n_{\text{SRR}} (\alpha_{yy} + \gamma_{zz}) + 16\pi^2 n_{\text{SRR}}^2 (\alpha_{yy}\gamma_{zz} - \beta_{\text{ME},yz}\beta_{\text{EM},zy}). \quad (3.28)$$

A detailed derivation of this equation will be provided in Chapter 13. Looking now at the explicit expressions as given by equations (3.19-3.22), one observes that the last term in equation (3.28) in brackets vanishes, giving

$$n^2 = 1 + 4\pi n_{\text{SRR}} (\alpha_{22} + \gamma_{33}). \quad (3.29)$$

One takes the square root of both sides of equation (3.29) to determine n . The branch cut must be chosen such that the imaginary part of n is positive in order to describe a passive material. Aiming for the situation where the real part of n becomes negative, the imaginary part of n^2 must therefore be negative. However, according to equation (3.29) the imaginary part of n^2 is always positive, as the imaginary parts of the polarizabilities are positive. Therefore, the split ring resonator alone cannot constitute a medium. The product of α_{yy} and γ_{zz} could provide a negative imaginary part, but this contribution is exactly cancelled by the bianisotropy. This illustrates the parasitic effect of the bianisotropy [34].

By adding another component negative refraction can still be obtained. A widely-used choice are cut-wires with electric resonances in the vicinity of the SRR resonances. In the dilute limit, one can add the contribution from the cut-wires directly to the macroscopic dielectric constant, as follows,

$$\epsilon_{22} = 1 + 4\pi n_{\text{SRR}}\alpha_{yy} + 4\pi n_{\text{WIRE}}\tilde{\alpha}_{yy}, \quad (3.30)$$

where n_{WIRE} denotes the density of the cut-wires and $\tilde{\alpha}_{22}$ their polarizabilities. The index of refraction is then determined via

$$n^2 = 1 + 4\pi n_{\text{SRR}} (\alpha_{yy} + \gamma_{zz}) + 4\pi n_{\text{WIRE}}\tilde{\alpha}_{yy} + 16\pi n_{\text{SRR}}n_{\text{WIRE}}\tilde{\alpha}_{yy}\gamma_{zz}. \quad (3.31)$$

With equation (3.31) it can be seen that the medium can now exhibit a negative index of refraction. This result has been demonstrated experimentally [33, 47].

Chapter 4

Basic linear response theory

The basic linear response formalism that is needed in order to understand the behavior of matter in electromagnetic fields is presented in this chapter. We start by reviewing major results from general linear response theory, and then analyze the density response and discuss two types of elementary excitations of electronic systems: single-particle excitations and plasmons. After this we proceed next to the conductivity enabling us to determine the dynamical response to arbitrary electromagnetic fields. We then discuss the connection of the results here with the circuit models from the previous chapter. We further analyze the different damping mechanisms of the elementary excitations under consideration. By introducing eigenmode expansions of the response functions we set up the fundamental equations that lay the foundation for the continuum model discussed in Chapter 6.

4.1 General response theory

We start with a Hamiltonian in second quantized form that consists of an unperturbed part \hat{H}_0 whose eigenvectors $|i\rangle$ and eigenvalues ϵ_i are known, and a second part \hat{V} describing an external perturbation:

$$\hat{H} = \hat{H}_0 + \hat{V} = \sum_i \epsilon_i \hat{c}_i^\dagger \hat{c}_i + \underbrace{\sum_{ij} B_{ij} \hat{c}_i^\dagger \hat{c}_j}_{\hat{B}} F_{\text{ext}}(t), \quad (4.1)$$

where we call $F_{\text{ext}}(t)$ external force. We are interested in the effect of the external force on the expectation value of an observable $\hat{A} = \sum_{ij} A_{ij} \hat{c}_i^\dagger \hat{c}_j$. We assume that the perturbation vanishes for $t \rightarrow -\infty$. We employ standard time-dependent perturbation theory at finite temperature and work in the interaction picture (denoted by a subscript I), such that the

time-evolution of the operators is determined by the unperturbed time evolution, \hat{U}_0 ,

$$\hat{A}_I = \hat{U}_0^\dagger(t) \hat{A} \hat{U}_0(t), \quad (4.2)$$

where $\hat{U}_0(t)$ reads as follows,

$$\hat{U}_0(t) = \exp\left(-i\hat{H}_0 t\right). \quad (4.3)$$

Note that we set $\hbar = 1$. So one has for \hat{A}_I ,

$$\hat{A}_I(t) = \sum_{ij} A_{ij} \exp(i(\epsilon_i - \epsilon_j)t) \hat{c}_i^\dagger \hat{c}_j. \quad (4.4)$$

The time-evolution of the states is given by

$$|\Psi_I(t)\rangle = \hat{U}_I |\Psi(-\infty)\rangle, \quad (4.5)$$

and time-evolution of the grand-canonical density operator $\hat{\rho}_I$ in the interaction picture is given as

$$\hat{\rho}_I(t) = \hat{U}_I^\dagger(t) \hat{\rho}_0 \hat{U}_I(t), \quad (4.6)$$

where $\hat{\rho}_0$ is the density operator of system without the external perturbation. The time-evolution operator \hat{U}_I is defined as

$$\hat{U}_I(t) = \hat{\mathcal{T}} \exp\left(-i \int_{-\infty}^t dt' \hat{B}_I(t') F_{\text{ext}}(t')\right), \quad (4.7)$$

where $\hat{\mathcal{T}}$ is the time ordering operator.

The change in the expectation value of \hat{A} is given by

$$\delta A(t) = \text{Tr}(\hat{\rho}_I(t) \hat{A}_I(t)) - \text{Tr}(\hat{\rho}_0 \hat{A}). \quad (4.8)$$

In the case of small perturbations, one can perform a Taylor series expansion of the time-evolution operator to first order in the external force, $F_{\text{ext}}(t)$, as follows:

$$\delta A(t) = \int_{-\infty}^t dt' i \text{Tr} \left(\hat{\rho}_0 [\hat{A}_I(t), \hat{B}_I(t')] \right) F_{\text{ext}}(t'). \quad (4.9)$$

We are now in the position to define the dynamic susceptibility as

$$\chi_{AB}(t, t') = i\Theta(t - t') \text{Tr} \left(\hat{\rho}_0 [\hat{A}_I(t), \hat{B}_I(t')] \right), \quad (4.10)$$

where the step function Θ expresses that the response is causal, i.e., that the reaction of the system will always occur at a later time than that of the stimulus of the external

force. Hence, the response function is described as retarded. Using the definition of the response function from equation (4.10), equation (4.9) can be rewritten in more concise form as follows:

$$\delta A(t) = \int_{-\infty}^{\infty} dt' \chi_{AB}(t, t') F_{\text{ext}}(t'). \quad (4.11)$$

For further evaluation we employ the following expression,

$$\text{Tr}(\hat{\rho}_0 \hat{c}_i^\dagger \hat{c}_j) = f(\epsilon_i) \delta_{ij} \quad (4.12)$$

where the Fermi function f for a given chemical potential μ is denoted as

$$f(\epsilon) = \frac{1}{1 + \exp(\beta(\epsilon - \mu))}. \quad (4.13)$$

Utilizing equations (4.10) and (4.4)-(4.13), we now arrive at an expression for the susceptibility:

$$\chi_{AB}(t, t') = i\Theta(t - t') \sum_{ij} A_{ij} B_{ji} (f(\epsilon_i) - f(\epsilon_j)) \exp(i(\epsilon_i - \epsilon_j)(t - t')). \quad (4.14)$$

The fact that the susceptibility depends only on the difference between the two time variables highlights the time translational invariance of equilibrium correlators. We now consider the Laplace transform of equation (4.14) and use the convolution theorem to obtain

$$\delta A(z) = \chi_{AB}(z) F_{\text{ext}}(z) \quad (4.15)$$

where $z = \omega + i\eta$ and $\eta \in \mathbb{R}^+$, in order to ensure the convergence of the Laplace transform of χ_{AB} . Equation (4.15) implies that the system under consideration reacts in the linear regime with the same frequency as the external force. The Laplace transform of χ_{AB} reads

$$\chi_{AB}(z) = \sum_{ij} A_{ij} B_{ji} \frac{f(\epsilon_i) - f(\epsilon_j)}{\epsilon_j - \epsilon_i - z}. \quad (4.16)$$

In the limit $\eta \rightarrow 0^+$, one can employ the following expression,

$$\lim_{\eta \rightarrow 0^+} \frac{1}{\epsilon_j - \epsilon_i - \omega - i\eta} = \mathcal{P} \frac{1}{\epsilon_j - \epsilon_i - \omega} + i\pi \delta(\epsilon_j - \epsilon_i - \omega) \quad (4.17)$$

where \mathcal{P} denotes the principal value. Note that the susceptibility acquires an imaginary part when the frequency of the external perturbation exactly matches the excitation energy $\epsilon_j - \epsilon_i$. In this case the system absorbs power [45, 48] according to

$$P(\omega) = \frac{1}{2} \omega F_{\text{ext}}^*(\omega) \text{Im}(\chi_{BB}(\omega)) F_{\text{ext}}(\omega). \quad (4.18)$$

In real systems, however, there are processes that lead to a decay of the excited states. Note that these processes are not contained in the original Hamiltonian. In principle one could add coupling terms to a bath or interaction effects in order to include dephasing processes. Solving then for the new single-particle states leads to shifted energy levels. In addition, the excited state energies acquire an imaginary part being the reciprocal lifetime. In the following, we will assume that the lifetimes of all excited states are identical. Repeating then the calculation of the susceptibility leads to the same result as in equation (4.16), but where η has a finite value. Consequently, the imaginary part of the response function in the vicinity of a resonance is not a δ -function anymore, but has a Lorentzian lineshape,

$$\Im(\chi_{BB}(\omega)) = \sum_{ij} A_{ij} B_{ji} (f(\epsilon_i) - f(\epsilon_j)) \frac{\eta}{(\epsilon_j - \epsilon_i - \omega)^2 + \eta^2}. \quad (4.19)$$

Now the system can absorb power, even if the resonance condition $\omega = \epsilon_j - \epsilon_i$ is not exactly satisfied. The absorbed power will have a maximum on resonance, so one can identify excitations of a system in a certain frequency window by calculating the absorbed power. The position of each peak determines the resonance frequency, while the peak-width gives the damping.

We will consider the physics of the relaxation processes in this thesis by using a finite value for η . A summary of the most important damping mechanisms will be given in Section 4.4.

So far an effectively non-interacting system has been considered. In general, however, the Hamiltonian contains (i) a non-interacting piece \hat{H}_0 , (ii) an interacting piece, and (iii) an external perturbation, respectively:

$$\hat{H} = \hat{H}_0 + \sum V_{ijkl} \hat{c}_i^\dagger \hat{c}_j^\dagger \hat{c}_k \hat{c}_l + \hat{B}f(t). \quad (4.20)$$

Equation (4.20) denotes a much more complicated situation where one not only performs perturbation theory in the external forces, but also in the presence of interactions. We shall investigate the density response and show in the next section in doing so, how this problem, in principle, can be solved to linear order in the external perturbation. The Random Phase Approximation (RPA) shall also be introduced and systematic improvements to this approximation shall be discussed.

4.2 Density response and RPA

4.2.1 Response functions

The coupling of an electronic system to an external scalar potential Φ_{ext} is described by the following Hamiltonian,

$$\hat{H} = \int d^3\mathbf{r} \hat{\rho}(\mathbf{r})\Phi_{\text{ext}}(\mathbf{r}). \quad (4.21)$$

The induced (charge) density $\delta\rho$ is defined as the response to the potential, and is given by

$$\delta\rho(\mathbf{r}, \omega) = \int d^3\mathbf{r}' \chi_{\text{ext}}(\mathbf{r}, \mathbf{r}', \omega)\Phi_{\text{ext}}(\mathbf{r}', \omega) \quad (4.22)$$

where χ_{ext} is the (retarded) density-density correlation function,

$$\chi_{\text{ext}}(\mathbf{r}, \mathbf{r}', \omega) = \int dt e^{i\omega t - \eta t} \langle [\hat{\rho}(\mathbf{r}, t), \hat{\rho}(\mathbf{r}', 0)] \rangle \Theta(t). \quad (4.23)$$

We shall make use of the shorthand notation for the integral in equation (4.23)

$$\delta\rho = \chi_{\text{ext}}\Phi_{\text{ext}} \quad (4.24)$$

in this body of work. We define the total potential $\Phi_{\text{tot}} = \Phi_{\text{ext}} + \Phi_{\text{ind}}$ as the sum of the external potential and an induced Hartree potential Φ_{ind} , given by

$$\Phi_{\text{ind}} = \tilde{v}^{\text{H}}\delta\rho, \quad (4.25)$$

with

$$\tilde{v}^{\text{H}}(\mathbf{r}, \mathbf{r}') = \frac{1}{|\mathbf{r} - \mathbf{r}'|}. \quad (4.26)$$

We express the irreducible response function χ_{irr} as

$$\delta\rho = \chi_{\text{irr}}\Phi_{\text{tot}} = \chi_{\text{ext}}\Phi_{\text{ext}} \quad (4.27)$$

and can then solve for the response function in terms of the irreducible function,

$$\chi_{\text{ext}} = \varepsilon^{-1}\chi_{\text{irr}}. \quad (4.28)$$

Here we have introduced the dielectric function ε , defined as:

$$\varepsilon(\mathbf{r}, \mathbf{r}', \omega) = \delta(\mathbf{r} - \mathbf{r}') - \int d^3\mathbf{r}'' \chi_{\text{irr}}(\mathbf{r}, \mathbf{r}'', \omega)\tilde{v}^{\text{H}}(\mathbf{r}'', \mathbf{r}'). \quad (4.29)$$

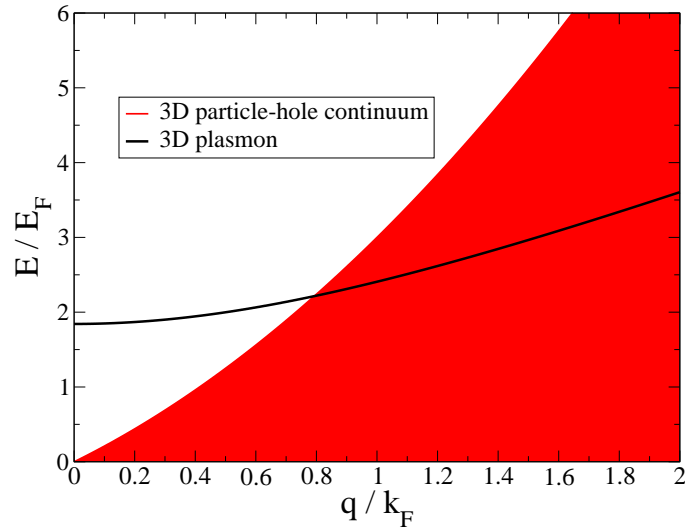


Figure 4.1: Single-particle excitations and plasmons for a homogeneous electron gas in three dimensions.

4.2.2 Meaning of the poles

The poles of the external response function correspond to charge-neutral excitations of the system under consideration: single-particle excitations, excitons or plasmons. Charge-neutral means that the charge of the system is not changed during the excitation process. Before we relate the different excitations to the response functions, we give a brief overview over the possible charge-neutral electronic excitations in metals, insulators, and semiconductors:

- i) In metals one distinguishes two types of excitations: intraband single-particle excitations and plasmons. The intraband single-particle excitations are just particle-hole pairs where the excitation energy corresponds to the energy difference of two single-particle states. In contrast, the energy scale of the plasmonic excitations is mainly determined by the classical restoring forces.
- ii) In insulators and semiconductors one observes interband single-particle excitations and interband plasmons. In addition one also has excitons, i.e. bound particle-hole states. In this case the energy is lowered compared to the single-particle excitation energy due to the attraction of the electron and the hole via the Coulomb interaction.

In macroscopic metallic systems, the long wavelength plasmon peaks and the single-particle resonances are well separated, as can be seen from Figure 4.1.

When the plasmon dispersion penetrates the particle-hole continuum, the plasmons decay due to Landau damping.

We will now analyze how the resonances are changed when going from χ_{irr} to χ_{ext} . Assume now that the poles of χ_{irr} are known. If a resonance is not accompanied by a response of the density, the Hartree potential vanishes and the resonance therefore appears as a pole of both χ_{irr} and χ_{ext} . In order to understand what happens in the other case, we scale the Hartree potential by a factor ν with $0 \leq \nu \leq 1$, i.e. \tilde{v}^{H} in equation (4.29) is replaced by $\nu\tilde{v}^{\text{H}}$. The poles of χ_{ext} then equal the poles of χ_{irr} in the limit $\nu \rightarrow 0$. If one increases now ν , the shape of the induced density may change due to a redistribution of the density driven by the Hartree potential. The total excitation energy, i.e., the energy that corresponds to a pole of χ_{ext} , then comprises the original energy, i.e., the energy that corresponds to a pole of χ_{irr} , and the electric energy stored in the density response. So each pole of χ_{irr} must flow to one pole of χ_{ext} when ν goes from zero to one. As the shifted poles are not present in χ_{irr} , they must be zero-modes of the dielectric function. This means that there exists at least one eigenvector at the excitation energy with an eigenvalue of zero. In this work, we are interested in modes that are accompanied by a response of the density, so we can identify these modes by looking for frequencies at which ε has a zero-mode. The remaining task is then to distinguish single-particle excitations and plasmons. Plasmons are standing charge density waves with a long wavelength. The charge oscillations originate from the collective motion of electrons. Note that the long-range part of the Coulomb interaction sustains the structure of the plasmon. Each plasmon is accompanied by strong electric fields making these modes very sensitive to a scaling of ν . The normalized induced density corresponding to the plasmon will be called plasmonic density profile $\pi(\mathbf{r})$. The plasmonic excitations of various systems will be studied in great detail in Chapter 7. Compared to the plasmons, the induced density of a single-particle excitation is either localized or spatially fluctuating with short wavelengths, resulting from an incoherent superposition of excitations described by χ_{irr} . Therefore, the restoring forces are rather weak compared to plasmons. So these modes will barely move with increasing ν .

4.2.3 Random Phase Approximation

In the meantime, our immediate task is the calculation of χ_{irr} . A common used approximation is the Random Phase Approximation, where one approximates χ_{irr} by the response function of the non-interacting system [49]. That is, one uses equation (4.15), where the matrix elements are calculated with the eigenfunctions $\psi_{\mu}(\mathbf{r})$ of the Hartree-Hamiltonian and the energies are the corresponding eigenvalues ϵ_{μ} . We shall denote the response func-

tion of the non-interacting system by a superscript (0). The explicit expression for the density-density correlation function thus reads:

$$\chi^{(0)}(\mathbf{r}, \mathbf{r}') = e^2 \sum_{\mu, \nu} \psi_{\mu}(\mathbf{r}) \psi_{\nu}(\mathbf{r}') \psi_{\mu}(\mathbf{r}) \psi_{\nu}(\mathbf{r}') \frac{f(\epsilon_{\mu}) - f(\epsilon_{\nu})}{\epsilon_{\nu} - \epsilon_{\mu} - \omega - i\eta}. \quad (4.30)$$

The diagrammatic representation of the density propagator is given in Figure 4.2. A common name for this diagram is bubble-diagram. For an introduction to diagrammatic

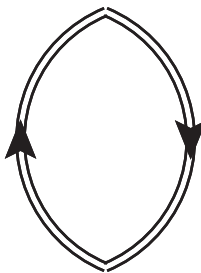


Figure 4.2: Diagrammatic representation of the density propagator.

techniques we refer to the standard textbooks [50, 51].

In the zero temperature limit, the Fermi functions are simply Θ -functions. This means that there exist contributions only, if one index corresponds to an occupied state and the other one to an unoccupied state. These particle-hole pairs correspond to single-particle excitations of the non-interacting system. If one now goes to the interacting case, there are two possible elementary excitations: (i) renormalized single-particle excitations (RSPEs), and (ii) plasmons. The transition from the non-interacting to the interacting case can also be depicted by using Feynman diagrams as shown in Figure 4.3.

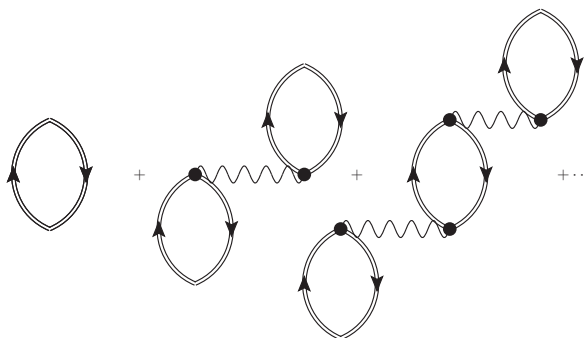


Figure 4.3: Summation of the bubble-diagrams.

In order to demonstrate the different behavior of the different types of excitations with increasing Coulomb interaction, we give a simple example by considering a linear chain

with 50 sites at half-filling. The results are depicted in Figure 4.4. One observes that the square of the frequencies of some modes grows linearly with the interaction strength. These modes are plasmonic excitations. The remaining modes barely move, so they correspond to RSPEs. We will give a more detailed analysis of the resonances in Section 7.2.

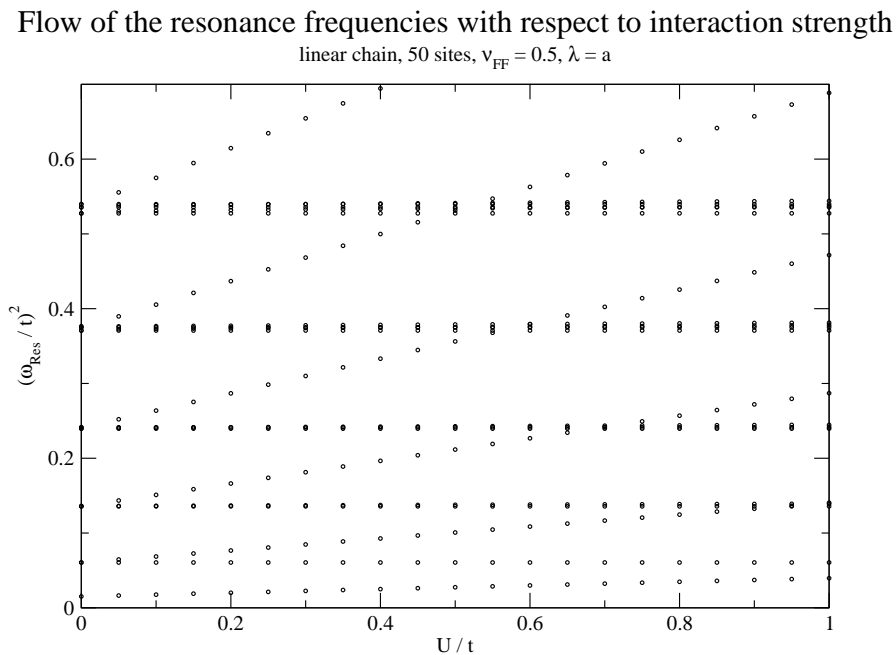


Figure 4.4: Flow of the excitation energies with increasing electron-electron interaction strength.

4.2.4 Beyond the Random Phase Approximation

In order to systematically improve upon the Random Phase Approximation, one must take into account further corrections for the single-particle levels and the response function. The corrections for the single-particle levels will be discussed when the Hartree-Fock method is introduced. For the moment we will only consider contributions to the response function. Within RPA, the electron-hole pairs constituting the response function are non-interacting. One can now take the bare Coulomb interaction of the electrons and holes self-consistently into account, leading to a lowering of the electron-hole excitation energies. The corresponding method is called time-dependent Hartree-Fock or RPAE (Random Phase Approximation including exchange) [52, 53]. The inclusion of

Fock exchange is depicted in the diagrammatic representation by a ladder summation in the bubble diagrams as shown in Figure 4.5. In real systems, however, the Coulomb



Figure 4.5: Diagrammatic representation of the ladder summation.

interaction is screened due to the presence of other particles. A perturbative treatment of the inclusion of screening can be found in the literature [54, 55]. The full self-consistent calculations requires solving the so-called Bethe-Salpeter equation that determines the effective electron-hole interaction. The corresponding diagrams are depicted in Figure 4.6. Solving the Bethe-Salpeter equation is quite common in solid state physics and has

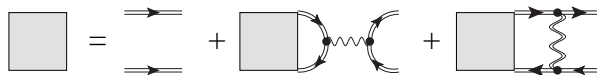


Figure 4.6: Diagrammatic representation of Bethe-Salpeter equation.

recently been applied to molecules [56, 57, 58]. Going beyond RPA is necessary if one wants to describe excitons.

4.3 Dynamical conductivity

So far, only longitudinal electric fields have been considered. Longitudinal means the curl vanishes, so that such fields may be derived as the gradient of the scalar potential. In this section we now generalize the response formalism such that transverse electric fields and magnetic fields can be taken into account, too. Transverse fields have the properties that their divergence vanishes. For that reason, the magnetic field can be obtained as the curl of the vector potential \mathbf{A} . We introduce the external dynamical conductivity $\sigma_{\text{ext}}(\mathbf{r}, \mathbf{r}', \omega)$ where the spatial dependence arises from the fact that both the induced current density $\delta\mathbf{j}(\mathbf{r}, \omega)$ and the external electric field $\mathbf{E}_{\text{ext}}(\mathbf{r}, \omega)$ may depend on the position. The induced current density is given within the linear regime by

$$\delta\mathbf{j}(\mathbf{r}, \omega) = \int d^3\mathbf{x}' \sigma_{\text{ext}}(\mathbf{r}, \mathbf{r}', \omega) \mathbf{E}_{\text{ext}}(\mathbf{r}', \omega), \quad (4.31)$$

and we once again utilize the shorthand notation $\delta\mathbf{j} = \sigma_{\text{ext}}\mathbf{E}_{\text{ext}}$. The induced current itself is the source of an induced electric field \mathbf{E}_{ind} we now want to calculate. We employ the Coulomb gauge,

$$\text{div}\mathbf{A} = \mathbf{0}, \quad (4.32)$$

so the wave equation for \mathbf{A} reads

$$\square\mathbf{A} = \frac{4\pi}{c}\mathbf{j}_{\text{trans}} \quad (4.33)$$

This means that the restoring longitudinal electric fields are determined by the longitudinal current, \mathbf{j}_{long} , while transverse fields arise from the transverse current, $\mathbf{j}_{\text{trans}}$. The induced density $\delta\rho$ is determined via the continuity equation,

$$-i\omega\delta\rho + \text{div}\delta\mathbf{j} = 0, \quad (4.34)$$

that gives rise to the longitudinal induced electric field $\mathbf{E}_{\text{ind,long}}$ which, in turn, is the negative gradient of the Hartree potential (4.25),

$$\mathbf{E}_{\text{ind,long}}(\mathbf{r}, \omega) = -\text{grad} \int d^3\mathbf{r}' \frac{\delta\rho(\mathbf{r}', \omega)}{|\mathbf{r} - \mathbf{r}'|}. \quad (4.35)$$

Utilizing the continuity equation (4.34) and

$$\Delta \frac{1}{|\mathbf{r} - \mathbf{r}'|} = -4\pi\delta(\mathbf{r} - \mathbf{r}') \quad (4.36)$$

one finds

$$\delta\mathbf{j}_{\text{long}} = -\frac{i\omega}{4\pi}\mathbf{E}_{\text{ind,long}}. \quad (4.37)$$

In order to calculate the induced transverse electric field, one first has to determine the transverse current, given by:

$$\delta\mathbf{j}_{\text{trans}} = \delta\mathbf{j} - \delta\mathbf{j}_{\text{long}} = \delta\mathbf{j} + \frac{i\omega}{4\pi}\mathbf{E}_{\text{ind,long}}. \quad (4.38)$$

The transverse vector potential \mathbf{A} is given as a solution of the wave equation with the transverse current as source,

$$\mathbf{A}(\mathbf{r}, \omega) = \frac{1}{c} \int d^3\mathbf{r}' \frac{\exp(i\omega|\mathbf{r} - \mathbf{r}'|/c)}{|\mathbf{r} - \mathbf{r}'|} \delta\mathbf{j}_{\text{trans}}(\mathbf{r}'). \quad (4.39)$$

The transverse electric field results directly from the vector potential \mathbf{A} via

$$\mathbf{E}_{\text{ind,trans}} = i\frac{\omega}{c}\mathbf{A}. \quad (4.40)$$

Adding the longitudinal and the transverse induced electric fields together yields the total induced field,

$$\mathbf{E}_{\text{ind}} = \left(-\frac{1}{i\omega} v^{\text{E}} + i\omega \left[v^{\text{M}} + \frac{1}{4\pi} v^{\text{M}} v^{\text{E}} \right] \right) \delta \mathbf{j}, \quad (4.41)$$

where we have introduced the matrices v^{E} and v^{M} ,

$$v_{ij}^{\text{E}}(\mathbf{r}, \mathbf{r}') = \frac{\partial}{\partial r_i} \frac{1}{|\mathbf{r} - \mathbf{r}'|} \frac{\partial}{\partial r'_j}, \quad (4.42)$$

$$v_{ij}^{\text{M}}(\mathbf{r}, \mathbf{r}') = \frac{1}{c^2} \delta_{ij} \frac{\exp(i\omega|\mathbf{r} - \mathbf{r}'|/c)}{|\mathbf{r} - \mathbf{r}'|}. \quad (4.43)$$

The total electric field \mathbf{E}_{tot} is just the sum of the external and the induced fields

$$\mathbf{E}_{\text{tot}} = \mathbf{E}_{\text{ext}} + \mathbf{E}_{\text{ind}}. \quad (4.44)$$

With the use of the following expression

$$\delta \mathbf{j} = \sigma_{\text{irr}} \mathbf{E}_{\text{tot}} \quad (4.45)$$

we can define the irreducible conductivity σ_{irr} that can be calculated in a systematic manner via perturbation theory. Plugging equation (4.41) into equation (4.44) and utilizing equation (4.45), the response to the external field can be written in terms of σ_{irr} which is the main result of this section:

$$\boxed{\delta \mathbf{j} = \frac{1}{\sigma_{\text{irr}}^{-1} - i\omega[v^{\text{M}} + v^{\text{M}}v^{\text{E}}] + \frac{1}{i\omega}v^{\text{E}}} \mathbf{E}_{\text{ext}}}. \quad (4.46)$$

Note that the irreducible conductivity is just the dynamical conductivity that is measured in experiments, i.e., when one detects the total current and the total electric field. We now introduce a matrix Σ via

$$\Sigma(\omega) = \sigma_{\text{irr}}^{-1}(\omega) - i\omega[v^{\text{M}}(\omega) + v^{\text{M}}(\omega)v^{\text{E}}] + \frac{1}{i\omega}v^{\text{E}} \quad (4.47)$$

The resonance frequencies and the corresponding life times of renormalized single-particle and plasmonic excitations are given as the complex roots z of the determinant of Σ . Compared to the density response introduced in the previous section, the possible plasmonic excitations here are not only limited to longitudinal plasmons, but transverse ones are also included.

As a simple example we calculate the plasmonic excitations of a homogeneous electron gas in three dimensions. We approximate the irreducible conductivity by the Drude conductivity in the limit of zero damping,

$$\sigma_{\text{irr}}(\omega) = \frac{1}{-i\omega} \frac{e^2 n}{m}. \quad (4.48)$$

For the calculation of the longitudinal modes one needs v^E ,

$$v^E = \frac{4\pi}{q^2} (-q^2) = -4\pi, \quad (4.49)$$

and one has

$$\Sigma(\omega) = -i\omega \frac{m}{e^2 n} - \frac{1}{i\omega} 4\pi. \quad (4.50)$$

The longitudinal resonance frequency derived from the condition $\Sigma(\omega) = 0$ reads

$$\omega = \sqrt{\frac{4\pi e^2 n}{m}}, \quad (4.51)$$

which is just the usual plasma frequency in three dimensions. In the transverse case one needs v^M ,

$$v^M(\omega) = \frac{1}{k^2 - \omega^2/c^2}. \quad (4.52)$$

Repeating the same steps as in the longitudinal case, one finds the following dispersion relation for the transverse modes

$$\omega = \sqrt{\frac{4\pi e^2 n}{m} + c^2 k^2}, \quad (4.53)$$

recovering a well-known result [45]. The dispersion of the transverse plasmons comprises the longitudinal plasma frequency and the free dispersion of electromagnetic wave. Thus, the transverse plasmon can be considered as a combined excitation of the electron gas and the electromagnetic field. Such excitations are usually called plasmon polaritons.

If one now compares the frequency dependence of Σ with the frequency dependence of the impedance, it can be seen that the longitudinal electric restoring forces described by v^E are equivalent to the classical capacitance. The magnetic restoring forces described by v^M , on the other hand, are the analogue of the inductance. It should be noted that v^M is frequency dependent, whereas in the common \mathcal{LRC} models one works with frequency independent inductances neglecting retardation effects. The non-trivial part is the inverse of the dynamical conductivity. This quantity contains all information about the damping, which shall be discussed in the next section. It furthermore contains the physics of the acceleration of the particles like in Drude theory, leading to an additional inductance term that is proportional to the frequency. Lastly, there also exist quantum corrections. We shall see later on that single-particle excitations lead to a renormalization of the capacitance. Note that v^E , v^M , and σ_{irr} are matrices, whereas \mathcal{L} , \mathcal{R} , and \mathcal{C} are numbers.

4.4 Damping

The induced charge and current densities will oscillate, even if the external perturbation is switched off. Due to relaxation processes, however, the amplitude of the oscillations will decay in time. If the typical time scale of the relaxation dynamics is much lower than the characteristic time scales of the oscillation, a Markow approximation can be employed [48], producing the following effective equation of motion in the absence of external fields,

$$\partial_t \delta\rho(\mathbf{r}, t) = \left(-\frac{\eta}{\hbar} + i\omega \right) \delta\rho(\mathbf{r}, t). \quad (4.54)$$

Here, η denotes the energy scale of the relaxation processes. Equation (4.54) shows how the amplitude of the induced charge oscillations takes the form of an envelope function that decays exponentially in time. The evolution of induced dipole with respect to time, after the external field has been switched off, is plotted in figure 4.7, serving to illustrate this decay.

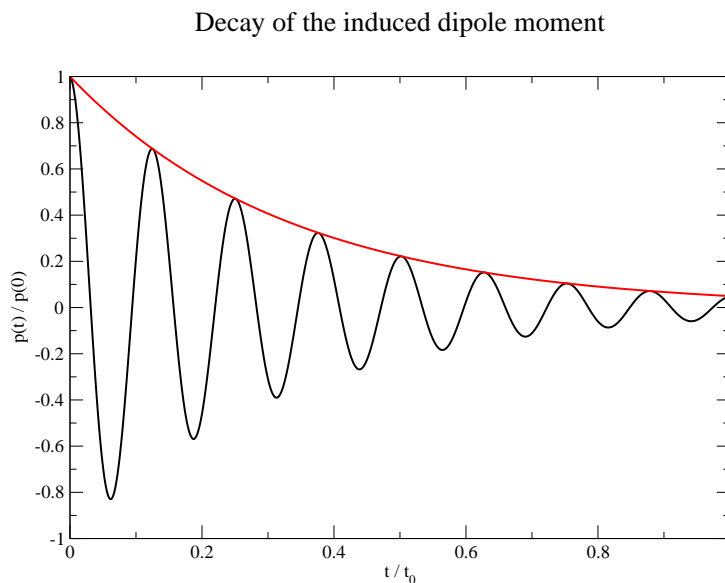


Figure 4.7: Decay of the induced dipole moment, when the external electric field is switched off. The red curve is an exponential envelope.

In principal, the damping may depend on the excited state $|i\rangle$ under consideration. The damping parameter η_i can be calculated by employing Fermi's golden rule,

$$\eta_i = \frac{2\pi}{\hbar} \sum_f |\langle f | \hat{V} | i \rangle|^2 \delta(\epsilon_f - \epsilon_i) \quad (4.55)$$

where the sum runs over all possible final states $|f\rangle$ that can be reached via the operator \hat{V} . The operator \hat{V} can describe for example the coupling of the electrons to phonons or

photons. It can also contain electronic correlation that is not described within the Hartree Fock theory.

The three important microscopic dephasing mechanisms are Umklapp scattering, electron-phonon interaction and radiation of photons:

- i) Electron-electron Umklapp scattering processes result from the underlying atomic lattice. The total momentum in electron-electron scattering processes is conserved up to vectors of the reciprocal lattice [59]. The Umklapp scattering flips the momentum of electrons with Fermi momentum, leading to a decay of the longitudinal current propagator. The density-density correlation function must therefore decay in the same manner as a direct consequence of the continuity equation. For explicit calculations see [59, 60].
- ii) In the presence of electron-phonon interaction, plasmons can decay into particle hole pairs via absorption or emission of phonons. The particle hole pairs can then relax via Umklapp scattering, further electron-phonon interaction or by emission of photons. Detailed calculations can be found in [51, 60, 61].
- iii) The induced oscillating charge density wave is a source of radiation fields. So the system can relax via the emission of photons.

4.5 Eigenmode expansion

We now show a viable method for analytical calculations of the response functions if one has an approximation for eigenvectors of either the conductivity or the density-density correlation function. The eigenvectors $|\xi_i(\omega)\rangle$ of $\Sigma(\omega)$ are introduced here. The induced current is expressed as:

$$\delta\mathbf{j}(\omega) = \sum_i |\xi_i(\omega)\rangle \frac{1}{\langle \xi_i(\omega) | \Sigma(\omega) | \xi_i(\omega) \rangle} \langle \xi_i(\omega) | E \rangle. \quad (4.56)$$

The matrix Σ will have a zero-mode, whenever ω coincides with a resonance frequency ω_j . The corresponding eigenvector in such a situation will be denoted by $|\xi_j(\omega_j)\rangle$. In this work, we are mainly interested in the system behavior in the vicinity of resonances, and as such we expand the eigenvectors as follows

$$|\xi_j(\omega)\rangle = |\xi_j(\omega_j)\rangle + \partial_\omega |\xi_j(\omega)\rangle|_{\omega=\omega_j} (\omega - \omega_j) + \mathcal{O}((\omega - \omega_j)^2). \quad (4.57)$$

Assuming that the eigenvector does not change significantly in the proximity of the resonance, we disregard the term proportional to $\omega - \omega_j$ to obtain the following expression

for the current in the vicinity of the j -th resonance,

$$\delta \mathbf{j}(\omega) = |\xi_j(\omega_j)\rangle \frac{1}{\langle \xi_j(\omega_j) | \Sigma(\omega) | \xi_j(\omega_j) \rangle} \langle \xi_j(\omega_j) | \mathbf{E}_{\text{ext}} \rangle. \quad (4.58)$$

Equation (4.58) clearly illustrates how the profile of the induced current at the j -th resonance is determined by $|\xi_j(\omega_j)\rangle$. If one calculates the root of the denominator in equation (4.58), one obtains approximate resonance frequencies.

Keeping in mind that the excitations we are after are longitudinal plasmons, we start with the density profiles of the plasmonic excitations, and then determine via the continuity equation the corresponding longitudinal current density profiles. The density profiles of simple geometries are easily obtained by considering the standing waves excited by the external electric field. The normalized eigenvectors of χ_{ext} will be denoted as $|\Pi_j(\omega)\rangle$. The density profiles are then given by

$$|\pi_j\rangle = |\Pi_j(\omega_j)\rangle. \quad (4.59)$$

Note that density profiles obtained via the continuity equation have to be normalized. The density-density correlation function can also be utilized in place of the conductivity, as long as one is only interested in the longitudinal plasmons. One then considers the density profiles that are the eigenvectors of the external density-density correlation function. One starts with the response equation

$$\delta \rho = \frac{\mathbb{1}}{\chi_{\text{irr}}^{-1} - \tilde{v}^{\text{H}}} \Phi_{\text{ext}}, \quad (4.60)$$

expands in the eigenbasis of χ_{ext} and then considers the response in the vicinity of the j -resonance in the same manner as it was done for the conductivity,

$$\delta \rho(\omega) = |\pi_i\rangle \frac{1}{\langle \pi_i | \chi_{\text{irr}}^{-1}(\omega) - \tilde{v}^{\text{H}} | \pi_i \rangle} \langle \pi_i | \Phi_{\text{ext}} \rangle. \quad (4.61)$$

Finding the roots of denominator leads again to the approximate resonance frequencies. In order to simplify the calculation further, we replace $\langle \pi_j | \chi_{\text{irr}}^{-1}(\omega) | \pi_j \rangle$ by $1 / \langle \pi_j | \chi_{\text{irr}}(\omega) | \pi_j \rangle$. This replacement has to be checked for each system under consideration. If the replacement is approximately valid, one finally has χ_{ext} ,

$$\chi_{\text{ext}}(\mathbf{r}, \mathbf{r}') = \sum_j \pi_j(\mathbf{r}) \pi_j(\mathbf{r}') \frac{\langle \pi_j | \chi_{\text{irr}} | \pi_j \rangle}{1 - \langle \pi_j | \tilde{v}^{\text{H}} | \pi_j \rangle \langle \pi_j | \chi_{\text{irr}} | \pi_j \rangle}. \quad (4.62)$$

This equation provides the basis for all analytical calculations presented in this work.

Chapter 5

Discretized Model

5.1 Definition of the model

The systems under consideration are described by the following tight-binding Hamiltonian in the jellium approximation:

$$\hat{H} = \hat{H}_{\text{atom}} + \hat{H}_{\text{hop}} + \hat{H}_{\text{bg}} + \hat{H}_{\text{elbg}} + \hat{H}_{\text{int}} + \hat{H}_{\text{ext}}, \quad (5.1)$$

where

$$\hat{H}_{\text{hop}} = -t \sum_{\langle i,j \rangle} \hat{c}_i^\dagger \hat{c}_j + \text{h.c.}, \quad (5.2)$$

$$\hat{H}_{\text{bg}} = \frac{1}{2} \rho_{\text{bg}}^2 \sum_{i,j} v_{ij}, \quad (5.3)$$

$$\hat{H}_{\text{elbg}} = -e \rho_{\text{bg}} \sum_{i,j} v_{ij} \hat{c}_j^\dagger \hat{c}_i, \quad (5.4)$$

$$\hat{H}_{\text{int}} = \frac{1}{2} e^2 \sum_{i,j} v_{ij} \hat{c}_i^\dagger \hat{c}_i \hat{c}_j^\dagger \hat{c}_j, \text{ and} \quad (5.5)$$

$$\hat{H}_{\text{ext}} = -e \sum_i \Phi_i^{\text{ext}} \hat{c}_i^\dagger \hat{c}_i \quad (5.6)$$

with

$$v_{ij} = \frac{1}{\sqrt{(\mathbf{r}_i - \mathbf{r}_j)^2 + \lambda^2}} \quad (5.7)$$

where the indices i, j denote the lattice sites. We consider N_{sites} lattice sites with a lattice spacing of a . The number of electrons N_{el} is determined by the filling fraction ν_{ff} via

$$N_{\text{el}} = 2\nu_{\text{FF}} N_{\text{sites}}, \quad (5.8)$$

where the factor of two takes into account the electron spin.

The first term (equation (5.2)) describes the hopping of the electrons between neighboring sites denoted by $\langle i, j \rangle$, where the hopping parameter t defines the kinetic energy scale. The second term (equation (5.3)) is just a constant energy shift representing the self-interaction energy of the homogeneous charge density ρ_{bg} with itself. In all cases we select ρ_{bg} such that the total charge of the background is equal to the total charge of the electrons. Then the third term (equation (5.4)) describes the Coulomb interaction of the electrons with the background. The fourth term (equation (5.5)) takes the inter-electronic Coulomb interaction into account. The energy scale of the Coulomb interactions is in units of $U = e^2/a$, where e is the electron charge. The position of the atoms are given by \mathbf{r}_i . The interaction potential v_{ij} has the feature that one recovers the bare Coulomb interaction at long distances, while for short distances the spatial structure of the atomic orbitals described by the parameter λ becomes important. Its value depends on the atomic orbitals and reflects the different orbital shapes. Finally, the last term (equation (5.6)) couples the electrons to an external time-dependent scalar potential $\Phi_{\text{ext},i}$.

5.2 Electronic structure

5.2.1 Hartree theory

Hartree theory provides the most straightforward model for taking the electron-electron interaction into account. In this approximation, each electron interacts only with the total average electronic density of the other electrons. The corresponding effective Hamiltonian is expressed as,

$$\hat{H}_{\text{H}} = \hat{H}_{\text{hop}} + \hat{H}_{\text{bg}} + \hat{H}_{\text{elbg}} - e \sum_i \Phi_{\text{H},i} \hat{c}_i^\dagger \hat{c}_i. \quad (5.9)$$

The Hartree potential Φ_{H} is defined as

$$\Phi_{\text{H},i} = \sum_j v_{ij} \rho_j, \quad (5.10)$$

where the electron charge density ρ is given by

$$\rho_i = -2e \sum_\mu f(\epsilon_\mu) |\psi_{\mu,i}|^2 \quad (5.11)$$

and f denotes the Fermi distribution and ψ_μ the single particle states. In principle, the eigenvalue problem of the Hartree Hamiltonian must be solved self-consistently, owing to the fact that it depends on the density. However, if the electron density is uniform,

the Hartree potential and the electrostatic potential from the background cancel each other out. Even if the electron density is not exactly uniform, the cancellation is still approximately valid. This can be illustrated by a one-dimensional chain of length L . The wave functions for such a case are $\psi_\mu(x) = \sqrt{2/L} \sin((\pi/L)\mu x)$, and the ground state charge density at zero temperature is expressed as:

$$\rho(x) = -e \sum_{\mu=1}^{N_{\text{el}}/2} \psi_\mu^2(x) \quad (5.12)$$

$$= -e \frac{N_{\text{el}}}{L} - e \frac{1}{L} + e \frac{\sin\left(\left(1 + N_{\text{el}}\right)\frac{\pi}{L}x\right)}{\sin\left(\frac{\pi}{L}x\right)L}. \quad (5.13)$$

The first term on the RHS is just the negative of ρ_{bg} . The second and the third term describe the impact of Friedel oscillations [62].

5.2.2 Hartree-Fock theory

The Hartree theory from the previous section is derived from a product *Ansatz* of single-particle wave functions, combined with the variational principle. Note that this *Ansatz*, however, neglects the fact that the wave function of the electrons must be antisymmetric with respect to the permutation of two electrons. Starting from a single Slater determinant and applying the variational principle, one eventually ends up with the Hartree Fock equations. In addition to the Hartree potential from the previous section, one also obtains a non-local exchange contribution. The Fock operator,

$$\hat{F} = \hat{H}_{\text{H}} + e \sum_{i,j} \Phi_{\text{F},ij} \hat{c}_i^\dagger \hat{c}_j. \quad (5.14)$$

acts as an effective Hamiltonian, where $\Phi_{\text{F},ij}$ is the (non-local) exchange or Fock term $\Phi_{\text{F},ij}$

$$\Phi_{\text{F},ij} = v_{ij} \rho_{ij} \quad (5.15)$$

with the density matrix ρ_{ij} ,

$$\rho_{ij} = -e \sum_{\mu} f(\epsilon_{\mu}) \Psi_{\mu,i} \Psi_{\mu,j}. \quad (5.16)$$

Because the Fock operator depends on the wave functions, the Hartree-Fock equations,

$$\sum_j F_{ij} \Psi_{\mu,j} = \epsilon_{\mu} \Psi_{\mu,i}, \quad (5.17)$$

become an eigenvalue problem that must be solved in a self-consistent manner.

While the impact of the Hartree term on the single-particle levels in the jellium approximation is quite weak, the Fock exchange leads to an increase of the Fermi velocity which even diverges in the continuum limit [63]. This divergency is unphysical and a result of the Hartree-Fock approximation. However, it can be cured by replacing the bare Coulomb interaction by the screened interaction [50, 64], and the Fermi velocity then acquires a finite value. In finite systems, the Fock exchange overestimates the HOMO-LUMO gap which can be cured in the same manner.

5.3 Response functions and calculation of the induced density

5.3.1 Hartree theory

The density-density correlation function for the non-interacting system is expressed as, see equation (4.30),

$$\chi_{ij}^{(0)}(\omega) = -2 \sum_{\mu\nu} \psi_{\mu,i} \psi_{\nu,i} \psi_{\nu,j} \psi_{\mu,j} \frac{f(\epsilon_\mu) - f(\epsilon_\nu)}{\epsilon_\nu - \epsilon_\mu - \omega - i\eta}, \quad (5.18)$$

where the factor of 2 arises from the spin of the electrons. The response equation reads

$$\delta\rho_i(\omega) = \sum_j \chi_{ij}^{(0)}(\omega) (\Phi_{\text{ext},j}(\omega) + \Phi_{\text{ind},j}(\omega)), \quad (5.19)$$

where the induced potential is just the Hartree potential given by

$$\Phi_{\text{ind},i}(\omega) = \sum_j v_{ij} \delta\rho_j(\omega) \quad (5.20)$$

The dielectric matrix $\varepsilon(\omega)$ in RPA reads

$$\varepsilon_{ij}(\omega) = \delta_{ij} - \sum_k \chi_{ik}^{(0)}(\omega) v_{kj}, \quad (5.21)$$

the response equation reads

$$\sum_j \varepsilon_{ij}(\omega) \delta\rho_j(\omega) = \sum_j \chi_{ij}^{(0)}(\omega) \Phi_{\text{ext},j}(\omega). \quad (5.22)$$

5.3.2 Hartree-Fock theory

The restoring forces at the Hartree-Fock level are considered non-local when compared to those of the Hartree theory from section 5.3.1. In place of the density-density correlation

function one must therefore work with the correlation function of the density matrices,

$$\chi_{ijkl}^{(0)}(\omega) = -2 \sum_{\mu\nu} \psi_{\mu,i} \psi_{\nu,j} \psi_{\nu,k} \psi_{\mu,l} \frac{f(\epsilon_\mu) - f(\epsilon_\nu)}{\epsilon_\nu - \epsilon_\mu - \omega - i\eta}. \quad (5.23)$$

The induced charge density matrix $\delta\rho_{ij}(\omega)$ gives rise to an induced Hartree potential and a non-local exchange potential,

$$\Phi_{\text{ind},ij}(\omega) = \delta_{ij} \sum_k v_{jk} \delta\rho_{kk}(\omega) - \frac{1}{2} v_{ij} \delta\rho_{ij}(\omega). \quad (5.24)$$

The response equation then reads

$$\delta\rho_{ij}(\omega) = \sum_{kl} \chi_{ijkl}^{(0)} (\delta_{kl} \Phi_{\text{ext},k}(\omega) + \Phi_{\text{ind},kl}(\omega)), \quad (5.25)$$

where $\Phi_{\text{ext},i}(\omega)$ is a local external potential. Plugging equation (5.24) into equation (5.25), one can bring all term containing $\delta\rho_{ij}(\omega)$ onto one side and finds the following set of linear equations,

$$\sum_{kl} \left(\delta_{ik} \delta_{jl} - \delta_{kl} \sum_m \chi_{ijmm}^{(0)}(\omega) v_{mk} + \frac{1}{2} \chi_{ijkl}^{(0)} v_{kl} \right) \delta\rho_{kl} = \sum_k \chi_{ijkk}^{(0)} \Phi_{\text{ext},k}. \quad (5.26)$$

Based on the response equation above, one can define an effective non-local dielectric matrix $\epsilon_{ijkl}(\omega)$,

$$\epsilon_{ijkl}(\omega) = \delta_{ik} \delta_{jl} - \delta_{kl} \sum_m \chi_{ijmm}^{(0)}(\omega) v_{mk} + \frac{1}{2} \chi_{ijkl}^{(0)}(\omega) v_{kl}. \quad (5.27)$$

5.3.3 Response equations in particle-hole space

In quantum chemistry a commonly used approach within the context of time-dependent Hartree-Fock and time-dependent density functional theory, is the reformulation of the Dyson equation for the external response function,

$$\chi_{\text{ext},ij}(\omega) = \chi_{ij}^{(0)}(\omega) + \sum_{kl} \chi_{ik}^{(0)}(\omega) v_{kl} \chi_{\text{ext},lj}(\omega) \quad (5.28)$$

as an eigenvalue problem in particle-hole space for $T = 0$:

$$\begin{pmatrix} A & B \\ -B & -A \end{pmatrix} \begin{pmatrix} X \\ Y \end{pmatrix} = \omega \begin{pmatrix} X \\ Y \end{pmatrix}, \quad (5.29)$$

Here, X and Y are vectors in particle-hole space defined via the following expansion of the density response,

$$\delta\rho_i = \sum_{\mu,\bar{\nu}u} X_{\mu\bar{\nu}} \psi_{\mu,i}^* \psi_{\bar{\nu},i} + Y_{\mu\bar{\nu}} \psi_{\bar{\nu},i}^* \psi_{\mu,i} \quad (5.30)$$

where we use Greek letter to denote occupied states and use a bar in order to indicate virtual states. The excited states of the system are determined by the excitation operator \hat{E} acting on the groundstate Slater determinant,

$$\hat{E} = \sum_{\mu\bar{\nu}} X_{\mu\bar{\nu}} \hat{c}_{\bar{\nu}}^{\dagger} \hat{c}_{\mu} + Y_{\mu\bar{\nu}} \hat{c}_{\mu}^{\dagger} \hat{c}_{\bar{\nu}}. \quad (5.31)$$

The eigenvalues ω are the excitation frequencies and the eigenvectors $(X Y)^T$ determine the contributions of the individual single particle excitations of the non-interacting system to the excitations of the interacting system. The matrices A and B at the Hartree level are given by

$$A_{\mu\bar{\nu},\rho\bar{\sigma}} = (\epsilon_{\bar{\nu}} - \epsilon_{\mu}) \delta_{\mu\rho} \delta_{\bar{\nu}\bar{\sigma}} + 2(\mu\bar{\nu}|\rho\bar{\sigma}), \quad (5.32)$$

$$B_{\mu\bar{\nu},\rho\bar{\sigma}} = 2(\mu\bar{\nu}|\rho\bar{\sigma}), \quad (5.33)$$

where $(\mu\bar{\nu}|\rho\bar{\sigma})$ is defined by

$$(\mu\bar{\nu}|\rho\bar{\sigma}) = \sum_{l,m} \psi_{\mu,l} \psi_{\bar{\nu},l} v_{lm} \psi_{\rho,m} \psi_{\bar{\sigma},m} \quad (5.34)$$

with the summations going over all sites. When one is interested in the response at the Hartree Fock level, the corresponding expression for A and B are

$$A_{\mu\bar{\nu},\rho\bar{\sigma}} = (\epsilon_{\bar{\nu}} - \epsilon_{\mu}) \delta_{\mu\rho} \delta_{\bar{\nu}\bar{\sigma}} + 2(\mu\bar{\nu}|\rho\bar{\sigma}) - (\bar{\nu}\bar{\sigma}|\mu\rho), \quad (5.35)$$

$$B_{\mu\bar{\nu},\rho\bar{\sigma}} = 2(\mu\bar{\nu}|\rho\bar{\sigma}) - (\rho\bar{\nu}|\mu\bar{\sigma}). \quad (5.36)$$

In many cases, one is not interested in the full excitation spectrum, but only in the lowest excitations. A typical approach is then utilizing an iterative diagonalization algorithm like the Lanczos or the Davidson algorithm in order to obtain the lowest eigenvalues.

5.4 Implementation

Two C++ programs were written for the purpose of carrying out the numerical simulations. The first program, `gen_coord`, generates files with the coordinates of the atoms for given geometries like straight wires, rectangles, boxes, or rings with vacancies. The second program, `rpa`, performs the electronic structure calculations and the calculation of the induced densities. Additional properties such as polarizabilities are obtained from the induced densities as well. The `rpa` program requires two input files: first, a coordinate file `coord`, where the positions of the atoms are specified in Cartesian coordinates, and second a file named `rpa.inp`, which specifies all parameters that are needed for the calculation via control keywords listed in table 5.1.

keyword	description
<i>eta</i> η	damping in units of t
<i>nel</i> N_{el}	number of paired electrons
<i>lambda</i> λ	effective width λ of the ring in units of a
<i>freq</i> f_{min} f_{max} steps	frequency window of the external potential
<i>Coulomb</i> U	Coulomb interaction energy scale U in units of t
<i>hf</i>	Hartree Fock control flag
<i>temp</i> T	temperature in units of t
<i>iter</i>	determine the induced density by iteration
<i>invert</i>	determine the induced density by solving a linear system of equations and calculate the eigenvalues of the dielectric function

Table 5.1: Keywords of the program `rpa`

When the `rpa` program is called, it first reads both input files and sets up all parameters. The tight-binding Hamiltonian is then constructed from the given coordinates. The coordinates are assumed to be given in units of the lattice spacing a , where the program identifies two atoms as neighbors if the distance between them is within the range of $0.9a - 1.1a$. The tight-binding Hamiltonian is then diagonalized, and the energies and orbitals are written onto hard disk, but also kept in memory. If the *hf* flag is found in `rpa.inp`, the program performs a Hartree-Fock calculation: It constructs the density matrix from the tight-binding orbitals according to equation (5.16), and then sets up the Fock matrix according to equations (5.9) and (5.14). In order to improve upon the convergence behavior of the Hartree Fock iterations, the Fock matrix that is diagonalized is calculated as the average of the old Fock matrix from the previous iteration (this is just the tight binding matrix in the first iteration) and the most recently calculated Fock matrix. After diagonalization the change in the density is calculated by subtracting the electronic density of the previous iteration from the density calculated from the orbitals obtained by the diagonalization. If the absolute value of the change at each lattice point is below a given threshold, the orbitals and energies are again written to hard disk and kept in memory, replacing the tight-binding orbitals and energies, respectively. Otherwise, a new Fock matrix is constructed, and the whole procedure is repeated until the convergence criteria are satisfied.

Having obtained single-particle states and the corresponding energies, the program goes on to calculate the induced density, if a response flag is found in `rpa.inp`. Depending on the choice of the response flag, the program uses different methods in order to solve equation (5.22). The flag *iter* tells the program to find a solution by iteration. A preliminary idea

for such an iteration is:

$$\delta\rho_i = \sum_j \chi_{ij}^{(0)} \left(\Phi_{\text{ext},j} + \sum_k v_{jk} \delta\rho_k \right). \quad (5.37)$$

This iteration procedure simply corresponds to a direct summation of a geometric series. In the vicinity of single particle and plasmonic resonances, however, one encounters numerical convergence problems, i.e. the induced density diverges. In order to analyze this behavior we transform into the eigenbasis of $\chi^{(0)}v$. The convergence of the geometric series is then verified by the eigenvalues of $\chi^{(0)}v$: The absolute value of all eigenvalues must be less than one, otherwise the geometric series will diverge. In such a situation, neither damping techniques nor DIIS lead to a convergent result. Note that the program first calculates the total potential and then performs the integral with the response function. The integration is done in two steps: (i) An intermediate $\Phi_{\nu\mu}$ is calculated,

$$\Phi_{\nu\mu} = \sum_j \psi_{\nu,j} \psi_{\mu,j} \Psi_{\text{tot},j}. \quad (5.38)$$

(ii) This can be utilized to calculate the induced density,

$$\delta\rho_i = -2 \sum_{\mu\nu} \psi_{\mu,i} \psi_{\nu,i} \frac{f(\epsilon_\mu) - f(\epsilon_\nu)}{\epsilon_\nu - \epsilon_\mu - \omega - i\eta} \Phi_{\nu\mu}. \quad (5.39)$$

Therefore, each step of the iteration scales like $\mathcal{O}(N_{\text{sites}}^3)$.

The convergence behavior, however, can be significantly improved by rewriting equation (5.37) in the following way:

$$\delta\rho_i = \frac{1}{1 - \sum_j \chi_{ij}^{(0)} v_{ji}} \sum_j \chi_{ij}^{(0)} \left(\Phi_{\text{ext},j} + \sum_{i \neq k} v_{jk} \delta\rho_k \right). \quad (5.40)$$

The induced density in equation (5.40) achieves faster convergence, if the damping is more than twice that of the mean level spacing. However, compared to previous iteration scheme, the scaling behavior increases significantly from $\mathcal{O}(N_{\text{sites}}^3)$ to $\mathcal{O}(N_{\text{sites}}^4)$.

Finally, the program calculates the electric dipole moments and the absorbed power. The dipole moments $\mathbf{p}(\omega)$ are calculated via

$$\mathbf{p}(\omega) = \sum_i \mathbf{r}_i \delta\rho_i. \quad (5.41)$$

The absorbed power is determined by utilizing equation (4.18),

$$P(\omega) = \frac{1}{2} \omega \sum_i \Phi_{\text{ext},i} \delta\rho_i. \quad (5.42)$$

The most robust results are obtained by directly solving the linear systems of equation using the LAPACK routine `zgesv`. With this, the damping can be made even smaller than the mean level spacing. All results of this dissertation were obtained by this procedure. If not stated otherwise, all numerical results are obtained at the Hartree level. In addition, we implemented a solution for the response equations in particle-hole space using Mathematica [65]. This program has been used for the calculation of all density profiles via equation (5.30) shown in this work.

Chapter 6

Continuum model

In order to gain a better understanding of the results obtained with the discretized model, we employ a continuum model. In addition, the continuum model enables us to find analytic expressions for the plasmon frequencies in simple geometries and for the polarizabilities of SRRs. These analytical expressions allow to study in impact of the different model parameters on the response properties.

6.1 The model

We assume that both the electronic dispersion and the plasmonic density profiles are given. For all geometries, we consider density profiles that describe standing waves via cosine functions in one dimension, and the density in the co-dimensions is further assumed to be homogeneous. This latter assumption neglects the role of the boundaries on the density profiles in the co-dimension. As a simple example consider a rectangular geometry that lies in the xy -plane with length L in the x -direction and width b in the y -direction. The geometry is depicted in Figure 6.1.

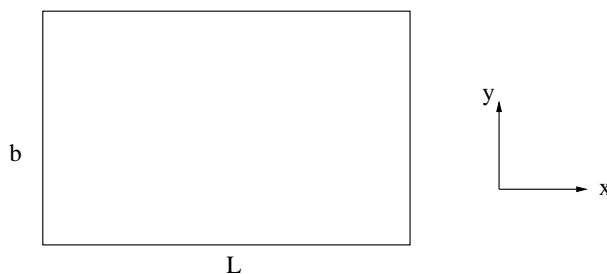


Figure 6.1: Sample rectangle geometry with length L and width b

In order to identify the possible standing wave patterns of the density, we start with the

wave patterns of the current density. The plasmons shall be excited by an electric field pointing into the x -direction, so the current density at each point will be parallel to the x -direction. For $x = 0$ and $x = L$ it must vanish, as otherwise particles would enter or leave the system under consideration. The current density profiles therefore read

$$\xi_i(x) = \sqrt{\frac{2}{Lb}} \sin\left(\frac{\pi}{L} i x\right) \quad \text{with } i = 1, 2, \dots \quad (6.1)$$

Utilizing the continuity equation one can easily calculate the density profiles,

$$\pi(x) = \sqrt{\frac{2}{Lb}} \cos\left(\frac{\pi}{L} i x\right) \quad \text{with } i = 1, 2, \dots, \quad (6.2)$$

Armed with the density profiles, the next task then becomes the determination of the density-density correlation function of the non-interacting system, as approximated by the density-density correlation in Fourier space. Note that we also neglect the off-diagonal elements of the correlation function, i.e., elements which contain information about the finite size of the sample.

The actual calculation of the response in d dimensions comprises several steps:

- i) First, the density profiles π_i of the plasmonic excitations of interest and the corresponding wave vectors q_i are determined. A reasonable guess is typically obtained by searching for the standing waves that can be excited by a given external electric field.
- ii) Before one can calculate the response function, one also needs the electronic dispersion. We will mainly consider the cases with free dispersion or cosine bands.
- iii) The response function is subsequently determined via

$$\chi^{(0)}(\mathbf{q}, z) = -2 \int \frac{d^d \mathbf{k}}{(2\pi)^d} f(\epsilon(\mathbf{k})) \frac{1}{z - (\epsilon(\mathbf{k}) - \epsilon(\mathbf{k} - \mathbf{q}))} - \frac{1}{z - (\epsilon(\mathbf{k} + \mathbf{q}) - \epsilon(\mathbf{k}))} \quad (6.3)$$

which follows from equation (4.30) by using plane waves as single-particle wave function and by taking the Fourier transformation. It is a general expression found in many textbooks [50, 66].

- iv) Next, the matrix elements of the Coulomb interaction are computed,

$$v(q_i) = \int d^d \mathbf{r} d^d \mathbf{r}' \pi_i(\mathbf{r}) \pi_i(\mathbf{r}') \frac{1}{\sqrt{(\mathbf{r} - \mathbf{r}')^2 + \lambda^2}}. \quad (6.4)$$

- v) The plasmon frequencies and lifetimes are then obtained by finding the roots z_i of the dielectric function in the complex plane,

$$1 - v(q_i) \chi^{(0)}(q_i, z_i) = 0. \quad (6.5)$$

vi) Finally, the response function of the interacting system at the RPA level is given by

$$\chi(\mathbf{r}, \mathbf{r}', \omega) = \sum_i \pi_i(\mathbf{r}) \pi_i(\mathbf{r}') \frac{\chi^{(0)}(q_i, \omega)}{1 - \chi^{(0)}(q_i, \omega) v(q_i)}. \quad (6.6)$$

6.2 Comparison between continuum and discretized model

i) Single particle excitation energies:

In order to analyze the difference of the single particle excitation energies, we consider a linear chain with N sites and a given filling fraction ν_{FF} . The diagonalization of the corresponding tight-binding Hamiltonian leads to the single particle energies ϵ_μ ,

$$\epsilon_\mu = -2t \cos\left(\frac{\pi}{N+1}\mu\right) \quad \text{with } \mu = 1, \dots, N. \quad (6.7)$$

The excitation energy from the highest occupied state into the j -th virtual state is given by,

$$\Delta_{\text{disc}} = -2t \left(\cos\left(\frac{\pi}{N+1}(\nu_{\text{FF}}N + j)\right) - \cos\left(\frac{\pi}{N+1}\nu_{\text{FF}}N\right) \right). \quad (6.8)$$

In the continuum model one has a cosine band,

$$\epsilon(k) = -2t \cos(ka). \quad (6.9)$$

The low-lying excitation energies from the Fermi level into empty states for single particle excitations with momentum q are given by

$$\Delta_{\text{cont}}(q) = -2ta(\cos((k_{\text{F}} + q)a) - \cos(k_{\text{F}}a)), \quad (6.10)$$

where the Fermi momentum k_{F} is given by $k_{\text{F}}a = \nu_{\text{FF}}\pi$. One then performs a Taylor expansion for small qa and finds

$$\Delta_{\text{cont}}(q) = 2ta \sin(k_{\text{F}}a)q + \mathcal{O}(q^2a^2). \quad (6.11)$$

Due to the finite size of the chain, the momentum is not a continuous number, but quantized. Its possible values are given by

$$q = \frac{\pi}{(N-1)a}\nu \quad \text{with } \nu = 1, \dots, N-1. \quad (6.12)$$

In order to analyze the finite-size corrections, we calculate the ratio $\Delta_{\text{cont}}/\Delta_{\text{disc}}$ and perform a Taylor expansion for large N ,

$$\frac{\Delta_{\text{cont}}}{\Delta_{\text{disc}}} = 1 + \frac{2}{N} + \frac{\pi\nu_{\text{FF}}}{\tan(\nu_{\text{FF}}\pi)} \frac{1}{N} - \frac{\pi j}{\tan(\nu_{\text{FF}}\pi)} \frac{1}{N}. \quad (6.13)$$

One observes that the deviation of the single-particle energies vanishes, if one goes to big system sizes ($N \rightarrow \infty$) and considers only the low-lying excitations ($j \ll N$). Looking at the terms in more detail, one observes that the second term depends only on the system size. The third term depends on the filling fraction and takes into account that the Fermi velocities of the discrete and the continuum model differ. This term vanishes for the case of half filling and diverges in the limit of a full band. In the limit of an empty band, $\nu_{\text{FF}} \rightarrow 0$, the term reads $1/N$. The fourth term is a result of the linearization of the excitation energies in the continuum model and is not present if one uses equation (6.10) instead of equation (6.11). This term diverges if the filling fraction goes either to zero or to one. Note that both cases are not physical as there are no electronic excitations possible within an empty or a full band.

ii) Reflection oscillations:

The quasiparticle-quasihole pairs constituting a plasmonic density wave are reflected at the boundaries of the sample. The interference of the incident and the reflected wave leads to additional oscillations in the induced density that were absent without the boundaries. We will denote these oscillations as reflection oscillations. We will check the importance of these oscillations for each case studied in this work by comparing results obtained with the discrete model to those obtained with the continuum model.

Chapter 7

Longitudinal plasmons in simple geometries

7.1 Introduction

In Chapters 5 and 6 both a numerical and an analytical model were developed in order to describe plasmonic resonances. In this chapter we intend to analyze the plasmonic excitations in simple geometries with the aim to study the impact of the finite system size and to compare the results of the two models. In addition we also make contact to calculations with periodic boundary conditions.

The general expression for the plasmon dispersion reads in the limit of long wavelengths

$$\omega^2(q_i) = e^2 c_1 v(q_i) q_i^2 + c_2 q_i^2, \quad (7.1)$$

where the first term describes the classical restoring forces and the second term takes into account the contribution from single-particle excitations. The coefficients c_1 and c_2 are solely determined by the electronic structure, but are independent of the system size. So the single-particle contribution scales with L^{-2} and becomes important when the system size is decreased. The finite size enters via the selection rule for q_i . The influence of the boundaries is also contained in the matrix elements of the Coulomb kernel which will be discussed for an example in 3D, 2D, and 1D. When using periodic boundary conditions, $v(q_i)$ is just the Fourier transform of the Coulomb kernel.

7.2 Identification of plasmons

We have discussed in Section 4.2 that the density response of an interacting electronic system comprises two different excitations: plasmons and renormalized single particle ex-

citations. These excitations can be seen as peaks in the absorption spectrum, i.e., the plot of the absorbed power versus the frequency of the external fields. In addition, both types of resonances appear as zero modes when studying the flow of the eigenvalues of the dielectric function with respect to changes in frequency. However, the flow of the resonances with the interaction strength is completely different for the two types of modes. While the square of plasmon frequency depends roughly linearly on the interaction strength, the single-particle resonances barely move when the interaction strength is increased.

We will now use the flow criterion from Section 4.2 in order to distinguish single-particle and plasmonic resonances. As an example we study the excitations of a tight-binding chain consisting of 50 sites with a filling fraction of $1/2$. The flow of the excitation energies with increasing interaction strength is depicted in Figure 7.1.

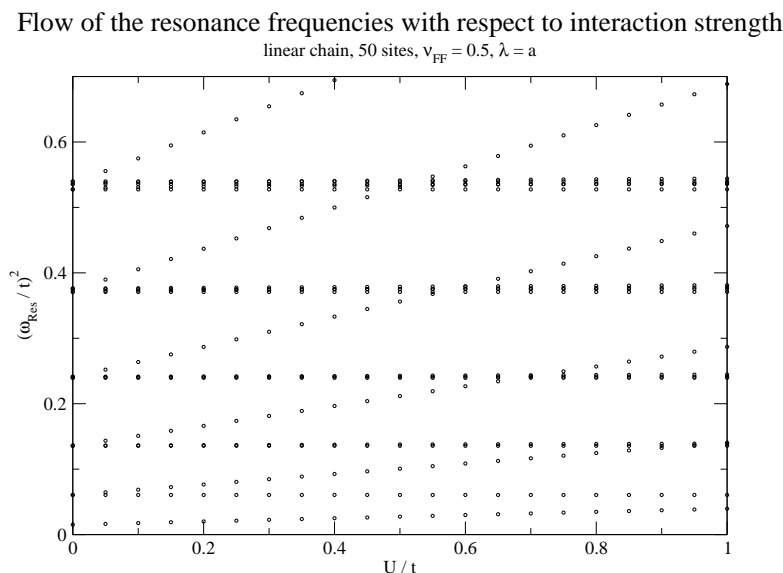


Figure 7.1: Flow of the excitation energies with scaling the Hartree kernel in the response equation.

One can clearly distinguish both types of resonances: The single-particle resonances barely move, while the square of the plasmon frequency depends linearly on the interaction strength. As a next step we analyze the plasmonic density profiles of the four lowest plasmons shown in Figure 7.2 and compare them to the profiles used in the continuum model.

One observes that one can assign to each plasmon a wave vector by looking of the envelope of the density profile. One also sees the reflection oscillations. Because these oscillations have to vanish when the boundary is removed, we consider a ring geometry. The density

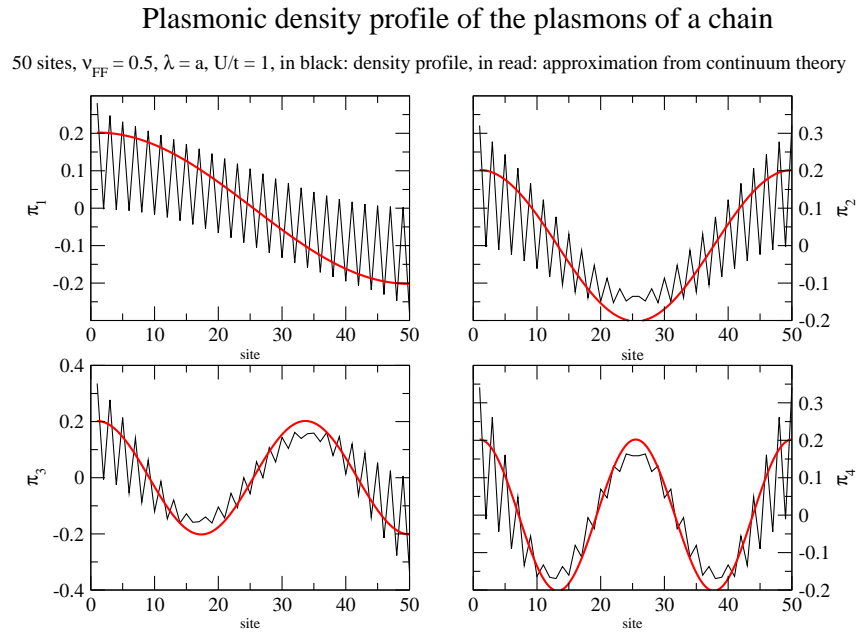


Figure 7.2: Density profiles of the plasmons of a tight binding chain with 50 sites

profiles are once again calculated and compared to those obtained from the continuum theory (7.3). At first glance, one can see that there are no reflection oscillations.

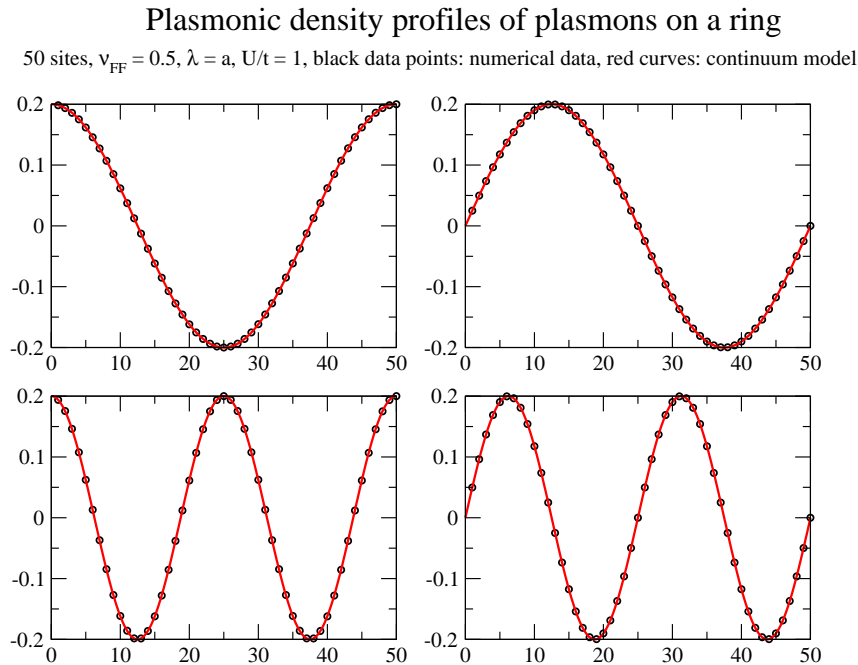


Figure 7.3: Plasmonic density profiles on a ring

The remaining excitations that barely move must be RSPEs. If one looks at the den-

sity profiles of the RSPEs that are depicted one sees the the envelope does not exhibit oscillations with a small wave vector.

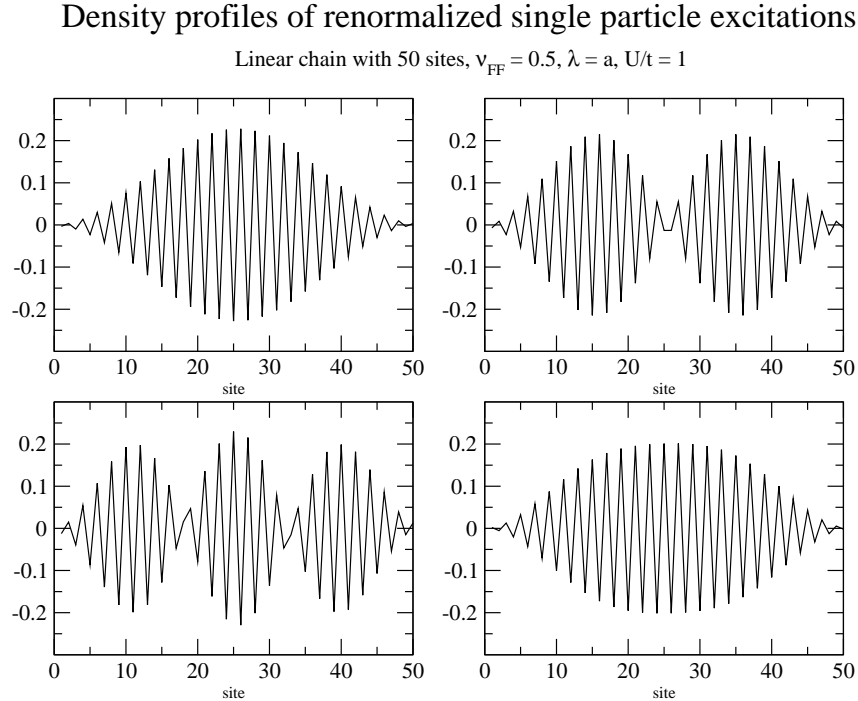


Figure 7.4: Density profiles of renormalized single particle excitations

The movement of the plasmons with scaling the Coulomb interaction can also be seen in Figure 7.5 where the absorption spectra for different values of U are shown. In addition absolute values of the eigenvalues of the dielectric function are shown.

As we have already identified the plasmonic resonances, we highlight them in orange in Figure 7.5 and highlight some RSPEs in purple. One sees that the flow of the eigenvalues exhibits two different peak shapes. The peaks of the RSPEs are narrow which is an imprint of the resonance structure of $\chi^{(0)}$. One also observes that the minimum of the peaks of plasmonic resonances is much closer to zero than for the RSPEs. We looked at the numerical data and found that the real part of the eigenvalues in both cases is close zero, however, in the vicinity of a resonance of $\chi^{(0)}$ acquires a non-negligible imaginary part leading to an imaginary part for the eigenvalue of the dielectric function. It is therefore possible to distinguish plasmons and RPSEs by studying the eigenvalues of the dielectric constant. In the following, all plasmons will be identified using this approach.

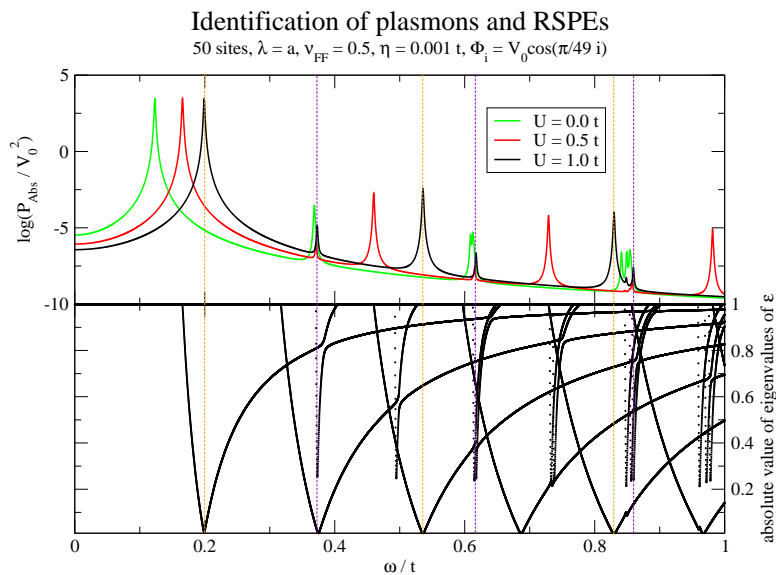


Figure 7.5: Plasmonic (orange dashed lines) and renormalized single particle excitations (violet dashed lines) of a tight binding chain. The external potential is chosen to yield a strong absorption for the first plasmonic wave.

7.3 Cuboid geometry in 3D

7.3.1 Parabolic dispersion

In this section, we investigate the plasmonic excitations of an electron liquid in a cuboid geometry with periodic boundary conditions. We denote its length along the z -direction by L and its cross section area by A . The geometry is depicted in Figure 7.6. We first derive the plasmonic dispersion relation of an electron gas with free dispersion and obtain the well-known result for the plasmon dispersion.

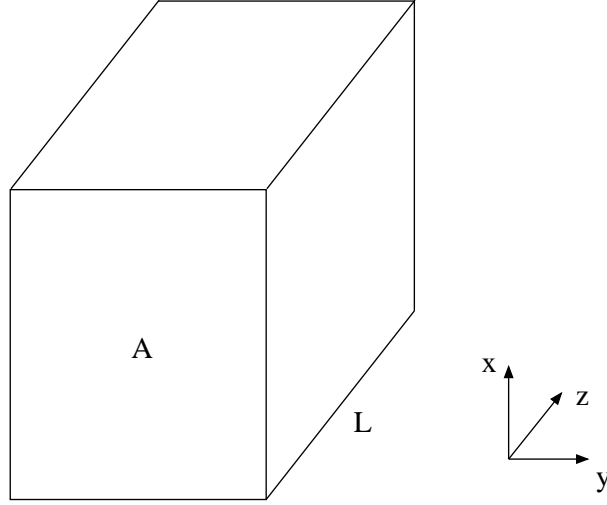
The dispersion relation of free electrons is given by,

$$\epsilon(\mathbf{q}) = \frac{q^2}{2m} \quad (7.2)$$

where m denotes the electron mass. Due to the finite length, only the following wave vectors q are possible,

$$q = \frac{\pi}{L} i \quad \text{with } i = 1, 2, \dots \quad (7.3)$$

We start with the expression for the density-density correlation function within the Ran-

Figure 7.6: Cuboid geometry with length L and cross section area A .

dom Phase Approximation [66],

$$\chi^{(0)}(\mathbf{q}, z) = -2 \int \frac{d^3\mathbf{k}}{(2\pi)^3} f(\epsilon(\mathbf{k})) \left(\frac{1}{z - (\mathbf{k}^2 - [\mathbf{k} - \mathbf{q}]^2)/(2m)} - \frac{1}{z - ([\mathbf{k} + \mathbf{q}]^2 - \mathbf{k}^2)/(2m)} \right), \quad (7.4)$$

then perform a Taylor expansion for small wave vectors $q \ll k_F$,

$$\chi^{(0)}(\mathbf{q}, z) = \int d^3\mathbf{k} \left(\frac{q^2}{4\pi^3 m z^3} + \frac{q^2 \mathbf{k} \cdot \mathbf{q}}{2\pi^3 m^2 z^3} + \frac{3q^2 (\mathbf{k} \cdot \mathbf{q})^2}{4\pi^3 m^3 z^4} + \mathcal{O}(k^3 q^5 m^{-4} z^{-5}) \right), \quad (7.5)$$

and integrate in spherical coordinates

$$\chi^{(0)}(q, z) = \frac{e^2 n_{3D} q^2}{m} \left(1 + \frac{3}{5} \frac{\left(\frac{k_F q}{m}\right)^2}{z^2} \right) + \mathcal{O}(k_F^4 q^6 m^{-5} z^{-6}), \quad (7.6)$$

where we have made use of the fact that the particle density n_{3D} is related to the Fermi momentum via

$$n_{3D} = \frac{k_F^3}{3\pi^2}. \quad (7.7)$$

Note that the result depends only on the modulus of \mathbf{q} , which simply reflects the isotropy of the homogeneous electron gas. The Fourier transform of the Coulomb interaction in 3D is

$$v(\mathbf{q}) = \frac{4\pi}{q^2}, \quad (7.8)$$

so we have for the dielectric function,

$$\varepsilon(q, z) = 1 - \frac{4\pi e^2 n_{3D}}{m} \left(1 + \frac{3}{5} \frac{\left(\frac{k_F q}{m}\right)^2}{z^2} \right). \quad (7.9)$$

As discussed in Section 4.2, we have to find the roots of ε in order to obtain the plasmonic dispersion relation:

$$\omega_{\text{pl}}^2(q) = \frac{4\pi e^2 n_{3D}}{m} + \frac{3}{5} \frac{k_F^2}{m^2} q^2. \quad (7.10)$$

The first term of the dispersion relation in equation (7.10) is independent of q , reflecting the fact that the electric field arising from a homogeneously charged plane is independent of the distance to the plane. The second term takes single particle excitations into account. In order to relate this to the circuit theory, we must first calculate the external conductivity via

$$\sigma_{\text{ext}}(q, \omega) = \frac{i\omega}{q^2} \chi_{\text{ext}}(q, \omega). \quad (7.11)$$

The total current passing through the cross section of the box can easily be calculated from the current density j_z . It is just $j_z A$. If the electric field is constant along the z -axis, the corresponding voltage drop U_{ext} at the ends of the box is $E_{\text{ext},z} L$. Comparing $j_3 = \sigma_{\text{ext}} E_{\text{ext},z}$ with $I = Z^{-1} U_{\text{ext}}$ one can now see that

$$Z = \frac{L}{\sigma_{\text{ext}} A}. \quad (7.12)$$

The circuit parameters can simply be read off from the equation above,

$$\mathcal{L} = \frac{Lm}{Ae^2 n_{3D}}, \quad (7.13)$$

$$\mathcal{C}^{-1} = \left(\frac{A}{4\pi L} \right)^{-1} + \left(\frac{5e^2 A k_F m}{9\pi^2 L q^2} \right)^{-1}, \quad (7.14)$$

$$\mathcal{R} = \frac{2Lm}{Ae^2 n_{3D}} \eta. \quad (7.15)$$

The inductance is related to the acceleration of the electrons due to the external force. It is exactly the same term one would have obtained from the Drude conductivity. One observes further that the capacity takes the form of a series of two capacitors,

$$\mathcal{C}^{-1} = \mathcal{C}_{\text{classical}}^{-1} + \mathcal{C}_{\text{quantum}}^{-1}, \quad (7.16)$$

where the first capacity $\mathcal{C}_{\text{classical}}$ arises from the classical restoring forces, and the second one is a pure quantum mechanical term resulting from the single-particle excitations,

$$\mathcal{C}_{\text{quantum}} = \frac{5e^2 A k_F m}{9\pi^2 \hbar^2 L q^2}, \quad (7.17)$$

where we have written \hbar out explicitly in order to highlight the quantum nature of the term. Note that this capacitance is quantized through its dependency on the wave vector q . In the classical limit, $\hbar \rightarrow 0$, the inverse quantum capacity vanishes, so the total capacity equals the classical one.

7.3.2 Tight-binding cubes : cos-dispersion

In this section we specialize to cubic geometries, $A = L^2$. We consider an external potential with a wave vector parallel to the z -axis. The density profiles are expressed as

$$\pi_i(\mathbf{r}) = \sqrt{\frac{2}{L^3}} \cos\left(\frac{\pi}{L} i z\right), \quad (7.18)$$

where we have made use of the assumptions from Chapter 6. The electronic dispersion is just the usual sum of cosine bands,

$$\epsilon(\mathbf{k}) = -2t \cos(k_x a) - 2t \cos(k_y a) - 2t \cos(k_z a). \quad (7.19)$$

where t denotes the hopping parameter. As we did for the quadratic dispersion, we calculate the density density correlation function, as in the last section, but now use the tight binding dispersion relation in this case. The same steps are repeated, yielding the following expression,

$$\chi^{(0)}(q, \omega) = \frac{2}{\pi} \int_{S_F} \frac{d^2 \mathbf{k}}{(2\pi)^2} \left(2ta \sin(k_z a) \frac{q^2}{z^2} + (2ta \sin(k_z a))^3 \frac{q^4}{z^4} \right) \quad (7.20)$$

where S_F denotes the Fermi surface depicted in Figure 7.7 and The integrals cannot be solved analytically, and so we evaluate them numerically and obtain,

$$\chi^{(0)}(q, \omega) \approx 0.66828 at \frac{q^2}{z^2} + 2.15265 a^3 t^3 \frac{q^4}{z^4} \quad (7.21)$$

The matrix elements of the Coulomb kernel are

$$v(q_i) = \frac{2}{L^3} \int d^3 \mathbf{r} \int d^3 \mathbf{r}' \cos(q_i z) \cos(q_i z') \frac{1}{\sqrt{(\mathbf{r} - \mathbf{r}')^2 + \lambda^2}}. \quad (7.22)$$

Now using a trigonometric addition theorem, one can rewrite the product of the cosines as a sum of two cosines. In the limit of big system sizes ($L \rightarrow \infty$) one obtains

$$\begin{aligned} v_\infty(q_i) &= \int d^3 \mathbf{r} \cos(q_i z) \frac{1}{\sqrt{\mathbf{r}^2 + \lambda^2}} \\ &+ \lim_{L \rightarrow \infty} \frac{1}{L^3} \int d^3 \mathbf{r} \int d^3 \mathbf{r}' \cos(q_i [z + z']) \frac{1}{\sqrt{(\mathbf{r} - \mathbf{r}')^2 + \lambda^2}} \end{aligned} \quad (7.23)$$

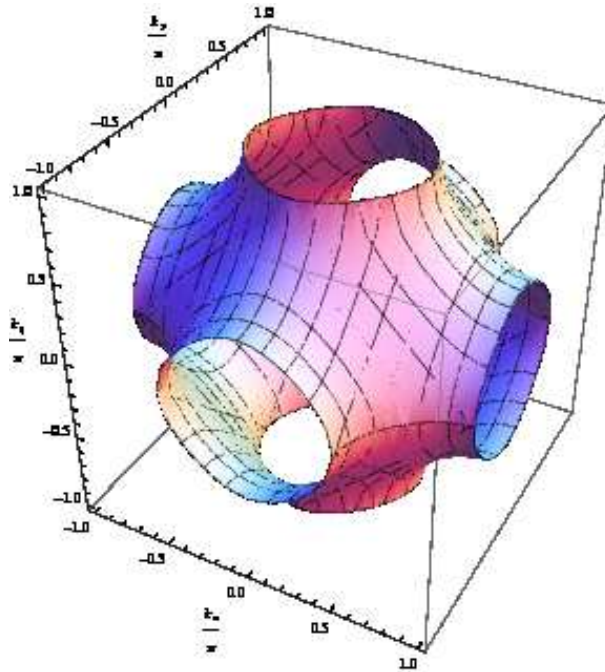


Figure 7.7: Fermi surface of a cube at half filling with cosine bands for the electronic dispersion.

The first term is just the Fourier transform of the Coulomb kernel, $4\pi\lambda K_1(\lambda q_i)$, where K_1 is a modified Bessel function of the second kind. In the limit $\lambda \rightarrow 0$, one recovers the known result $4\pi/q_i^2$. The second term gives a finite contribution even in the thermodynamic limit. We have calculated the Coulomb kernel for three different system sizes and compared it to the Fourier transform of the first term. The results are depicted in Figure 7.8.

At first glance, one sees that the Coulomb kernel deviates from $4\pi/q^2$ for high wave vectors ($\lambda q > 0.1$) due to its λ -dependency. In this limit, the oscillation of the plasmonic wave occurs at length scales that are comparable to those of the orbitals.

The results for the finite systems also approach the values of the infinite system with periodic boundary conditions when the system size is increased. Such agreement for a given finite size improves, when one goes to higher wave vectors. However, if one keeps the number of nodes fixed in the limit of long wavelengths and then increases the system size, the flow of the Coulomb kernel does not reach the value of $2\pi/q$, but instead deviates up to 65%. In order to analyze this deviation, we have calculated the matrix elements of the Coulomb kernel in the thermodynamic limit for modes with up to 20 nodes. The results are shown in Figure 7.9, where it is evident that the deviation quickly decreases when the number of nodes is increased.

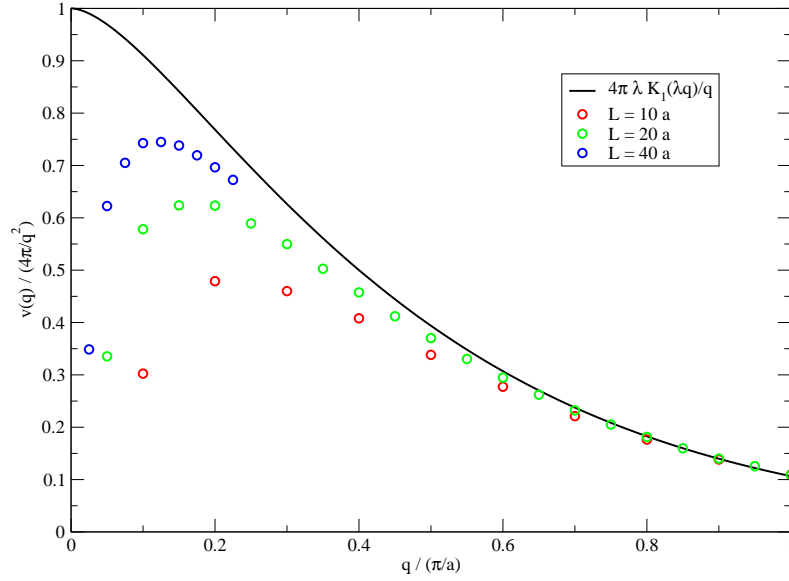


Figure 7.8: Coulomb kernel in cube geometries.

The deviations of the data points in Figure 7.9 from unity result from the second term in equation (7.23). In accordance with the recipe presented in Chapter 6 we are in the position to determine the plasmonic dispersion relation by finding the roots of the dielectric function. We finally arrive at the following expression:

$$\omega_{\text{pl}}^2(q_i) \approx 0.66828 \frac{e^2}{a} t v(q_i) q_i^2 + 3.22118 t^2 a^2 q_i^2. \quad (7.24)$$

In order to compare this result to the dispersion of the plasmons based on a free electronic dispersion, we choose for t a value of $1/(2m a^2)$ such that for small filling fractions both dispersion relations coincide. Equation (7.24) then reads

$$\omega_{\text{pl}}^2(q_i) \approx 0.33414 \frac{e^2}{a} \frac{1}{m a^2} v(q_i) q_i^2 + 0.80530 \frac{1}{m^2 a^2} q_i^2, \quad (7.25)$$

and the corresponding expression based on the free electronic dispersion is obtained from equation (7.10),

$$\omega_{\text{pl, free}}^2(q_i) \approx \frac{1}{2} \frac{e^2}{a} \frac{1}{m a^2} v(q_i) q_i^2 + 3.61753 \frac{1}{m^2 a^2} q_i^2. \quad (7.26)$$

where we now use the matrix elements of the Coulomb kernel in order to take the finite size of the sample into consideration. It is evident from equations (7.25) and (7.26) that the plasmon frequency for the free electronic dispersion is higher due to a higher Fermi velocity.

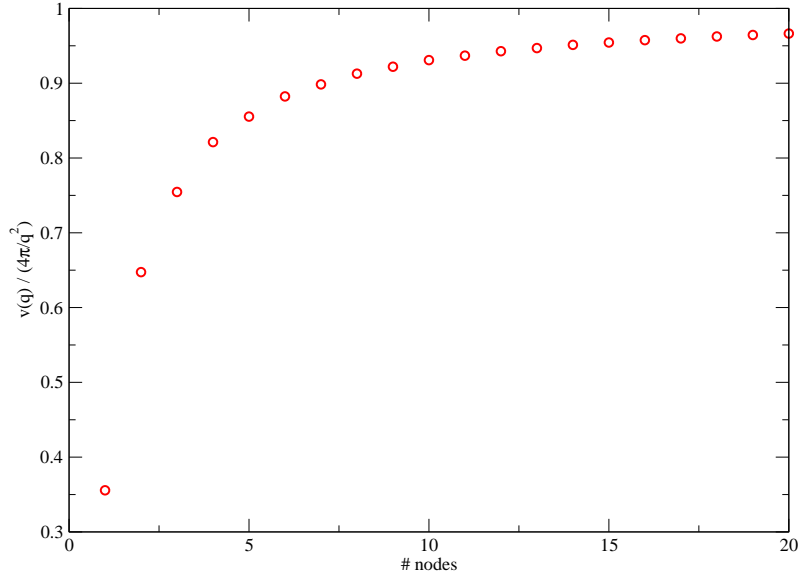


Figure 7.9: Coulomb kernel of cube geometries in the thermodynamic limit.

Finally, we study the dependence of the plasmon frequencies on the system size. Considering the first term in equation (7.1), the appearance of the matrix elements of the Coulomb kernel changes scaling behavior compared to the second term. Via a simple rescaling of the coordinates, equation (7.22) can be brought into the following form:

$$v(q_i) = 2L^2 \int_0^1 d\xi_1 \int_0^1 d\xi_2 \int_0^1 d\xi_3 \int_0^1 d\xi'_1 \int_0^1 d\xi'_2 \int_0^1 d\xi'_3 \frac{\cos(i\pi\xi_1) \cos(i\pi\xi'_1)}{\sqrt{(\xi - \xi')^2 + (\lambda/L)^2}}. \quad (7.27)$$

If the system size is much larger than the orbital size encoded in λ , the product of $v(q_i)$ and q_i^2 is independent of system size. However, when both length scales are of the same order of magnitude, the matrix elements of the Coulomb kernel decrease with respect to decreasing the system size, as in this limit the λ -dependence becomes important. This is evident by looking at Figure 7.8.

7.3.3 Comparison between continuum model and numerics

We now compare the results from the continuum theory with the results obtained from the numerical simulations.

As can be seen from Figure 7.10, the difference between the plasmon frequencies obtained from the continuum model and the numerics decreases when the system size is increased, also shown by the inset. In all cases, the plasmon frequencies from the continuum model

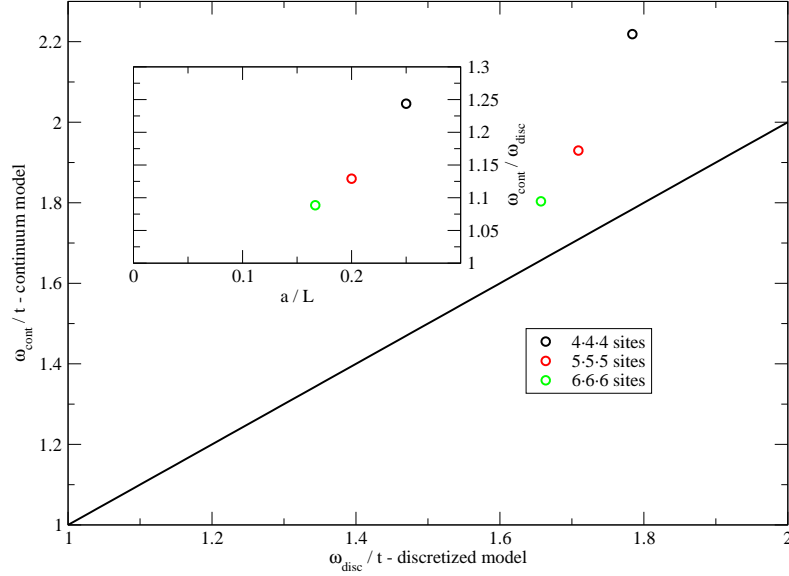


Figure 7.10: Plasmon frequencies in tight binding cubes at half-filling. Model parameters: $\nu_{\text{FF}} = 0.5$, $\lambda = a$, and $U = t$.

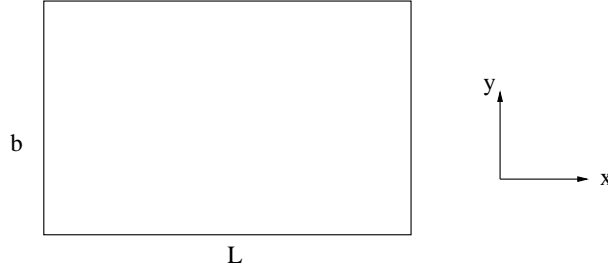
lie above the values obtained with the numerics. This results from the neglect of the reflection oscillations in the plasmonic density profile, as these additional oscillations serve to decrease the classical restoring force. According to the analysis of Chapter 6 concerning the single-particle energies, we know that the deviation for these energies are between 34% and 50%.

7.4 Rectangular geometry in 2D

7.4.1 Parabolic electronic dispersion

We assume that we have a rectangular geometry with the width b and length L . The geometry is depicted in Figure 7.11. We once again employ the free dispersion relation for the electrons as we did in the last section. The irreducible density-density correlation function reads in RPA

$$\chi^{(0)}(\mathbf{q}, z) = -2 \int \frac{d^2\mathbf{k}}{(2\pi)^2} f(\epsilon(\mathbf{k})) \left(\frac{1}{z - (\mathbf{k}^2 - [\mathbf{k} - \mathbf{q}]^2)/(2m)} - \frac{1}{z - ([\mathbf{k} + \mathbf{q}]^2 - \mathbf{k}^2)/(2m)} \right). \quad (7.28)$$

Figure 7.11: Rectangular geometry with length L and width b .

We proceed in the same manner as in Section 7.3.1. The Fourier transform of the Coulomb kernel is

$$v(q) = \frac{2\pi}{q}, \quad (7.29)$$

giving the plasmonic dispersion relation,

$$\omega_{\text{pl}}(q) = \frac{2\pi e^2 n_{2\text{D}}}{m} q + \frac{3}{4} \frac{k_{\text{F}}^2}{m^2} q^2, \quad (7.30)$$

where q is fixed by the condition

$$q = \frac{\pi}{L} i \quad \text{with } i = 1, 2, \dots \quad (7.31)$$

Note that compared to the 3D case the plasmon frequency vanishes when the wave vector of the external field goes to zero, while in 3D the classical term is independent from q , as can be seen from equation (7.10). The q -dependency of the classical contribution in 2D is due to the fact that the restoring electric field from a homogeneously charged line drops off with the reciprocal of the distance.

For the calculation of the circuit parameters, we employ again expression (7.11). The voltage drop is like in the 3D case $E_{\text{ext}}L$, but the current is jb . The circuit parameters are then given by

$$\mathcal{L} = \frac{Lm}{e^2 b n_{2\text{D}}}, \quad (7.32)$$

$$\mathcal{C}^{-1} = \left(\frac{b}{2\pi L q} \right)^{-1} + \left(\frac{2be^2 m}{3\pi L q^2} \right)^{-1}, \quad (7.33)$$

$$\mathcal{R} = \frac{2Lm}{e^2 b n_{2\text{D}}} \eta. \quad (7.34)$$

As for 3D case, the capacity is composed of a portion arising from the classical restoring forces, as well as a part involving a quantum correction.

7.4.2 Half-filled tight-binding rectangles

We start with the same rectangular geometry as we did in the last section. The expected plasmonic excitations, as a response to longitudinal excitations, are standing waves along the x - or the y -axis. If the wave vector of the external potential is parallel to the y -direction, the density profile becomes

$$\pi_i(x, y) = \sqrt{\frac{2}{bL}} \cos\left(i\frac{\pi}{L}y\right). \quad (7.35)$$

The electronic dispersion within the tight-binding approximation is given by the following expression:

$$\epsilon(\mathbf{k}) = -2t \cos(k_x a) - 2t \cos(k_y a). \quad (7.36)$$

The Fermi energy is zero, as the filling fraction is $1/2$. Thus, the Fermi surface is given by the parameterization $\cos(k_x a) = -\cos(k_y a)$.

We take the usual expression for the response function of the non-interacting system,

$$\chi^{(0)}(q_i, z) = -2 \int \frac{d^2\mathbf{k}}{(2\pi)^2} \left(\frac{1}{z - (-2t \cos(k_y a) + 2t \cos(k_y a - qa))} - \frac{1}{z - (-2t \cos(k_y a + q_i a) + 2t \cos(k_y))} \right) f(\epsilon(\mathbf{k})), \quad (7.37)$$

repeating the strategy from the last section (Taylor expansion for small wave vectors and integration) to find that

$$\chi^{(0)}(q, z) = \frac{8}{\pi^2} t \frac{q^2}{z^2} + \frac{64}{3\pi^2} a^2 t^3 \frac{q^4}{z^4}. \quad (7.38)$$

According to the recipe from Chapter 6, the next step is the calculation of the matrix element of the Coulomb kernel,

$$v(q_i) = \int_0^L d^2\mathbf{r} \int_0^L d^2\mathbf{r}' \frac{\pi_i(\mathbf{r})\pi_i(\mathbf{r}')}{\sqrt{(\mathbf{r} - \mathbf{r}')^2 + \lambda^2}}. \quad (7.39)$$

Similar to the 3D case, we can rewrite the matrix element as a sum of two contributions. In the limit of $L \rightarrow \infty$ and $b \rightarrow \infty$, one term once again corresponds to the Fourier transform of the Coulomb kernel, $2\pi \exp(-\lambda q)/q$, while a second term reflects the absence of periodic boundary conditions. We focus only on square geometries in the analysis of these terms. We have obtained the matrix elements according to equation (7.39) for three different system sizes and compared them with the Fourier transform of the Coulomb kernel. The results are depicted in Figure 7.12.

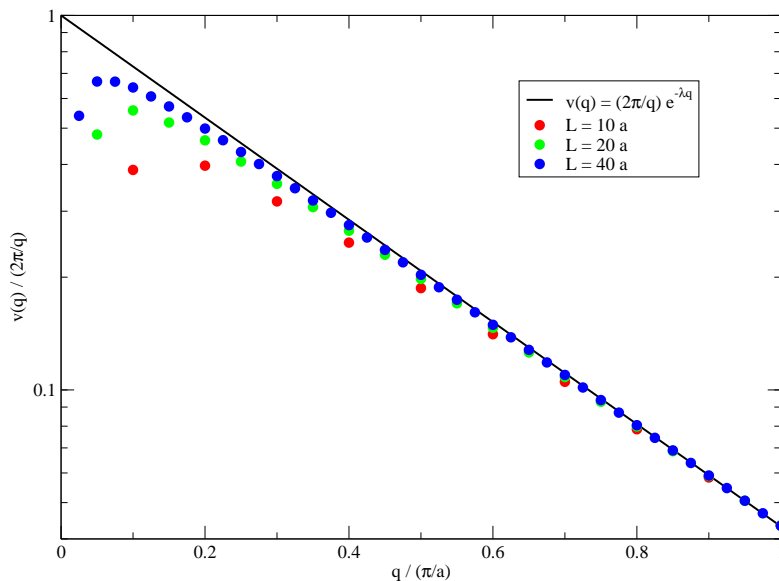


Figure 7.12: Coulomb kernel for quadratic geometries.

Analogous observations can be made as in the 3D case:

- i) If the wavelength becomes of the order of the orbital size, the deviation between the matrix element of the Coulomb kernel and $2\pi/q$ can become very large.
- ii) For a fixed wave vector, the matrix elements of the Coulomb kernel approach the Coulomb kernel with periodic boundary conditions.
- iii) The matrix elements of the Coulomb kernel of lowest resonances deviate up to 60% when going to the thermodynamic limit. We have calculated the matrix elements for the lowest twenty modes and plotted them in Figure 7.13. One can see that the deviation quickly drops off when increasing the number of nodes.

In order to find the plasmon frequencies, we must find the roots of the dielectric function. Neglecting any damping, the plasmon dispersion can be written as

$$\omega^2(q_i) = \frac{8}{\pi^2} t e^2 v(q_i) q_i^2 + \frac{8}{3} t^2 a^2 q_i^2. \quad (7.40)$$

We study once again the scaling behavior of the plasmon frequency with respect to the system size. We know from section 7.3.2 that the second term scales with the reciprocal of the square of the system size. By employing the same rescaling for the matrix elements of the Coulomb kernel as done in section 7.3.2, one finds that the first term scales with the reciprocal of the system size, as long as L is much bigger than λ . If both quantities are

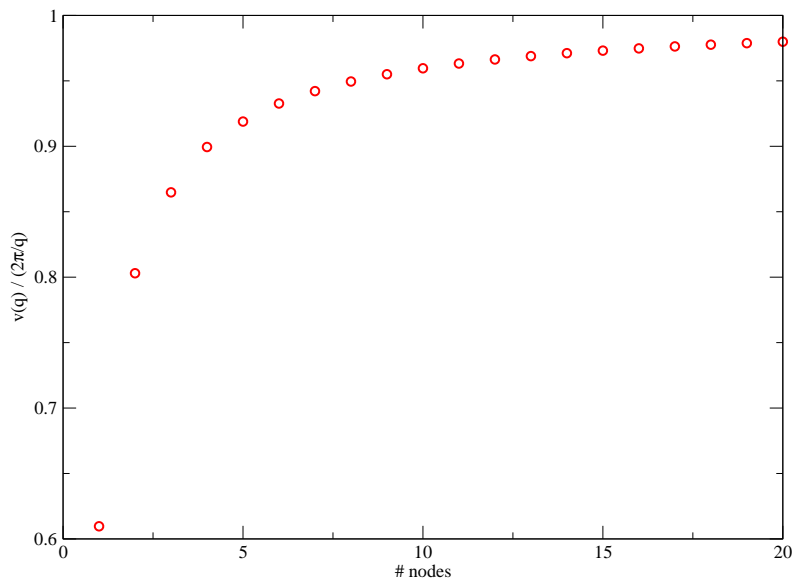


Figure 7.13: Coulomb kernel for a square in the thermodynamic limit.

of the same order of magnitude, the matrix elements of the Coulomb kernel will decrease when the system size is decreased.

7.4.3 Comparison of analytics with numerics

We now compare the plasmon frequencies obtained from numerical and analytical calculations. The systems under consideration are tight-binding squares at half-filling. Unlike the calculations in the last section, we not only calculated the first resonance here, but also obtained higher ones. We depict the comparison of the numerics with the continuum model in Figure 7.14. The different colored circles correspond to various system sizes. A circle of a certain color with the lowest frequency corresponds to the plasmonic excitation with one node. The next circle of the same color but with a higher frequency corresponds to the excitation with two nodes, the next circle in the series corresponds to the excitation with three nodes, and so on and so forth.

At first, one observes that the numerical and analytical results based on the continuum model from the last section agree more closely with each other when the system size is increased. We have already given an explanation of this behavior in Section 7.3.3. In addition, one also sees that the deviation between the numerical results and the results

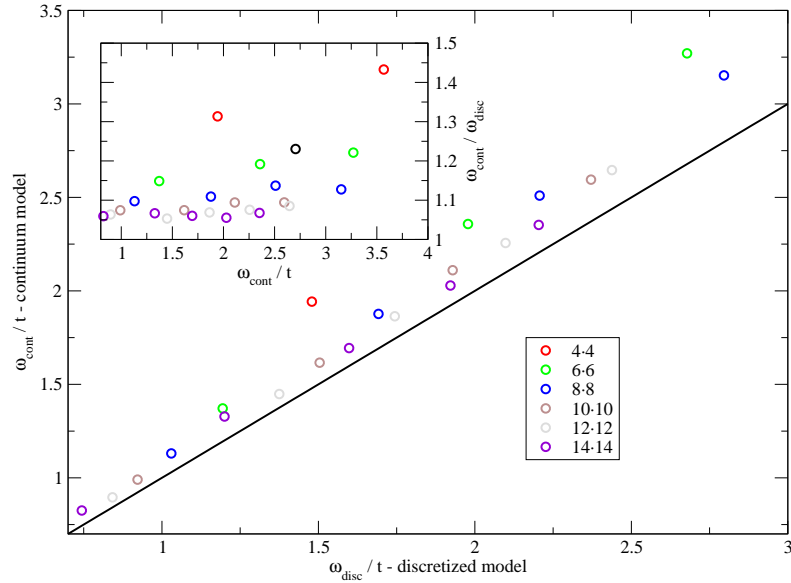


Figure 7.14: Plasmon dispersion in square geometries.

from the continuum model increases as one goes to higher excitations. The good agreement shows that the assumption that the plasmonic density profiles are constant in the dimensions perpendicular to the propagation direction of the is valid even for relatively structures. The inset shows that the continuum model can make predictions for the plasmon frequencies with an accuracy of 10% for system sizes bigger than $10 \cdot 10$.

We have also tested the continuum model for a set of tight-binding rectangles against the numerical implementation, as shown in Figure 7.15.

Similar observations can be made as for the squares. However, in addition one also sees that the agreement for a $L \times b$ rectangular is much better than for $b \times L$, if $L > b$. This suggests that the Friedel oscillations along the q -direction are the main source of the deviation. This also implies that the assumption that the density is homogeneous in the co-dimensions appears to be valid even for small lengths.

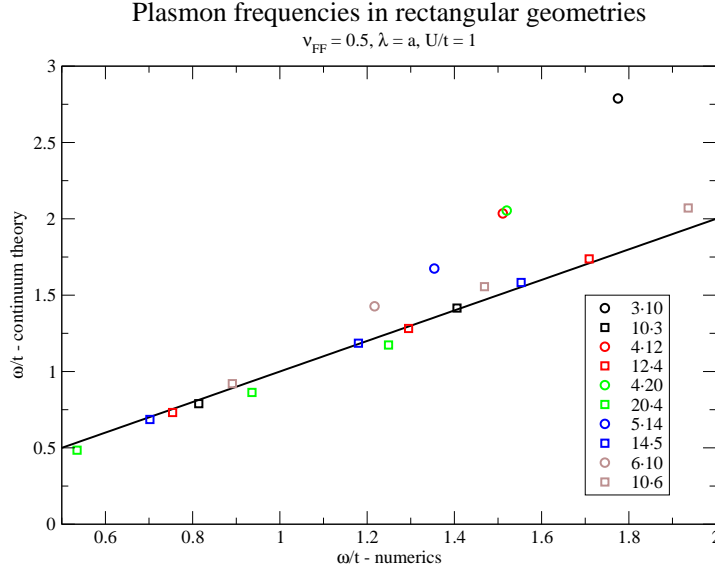


Figure 7.15: Plasmons in rectangular geometries.

7.5 One dimensional systems

7.5.1 General dispersion

We consider a 1D wire with length L , where the electronic dispersion is denoted by $\epsilon(k)$. The Random Phase Approximation for the irreducible density density correlation function is

$$\chi^{(0)}(q, \omega) = -2 \int \frac{dk}{2\pi} \left(\frac{1}{z - (\epsilon(k) - \epsilon(k - q))} - \frac{1}{z - (\epsilon(k + q) - \epsilon(k))} \right) f(\epsilon(k)). \quad (7.41)$$

After performing a Taylor expansion for small momenta, the integration yields

$$\chi^{(0)}(q, z) \approx \frac{2q^2 v_{\text{F}}}{\pi} \frac{z^2 + v_{\text{F}}^2 q^2}{z^4}, \quad (7.42)$$

where we have assumed that the electronic dispersion is even with respect to the wave vector, i.e., $\epsilon(q) = \epsilon(-q)$. In addition, we have neglected a term involving a third derivative of the electronic dispersion.

If we denote the matrix elements of the Coulomb kernel by $v(q)$, the dielectric constant is given by

$$\epsilon(q, z) = 1 - v(q) \chi^{(0)}(q, z). \quad (7.43)$$

From this we can extract the plasmon dispersion relation as follows

$$\omega_{\text{pl}}^2(q) = \frac{2}{\pi} e^2 v(q) v_{\text{F}} q^2 + v_{\text{F}}^2 q^2. \quad (7.44)$$

The density response function is given by

$$\chi_{\text{ext}}(q, \omega) = \frac{\frac{2}{\pi} e^2 v_{\text{F}} q^2}{\omega_{\text{pl}}^2(q) - 2i\eta\omega - \omega^2}. \quad (7.45)$$

We attempt once again to establish a connection between the conductivity and the phenomenological parameters from circuit theory. For this purpose, we consider an external homogeneous electric field E_{ext} along the wire with potential $E_{\text{ext}}L$. In one dimension the current and the current density are identical, so we have

$$Z = \frac{L}{\sigma}. \quad (7.46)$$

We then make a comparison with the corresponding expression from circuit theory,

$$\frac{i\omega \frac{2e^2 v_{\text{F}}}{\pi L}}{\omega_{\text{pl}}^2(q)^2 - 2i\eta\omega - \omega^2} = \frac{i\omega \frac{1}{\mathcal{L}}}{\omega^2 + i\frac{\mathcal{R}}{\mathcal{L}} - \frac{1}{\mathcal{L}\mathcal{C}}}, \quad (7.47)$$

where we have disregarded the term $-\eta^2$ in the denominator of the lefthand side of equation (7.47). A simple comparison of coefficients yields

$$\mathcal{L} = \frac{\pi L}{2e^2 v_{\text{F}}}, \quad (7.48a)$$

$$\mathcal{R} = 2\eta\mathcal{L} = \frac{\pi\eta L}{e^2 v_{\text{F}}}, \quad (7.48b)$$

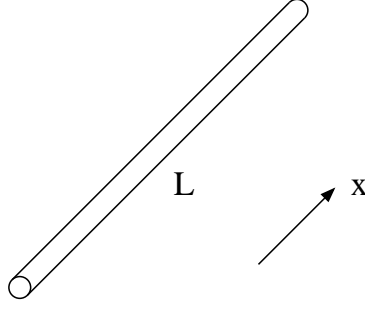
$$\mathcal{C}^{-1} = \left(\frac{1}{v(q)Lq^2} \right)^{-1} + \left(\frac{2}{\pi} \frac{e^2/L}{v_{\text{F}}q} \frac{1}{q} \right)^{-1}. \quad (7.48c)$$

The inductance is once again related to the acceleration of the electrons, as we have already seen in the case of two and three dimensions. The inverse capacitance comprises two different parts, the first one resulting from the classical restoring forces and the second one originating from single particle excitations. The second one is also called quantum capacitance.

Similar results have been derived in the literature [16]. However, the results presented in this work differ on some accounts. The kinetic inductance (7.48b) calculated in [16] is different by a factor of 2, owing to a neglect of spin. The quantum capacitance also deviates by a factor of $2/\pi^2$. This can be traced back to an earlier assumption made in [16], namely that the separated charges are $\pm e$. A more detailed analysis based on the plasmonic density profiles, in fact, reveals that the product of the separated charges within our model is $2e^2/\pi^2$ which explains the different pre-factors.

Straight wire profile

As a first application of the general plasmon dispersion derived in the previous section,

Figure 7.16: 1D wire with length L .

we study the plasmonic excitations of a straight wire that is parallel to the x -direction. The length of the wire is L . The geometry is shown in Figure 7.16.

The density profiles are expressed as

$$\pi_i(x) = \sqrt{\frac{2}{L}} \cos\left(i\frac{\pi}{L}x\right), \quad (7.49)$$

where L denotes the wire length. The electronic dispersion is chosen to be a cosine band,

$$\epsilon(k) = -2t \cos(ka). \quad (7.50)$$

The only missing information now involves the matrix elements of the Coulomb kernel,

$$v(q_i) = \int_0^L dx \int_0^L dx' \frac{\pi_i(x)\pi_i(x')}{\sqrt{(x-x')^2 + \lambda^2}}. \quad (7.51)$$

We have observed in the 3D and 2D cases that the matrix elements of the Coulomb kernel are different from the Fourier transform of the Coulomb kernel for long wave lengths due to the effect of the boundaries. We have therefore calculated the Coulomb kernel for three different system sizes as shown in Figure 7.17.

It becomes evident once more that the Coulomb kernel approaches the Fourier transform for a fixed wavelength when the system size is increased. However, in contrast to 3D and 2D the matrix element of Coulomb kernel of the plasmon with one node approaches the Fourier transform in the thermodynamic limit. For the purpose of illustration, we have plotted the flow of the Coulomb kernel of the plasmonic mode with one node for different system sizes in Figure 7.17.

Finally, we analyze the scaling behavior of the plasmon frequency with respect to the system size. The second term in equation (7.44) scales in the same manner as in the cases of 2D and 3D. The first term scales roughly like $L^{-2} \ln(L/\lambda)$, which can easily be seen by rescaling the variables as it was done for the cases in 2D and 3D.

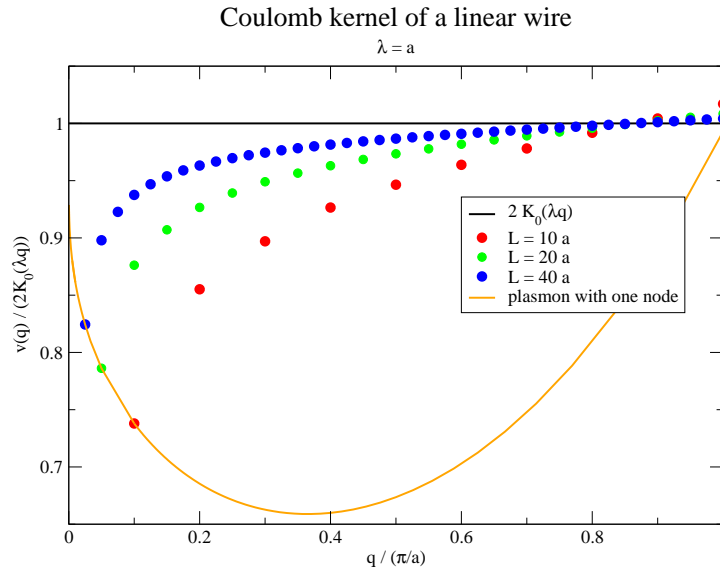
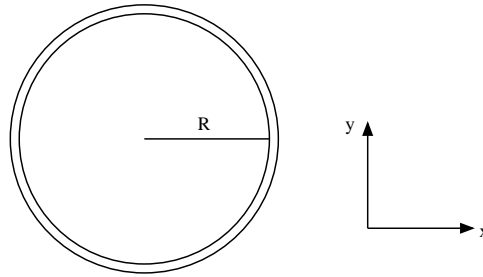


Figure 7.17: Coulomb kernel of a linear wire.

Figure 7.18: Circle with radius R .

Ring profile

We now consider a ring with radius R . The geometry is depicted in Figure 7.18. We assume that there exists the same dispersion, similar to the wire from the previous section. Unlike the straight wire from the previous section, a ring can only exhibit plasmons with an even number of nodes. However, each plasmonic mode is twofold degenerate, as one can rotate the density profile by 90 degrees (see Figure 7.3), producing a density profile that is orthogonal to the original one. If we denote the circumference of the ring by L , the plasmonic density profiles become

$$\pi_i(\phi) = \sqrt{\frac{2}{L}} \cos(\phi i). \quad (7.52)$$

Thus, the matrix elements of the Coulomb kernel are given by the following expression

$$v(q_i) = \int_0^{2\pi} d\phi R \int_0^{2\pi} d\phi' R \frac{\pi_i(\phi)\pi_i(\phi')}{\sqrt{2R^2 - 2R^2 \cos(\phi - \phi') + \lambda^2}}. \quad (7.53)$$

7.5.2 Comparison of continuum theory to numerics

We now compare the results from the numerics and the continuum model with one another. We consider linear chains with a filling fraction of 0.5 and rings with a filling fraction of 0.5. The results are summarized in Figures 7.19 and 7.20.

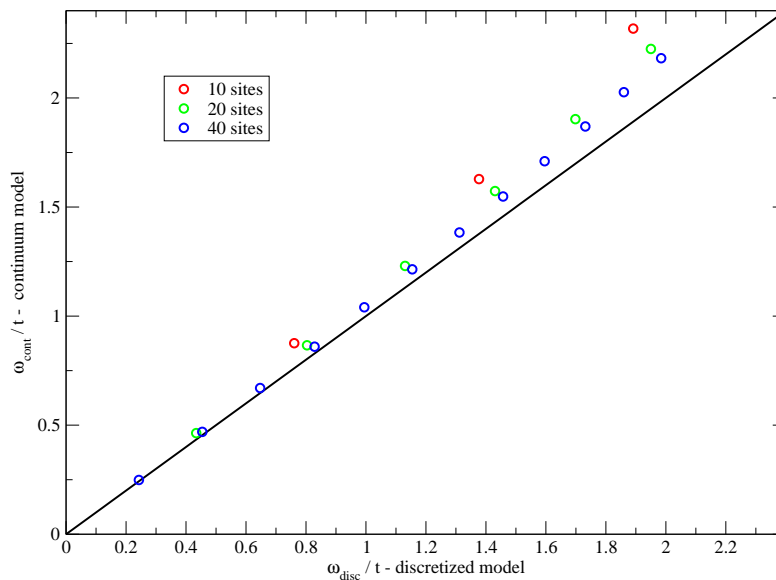


Figure 7.19: Plasmon dispersion for a linear chain.

As in the 3D and 2D case, the agreement between the numerics and the continuum model improves when the system size is increased. The deviation on the other hand increases for a fixed system size when going to higher wave vectors. A comparison of the data for the lines and the circles shows that the deviation from the continuum model and the numerics is smaller for the rings when compared to that of the lines. This suggests once again that the main reason for the deviation is from the neglect of the reflection oscillations for the plasmonic density profiles of the line.

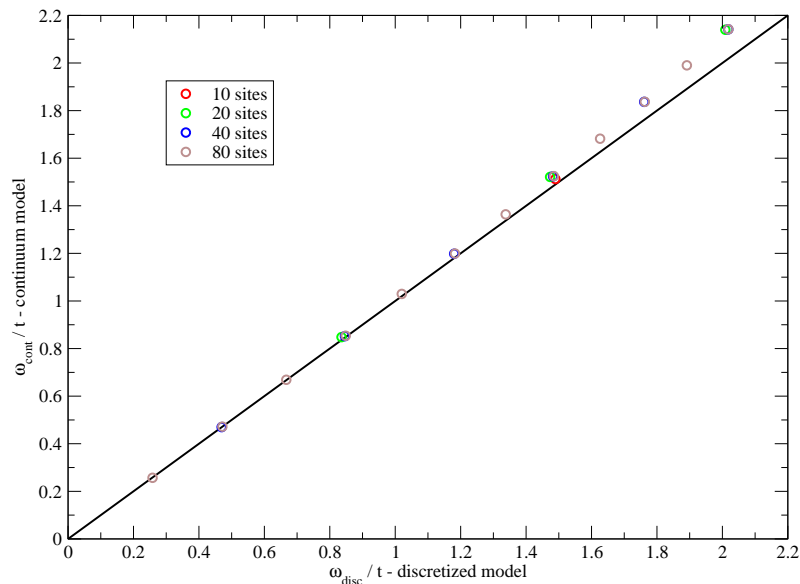


Figure 7.20: Plasmon dispersion on circles

7.6 Generalization and summary

We have reformulated the well-known results for the plasmon dispersion in 3D, 2D, and 1D [67] by reviewing the expressions based on a free electronic dispersion and the assumption of periodic boundary conditions. We then calculated the plasmon dispersion for finite systems by employing the continuum model from Chapter 6, verified the results against numerical simulations, and found good agreement between the two. This suggests that the model is capable of describing the plasmonic resonances for other geometries and electronic structures than presented in this chapter, too. Examples of relevant structures are spherical geometries, serving as models for the description of plasmonic excitations of metal clusters and fullerenes, or cylinders with applications in the field of carbon nanotubes.

We have discussed the effect of the finite size and the boundary on the Coulomb interaction. In addition, we have found that the scaling behavior of the classical piece of the plasmon dispersion is exactly the same as if one would calculate the classical restoring forces based on charged plates, wires or point charges. We also noticed that the restoring forces are reduced when the system size is comparable to the orbital size.

We have further established a connection to the circuit models by providing explicit expressions for the circuit parameters. In order to do so, we calculated the current by integration over the cross section the wave vector of the external field is perpendicular

	3D	2D	1D
$\omega_{\text{pl}}^2(q)$	$\frac{4\pi e^2 n_{3\text{D}}}{m} + \frac{3}{5} \left(\frac{k_{\text{F}}}{m}\right)^2 q^2$	$\frac{2\pi e^2 n_{2\text{D}}}{m} q + \frac{3}{4} \left(\frac{k_{\text{F}}}{m}\right)^2 q^2$	$\frac{2e^2 n_{1\text{D}} K_0(\lambda q)}{m} q^2 + \left(\frac{k_{\text{F}}}{m}\right)^2 q^2$
\mathcal{L}_{kin}	$\frac{Lm}{e^2 A n_{3\text{D}}}$	$\frac{Lm}{e^2 b n_{2\text{D}}}$	$\frac{Lm}{e^2 n_{1\text{D}}}$
$\mathcal{C}_{\text{classical}}$	$\frac{A}{4\pi L}$	$\frac{b}{2\pi L q}$	$\frac{1}{2L K_0(\lambda q) q^2}$
$\mathcal{C}_{\text{quantum}}$	$\frac{5e^2 A k_{\text{F}} m}{9\pi^2 \hbar^2 L q^2}$	$\frac{2e^2 b m}{3\pi \hbar L q^2}$	$\frac{2e^2 m}{\pi k_{\text{F}} \hbar^2 q^2 L}$

Table 7.1: Plasmon dispersion in 1D-3D.

to. Additionally, we obtained the corresponding voltage drop by integrating the external electric field. The appearing geometrical factors, such as the cross section area and some lengths, entered the expressions for the circuit parameters, but did not come into play for the plasmon dispersion equations. Therefore, the description based on densities and current densities appears to be more favorable. This is especially true, when the wave vector of the external field points into an arbitrary direction and is not parallel to a side of the slab under consideration, the current density is not constant within the planes with the wave vector as a normal, and thus, one would lose information about the spatial structure of the current density upon integration.

The plasmon dispersions and circuit parameters are summarized for a parabolic electronic dispersion in Table 7.1.

Chapter 8

The Split Ring Resonator

8.1 Introduction

The molecular split ring resonators we want to address in this chapter are organic ring molecules that are composed of an delocalized π -system and methylene groups acting effectively as an interruption of the π -system. An example of such a system is depicted in Figure 8.1.

The low-lying electronic excitations of these molecules occur in the π -system, so our model description will focus mainly on it. We will treat the π -electrons within the jellium approximation. The electrons of the σ -system screen the charges of the atomic nuclei such that the π -electrons experience the whole σ -framework as a homogeneously charged background. The interaction of the π -electrons among each other at the Hartree level, the interaction of the electrons with the background and the self-interaction of the background roughly cancel, as discussed in Section 5.2.1. The slit will be modeled as a tunneling barrier.

We will study the response behavior of the SRRs by employing both the discretized model from chapter 5 and the continuum model from Chapter 6. First, we discuss the coupling of the external light field to the molecule. We will then proceed to determine the plasmonic waves, calculate their dispersion and compare the results from the numerics and the continuum model. Next, we will compute the polarizabilities and make again a comparison of the results obtained with both methods. Armed with the knowledge acquired from this analysis, we will be in the position to discuss how to tune the electromagnetic response properties of single SRRs.

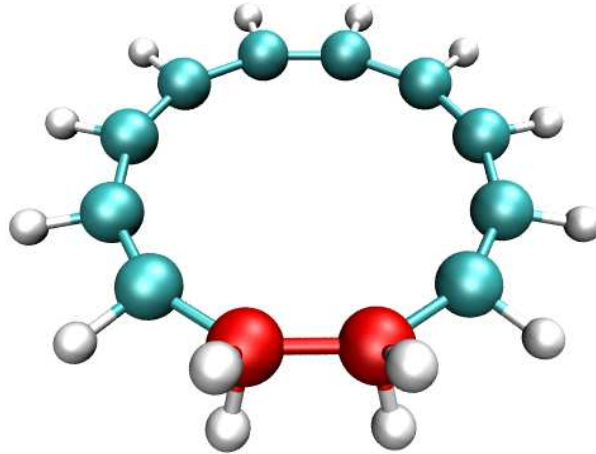


Figure 8.1: Model ring molecule as an SRR. Note that the structure will not stay planar when a geometry relaxation is performed. We have colored the carbon atoms that constitute the π -system in blue and the slit atoms in red.

8.2 Definition of the model systems

8.2.1 Geometry the SRR

In this section we show the geometry of the SRRs under consideration. In the discrete model, the geometry of the SRR is fixed by specifying the number of sites N , the distance between two neighboring sites a , and the number of vacancies N_{vac} , as shown in Figure 8.2.

In the continuum model, one uses the length L and an opening angle $2\phi_0$ for the specifi-

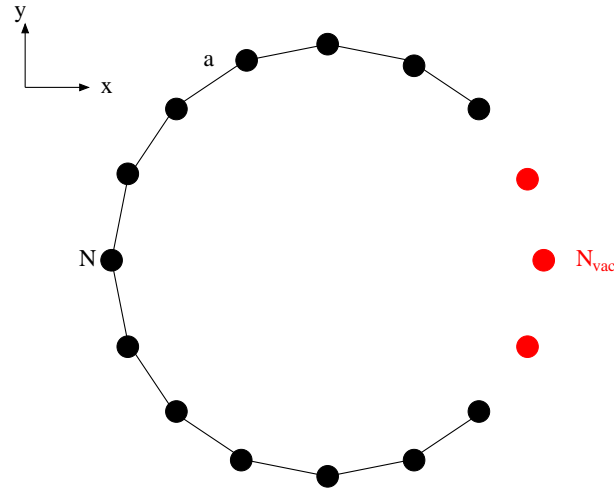


Figure 8.2: Description of the SRR in the discretized model. a denotes the lattice constant. The black dots are lattice site and their number is N . Vacancies are depicted by red dots and their number is N_{vac} .

cation of the geometry, as shown in Figure 8.3.

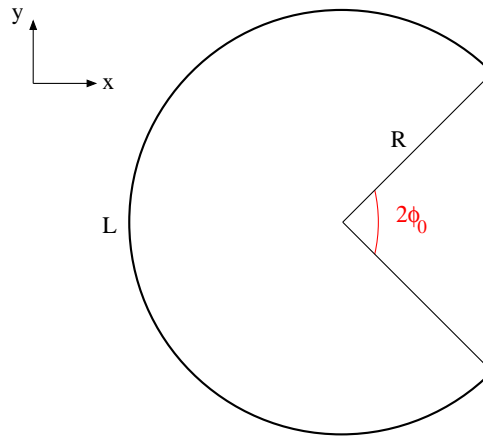


Figure 8.3: Description of the SRR in the continuum model. The length is denoted by L and the opening angle is $2\phi_0$.

Note that $L = (N - 1)a$ and $2\phi_0 = \pi(N_{\text{vac}} + 2)/(N + N_{\text{vac}})$.

8.2.2 External fields

Both the wave vector of the external light field and its electric field are supposed to lie in the xy -plane. Hence, the magnetic field vector is parallel to the z -axis. Concerning

now the electric field, we will be interested in the cases where the field vector is either parallel to the x -axis (see Figure 8.4 - left) or to the y -axis (see Figure 8.4 - middle). The magnetic field gives rise to a longitudinal electric field along the ring (see Figure 8.4 - right).

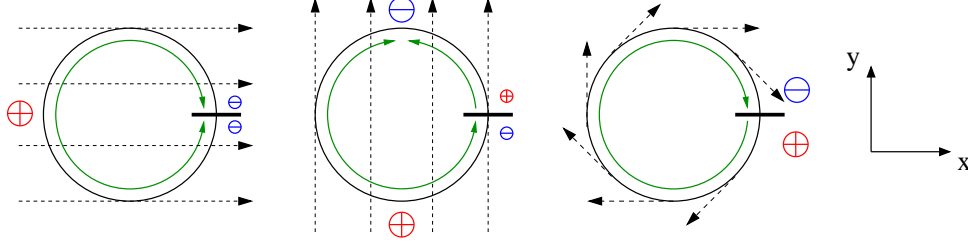


Figure 8.4: The external field configurations of the light field within the dipole approximation: Dashed arrows indicate the direction of the E -field. The B -field is perpendicular to the plane. The red circles with a plus sign indicate the accumulation of positive charges and the blue circles symbolize the accumulation of negative charges. The green arrows depict the current flow.

8.3 Plasmonic excitations

8.3.1 Density profiles

The plasmonic excitations of the molecular SRRs are easily understood if one has a look at the possible standing waves on the ring geometry, as they determine the plasmonic density profiles,

$$\pi_m(\phi) = \frac{1}{\sqrt{(\pi - \phi_0)R}} \cos\left(\frac{\phi - \phi_0}{\pi - \phi_0} \frac{m}{2}\pi\right). \quad (8.1)$$

By inspection of the shape of the plasmonic density profiles that are shown in Figure 8.5, one observes that for an odd number of nodes the charge densities at the different sides of the slit are different, whereas for an even number of nodes the sign of the charge densities at both sides of the slit are identical.

The accumulation of charges with different signs at the ends of the slit results from either an electric field parallel to the y -axis or a magnetic field parallel to the z -axis, so both fields excite plasmons with an odd number of nodes. As an electric field parallel to the x -axis accumulates charges with the same sign at the ends of the slit, this field excites plasmons with an even number of nodes. The group theoretical considerations in the next subsection will give the proofs of these statements.

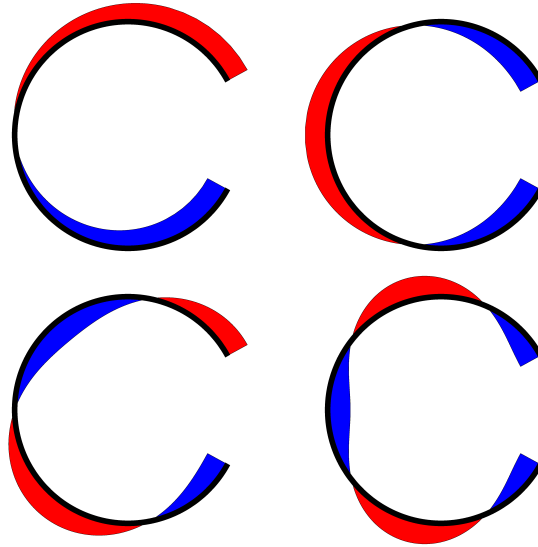


Figure 8.5: Plasmonic density profiles for an SRR.

8.3.2 Symmetry considerations

A systematic way of analyzing the plasmonic excitations of the SRRs is based on group theory. The point group of a single SRR is C_{2v} . In order to understand which plasmons are excited by which external field, one must classify both the plasmonic excitations and the external fields in terms of the irreducible representations of C_{2v} , given in character Table 8.1.

	E	C_2	σ_v	σ'_v	
A_1	1	1	1	1	T_x
A_2	1	1	-1	-1	R_x
B_1	1	-1	1	-1	T_y, R_z
B_2	1	-1	-1	1	T_z, R_y

Table 8.1: Character table of the point group C_{2v} .

Note that one has to be careful, as the conventional choice of the coordinate system used in group theory does not coincide with the coordinate system we have chosen for the SRR. Therefore, we added the transformation behavior of translations T along the coordinate axes and rotations R around the coordinate axes to the character table.

In order to determine the transformation behavior of the plasmonic excitations, we analyze the transformation properties of the plasmonic density profiles. We know that the character for the identity operation will always be one. If we consider a plasmon

with an odd number of nodes, the density profile will change its sign under a C_2 - or a σ'_v -transformation, but stays invariant under a σ_v -transformation. So we know that plasmons with an odd number of nodes transform like B_1 ,

$$\Gamma_{\text{odd}} = (1 \quad -1 \quad 1 \quad -1) = B_1. \quad (8.2)$$

Considering now the density profile with an even number of nodes, one easily sees that it is invariant under all transformations, so the corresponding plasmons transform like the totally symmetric irreducible representation A_1 ,

$$\Gamma_{\text{even}} = (1 \quad 1 \quad 1 \quad 1) = A_1. \quad (8.3)$$

As a next step, we analyze the transformation behavior of the potentials originating from the external fields. The electric field along the x -axis transforms as A_1 , the electric field along the y -axis and the magnetic field along the z -axis as B_1 . An inspection of the corresponding potentials shows that each potential transforms in the same manner as the corresponding field. In order to check, if the external potential excites a certain plasmon, one has to analyze the response equation

$$\delta\rho(\mathbf{r}, z) = (-e)^2 \sum_{\mu\nu} \Psi_\mu(\mathbf{r})\Psi_\nu(\mathbf{r}) \frac{f(\epsilon_\mu) - f(\epsilon_\nu)}{\epsilon_\nu - \epsilon_\mu - z} \int d^3\mathbf{x}' \Psi_\nu(\mathbf{r}')\Psi_\mu(\mathbf{r}')\Phi_{\text{ext}}(\mathbf{r}'). \quad (8.4)$$

At first, we analyze the matrix elements of the external potential. The states Ψ_μ and Ψ_ν transform like Γ_μ and Γ_ν , the irreducible representation Φ_{ext} transforms as is denoted by Γ_{ext} . In the following, we consider an arbitrary point group, so the results will not be restricted to C_{2v} . If one applies the Wigner-Eckart theorem to equation (8.4), the induced density must transform as the same irreducible representation like the external potential. This means in return that the knowledge of the plasmonic density profile enables one to determine by which external field a plasmon can be excited. Thus, plasmons with an odd number of nodes can only be excited by electric fields parallel to the y -axis or magnetic fields perpendicular to the ring plane and that plasmons with an even number of nodes can only be excited by an electric field parallel to the x -axis. So we have given a group theoretical proof of the claim from the previous section.

We are now in the position to analyze the effect of the introduction of further slits. The arrangement of the slits shall be such that two neighboring slits are equidistant. The point group of an SRR with n slits is then D_{nh} . A direct inspection of the character tables shows that all three types of external fields excite different plasmons for the case $n = 2$. If $n \geq 3$, the plasmons excited by electric fields are twofold degenerate, while the magnetic field perpendicular to the ring plane excites plasmons transforming like another irreducible representation. It should be noted that the possibility to excite the same

plasmon by an electric field in the ring plane and a magnetic field perpendicular to it exists only for the case of the single-slit ring resonator - at least if one considers ring geometries. The group theoretical analysis can also be performed for other geometries, of course. A very interesting case are resonators whose point group is the symmetry group of the pure rotations of a tetrahedron, an octahedron, or an icosahedron, because all plasmons excited by external electric and magnetic fields transform according to the same irreducible representation. A material that is built from these building blocks exhibits electric and magnetic resonances at the same frequencies.

8.3.3 Plasmon dispersion on SRRs

We have already derived the plasmon dispersion for one dimensional systems in Section 7.5.1,

$$\omega^2(q_m) = \frac{2}{\pi} e^2 v(q_m) v_F q_m^2 + v_F^2 q_m^2. \quad (8.5)$$

Here, q_m is given by

$$q_m = \frac{\pi}{L} m, \quad (8.6)$$

and $v(q_m)$ is given by,

$$v(q_m) = \frac{1}{\pi - \phi_0} \int_{\phi_0}^{2\pi - \phi_0} d\phi \int_{\phi_0}^{2\pi - \phi_0} d\phi' \cos\left(\frac{\phi - \phi_0}{2\pi - 2\phi_0} q_m L\right) \frac{1}{\sqrt{2 - 2\cos(\phi - \phi') + \lambda^2/R^2}} \cos\left(\frac{\phi' - \phi_0}{2\pi - 2\phi_0} q_m L\right) i. \quad (8.7)$$

Bending a straight wire into an SRR

In order to analyze the impact of the geometry on the restoring forces, we bend a straight wire to an SRR geometry, where we keep the length of the wire fixed. The filling fraction is set to 0.5, so the Fermi velocity equals $2ta$, and the energy scale of the Coulomb interaction U is equal to the energy scale of the kinetic energy t , $U = t$. We then divide the square of the plasmon frequency by $(2taq)^2$; the resulting expression on the right-hand side then solely depends on the restoring forces,

$$\frac{\omega_{\text{bend}}^2(q_m)}{(2taq_m)^2} = \frac{1}{\pi} v(q_m) + 1. \quad (8.8)$$

We consider the ten plasmons with the lowest energy and compare the results from the numerical calculation (100 sites) with the analytical expressions, as depicted in Figure 8.6.

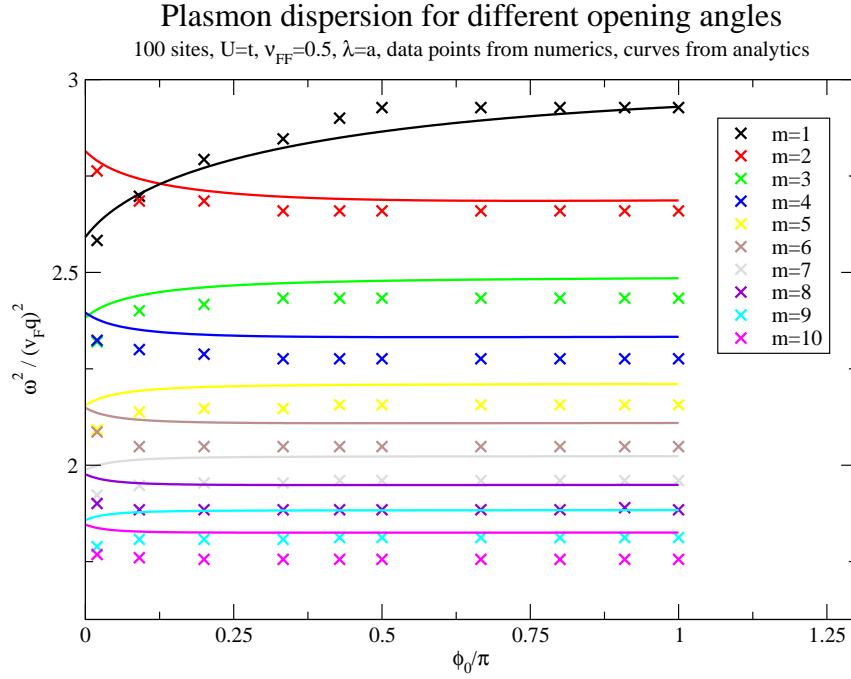


Figure 8.6: Dependence of the plasmon frequencies on the opening angle of the SRR.

The numerical plasmonic excitation frequencies were obtained by studying the flow of the absolute values of the eigenvalues of the dielectric matrix under the variation of the frequency.

One directly sees the good agreement between the analytical and the numerical results for the restoring force, as the deviations lie only in a range of a few percents. The flow of the excitation energies, however, is just opposite as one would naively expect. Looking at Figure 8.4 suggests that the frequency for plasmons with an odd number of nodes should go up as the two charges at the slit lead to an increase of the restoring force, whereas for an even number of nodes the opposite should occur. Such a behavior is expected for 3D systems as the restoring forces are then independent from the distance. In one dimension, however, the force drops off with the reciprocal distance, so the main contribution comes from the neighboring sites.

For the purpose of illustration and simplicity we employ a point charge model. We associate with each minimum and maximum of the plasmon density a single point charge. The strength Q of the charge is determined by integrating the charge density around the extremum under consideration between the neighboring nodes. The charge of each maximum will be $+Q$ and the one for each minimum will be $-Q$ - except for extrema at the ends, where the charges are $\pm Q/2$. We have sketched the point charge model of the first four resonances in Figure 8.7 where we have denoted the positive charges by red circles with a plus and the negative ones by blue circle with a minus. The factor of $1/2$

is depicted by using different radii.

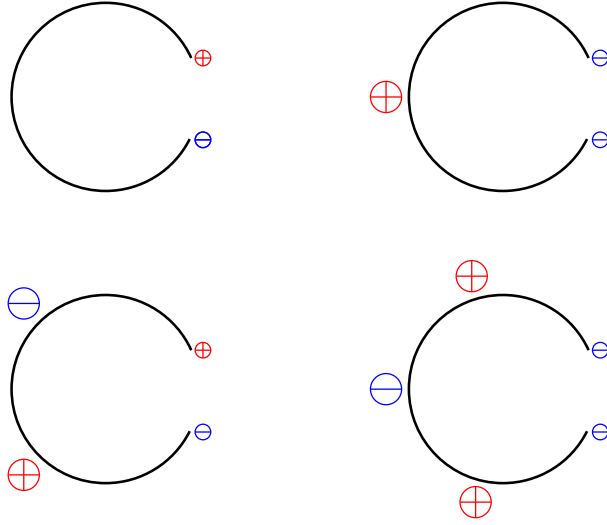


Figure 8.7: Point charge model of the lowest resonances of an SRR

The point charge model can mathematically be defined by giving the density profile

$$\pi_{\text{PC}}(\mathbf{r}) = \sum_i Q_i \delta(\mathbf{r} - \mathbf{R}_i) \quad (8.9)$$

where Q_i are the charges and \mathbf{R}_i their positions. We calculate the matrix elements of the Coulomb kernel using the point charge model in order to check if this model provides a qualitative description of the dependency of the restoring forces on the opening angle. The results are shown in Figure (8.8).

One sees that the point charge model shows the same trends as the continuum model concerning the dependency on ϕ_0 . It gives a correct description whether the plasmon frequency increases when the opening angle is increased.

Finally, one can observe in Figure 8.6 that the matrix elements of the Coulomb kernel for excitations with $m \geq 3$ show up in pairs if the opening angle is small. When going from a plasmon with an even number of nodes to the next higher one, the density profile acquires one additional node, but now the sign of charge densities are equal. So the number of nodes between positive and negative charge densities is not changed. Therefore, the matrix elements of the Coulomb kernel have similar values in both cases.

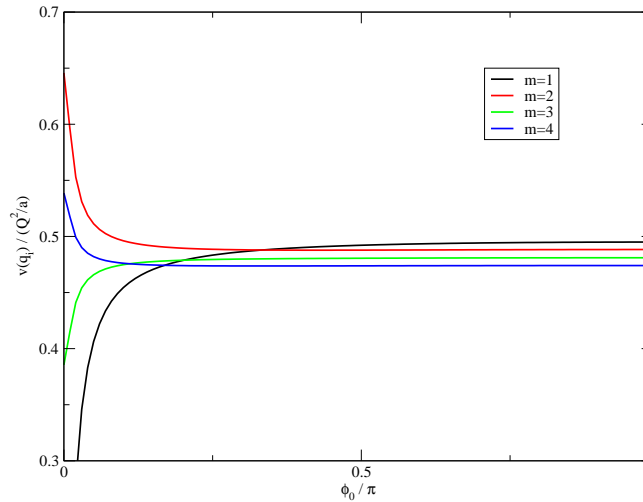


Figure 8.8: Matrix elements of the Coulomb kernel calculated with the point charge model.

Impact of the filling fraction

We have calculated the plasmon frequencies of the ten lowest excitations for an SRR with 100 sites, 2 vacancies, $\lambda = a$, and $U = t$, varying the filling fraction from 0.1 to 0.9 in steps of 0.1. The results are depicted in Figure 8.9. One observes that the modes are

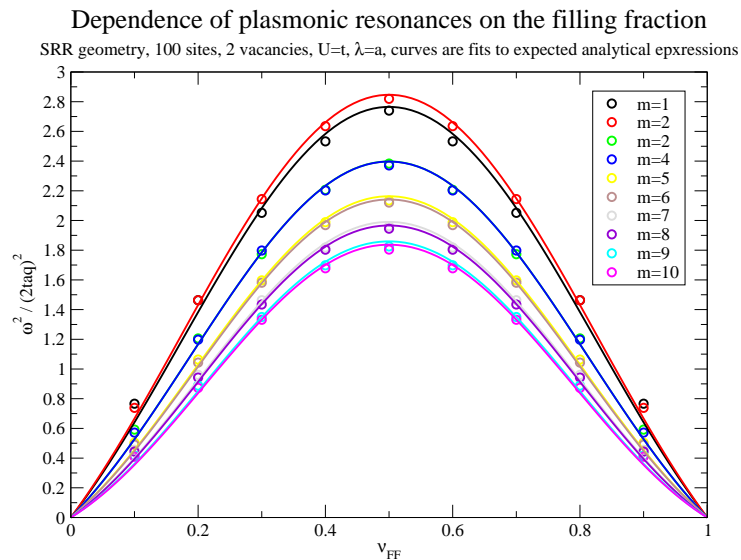


Figure 8.9: Numerical plasmon frequencies for an SRR with 100 sites and 2 vacancies for various filling fractions. The continuous curves are obtained by fitting the numerical data to the expected analytical expression.

symmetric with respect to $\nu_{\text{FF}} = 0.5$. This is a direct consequence of the particle-hole symmetry of the electronic dispersion. We have then calculated the matrix elements of the Coulomb kernel, utilizing the continuum model, and performed a least square fit of the data from the discretized model to the expression of the plasmon dispersion from the continuum model, equation (8.5), in order to obtain the Fermi velocity. The fit values are then compared with the values one would expect from the following expression

$$v_{\text{F}} = \left. \frac{\partial(-2t \cos(ka))}{\partial k} \right|_{k=k_{\text{F}}} = 2ta \sin(\nu_{\text{FF}}\pi). \quad (8.10)$$

The results are shown in Figure 8.10.

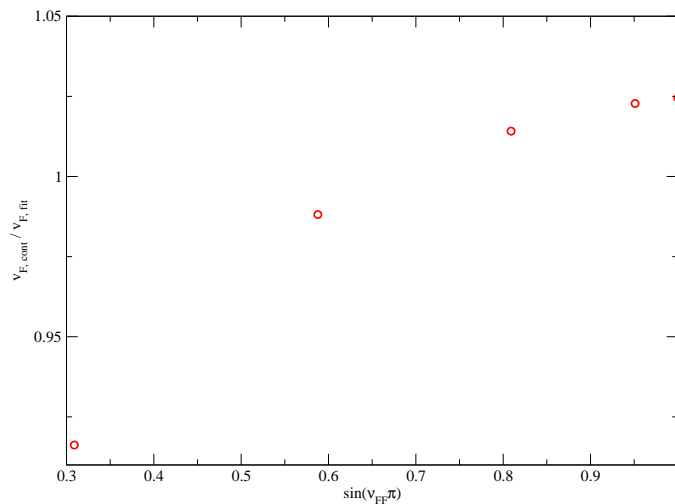


Figure 8.10: Comparison of the Fermi velocity for different filling fractions obtained by fitting of data from the discretized model to the plasmon dispersion of the continuum model and the expected value given by equation (8.5). Model parameters: 100 sites, 2 vacancies, $\lambda = a$, and $U = t$.

Changing the Coulomb energy scale

In order to study the impact of the Coulomb energy scale, we consider the first ten plasmonic excitations obtained from numerical calculations for a half-filled SRR-geometry with 100 sites and 2 vacancies. We have determined the frequencies for the values of U/t from 0 to 4 and plotted them in Figure 8.11. This plot once again shows the pairing of the matrix elements of the Coulomb kernel.

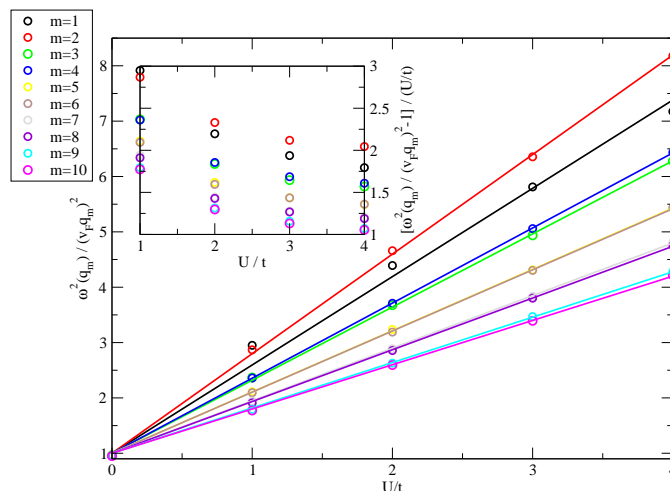


Figure 8.11: Numerical plasmon frequencies for an SRR with 100 sites and 2 vacancies for different interaction strengths, $\lambda = a$.

However, we did not choose to plot the frequency directly, but rather the square of the frequencies, as they are proportional to the ratio of the Coulomb energy scale and the kinetic energy scale:

$$\frac{\omega_{\text{Coul}}^2(q_m)}{(v_F q_m)^2} = \frac{1}{\pi} \frac{U}{t} v(q_m) + 1 \quad (8.11)$$

The division by the square of the single particle excitation energies is supposed to yield a result that only depends on the restoring forces contained in $v(q_m)$ and the ratio U/t . Figure 8.11 shows the expected linear behavior from the analytical expression. Besides, one can see that the axis interception lies for all excitations at 1. This means that the single particle excitations of the non-interacting system are also described well by the analytical theory. By means of a linear regression, we can determine the slope and compare it with $\frac{1}{\pi} v(q_m)$ from the analytical theory. We have depicted the results in Figure 8.12. One sees a good agreement between the continuum and the discretized model. For the modes with an even number of nodes, however, this agreement is better than for those modes with an odd number of nodes.

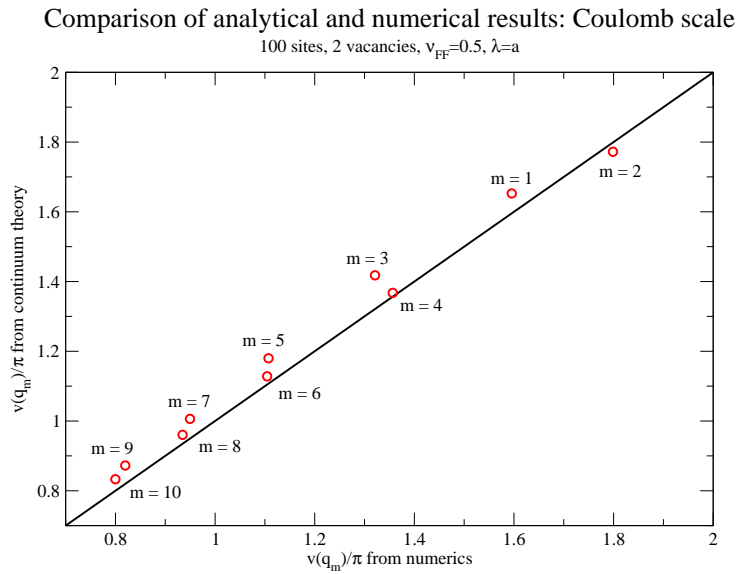


Figure 8.12: Comparison of the matrix elements of the Coulomb kernel obtained from the numerics and the continuum model.

Impact of the system size

Now, we compare the results of the numerical and continuum approximation under a scaling of the system size. We keep the slit angle (in the numerical model the ratio of sites and vacancies = 5/1), the filling fraction $\nu_F = 0.5$, the ratio $U/t = 1$ and $\lambda = a$ during the scaling fixed and compare the plasmon frequencies obtained from the numerical model and the continuum model in Figure 8.13. As for the cases studied in Chapter 7, one makes the observation that the agreement between the continuum theory and the discretized model becomes better when the system size is increased.

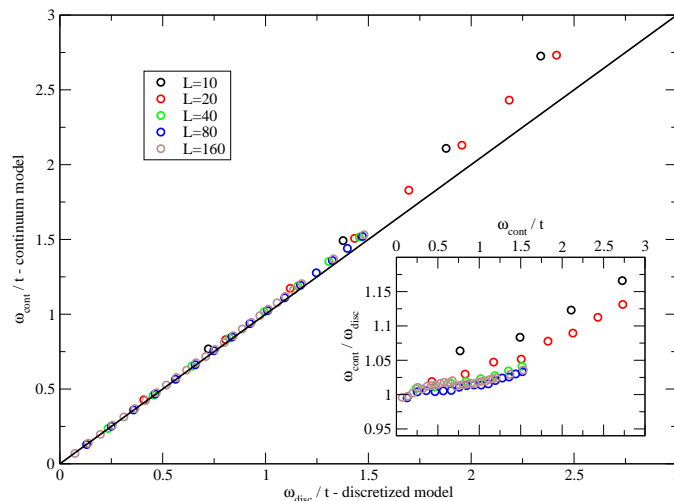


Figure 8.13: Comparison between data obtained with the discretized and continuum model for different system sizes. Model parameters: $N/N_{\text{vac}} = 5/1$, $\nu_{\text{FF}} = 0.5$, $\lambda = a$, and $U = t$.

Influence of a barrier potential

Finally, we analyze the impact of a barrier potential V_{barrier} with a non-zero tunneling probability. Starting from a ring geometry, one increases the potential on one site and arrives at a slit ring geometry. The model Hamiltonian in the absence of external fields then reads,

$$\hat{H} = -t \sum_{\langle i,j \rangle} \hat{c}_i^\dagger \hat{c}_j + V_{\text{barrier}} \hat{c}_1^\dagger \hat{c}_1. \quad (8.12)$$

The idea of this model is to interpolate between the SRR and the ring geometry.

The plasmonic excitations on the ring excited by longitudinal electric fields are two-fold degenerate, as we have seen in Section 7.5.1. The group theoretical argument for this degeneracy is that the potentials of a spatially homogeneous electric field along the x - or y -direction transform as the same irreducible representation. The introduction of the slit reduces the symmetry from $SO(2)$ to C_{2v} . As a direct consequence the degeneracies will be lifted. We have studied the flow of the lowest resonances of a ring with 50 sites upon increasing the potential at one site. The flow is depicted in Figure 8.14

We further show the corresponding density profiles of the excitations on the ring without a barrier potential and on the ring with the strongest barrier potential in Figure 8.15.

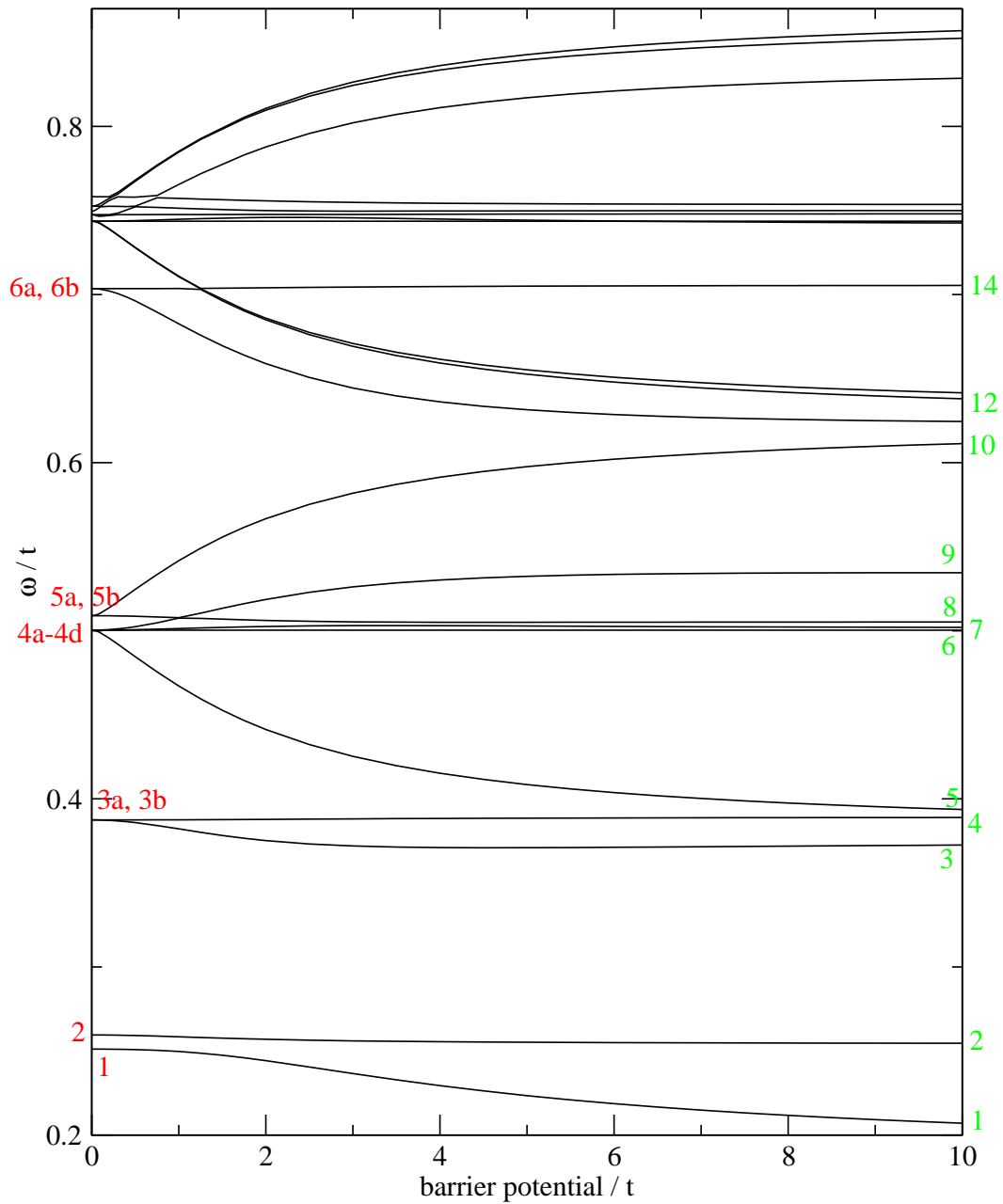


Figure 8.14: Flow of the excitation energies by introducing a barrier potential on one site. Arabic numbers denote the density profile as shown in Figure 8.15, and small Roman letters distinguish degenerate excitations.

Excitations **3a** and **3b** as well as **6a** and **6b** correspond to plasmonic excitations of the clean ring. All other excitations are RSPEs, where excitations **1** and **4a-4d** are not accompanied

by a response of the density. Such a case can occur when the electronic dispersion has a particle-hole symmetry, i.e., the dispersion is symmetric with respect to the Fermi level. So there are two particle-hole pairs fulfilling the resonance condition of a single-particle excitation with momentum q . The induced wave oscillations can oscillate in phase or with a phase shift of π . In such a case, the induced density waves are extinguished.

However, when introducing a barrier potential on one site, excitations **1** and **4d** evolve to the plasmonic excitations **1** and **9**. Note that plasmonic excitations with an odd number of nodes cannot exist on a clean ring due to the boundary conditions. The plasmons **3b** and **6a** become the RSPE **4** and **12**. Both excitations have in common that the current density (obtained e.g. via the continuity equation) does not vanish at the position where the barrier potential is introduced. When the barrier height is increased, the current density which is reflected at the barrier increases. The superposition of the incident and reflect waves leads to strong oscillations. The plasmonic excitations that stay plasmonic excitations do not change their energy when the barrier potential is increased. However, one can observe the appearance of the reflection oscillations in the density profiles.

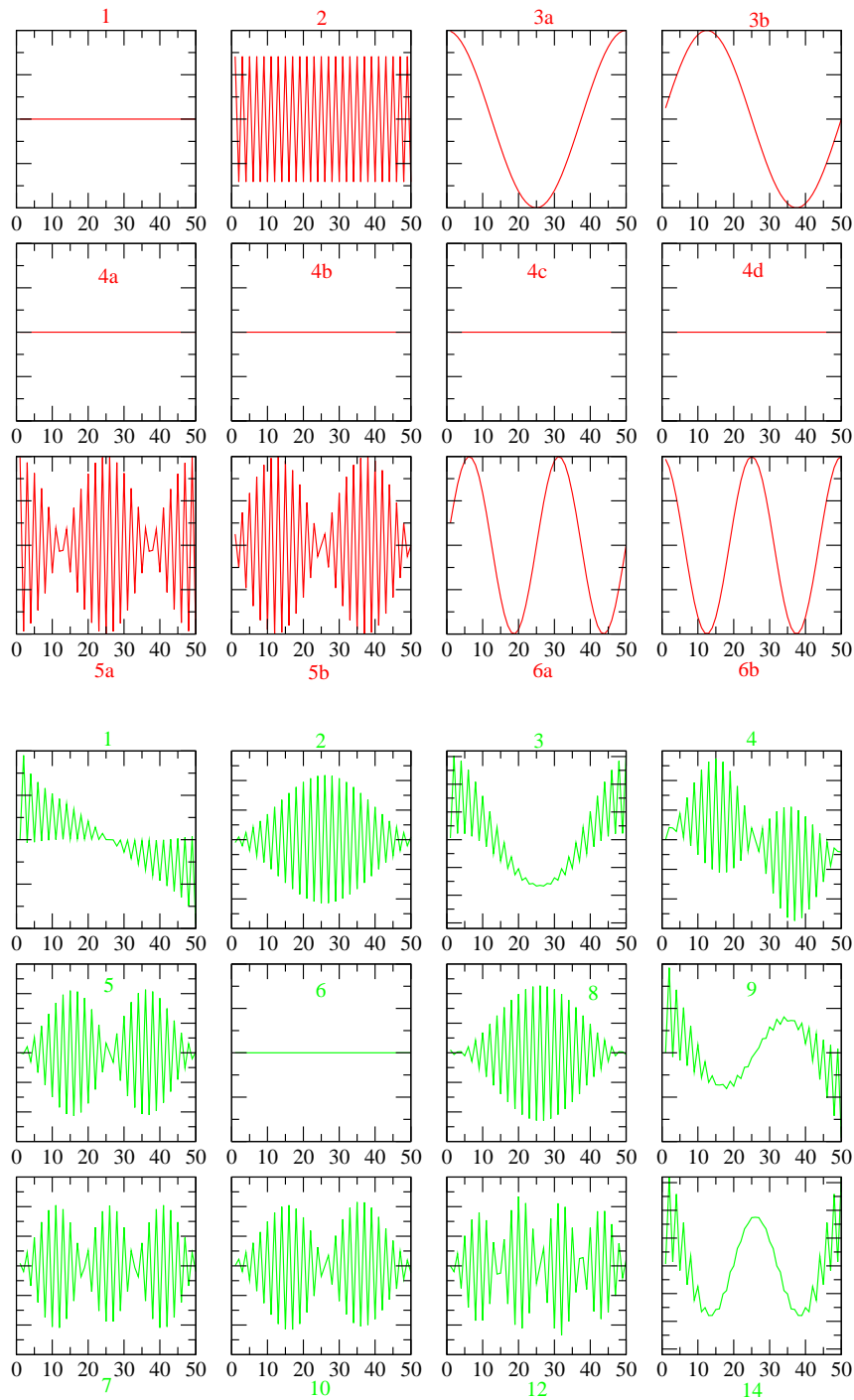


Figure 8.15: Top: Density profiles of the lowest 12 excitations of a ring with 50 sites. Bottom: Density profiles of the same excitations as in plot on top, but with a barrier potential on one site. Both: Arabic numbers denote the energy level as shown in Figure 8.14, and small Roman letters distinguish degenerate excitations. The labels of the y -axes in the plots have been omitted in order to keep the plots as simple as possible. The position on the ring is given on the x -axis in all plots, while the amplitude of the induced charge density is given on the y -axis.

8.4 Polarizabilities

8.4.1 Definition and general properties

The microscopic polarizabilities determine the electromagnetic moments \mathbf{p} and \mathbf{m} that are induced by external probing fields \mathbf{E}_{ext} and \mathbf{B}_{ext} ,

$$\begin{pmatrix} \mathbf{p} \\ \mathbf{m} \end{pmatrix} = \chi_{\text{Pol}} \begin{pmatrix} \mathbf{E}_{\text{ext}} \\ \mathbf{B}_{\text{ext}} \end{pmatrix} = \begin{pmatrix} \alpha & \beta_{\text{EM}} \\ \beta_{\text{ME}} & \gamma \end{pmatrix} \begin{pmatrix} \mathbf{E}_{\text{ext}} \\ \mathbf{B}_{\text{ext}} \end{pmatrix}, \quad (8.13)$$

where α and γ are the electric and the magnetic polarizability, respectively. A common name for β_{EM} and β_{ME} in the quantum chemistry literature is optical rotation tensor. We will call them electromagnetic and magnetoelectric polarizabilities.

Considering now the coupling Hamiltonian in the dipole approximation,

$$\hat{H} = -\hat{\mathbf{p}} \cdot \mathbf{E}_{\text{ext}} - \hat{\mathbf{m}} \cdot \mathbf{B}_{\text{ext}}, \quad (8.14)$$

the polarizabilities may be written as correlation functions of dipole moments,

$$\chi_{\text{Pol}} = - \begin{pmatrix} \chi_{\mathbf{p}\mathbf{p}} & \chi_{\mathbf{m}\mathbf{p}} \\ \chi_{\mathbf{p}\mathbf{m}} & \chi_{\mathbf{m}\mathbf{m}} \end{pmatrix}. \quad (8.15)$$

The explicit expressions for the operators of the electric and magnetic moment will be given in appendix (A). From their definition, it follows that the polarizabilities transform as second rank tensors under rotations. This property will be very useful when discussing media, where the single resonators are not aligned in a parallel manner, but rotated against each other. Onsager's symmetry relations imply on time reversal symmetry

$$\chi_{\mathbf{p}\mathbf{m}} = -\chi_{\mathbf{m}\mathbf{p}}. \quad (8.16)$$

Our explicit calculations will show that this relation is satisfied for the SRRs under consideration, see equations B.12 and B.13.

8.4.2 Symmetry considerations

As we know the transformation behavior of the plasmonic density profiles, we can easily find out which multipole moments must vanish due to symmetry. Starting with the plasmons with an odd number of nodes, transforming like B_1 , one directly sees from the character table 8.1 that these plasmons can give rise to an electric dipole moment in y -direction and a magnetic moment in z -direction, so the only non-vanishing component of β_{EM} is $\beta_{\text{EM},23}$, and for β_{ME} it has to be $\beta_{\text{ME},32}$. One further knows that the only non-vanishing component of γ is γ_{33} . Concerning the plasmons with an even number of nodes,

they can give only rise to an electric dipole moment in x -direction. As x and y transform according to different irreducible representations, one also knows that α_{12} and α_{21} have to vanish. A similar analysis has been carried out based on the transformation properties of the current [68].

If one introduces a second slit at the antipodal position of the first slit, the point group changes from C_{2v} to D_{2h} . Now the resonator has an inversion symmetry and therefore all elements of β_{EM} and β_{ME} must vanish. A look at the character tables of the groups D_{nh} with $n \geq 3$ shows that the elements have to vanish in these cases, too.

8.4.3 Expressions for the oscillator strengths from continuum theory

Employing the explicit expressions for the polarizabilities that have been derived in Section B.2, one can perform all integrals for the continuum model. Starting from the explicit expression for the density-density correlation function

$$\chi(\phi, \phi') = \sum_m \pi_m(\phi) \pi_m(\phi') \frac{e^2 v_F q_m^2}{\omega^2 - \omega_{\text{pl}}^2(q_m) - 2i\eta\omega}, \quad (8.17)$$

where π_m is given equation (8.1), one can perform the integrals shown in Section B.2 explicitly and finds for the microscopic polarizabilities

$$\alpha(\omega) = \sum_m \frac{f_{\alpha,m}}{\omega_{\text{pl}}^2(q_m) - \omega^2 - 2i\eta\omega}, \quad (8.18)$$

$$\beta_{\text{EM}}(\omega) = \sum_m \frac{f_{\beta,\text{EM},m}}{\omega_{\text{pl}}^2(q_m) - \omega^2 - 2i\eta\omega}, \quad (8.19)$$

$$\beta_{\text{ME}}(\omega) = \sum_m \frac{f_{\beta,\text{ME},m}}{\omega_{\text{pl}}^2(q_m) - \omega^2 - 2i\eta\omega}, \quad (8.20)$$

$$\gamma(\omega) = \sum_m \frac{f_{\gamma,m}}{\omega_{\text{pl}}^2(q_m) - \omega^2 - 2i\eta\omega}, \quad (8.21)$$

where we have introduced the oscillator strengths of the different modes $f_{\alpha,m}$, $f_{\beta,\text{EM},m}$, $f_{\beta,\text{ME},m}$, and $f_{\gamma,m}$, whose explicit expressions are

$$f_{\alpha,m} = \frac{2}{\pi} e^2 L v_F s_{1,m}^2(\phi_0) \begin{pmatrix} \sin^2 \phi_0 & 0 & 0 \\ 0 & \cos^2 \phi_0 & 0 \\ 0 & 0 & 0 \end{pmatrix}, \quad (8.22)$$

$$f_{\beta,\text{EM},m} = -i \frac{2}{\pi} \frac{e^2 L^2 v_F \omega_m}{c} s_{1,m}(\phi_0) s_{2,m}(\phi_0) \begin{pmatrix} 0 & 0 & 0 \\ 0 & 0 & \sin \phi_0 \\ 0 & 0 & 0 \end{pmatrix}, \quad (8.23)$$

$$f_{\beta,\text{ME},m} = -f_{\beta,\text{EM}}^T \quad (8.24)$$

$$f_{\gamma,m} = \frac{2}{\pi} \frac{e^2 L^3 v_F \omega_m^2}{c^2} s_{2,m}^2(\phi_0) \begin{pmatrix} 0 & 0 & 0 \\ 0 & 0 & 0 \\ 0 & 0 & 1 \end{pmatrix} \quad (8.25)$$

with

$$\omega_m = \omega(q_m), \quad (8.26)$$

$$s_{1,m}(\phi_0) = \frac{2\sqrt{2}}{(m^2 - 4)\pi^2 + 8\pi\phi_0 - 4\phi_0^2}, \quad (8.27)$$

$$s_{2,m}(\phi_0) = \frac{-((4+m)\pi - 4\phi_0)((-4+m)\pi + 4\phi_0) + m^2\pi^2 \cos(2\phi_0)}{\sqrt{2}m^2\pi^2((4+m)\pi - 4\phi_0)(\pi - \phi_0)((-4+m)\pi + 4\phi_0)}. \quad (8.28)$$

Note that the following property in the vicinity of resonances holds

$$\alpha\gamma - \beta_{\text{EM}}\beta_{\text{ME}} = 0. \quad (8.29)$$

This cancellation will be used in the second part of the thesis several times.

8.4.4 Obtaining oscillator strengths with the discretized model

On resonance, the imaginary part of electric polarizability has a maximum and reads

$$\Im(\alpha(\omega_m)) = \frac{f_{\alpha,m}}{2\eta\omega_m}. \quad (8.30)$$

In order to obtain the oscillator strengths for the discretized model, we calculated with the `rpa` program the imaginary part of the induced dipole moment as described in Section 5.4 and divided it by the strength external electric in order to calculate the imaginary part of the electric polarizability. We then determined its maxima and used equation (8.30) for the calculation of the oscillator strengths.

8.4.5 Comparison between discretized and continuum model

Influence of the slit angle

We calculated the oscillator strengths for 100 sites and different numbers of vacancies at half filling, $\lambda = a$ and $U = t$. For the continuum model the corresponding parameters were chosen. The comparison of the results from both methods is displayed in Figure 8.16. The influence of the slit angle on the oscillator strength can roughly be understood by considering point charges, as we did for the discussion of the plasmon frequencies when bending the wire. Starting with the mode with $m = 1$, one expects that the oscillator strength should increase with the opening angle, as the distance of the charges located at the ends of the slit increases and therefore the electric dipole moment also does. For the $m = 2$ mode, the distance relevant for the charge separation along the x -axis decreases with increasing opening angle. Thus, the dipole moment along this axis must decrease and the polarizability as well. This behavior agrees with the results from the numerics and the continuum model, as can be seen by inspection of Figure 8.16.

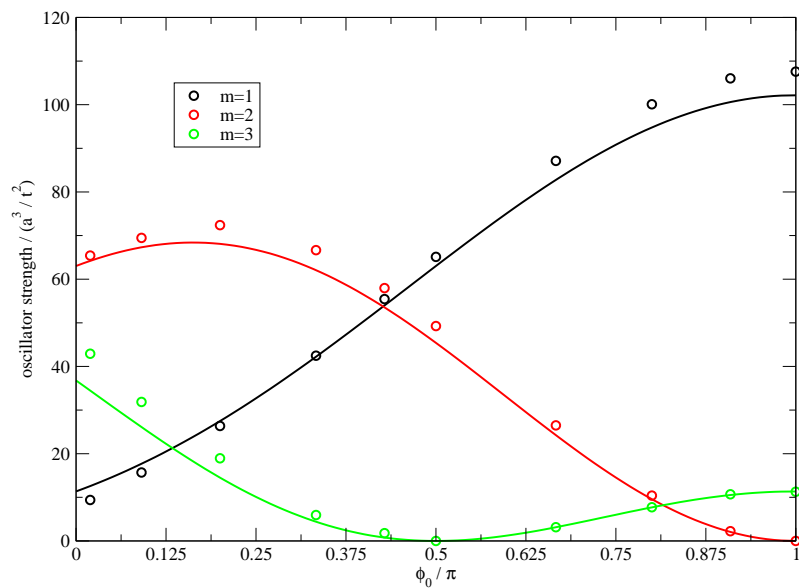


Figure 8.16: Influence of the slit angle on the oscillator strengths. Parameters: $\nu_{\text{FF}} = 0.5$, $U = t$, 100 sites, $\lambda = a$. The data points show values obtained with the discretized model, while the solid curves are obtained with the continuum model.

In order to make the comparison more quantitative, we have calculated the electric polarizabilities for the four lowest excitations using the point charge model. We used again

the density profiles of the point charge model and calculated the the polarizabilities in the same manner as we did when employing of density profiles of the continuum model. The results are depicted in Figure 8.17. The plots illustrate that the dependence of the oscillator strengths on the opening angle can be understood by employing a very simple point charge model. The deviations between the continuum model and the point charge model trace back to the spatial structure of the plasmons. However, the deviation becomes smaller, when the number of nodes is increased.

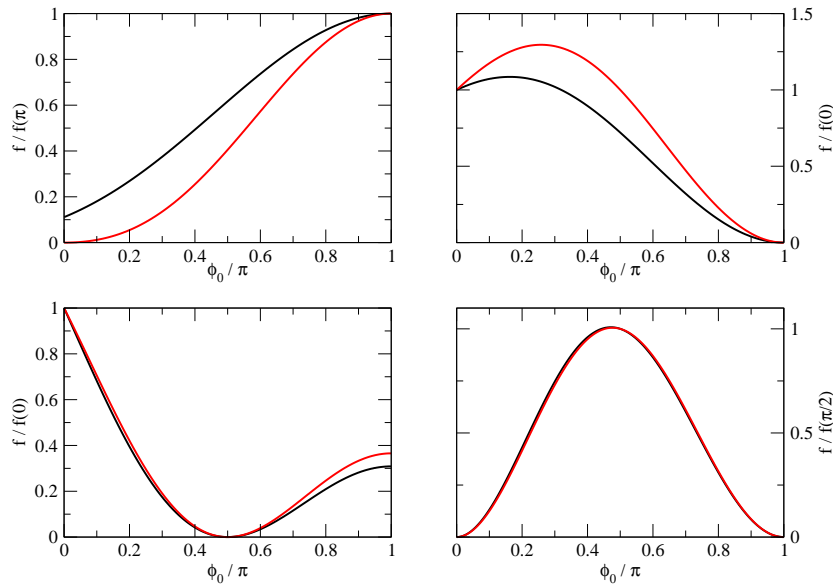


Figure 8.17: Comparison of the oscillator strengths obtained with the continuum model (black) and the point charge model (red). Top-left: $m = 1$, top-right: $m = 2$, bottom-left: $m = 3$, bottom-right: $m = 4$.

Dependence on the filling fraction

We calculated the electric oscillator strengths for different filling fractions utilizing both the `rpa` program and the continuum model. The results of both approaches are depicted in Figure 8.18

The expected impact of the filling fraction is contained in the Fermi velocity. As the oscillator strengths are linear in this quantity, they should be proportional to $\sin(\nu_{\text{FF}}\pi)$. Looking at Figure 8.18, one sees that the agreement is really good for the mode with $m = 2$. Concerning the mode with $m = 1$ and $m = 3$, however, the deviation of the

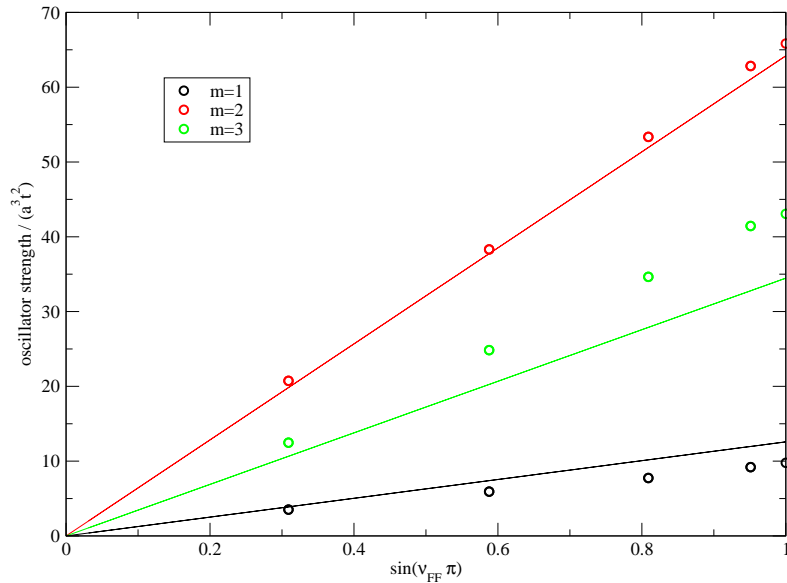


Figure 8.18: Influence of the filling fraction on the oscillator electric strengths. The data points were obtained by using the `rpa` program and the solid curves are based on the continuum model. Parameters: $N = 100$, $N_{\text{vac}} = 2$, $\lambda = a$, $U = t$.

numerical data from the data obtained with the continuum model shows a maximum for half filling. This indicates that the deviations might be due to the neglect of the Friedel oscillations for the plasmonic density profiles, because they are most pronounced for the case of half-filling.

Impact of the system size

In order to study the dependence of the system size on the electric oscillator strengths, we used again the `rpa` program and the continuum model. We started with 10 sites and doubled the system size until we reached a value of 160 sites. The results of both methods are shown in Figure 8.19. We decided not to plot the oscillator strengths directly, but divided them by the number of sites, in order to remove the trivial linear size dependence according to equation (8.22).

At first glance, one sees that the agreement of the numerical and analytical data becomes better when the system size is increased.

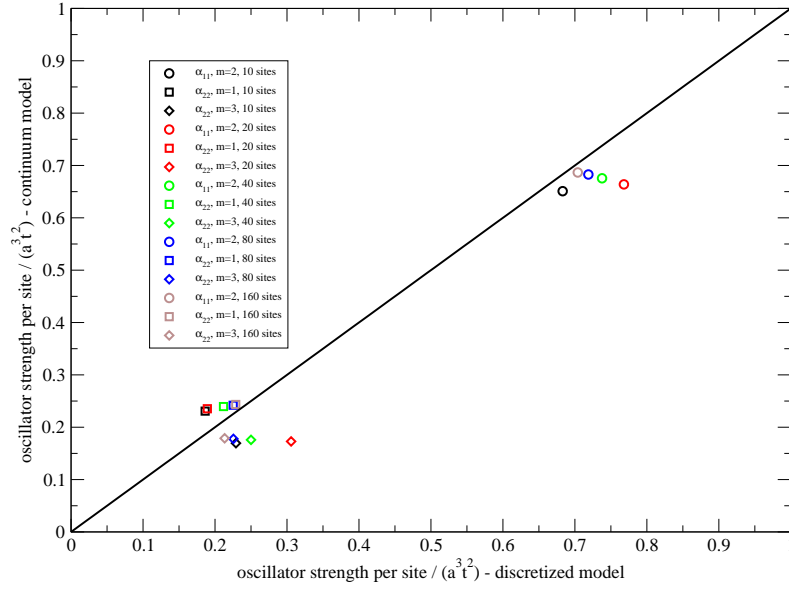


Figure 8.19: Impact of the system size on the oscillator strengths. The data points were obtained by using the `rpa` program and the solid curves are based on the continuum model. Parameters: $N/N_{\text{vac}} = 5/1$, $\lambda = a$, $U = t$, $\nu_{\text{FF}} = 0.5$.

Influence of the barrier potential

Lastly, we want to discuss the impact of the on-site barrier potential on the oscillator strengths of plasmons on a ring. The ring has 50 sites the filling fraction is $1/2$. Again, we have set $U = t$.

As the plasmonic modes with $m = 1$ and $m = 3$ evolve from single particle modes of the clean ring without any density response as previously shown, it is clear that the oscillator strengths of the clean ring are zero. When the potential increases, the plasmonic modes arise and therefore the oscillator strengths increase. One mode with $m = 2$ evolves from a plasmon to an RSPE with a density profile that is highly oscillating, so the oscillator strength decreases when the barrier potential is increased.

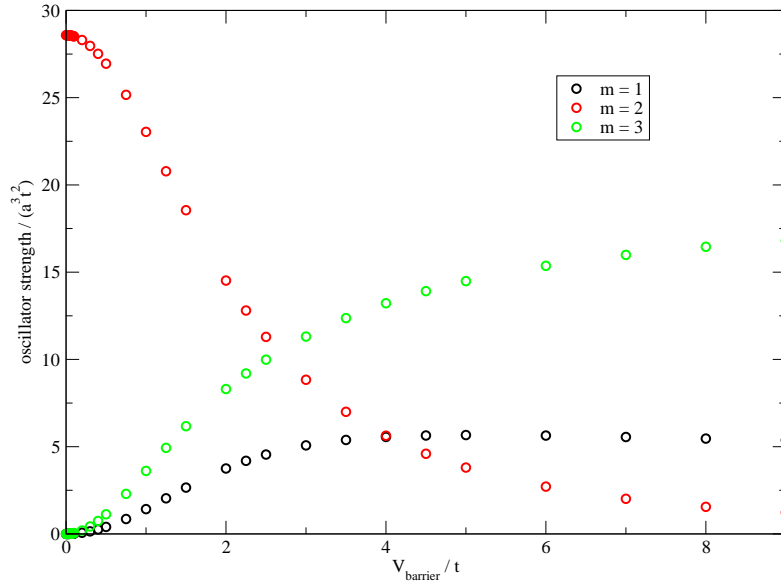


Figure 8.20: Influence of an on site barrier potential on the oscillator strengths. Parameters: 101 sites, $\nu_{\text{FF}} = 0.5$, $\lambda = a$, $U = t$.

8.5 Tuning the electromagnetic response

We are now in the position to analyze the tunability of the electromagnetic response properties.

8.5.1 Resonance frequency

The only model parameters that enter the expression for the plasmon dispersion, see equation (8.5), are the opening angle $2\phi_0$, the length of the wire L , and the Fermi velocity v_{F} . The opening angle and the length are pure geometry parameters, while the impact of the electronic structure is reflected in v_{F} .

Ignoring for a moment the dependence of $v(q_m)$ on the system size, one can see that the plasmon frequency is roughly proportional to L^{-1} and to the number of nodes. Looking at the explicit expression for $v(q_m)$ as given in equation (8.7), one observes that it only depends on the ratio λ/L . So we expect a stronger dependence of $v(q_m)$ on the system size for smaller systems. As an example, we calculate the plasmonic excitation energies of the plasmon with one node of alkene rings with a single slit with the aim to identify the range of carbon atoms such that the excitation occurs in the optical regime. We anticipate from the analysis based on quantum chemical calculations that will be given in the next chapter that the hopping parameter in this case is roughly 2.9 eV. The typical

system sizes in order to have plasmonic resonances in the optical regime are between 8 and 23 carbon atoms.

Knowing that the resonance frequency also depends on the opening angle $2\pi_0$, we can now fine tune the frequencies by changing this angle. We have seen in Section 8.3.3 that the Coulomb kernel of modes with an odd number of nodes increases when opening the SRR, while the opposite happens for modes with even nodes.

The Fermi velocity of the polyene chain can be altered by changing the filling fraction via doping, i.e. the replacement of carbon atoms of the π -system by boron or nitrogen atoms.

8.5.2 Oscillator strengths

We now turn to a discussion of the oscillator strengths. All oscillator strengths have in common that they are proportional to v_F . Naively, one might think that the scaling with L is different for the oscillatory strengths, but if one utilizes that the plasmon frequency is roughly proportional to L^{-1} , one finds that all oscillator strengths depend roughly linear on the system size. The magnetoelectric oscillator strength is smaller than the electric one by a factor of $\omega_m L/c$, the magnetic one is even smaller by a factor of $(\omega_m L/c)^2$. The influence of the opening angle for the electric resonances has already been discussed. The dependency of the magnetic oscillator strength on the opening angle is depicted in Figure 8.21. One observes that one can maximize the magnetic oscillator strength by choosing

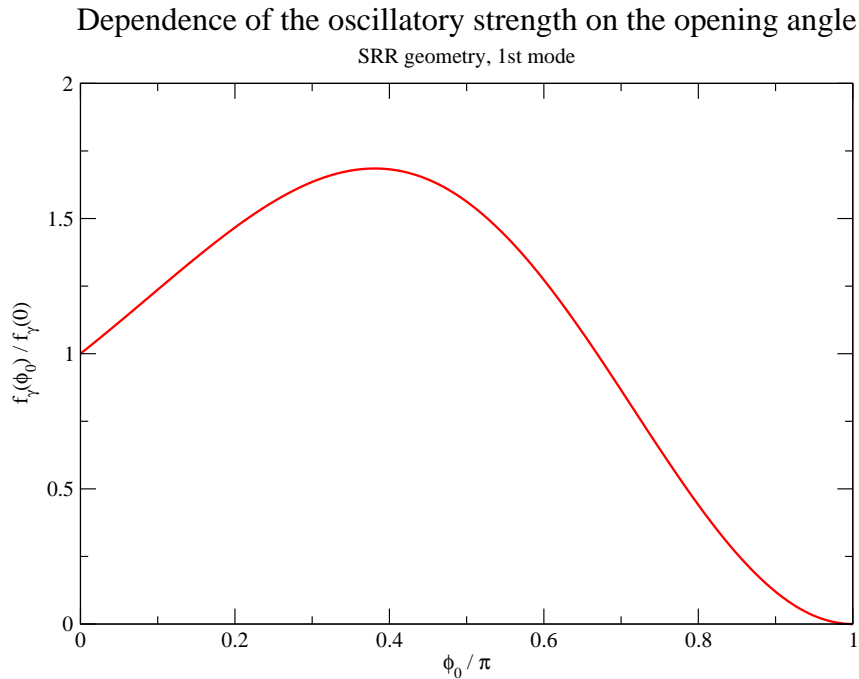


Figure 8.21: Influence of the opening angle on the magnetic oscillator strength.

$$\phi_0 \approx 68 - 69^\circ.$$

8.5.3 How to obtain strong magnetic resonances?

Finally, we discuss other possibilities to improve upon the task to obtain strong magnetic resonances. The main obstacle is to make the ratio $(\omega_m L/c)^2$ big. If ω scales with L^{-1} , the ratio will be constant when increasing L . However, if ω_m becomes independent of the system size, the ratio scales with L^2 and thus f_γ with L^3 . In order to change the scaling behavior of the plasmon frequency, there are several possibilities:

- i) One considers a ring with several slits where the length of each subunit is fixed. The system size is then increased by adding an additional subunit.
- ii) One considers a 3D system, as the plasmon frequency is independent of L .
- iii) One uses a band insulator where the HOMO-LUMO-gap mainly determines the energy scale of the excitations.

Chapter 9

Quantum chemical calculations for molecular systems

Based on the knowledge that we have obtained by analyzing the resonators in the previous chapters, we are now in the position to study the response behavior of real molecules by employing quantum chemical calculations. The model systems under consideration are polyenes where the plasmonic excitations occur in the π -system. We perform for each molecular system a ground state DFT calculation yielding one-particle energies and the corresponding states. We extract the Fermi velocity from the data by assigning a wave vector to each energy level of the π -system and by fitting the single-particle energies to a tight-binding Hamiltonian. The tight-binding Hamiltonian is given by

$$\hat{H} = - \sum_{i=0}^{\infty} \sum_{\delta=0}^{\infty} t_{\delta} \left(\hat{c}_i^{\dagger} \hat{c}_{i+\delta} + \hat{c}_i^{\dagger} \hat{c}_{i-\delta} \right), \quad (9.1)$$

where i labels the lattice sites and δ the δ -th neighboring site. The Hamiltonian can be diagonalized by Fourier transformation, leading to the following dispersion relation,

$$\epsilon(k) = -2 \sum_{\delta} t_{\delta} \cos(\delta k a), \quad (9.2)$$

where a is again the lattice constant. This model is extremely simplified as all bond distances are assumed to be identical. In fact, alternation of the bond lengths require that the hopping parameters depend on the lattice sites. The Fermi velocity of a half-filled band reads

$$v_{\text{F}} = -2 \sum_{\gamma=1}^{\infty} (-1)^{\gamma} (2\gamma + 1) t_{2\gamma+1} a. \quad (9.3)$$

Note that only the hopping parameters over an odd number of atoms enter the Fermi velocity. The length of the π -system is determined by adding the bond distances of all

carbon atoms constituting the π -system. Utilizing equation (8.5), we can calculate the plasmonic excitation energies, $\hbar\omega_{\text{pl}}$, and compare the values with those resulting from a TDDFT calculation. All TDDFT calculations were performed with the `escf` program of the quantum chemical program package TURBOMOLE [69]. In addition, we compare the oscillatory strengths obtained with both methods. Note that the oscillator strengths obtained with the `escf` program must be multiplied with a factor of three, as the program calculates rotational averaged oscillator strengths. The identification of the plasmonic resonances will be explained in Appendix D.

9.1 Polyene chains

As a first example we study the plasmonic excitations of the linear alkene chain, all-trans- $\text{C}_{20}\text{H}_{22}$. The ground state geometry was optimized at the DFT level using the BP86 functional [70, 71, 72, 73, 74] and the def2-SVP basis set [75]. The structure exhibits a small Peierls distortion as the bond distances of two neighboring carbon atoms alternate between the values $2.62a_0$ and $2.69a_0$. The geometry is depicted in Figure 9.1. The point group of the molecule is C_{2h} .

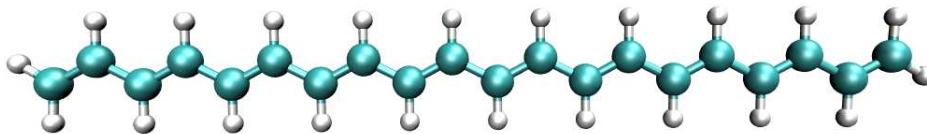


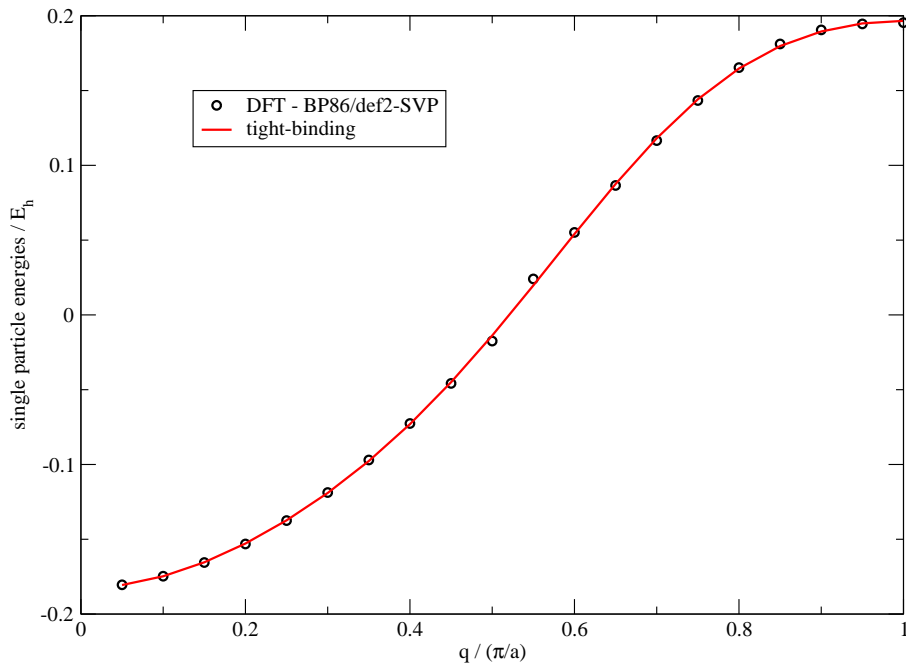
Figure 9.1: Ground state geometry of $\text{C}_{20}\text{H}_{22}$ at the DFT-level (BP86, def2-SVP).

The dispersion of the π -electrons was extracted from the energy levels obtained by the ground state calculation and is shown in Figure 9.2. These states are easily identified as they transform like a_u or b_g , while the orbitals of the σ -framework transform like a_g or b_u . A fit to the dispersion relation of a tight-binding Hamiltonian gives the hopping parameters that are listed in Table 9.1.

δ	1	2	3	4	5
t_δ/E_h	0.09717	-0.00502	-0.00223	0.00170	-0.00008

Table 9.1: Effective hopping parameters of $\text{C}_{20}\text{H}_{22}$.

The expectation is that the hopping matrix elements decay exponentially when δ is increased. In the case under consideration, however, the electronic structure is modified

Figure 9.2: Dispersion of π -electrons of $C_{20}H_{22}$.

due to a weak Peierls distortion. A more sophisticated *Ansatz* would incorporate hopping parameters that depend on the distance between the atoms. Such an *Ansatz*, however, would make the fitting procedure much more complicated. For that reason, we employ only the simple model. In addition, the HOMO–LUMO gap is increased by the exchange correlation potential. The hopping parameters must therefore model the impact of the Peierls distortion and the opening of a small gap. For that reason, we will call them effective hopping parameters. Here, they merely serve the determination of the Fermi velocity.

We extract the Fermi velocity from the dispersion relation via equation (9.3): $v_F = 0.58986E_h a_0$. Now we overall can calculate the plasmonic excitation energies and compare to the values obtained from TDDFT calculations. In addition, we show the guess of the plasmonic density profiles used for the calculations with the continuum model and the transition densities resulting from the TDDFT calculation in Table 9.2.

We observe the appearance of reflection oscillations in the plasmonic density obtained with TDDFT, as expected from the results of Chapter 7. The excitation energies obtained with both methods agree very well.

Finally, we compare the oscillator strengths obtained with the continuum model to those obtained from a TDDFT calculation. The values for the oscillator strengths are given in

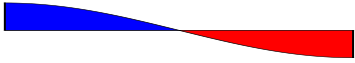
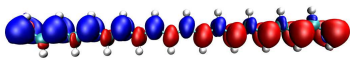
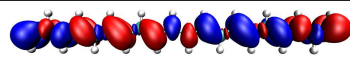
# nodes		continuum model	TDDFT
1	E_1/E_h	 0.0725	 0.0747
2	E_2/E_h	 0.1296	 0.1208
3	E_3/E_h	 0.1762	 0.1688

Table 9.2: Density profiles and plasmonic excitation energies of $C_{20}H_{22}$.

Table 9.3.

# nodes	f from continuum model in $E_h^2 a_0^3$	f from TDDFT in $E_h^2 a_0^3$
1	7.60	11.12
3	0.85	0.52

Table 9.3: Comparison between oscillator strengths obtained with the continuum model and TDDFT.

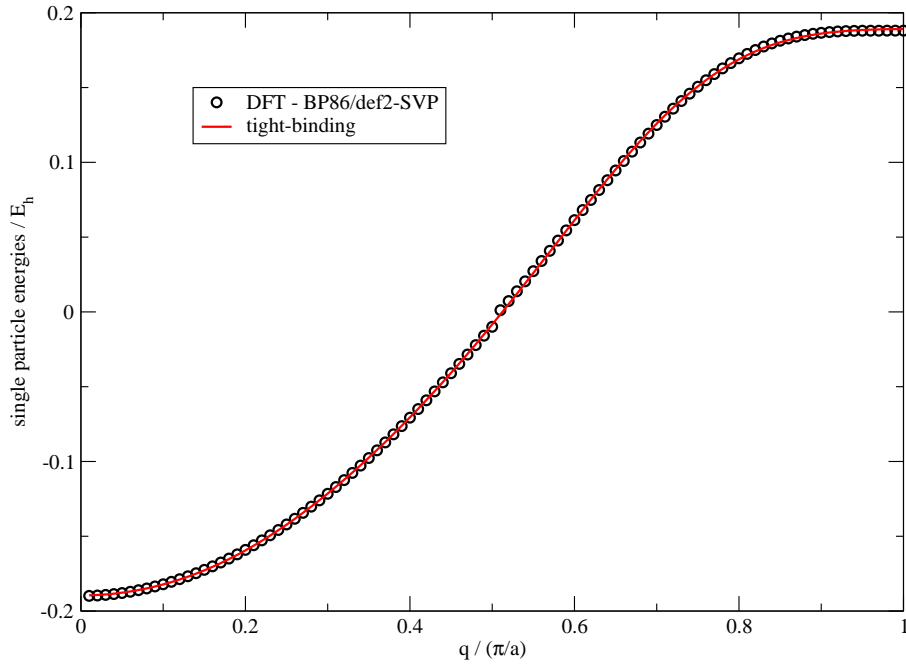
We have already seen in Chapter 8 that the deviation in the oscillatory strengths between the continuum model and the discretized model is more pronounced for smaller system sizes due to the neglect of Friedel oscillations.

As a second example, we analyze the plasmons of a linear all-trans alkene chain consisting of 100 carbon atoms. We proceed in the same manner as for the smaller chain we studied before. The bond lengths alternate between $2.60a_0$ and $2.73a_0$, indicating that the Peierls distortion is more pronounced than for the smaller chain. The dispersion of the π -electrons is depicted in Figure 9.3.

We again performed a fit to the dispersion of a tight-binding Hamiltonian, yielding the effective hopping parameters that are given in Table 9.4. We once again observe that the hopping parameters do not show the expected exponential decay with the distance due to the choice of the *Ansatz*.

We are now in the position to determine the excitation energies and compare them to the excitation energies obtained with TDDFT. The results are shown in Table 9.5.

We once again find a good agreement between both methods, as we expected from the results of Chapter 7, where we have seen several times that the agreement of continuum

Figure 9.3: Dispersion of π -electrons of $C_{100}H_{102}$.

δ	1	2	3	4
t_δ/E_H	0.09941	-0.00201	-0.00375	0.00216

Table 9.4: Effective hopping parameters of $C_{100}H_{102}$.

# nodes	E from continuum model in E_h	E from TDDFT in E_h
1	0.0194	0.0203
2	0.0364	0.0378
3	0.0518	0.0537
4	0.0660	0.0653

Table 9.5: Comparison of plasmonic excitation energies for $C_{100}H_{102}$ obtained with the continuum model and TDDFT.

model and discretized model became better when the system size was increased. The same observation can be made for the oscillator strengths shown in Table 9.6. Note that the oscillator strengths of the plasmonic excitations with 2 or 4 nodes vanish.

# nodes	f from continuum model in $E_h^3 a_0^3$	f from TDDFT in $E_h^2 a_0^3$
1	39.57	38.39
3	4.40	4.77

Table 9.6: Oscillator strengths for $C_{100}H_{102}$.

9.2 Influence of exact exchange

The situation from the previous section changes if exact exchange is included. As we have discussed in Chapter 4, the inclusion of exchange reduces the excitation energies of electron-hole pairs. However, one must also keep in mind that the inclusion of exchange has a direct impact on the electronic dispersion by opening a gap and favoring the formation of charge density waves. Thus the Peierls distortion will become much more pronounced. In order to study the impact of exchange, we have calculated the HOMO-LUMO gap and the excitation energies for the all-trans- $C_{20}H_{22}$ molecule whose response properties we analyzed in the previous section. We chose a set of DFT functionals with different fractions of Hartree Fock exchange and performed a time-dependent Hartree-Fock calculation in addition. We have used the TPSSH-functional [70, 71, 76, 77, 78] that contains 10% of exact exchange, the B3-LYP-functional [70, 71, 72, 79, 80] that contains 20% of exact exchange, and the BH-LYP-functional [70, 71, 72, 79, 81] that contains 50% of exact exchange.

The HOMO-LUMO gaps are depicted in Figure 9.4.

One observes that the HOMO-LUMO gap depends linearly on the fraction of exchange. By performing single point calculations with the relaxed geometry obtained at the DFT-BP86-level, we could identify the impact of the Peierls distortion on the gap. We have found that the major contribution to the gap does not come from the Peierls distortion, but rather from the shift of the single particle energies due to the Hartree-Fock exchange itself. For illustration, the ratio of the gaps for the relaxed structure and for the unrelaxed system is shown in Figure 9.5. We have also calculated the first b_{1u} -excitation energy for each relaxed geometry. The results are shown in Figure 9.6 and Table 9.7.

The division by the HOMO-LUMO gap makes apparent, if the effective force acting on the electrons is repulsive (>1) or attractive (<1) [82], as an attractive force leads to a decrease of the excitation energy, while a repulsive force increases the excitation energy. However, one should keep in mind that the Hartree-Fock exchange should be screened and therefore Hartree-Fock overestimates its contribution. Therefore the HOMO-LUMO gap obtained with groundstate calculation is overestimated and the non-local exchange restoring forces in the response calculation are overestimated as well. Therefore, the effective interaction

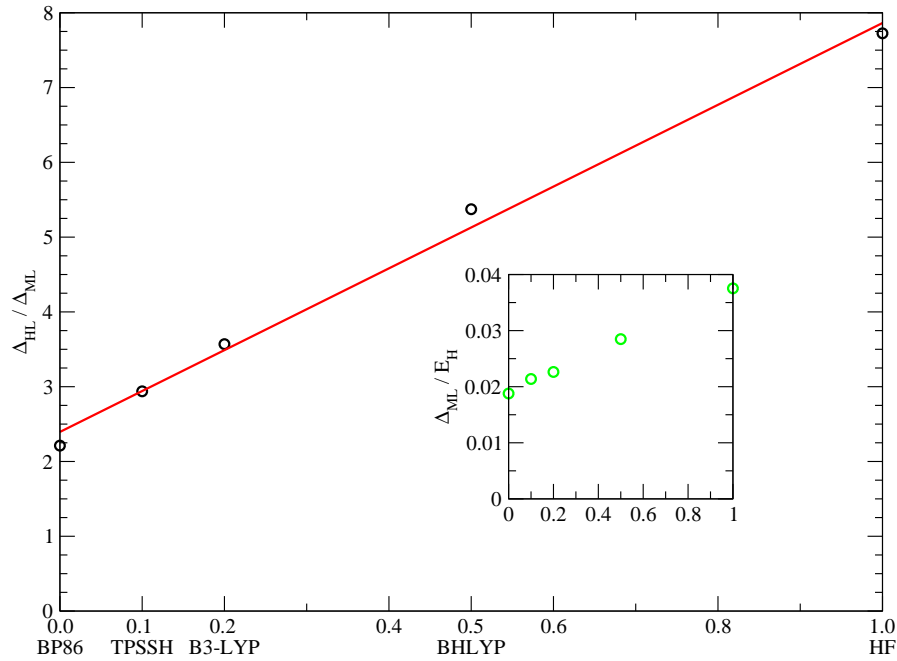


Figure 9.4: HOMO-LUMO gaps of for different fractions of Hartree-Fock exchange. Δ_{ML} is the mean level spacing.

Method	Excitation energy / E_h	oscillator strength / $E_h^2 a_0^3$
DFT/BP86	0.0747	11.12
DFT/B3-LYP	0.0859	11.51
DFT/BH-LYP	0.1071	12.61
HF	0.1353	14.64

Table 9.7: Excitation energies and oscillator strengths for different fraction of Hartree-Fock exchange.

seems attractive in the case of HF. This situation also occurs in the case of the BH-LYP functional.

We finally show how the induced density is changed when the fraction of Hartree-Fock exchange is increased. One can see that the structure of the envelope with one node becomes less apparent when the fraction of Hartree-Fock exchange is increased.

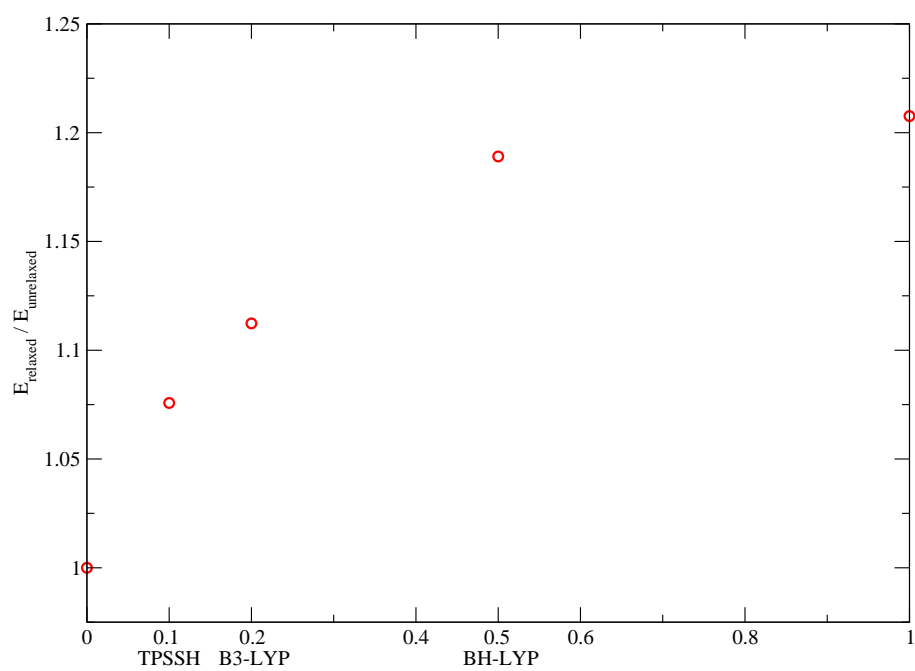


Figure 9.5: Influence of the Peilers distortion on the gap of $C_{20}H_{22}$ depending on the amount of Hartree-Fock exchange. E_{relaxed} is the gap for the relaxed structure, while $E_{\text{unrelaxed}}$ is the gap calculated with the BP86-structure.

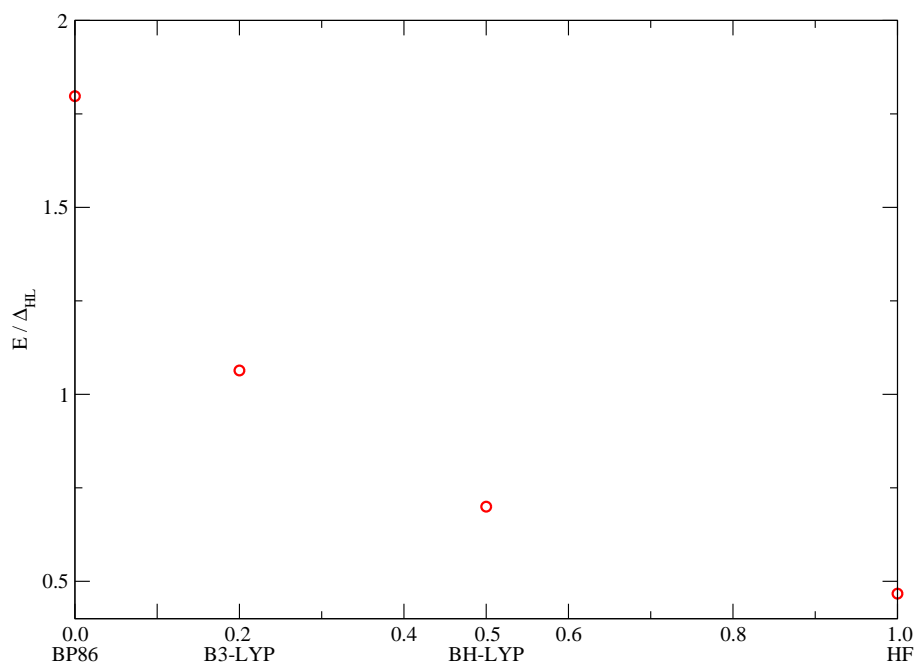


Figure 9.6: b_{1u} -excitation energies E for different fractions of Hartree-Fock exchange

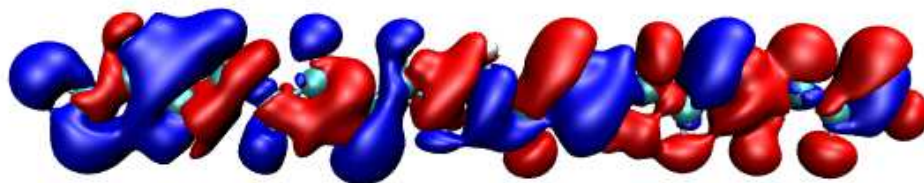


Figure 9.7: Lowest plasmon of $\text{C}_{20}\text{H}_{22}$ at the DFT-level with the B3-LYP functional.

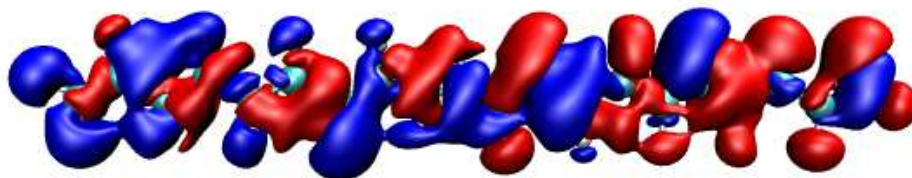


Figure 9.8: Lowest plasmon of $\text{C}_{20}\text{H}_{22}$ at the DFT-level with the BH-LYP functional.

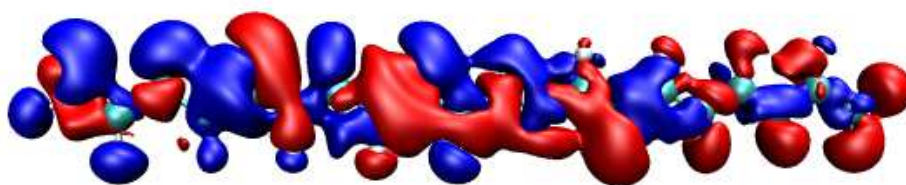


Figure 9.9: Lowest plasmon of C₂₀H₂₂ at the HF-level.

9.3 Rings

We have repeated the same strategy from Section 9.1 for the analysis of the plasmonic excitations of organic ring molecules. Note that no geometry optimization has been performed for the structures presented in this section, as the planar ring geometry is energetically not favorable for larger rings. However, there exists large classes of planar conjugated ring systems based on polyalkyne chains [83, 84]. Another possibility is the stabilization of the planar structure via bridges like spokes in a wheel [85].

First, we constructed a geometry of a ring consisting of 105 carbon atoms where all carbon-carbon distances are set to 150 pm. The slit is composed of 5 methylene units, i.e., 5 neighboring carbon atoms of the rings are saturated by adding two hydrogen atoms, while we add only one hydrogen atom to the other carbon atoms. This geometry will be denoted as closed ring.

The geometry of the closed ring is depicted in Figure 9.10 and the geometry of the open ring is shown in Figure 9.11. Note that the point group is C_{2v} compared to the chains.



Figure 9.10: Geometry of an SRR with 105 carbon atoms where the slit consists of 5 methylene units.

The single-point DFT-calculations and the TDDFT-calculations were performed using the BP86 functional and the def2-SVP basis set. As we did for the chains, we extracted the energies of the π -orbitals for the open ring and assigned a wave vector to each state. The resulting dispersion relation is depicted in Figure 9.12. As all distances between two neighboring carbon atoms are equal, the dispersion exhibits no contribution to the gap due to Peierls distortion. The effective hopping parameters shown in Table 9.8 result from the fit to dispersion relation of a tight-binding Hamiltonian. Compared to the previously discussed chain, the distances between two neighboring carbon are equal. The modulus of the effective hopping parameters now shows the expected exponential decay, but

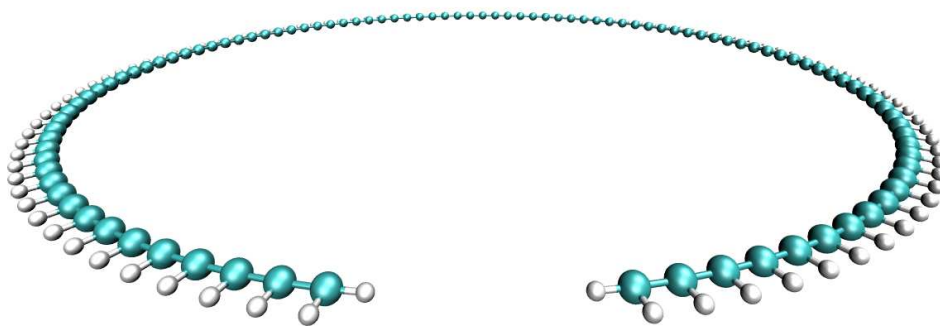


Figure 9.11: Geometry of the SRR depicted in Figure 9.10, but with the methylene units removed.

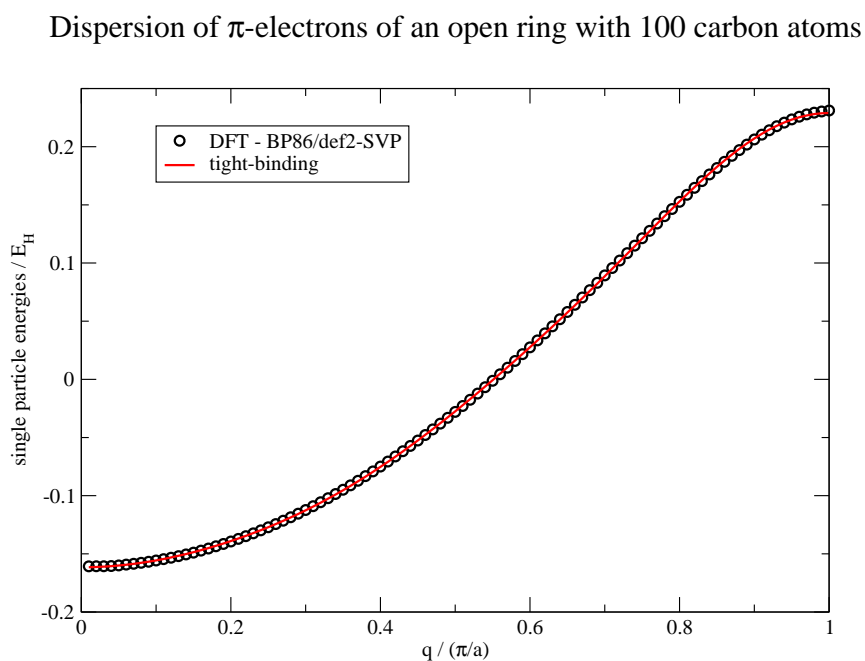


Figure 9.12: Dispersion of π -electron of $C_{100}H_{102}$.

there is still a sign oscillation in the effective hopping parameters.

δ	1	2	3	4	5
t_δ/E_h	0.09214	-0.01530	0.00436	-0.00154	0.00062

Table 9.8: Effective hopping parameters for the open ring geometry.

The Fermi velocity can be determined from the hopping parameters and the resulting excitation energies are listed in Table 9.9.

# nodes	E from continuum model in E_h	E from TDDFT for open ring in E_h	E from TDDFT for closed ring in E_h
1	0.0148	0.0148	0.0143
2	0.0297	0.0306	0.0292
3	0.0412	0.0417	0.0405

Table 9.9: Plasmonic excitation energies of molecular rings.

The agreement of excitations energies from the continuum model and TDDFT is very good. These results also indicate that the methylene groups act as an ideal slit and that their effect on both the electronic dispersion and therefore the excitation energies is small. The situation, however, changes, if one compares the oscillator strengths shown in Table 9.10.

# nodes	f from continuum model in $E_h^2 a_0^3$	f from TDDFT for open ring in $E_h^2 a_0^3$	f from TDDFT for closed ring in $E_h^2 a_0^3$
1	4.84	5.11	5.57
2	21.13	21.35	37.34
3	9.61	20.54	24.13

Table 9.10: Oscillator strengths of molecular rings.

The agreement between the oscillator strengths is best for the plasmon with one node. Note the huge deviation for the oscillator strengths of the two higher modes. This is especially surprising, as the agreement for the excitation energies is good.

9.4 Summary

We have shown in this chapter that the lowest plasmonic excitation energies and the corresponding oscillator strengths of organic alkene chains or rings can be determined - as long as exact exchange is neglected - by utilizing the continuum model with two quantities that can easily be obtained from ground state DFT calculations: the Fermi velocity and the length of the π -systems. A comparison with the results of TDDFT calculations has shown that the excitation energies agree very well. We have also found a

decent agreement for the oscillator strengths, where the deviations arise from the neglect of Friedel oscillations in the continuum model. In doing so, we have found a quantitative justification of the results obtained in the previous sections. We have also seen that for real alkene chains the electronic structure is more complicated than expected from a tight-binding Hamiltonian with only a single hopping parameter, as about 5 hopping parameters are needed for the quantitative parameterization of the electronic dispersion. We have further observed that several methylene units may work as an appropriate slit by comparing the excitation energies of a closed and an open ring.

Part II

From a single resonator to the medium:
The metamaterial

Chapter 10

Outline

We are now aiming at the calculation of the macroscopic response properties of crystals built up from single resonators. We have discussed the response behavior of the isolated resonators so far. In a crystal, however, the electromagnetic fields acting on a single resonator comprise not only the fields from the resonator itself and the external fields, but also the screening fields from all other resonators. The poles of the external response function determine then the combined excitations of the light field and the plasmons. Such excitations are known as plasmon-polaritons. One would have arrived at the same result by solving Maxwell's equations. The plasmon-polaritons correspond to poles of the photon propagator.

If one is interested in the polaritonic modes with wavelengths k^{-1} that are much larger than the size of the individual oscillators $kL \ll 1$, one can separate the two different length scales: One first calculates the response of a single resonator, taking into account the electric fields of the neighboring resonators. This process is denoted as plasmon hybridization, as the coupling of the single resonators leads to combined plasmonic modes, which will be analyzed in Chapter 11. The next step of the calculation involves averaging the dipole moments and fields over regions that are large compared to the resonator size, but small compared to the wavelengths k^{-1} of the polaritonic modes. This averaging procedure leads to macroscopic response functions. The outline of these calculations and explicit expressions for macroscopic response functions are given in Chapter 12. These response functions enter the Maxwell equations and one can finally determine the index of refraction or solve for the polaritonic dispersion relation. These calculations are performed in Chapter 13, where also the tunability of the refractive index is discussed.

Chapter 11

Plasmon hybridization

11.1 Two resonators

11.1.1 Two electric dipoles

As an introductory example to the coupling of plasmonic resonances, we study the response of two identical resonators in the electric dipole approximation. We will focus on the configuration depicted in Figure 11.1.

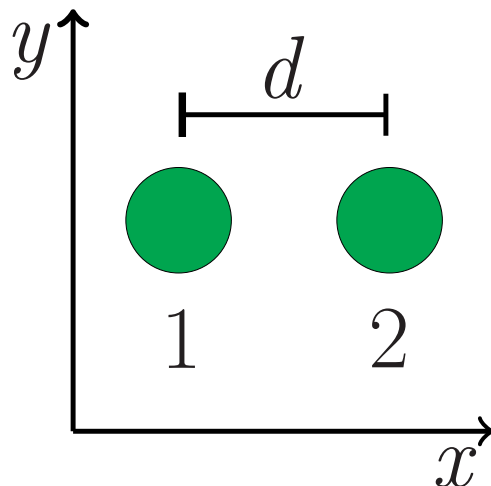


Figure 11.1: Two identical resonators.

The response of each individual dipole to an external electric field that lies in the plane

is described in terms of the polarizability

$$\alpha_{\text{iso}} = \begin{pmatrix} \alpha_{\text{iso},xx} & 0 & 0 & 0 \\ 0 & \alpha_{\text{iso},yy} & 0 & 0 \\ 0 & 0 & \alpha_{\text{iso},xx} & 0 \\ 0 & 0 & 0 & \alpha_{\text{iso},yy} \end{pmatrix}. \quad (11.1)$$

The upper left block of α_{iso} describes the response dipole 1 and the other block describes the response of dipole 2. The induced dipole moments are collected into a four-dimensional vector where the first two components are the dipole moments of dipole 1 and the other ones are the dipole components of dipole 2. The same is done for the external electric field.

$$\begin{pmatrix} p_x^{(1)} \\ p_y^{(1)} \\ p_x^{(2)} \\ p_y^{(2)} \end{pmatrix} = \begin{pmatrix} \alpha_{\text{iso},xx} & 0 & 0 & 0 \\ 0 & \alpha_{\text{iso},yy} & 0 & 0 \\ 0 & 0 & \alpha_{\text{iso},xx} & 0 \\ 0 & 0 & 0 & \alpha_{\text{iso},yy} \end{pmatrix} \begin{pmatrix} E_{\text{ext},x}^{(1)} \\ E_{\text{ext},y}^{(1)} \\ E_{\text{ext},x}^{(2)} \\ E_{\text{ext},y}^{(2)} \end{pmatrix} \quad (11.2)$$

The induced electric dipole of the neighboring resonator, however, gives rise to an electric field that acts in addition to the external field on the other dipole. But this dipole in return also gives rise to an electric field at the position of the other dipole. If this procedure is repeated self-consistently one obtains the total electric fields. The external polarizability is then simply determined via

$$\mathbf{p} = \alpha_{\text{ext}} \mathbf{E}_{\text{ext}} = \alpha_{\text{iso}} \mathbf{E}_{\text{tot}}. \quad (11.3)$$

For the calculation of the induced electric fields we assume that the distance of the dipoles is d , so the electric field at the position of the first dipole originating from the second dipole is given by

$$\begin{pmatrix} E_{\text{ind},x}^{(1)} \\ E_{\text{ind},y}^{(1)} \\ E_{\text{ind},x}^{(2)} \\ E_{\text{ind},y}^{(2)} \end{pmatrix} = \frac{1}{d^3} \begin{pmatrix} 0 & 0 & 2 & 0 \\ 0 & 0 & 0 & -1 \\ 2 & 0 & 0 & 0 \\ 0 & -1 & 0 & 0 \end{pmatrix} \begin{pmatrix} p_x^{(1)} \\ p_y^{(1)} \\ p_x^{(2)} \\ p_y^{(2)} \end{pmatrix}, \quad (11.4)$$

where the induced dipoles and the electric fields at the position of the dipoles are distinguished by a superscript. The response to the total field is then

$$\begin{pmatrix} p_x^{(1)} \\ p_y^{(1)} \\ p_x^{(2)} \\ p_y^{(2)} \end{pmatrix} = \alpha_{\text{iso}} \left[\begin{pmatrix} E_{\text{ext},x}^{(1)} \\ E_{\text{ext},y}^{(1)} \\ E_{\text{ext},x}^{(2)} \\ E_{\text{ext},y}^{(2)} \end{pmatrix} + \frac{1}{d^3} \begin{pmatrix} 0 & 0 & 2 & 0 \\ 0 & 0 & 0 & -1 \\ 2 & 0 & 0 & 0 \\ 0 & -1 & 0 & 0 \end{pmatrix} \begin{pmatrix} p_x^{(1)} \\ p_y^{(1)} \\ p_x^{(2)} \\ p_y^{(2)} \end{pmatrix} \right]. \quad (11.5)$$

We then bring the second term of the RHS of equation (11.5) onto the LHS,

$$\begin{pmatrix} 1 & 0 & -2\alpha_{\text{iso},xx}/d^3 & 0 \\ 0 & 1 & 0 & \alpha_{\text{iso},yy}/d^3 \\ -2\alpha_{\text{iso},xx}/d^3 & 0 & 1 & 0 \\ 0 & \alpha_{\text{iso},yy}/d^3 & 0 & 1 \end{pmatrix} \begin{pmatrix} p_x^{(1)} \\ p_y^{(1)} \\ p_x^{(2)} \\ p_y^{(2)} \end{pmatrix} = \alpha_{\text{iso}} \begin{pmatrix} E_{\text{ext},x}^{(1)} \\ E_{\text{ext},y}^{(1)} \\ E_{\text{ext},x}^{(2)} \\ E_{\text{ext},y}^{(2)} \end{pmatrix}. \quad (11.6)$$

Instead of a direct inversion of the matrix on the LHS, we determine its eigensystem:

eigenvalue	eigenvector
$1 - 2\alpha_{\text{iso},xx}$	$\mathbf{v}_{x,+} = (1, 0, 1, 0)^T/\sqrt{2}$
$1 + 2\alpha_{\text{iso},xx}$	$\mathbf{v}_{x,-} = (1, 0, -1, 0)^T/\sqrt{2}$
$1 - \alpha_{\text{iso},yy}$	$\mathbf{v}_{y,-} = (0, 1, 0, -1)^T/\sqrt{2}$
$1 + \alpha_{\text{iso},yy}$	$\mathbf{v}_{y,+} = (0, 1, 0, 1)^T/\sqrt{2}$

After introducing the projectors $P_{i,\pm} = \mathbf{v}_{i,\pm}\mathbf{v}_{i,\pm}^T$, one can easily solve for the induced dipole moments in terms of the external fields:

$$\begin{pmatrix} p_x^{(1)} \\ p_y^{(1)} \\ p_x^{(2)} \\ p_y^{(2)} \end{pmatrix} = \left(\frac{\alpha_{\text{iso},xx}}{1 - 2\alpha_{\text{iso},xx}/d^3} P_{x,+} + \frac{\alpha_{\text{iso},xx}}{1 + 2\alpha_{\text{iso},xx}/d^3} P_{x,-} \right. \\ \left. + \frac{\alpha_{\text{iso},yy}}{1 - \alpha_{\text{iso},yy}/d^3} P_{y,-} + \frac{\alpha_{\text{iso},yy}}{1 + \alpha_{\text{iso},yy}/d^3} P_{y,+} \right) \begin{pmatrix} E_{\text{ext},x}^{(1)} \\ E_{\text{ext},y}^{(1)} \\ E_{\text{ext},x}^{(2)} \\ E_{\text{ext},y}^{(2)} \end{pmatrix}. \quad (11.7)$$

If the external electric field is at the positions of the two resonators is identical, one has only contributions from $P_{i,+}$ with $i = x, y$. We now consider the polarizabilities in the vicinity of a resonance ω_0 ,

$$\alpha_{\text{iso},ii} = \frac{f_i}{\omega_0^2 - \omega^2 - 2i\eta\omega}, \quad (11.8)$$

and finally have for the external polarizabilities

$$\alpha_{\text{ext},xx} = \frac{f_x}{(\omega_0^2 - 2f_x/d^3) - \omega^2 - 2i\eta\omega}, \quad (11.9a)$$

$$\alpha_{\text{ext},yy} = \frac{f_y}{(\omega_0^2 + f_y/d^3) - \omega^2 - 2i\eta\omega}. \quad (11.9b)$$

One directly observes that the resonances are split compared to the isolated dipoles, but that the oscillator strengths remain unchanged. The magnitude of the splitting is determined by the mutual distance of the dipoles and the oscillator strength. It also

follows that the damping is not changed on this level of approximation, if η is independent of ω on this level of approximation.¹

So far, we have only discussed the modes that are excited when the external electric field is the same at the position of both dipoles. If the field, however, is non-uniform, the other two terms from equation (11.7) will contribute. The polarizabilities then read

$$\alpha_{\text{ext},xx} = \frac{f_x}{(\omega_0^2 + 2f_x/d^3) - \omega^2 - 2i\eta\omega}, \quad (11.11a)$$

$$\alpha_{\text{ext},yy} = \frac{f_y}{(\omega_0^2 - f_y/d^3) - \omega^2 - 2i\eta\omega}. \quad (11.11b)$$

Compared to the case when the external field was the same at both positions of the dipoles, one now observes the opposite behavior. For an electric field parallel to the x -axis the resonance frequency is increased, as the restoring forces are enhanced, whereas the restoring forces are decreased, when the external field lies parallel to the y -axis. So far, we have analysed how the different eigenmodes of the combined system of the two resonators can be understood by looking at the external electric fields and the induced dipoles.

Now we change the perspective by starting the analysis from the dipoles themselves. The possible combinations of the dipoles are a parallel and an anti-parallel alignment. In order to analyse the shift of the eigenmodes, we recall that the interaction energy W of an electric dipole \mathbf{p} within an electric field \mathbf{E} is given by

$$W = -\mathbf{p} \cdot \mathbf{E}. \quad (11.12)$$

One finds for the case considered here,

$$W = -\frac{1}{d^3}(2p_x^{(1)}p_x^{(2)} - p_y^{(1)}p_y^{(2)}). \quad (11.13)$$

This means that the energy is decreased if both dipole moments parallel to the x -direction are in parallel alignment, but increased in the case of an anti-parallel alignment. The opposite behaviour occurs for the dipole moments parallel to the y -direction. We summarize all modes in Figure 11.2.

¹The dipole model works very well if the distance between the dipoles is much larger than the spatial extension of the induced charge densities and if higher moments times powers of the wavevector are small compared to the dipole moments. If the opposite is the case, one has to take higher multipole moments into account in order to obtain quantitative results. One can either introduce further polarizabilities describing the induced higher multipole moments and the coupling to the gradients of the applied field or one can use the full density profile for the calculation of the matrix element of the Coulomb interaction,

$$v(q) = \langle \pi^{(1)} | v^{\text{H}} | \pi^{(1)} \rangle + \langle \pi^{(1)} | v^{\text{H}} | \pi^{(2)} \rangle. \quad (11.10)$$

The dipole model is then recovered by performing a multipole expansion of the second term on the RHS.

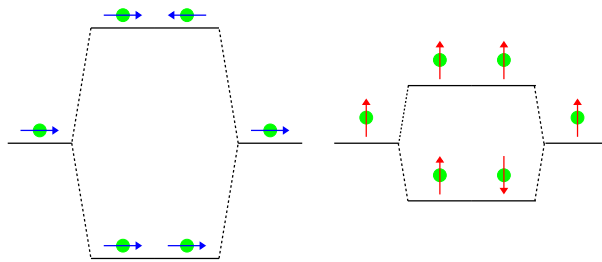


Figure 11.2: Hybridization of the resonances of two identical electric dipoles.

If the induced dipole moments are parallel to the connecting line of the resonators, one uses the term "longitudinal coupling", while one speaks of "transverse coupling" if the direction of the induced dipoles is perpendicular to the connecting line of the resonators [20].

In analogy to molecular orbital theory, one denotes the process of plasmonic coupling as plasmon hybridization. One can now continue with the question: "How do two different resonators couple?". The answer is obtained by performing the same calculation as above. However, one then finds that the shifts of the resonances are most pronounced when the resonance frequencies of the isolated resonators are identical, but they are very small in the limit when the difference between the resonance frequencies of the two resonators is large. The situation is depicted in Figure 11.3.

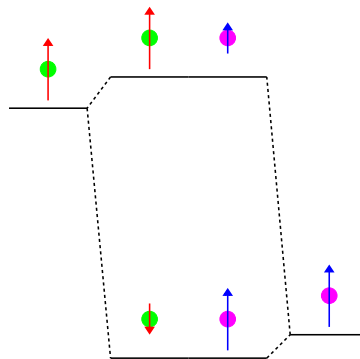


Figure 11.3: Hybridization of the resonances of two different dipoles.

The shift in the resonance frequency of one resonator is determined by the additional force exerted by the dipole field of the other resonator. If the resonance frequencies of both resonators are identical, the dipole fields of both resonators will be strong when they are excited by an external electric field. However, if the resonance frequencies differ, the electric field of one resonator will be much stronger than the field of the other such that the field of the resonator that is on resonance mainly determines the restoring force and

therefore its resonance frequency. The shifts also depend on the oscillator strengths of the resonators. It can be shown by a direct calculation that the square of the resonance frequency of the interacting resonators is roughly proportional to the product of the square root of the oscillator strengths of the isolated resonators. Remembering that the restoring forces of low-lying plasmonic excitations are much larger than the restoring forces of RSPEs, the largest effect on the shift of resonances comes from the coupling of plasmons.

11.1.2 Two SRRs

In this and all subsequent sections where we discuss the plasmon hybridization of SRRs on a dipole level, we consider only the response to electric fields in the y -direction and to magnetic fields in the z -direction, as we are mainly interested in the behavior of the response functions in the vicinity of the plasmonic resonances with an odd number of nodes. We therefore omit indices of the spatial components of the dipoles and electromagnetic fields in order to keep the notation simple.

Two geometries of interest are given in Table 11.1.

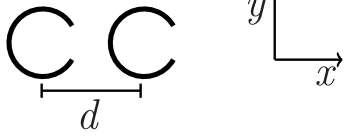
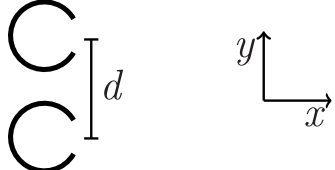
geometry		v	v'
$E_{\text{ext}} \uparrow$		$-1/d^3$	$-1/d^3$
$E_{\text{ext}} \uparrow$		$2/d^3$	$-1/d^3$

Table 11.1: Examples for configurations of two SRRs - including the coupling elements v and v' that we use for the discussion of plasmon hybridization.

We now extend the model from the previous section in order to determine the response of two SRRs in the dipole approximation.

Case $\beta = 0$:

We consider resonators where $\beta_{\text{EM, iso}}$ and $\beta_{\text{ME, iso}}$ are zero. The induced dipole moments

as a response to the external electromagnetic fields are determined via χ_{iso} ,

$$\begin{pmatrix} p^{(1)} \\ m^{(1)} \\ p^{(2)} \\ m^{(2)} \end{pmatrix} \chi_{\text{iso}} \begin{pmatrix} E_{\text{ext}}^{(1)} \\ B_{\text{ext}}^{(1)} \\ E_{\text{ext}}^{(2)} \\ B_{\text{ext}}^{(2)} \end{pmatrix} \quad (11.14)$$

with

$$\chi_{\text{iso}} = \begin{pmatrix} \alpha_{\text{iso},yy} & 0 & 0 & 0 \\ 0 & \gamma_{\text{iso},zz} & 0 & 0 \\ 0 & 0 & \alpha_{\text{iso},yy} & 0 \\ 0 & 0 & 0 & \gamma_{\text{iso},zz} \end{pmatrix}. \quad (11.15)$$

The induced electric and magnetic fields are given by

$$\begin{pmatrix} E_{\text{ind}}^{(1)} \\ B_{\text{ind}}^{(1)} \\ E_{\text{ind}}^{(2)} \\ B_{\text{ind}}^{(2)} \end{pmatrix} = \begin{pmatrix} 0 & 0 & v & 0 \\ 0 & 0 & 0 & v' \\ v & 0 & 0 & 0 \\ 0 & v' & 0 & 0 \end{pmatrix} \begin{pmatrix} p^{(1)} \\ m^{(1)} \\ p^{(2)} \\ m^{(2)} \end{pmatrix}, \quad (11.16)$$

Repeating the calculation from the previous section, one finds

$$\begin{pmatrix} p^{(1)} \\ m^{(1)} \\ p^{(2)} \\ m^{(2)} \end{pmatrix} = \left(\frac{\alpha_{\text{iso},yy}}{1 - v\alpha_{\text{iso},yy}} P_{\text{E},+} + \frac{\alpha_{\text{iso},yy}}{1 + v\alpha_{\text{iso},yy}} P_{\text{E},-} \right. \\ \left. + \frac{\gamma_{\text{iso},zz}}{1 - v'\gamma_{\text{iso},zz}} P_{\text{M},+} + \frac{\gamma_{\text{iso},zz}}{1 - v'\gamma_{\text{iso},zz}} P_{\text{M},-} \right) \begin{pmatrix} E_{\text{ext}}^{(1)} \\ B_{\text{ext}}^{(1)} \\ E_{\text{ext}}^{(2)} \\ B_{\text{ext}}^{(2)} \end{pmatrix}, \quad (11.17)$$

where P are again projectors onto the following vectors

$$\mathbf{v}_{\text{E},\pm} = (1, 0, \pm 1, 0)^{\text{T}}/\sqrt{2}, \quad (11.18a)$$

$$\mathbf{v}_{\text{M},\pm} = (0, 1, 0, \pm 1)^{\text{T}}/\sqrt{2}. \quad (11.18b)$$

One observes that the electric and magnetic dipole couplings are then independent of each other and finds for both dipoles symmetric and antisymmetric resonances. The shifts of the resonance frequencies, however, is different for the electric and magnetic dipoles, as the electric coupling is solely determined by the electric polarizability, while the magnetic coupling is solely based on the magnetic polarizability.

Case $\beta \neq 0$:

The situation changes if one includes magnetoelectric couplings. First, we analyze the situation where the resonators are in parallel alignment. The external response function χ_{ext} is defined via

$$\begin{pmatrix} p^{(1)} \\ m^{(1)} \\ p^{(2)} \\ m^{(2)} \end{pmatrix} = \chi_{\text{ext}} \begin{pmatrix} E^{(1)} \\ B^{(1)} \\ E^{(2)} \\ B^{(2)} \end{pmatrix}, \quad (11.19)$$

where the indices distinguish the two different resonators. The induced electric and magnetic field from one resonator at the position of the other one are given by

$$\begin{pmatrix} E_{\text{ind}}^{(1)} \\ B_{\text{ind}}^{(1)} \\ E_{\text{ind}}^{(2)} \\ B_{\text{ind}}^{(2)} \end{pmatrix} = \begin{pmatrix} 0 & 0 & v & 0 \\ 0 & 0 & 0 & v' \\ v & 0 & 0 & 0 \\ 0 & v' & 0 & 0 \end{pmatrix} \begin{pmatrix} p_1 \\ m_1 \\ p_2 \\ m_2 \end{pmatrix}, \quad (11.20)$$

where v and v' are numbers depending on the relative position of the dipoles. The calculation of the previous section is repeated in the same manner and one finds the following eigen-decomposition of χ_{ext} ,

$$\chi_{\text{ext}} = \frac{\alpha_{\text{iso},yy} + \gamma_{\text{iso},zz}}{1 - \alpha_{\text{iso},yy}v - \gamma_{\text{iso},zz}v'} P_1 + \frac{\alpha_{\text{iso},yy} + \gamma_{\text{iso},zz}}{1 + \alpha_{\text{iso},yy}v + \gamma_{\text{iso},zz}v'} P_2, \quad (11.21)$$

where the projectors P_1 and P_2 are determined from the eigenvectors \mathbf{v}_1 and \mathbf{v}_2 by taking the dyadic product of each eigenvector with itself. The eigenvectors are given by

$$\mathbf{v}_1 = \frac{1}{\sqrt{2|\alpha_{\text{iso},yy}|^2 + 2|\beta_{\text{EM}, \text{iso},yz}|^2}} (\alpha_{\text{iso},yy}, -\beta_{\text{EM}, \text{iso},yz}, \alpha_{\text{iso},zz}, -\beta_{\text{EM}, \text{iso},yz})^T, \quad (11.22a)$$

$$\mathbf{v}_2 = \frac{1}{\sqrt{2|\alpha_{\text{iso},yy}|^2 + 2|\beta_{\text{EM}, \text{iso},yz}|^2}} (\alpha_{\text{iso},yy}, -\beta_{\text{EM}, \text{iso},yz}, -\alpha_{\text{iso},zz}, \beta_{\text{EM}, \text{iso},yz})^T. \quad (11.22b)$$

Note that two eigenvalues are zero and the we also used the cancellation property of the polarizabilities in the vicinity of resonances. Compared to the coupling in the absence of magnetoelectric couplings electric and magnetic resonances are shifted by the same amount. Due to the magnetoelectric couplings the magnetic field of the induced magnetic moment of one dipole induces an electric dipole moment at the other SRR. The shift of the magnetic resonances is thus not only determined by the magnetic polarizability, but also by the electric one. As the electric polarizability exceeds the magnetic one by

a factor of $c^2/(L\omega)^2$, the coupling of the two resonators is mainly determined by the electric polarizability. One further expects that higher electric multipole moments are more important for the coupling than the magnetic dipole coupling when the distance between the resonators is reduced. It has been shown in the literature that the rule of thumb that the coupling of two resonators decreases with an increasing difference of the resonance frequencies holds for the anti-parallel configuration of two SRRs with different sizes [21].

11.2 Plasmonic bands in one dimension

11.2.1 Electric dipole coupling

We have seen in the last section that the electric coupling of two plasmonic resonators leads to two new coupled modes. In analogy to molecular orbital theory, one expects that an arrangement of resonators along an axis should lead to a plasmonic band structure. We denote the distance between the single resonators again as d , but consider only the dipole interaction with the nearest neighbor. For simplicity we assume that the particles are arranged along the x -axis. The geometry is shown in Figure 11.4.

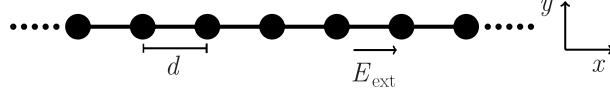


Figure 11.4: Geometry of a 1D chain of resonators with mutual distance d .

We further assume that the polarizability tensor has one non-vanishing diagonal entry, say $\alpha = \alpha_{\text{iso}}\hat{e}_x \otimes \hat{e}_x$, and that the external electric field is parallel to the x -axis. The x -component of the induced electric field from a neighboring dipole is given as $E_{\text{ind}} = 2p/d^3$. The response of the dipoles to the total field is then given by

$$\begin{pmatrix} p^{(1)} \\ p^{(2)} \\ p^{(3)} \\ p^{(4)} \\ \vdots \end{pmatrix} = \begin{pmatrix} \alpha_{\text{iso}} & 0 & 0 & 0 & \cdots \\ 0 & \alpha_{\text{iso}} & 0 & 0 & \cdots \\ 0 & 0 & \alpha_{\text{iso}} & 0 & \cdots \\ 0 & 0 & 0 & \alpha_{\text{iso}} & \cdots \\ \vdots & \vdots & \vdots & \vdots & \ddots \end{pmatrix} \left[\begin{pmatrix} E_{\text{ext}}^{(1)} \\ E_{\text{ext}}^{(2)} \\ E_{\text{ext}}^{(3)} \\ E_{\text{ext}}^{(4)} \\ \vdots \end{pmatrix} + \frac{1}{d^3} \begin{pmatrix} 0 & 2 & 0 & 0 & \cdots \\ 2 & 0 & 2 & 0 & \cdots \\ 0 & 2 & 0 & 2 & \cdots \\ 0 & 0 & 2 & 0 & \cdots \\ \vdots & \vdots & \vdots & \vdots & \ddots \end{pmatrix} \begin{pmatrix} p^{(1)} \\ p^{(2)} \\ p^{(3)} \\ p^{(4)} \\ \vdots \end{pmatrix} \right], \quad (11.23)$$

where the indices of p and E_{ext} denote the positions on the one dimensional lattice. In order to solve for the induced dipole moments, we transform into Fourier space: First of

all, we bring all terms with the dipole moments on the LHS

$$\left[\mathbb{1} - \frac{\alpha_{\text{iso}}}{d^3} \begin{pmatrix} 0 & 2 & 0 & 0 & \cdots \\ 2 & 0 & 2 & 0 & \cdots \\ 0 & 2 & 0 & 2 & \cdots \\ 0 & 0 & 2 & 0 & \cdots \\ \vdots & \vdots & \vdots & \vdots & \ddots \end{pmatrix} \right] \begin{pmatrix} p^{(1)} \\ p^{(2)} \\ p^{(3)} \\ p^{(4)} \\ \vdots \end{pmatrix} = \begin{pmatrix} \alpha_{\text{iso}} & 0 & 0 & 0 & \cdots \\ 0 & \alpha_{\text{iso}} & 0 & 0 & \cdots \\ 0 & 0 & \alpha_{\text{iso}} & 0 & \cdots \\ 0 & 0 & 0 & \alpha_{\text{iso}} & \cdots \\ \vdots & \vdots & \vdots & \vdots & \ddots \end{pmatrix} \begin{pmatrix} E_{\text{ext}}^{(1)} \\ E_{\text{ext}}^{(2)} \\ E_{\text{ext}}^{(3)} \\ E_{\text{ext}}^{(4)} \\ \vdots \end{pmatrix} \quad (11.24)$$

and use the transformation of the basis vectors into Fourier space,

$$\hat{e}_i = \frac{1}{\sqrt{L}} \sum_k \exp(ikd) \hat{e}_k, \quad (11.25)$$

where L denotes the length of the lattice. All matrices are then diagonal and one can easily solve for the dipole moments,

$$p(k) = \frac{\alpha_{\text{iso}}}{1 - 4\alpha_{\text{iso}}/d^3 \cos(kd)} E_{\text{ext}}(k). \quad (11.26)$$

Using now an expansion of α_{iso} in the vicinity of a resonance ω_0 , as we did in the last section, one finally has

$$\alpha_{\text{ext}}(k) = \frac{f}{\omega_{\text{Pl}}^2(k) - \omega^2 + 2i\eta\omega}, \quad \text{with } \omega_{\text{Pl}}^2(k) = \omega_0^2 - 4f/d^3 \cos(kd). \quad (11.27)$$

The resulting plasmonic band has a bandwidth of $8f/d^3$. If one includes the interaction with the next nearest neighbors (nnn), one can repeat the calculation in the same manner as previously discussed and finds the following plasmonic band,

$$\omega_{\text{Pl,nnn}} = \omega_0^2 - 4f/d^3 \cos(kd) - f/(2d^3) \cos(2kd). \quad (11.28)$$

The contribution of the interaction with the next nearest neighbors is smaller by a factor of 8 in the limit of long wavelengths, $kd \ll 1$.

11.2.2 Coupling of SRRs

We now consider a linear chain of molecular SRRs and take into account only the interaction of a resonator with its nearest neighbors. The geometry is depicted in Figure 11.5

We assume that the induced electric and magnetic fields arising from the nearest neighbor possess the following parameterizations

$$\begin{pmatrix} E_{\text{ind}} \\ B_{\text{ind}} \end{pmatrix} = \begin{pmatrix} v & 0 \\ 0 & v' \end{pmatrix} \begin{pmatrix} p \\ m \end{pmatrix}, \quad (11.29)$$

Figure 11.5: Geometry of 1D chain of SRRs with mutual distance d .

where $v = 2/d^3$ and $v' = -1/d^3$. The calculation of the last section is repeated, yielding the following expression for the response function of the interacting resonators,

$$\begin{pmatrix} \alpha_{\text{ext}} & \beta_{\text{ext}} \\ -\beta_{\text{ext}} & \gamma_{\text{ext}} \end{pmatrix} = \frac{1}{D} \begin{pmatrix} \alpha_{\text{iso}} - 2(\alpha_{\text{iso}}\gamma_{\text{iso}} + \beta_{\text{iso}}^2)v' \cos(kd) & \beta_{\text{iso}} \\ -\beta_{\text{iso}} & \gamma_{\text{iso}} - 2(\alpha_{\text{iso}}\gamma_{\text{iso}} + \beta_{\text{iso}}^2)v \cos(kd) \end{pmatrix}, \quad (11.30)$$

with

$$D = 1 - 2(\alpha_{\text{iso}}v + \gamma_{\text{iso}}v') \cos(kd) + 4(\alpha_{\text{iso}}\gamma_{\text{iso}} + \beta_{\text{iso}}^2)v v' \cos^2(kd). \quad (11.31)$$

If we use the cancellation of the polarizabilities in the vicinity of resonances, we finally have

$$\begin{pmatrix} \alpha_{\text{ext}} & \beta_{\text{ext}} \\ -\beta_{\text{ext}} & \gamma_{\text{ext}} \end{pmatrix} = \frac{1}{1 - 2(\alpha_{\text{iso}}v + \gamma_{\text{iso}}v') \cos(kd)} \begin{pmatrix} \alpha_{\text{iso}} & \beta_{\text{iso}} \\ -\beta_{\text{iso}} & \gamma_{\text{iso}} \end{pmatrix}. \quad (11.32)$$

As we have witnessed for the case of two resonators, the resonances of all polarizabilities are shifted by the same amount.

Assuming that we are only interested in the first resonance, $m = 1$, and that the opening angle is zero, we obtain for the plasmon dispersion

$$\omega^2(k) = \frac{\omega_0^2 - \frac{32}{9\pi^5}e^2L v_{\text{F}}v \cos(kd)}{1 + \frac{512}{225\pi^5}e^2c^{-2}L^3 v_{\text{F}}v' \cos(kd)}, \quad (11.33)$$

where ω_0 is the resonance frequency of the isolated resonator. As long as $\omega_0 L/c$ is small, where L is the size of the SRRs, one can neglect the second term in the denominator and obtains a plasmonic band as in the last section. If one increases L , but keeping the ratio L/d fixed, the energy of each state of the band decreases with L^{-2} . If one abandons to keep the ratio L/d fixed when increasing L , one approaches the limit of infinite dense packing. In this limit the assumption that one may take into account only the nearest neighbor interaction between the SRRs breaks down. If one still takes the limit $L \rightarrow \infty$, one finds that there are no propagating modes.

11.3 Three dimensional materials

Based on the experience from the previous sections, we can easily extend the concept of plasmon hybridization for the calculation of plasmonic band structures of three dimensional crystals made up of resonators. The resulting plasmonic band structures will be more complicated than for a wire, but at least in principle one can take the interaction between the single resonators completely into account. If one would use electromagnetic waves as external fields and use the complete radiation fields of all oscillating dipoles, one obtained the solution of the problem - within the dipole approximation. The resulting modes were then plasmon-polaritons. We shall demonstrate in appendix E that such a calculation can be performed analytically in a continuum limit.

In the meantime, we follow an alternative strategy: We split the radiation fields of the oscillators into longitudinal and transverse parts. For the plasmon hybridization we will take into account only the longitudinal electric fields. The transverse fields will be considered later on a macroscopic level by solving Maxwell's equations. Compared to the previous sections of this chapter, we abandon the dipole approximation and work with the full electric potential. We now consider a resonator within the medium. The total potential acting on this resonator comprises the external potential and the potentials from all other resonators, remembering that we have already included the induced potential of the resonator under consideration. We employ the continuum model for the further calculation and calculate the effect of the other resonators on the n -th resonance. If the frequency of the external field lies in the vicinity of the n -th resonance frequency, then one may assume that the n -th plasmon is excited in all resonators. The density propagator of the i -th resonator in the plasmonic eigenbasis is given by

$$\chi_{\text{iso},i}(q_n) = \frac{\frac{2}{\pi}v_F q^2}{\omega_{\text{pl}}^2(q_n) - \omega^2 - 2i\eta\omega}. \quad (11.34)$$

If we denote the eigenvector of the n -th resonance of the i -th resonator by $|n, i\rangle$, the response equation reads,

$$\begin{pmatrix} \omega^2 - \omega_{\text{pl}}^2(q_n) + 2i\eta\omega & -f_n \langle n, 1 | \tilde{v}^{\text{H}} | n, 2 \rangle & -f_n \langle n, 1 | \tilde{v}^{\text{H}} | n, 3 \rangle & \cdots \\ -f_n \langle n, 1 | \tilde{v}^{\text{H}} | n, 2 \rangle & \omega^2 - \omega_{\text{pl}}^2(q_n) + 2i\eta\omega & -f_n \langle n, 2 | \tilde{v}^{\text{H}} | n, 3 \rangle & \cdots \\ -f_n \langle n, 1 | \tilde{v}^{\text{H}} | n, 3 \rangle & -f_n \langle n, 2 | \tilde{v}^{\text{H}} | n, 3 \rangle & \omega^2 - \omega_{\text{pl}}^2(q_n) + 2i\eta\omega & \cdots \\ \vdots & \vdots & \vdots & \ddots \end{pmatrix} \begin{pmatrix} \langle n, 1 | \chi_{\text{ext}} | n, 1 \rangle \\ \langle n, 2 | \chi_{\text{ext}} | n, 2 \rangle \\ \langle n, 3 | \chi_{\text{ext}} | n, 3 \rangle \\ \vdots \end{pmatrix} \\ = \begin{pmatrix} -f_n \\ -f_n \\ -f_n \\ \vdots \end{pmatrix},$$

(11.35)

where we have introduced the abbreviation $f_n = \frac{2}{\pi}v_F q_n^2$. This linear system of equations can be solved again by transforming into Fourier space. One then finds that the plasmon frequency of the i -th resonator is shifted,

$$\omega_{\text{pl},i}^2(q_n) \rightarrow \omega_{\text{pl},i}^2 + \sum_{j \neq i} f_n \exp(i\mathbf{k} \cdot \mathbf{R}_j) \langle n, i | \tilde{v}^{\text{H}} | n, j \rangle, \quad (11.36)$$

where \mathbf{k} is the wave vector from the Fourier transformation and \mathbf{R}_j is the position of the j -th resonator. The oscillatory strength of each individual resonator, however, remains unchanged. If the molecular crystal has an infinite size, the resonance frequency of each resonator is shifted by the same amount. For typical densities of resonators, the summation of all other resonators converges quite fast, so only a few neighbors of the resonator under consideration must be taken into account. In such a case the resonance frequency throughout the whole crystal is shifted by the same amount with exception at the boundaries. If the typical length scale of the neighboring resonators that must be taken into account is L_N , one can perform a Taylor expansion of the frequency shift in the case $kL_N \ll 1$ such that the resonance frequency reads

$$\omega_i^2(q_n) = \sum_j \langle n, i | \tilde{v}^{\text{H}} | n, j \rangle f_n + v_F^2 q_n^2, \quad (11.37)$$

where the summation also includes $i = j$. In order to check if a selected set of neighbors gives a converged result one can systematically include further resonators into the set and determine the shift in the resonance frequency. If the additional shift in the resonance frequency is below a certain threshold, the set of selected resonators will be considered as sufficient. Note that the oscillatory strength of each individual resonator remains unchanged.

Chapter 12

Macroscopic medium theory

12.1 Maxwell equations in the presence of media

The electromagnetic fields in the presence of media comprise the contribution of external charge and current densities, ρ_{ext} and \mathbf{j}_{ext} and the induced charge and current densities inside of the medium. The Maxwell equations relate the electric and magnetic fields to the total sources, i.e. the sum of the external and the induced sources,

$$\text{div}\mathbf{E}_{\text{tot}} = 4\pi\rho_{\text{tot}}, \quad (12.1)$$

$$\text{div}\mathbf{B}_{\text{tot}} = 0, \quad (12.2)$$

$$\text{curl}\mathbf{E}_{\text{tot}} = -\frac{1}{c}\partial_t\mathbf{B}_{\text{tot}}, \quad (12.3)$$

$$\text{curl}\mathbf{B}_{\text{tot}} = \frac{4\pi}{c}\mathbf{j}_{\text{tot}} + \frac{1}{c}\partial_t\mathbf{E}_{\text{tot}}. \quad (12.4)$$

Taking the divergence of equation (12.4), one finds that $\partial_t\mathbf{E}_{\text{tot, long}}$ is equal to $-\mathbf{j}_{\text{tot, long}}$, so one can write

$$\text{curl}\mathbf{B}_{\text{tot}} = \frac{4\pi}{c}\mathbf{j}_{\text{tot, trans}} + \frac{1}{c}\partial_t\mathbf{E}_{\text{tot, trans}}. \quad (12.5)$$

This means that the magnetic field is solely determined by the transverse components of the current density and the electric field.

In typical experimental setups, however, one has only control over the external charge and current densities, making it desirable to have a set of equations at hand that enable one to determine the electromagnetic fields solely from the external sources. As the Maxwell equations are linear in both the sources and the fields, one can split the equations above into two sets of Maxwell equations, where in the first set only quantities with the subscript

"ext" appear

$$\operatorname{div}\mathbf{E}_{\text{ext}} = 4\pi\rho_{\text{ext}}, \quad (12.6)$$

$$\operatorname{div}\mathbf{B}_{\text{ext}} = 0, \quad (12.7)$$

$$\operatorname{curl}\mathbf{E}_{\text{ext}} = -\frac{1}{c}\partial_t\mathbf{B}_{\text{ext}}, \quad (12.8)$$

$$\operatorname{curl}\mathbf{B}_{\text{ext}} = \frac{4\pi}{c}\mathbf{j}_{\text{ext,trans}} + \frac{1}{c}\partial_t\mathbf{E}_{\text{ext,trans}}. \quad (12.9)$$

and in the second one only the induced quantities appear. In order to couple the two sets of equations, one needs a material equation or constitutive equation. One possibility is to invoke Ohm's law,

$$\mathbf{j}_{\text{ind}} = \sigma_{\text{ext}}\mathbf{E}_{\text{ext}}. \quad (12.10)$$

The induced charge density is to be determined via the continuity equation

$$\partial_t\rho_{\text{ind}} + \operatorname{div}\mathbf{j}_{\text{ind}}. \quad (12.11)$$

Typically one splits the fields in the following manner

$$\mathbf{E}_{\text{tot}} = \mathbf{D} - 4\pi\mathbf{P}, \quad (12.12)$$

$$\mathbf{B}_{\text{tot}} = \mathbf{H} + 4\pi\mathbf{M}, \quad (12.13)$$

where \mathbf{D} and \mathbf{H} are auxiliary fields, and employs the following set of Maxwell equations,

$$\operatorname{div}\mathbf{D} = 4\pi\rho_{\text{ext}}, \quad (12.14)$$

$$\operatorname{div}\mathbf{B} = 0, \quad (12.15)$$

$$\operatorname{curl}\mathbf{E}_{\text{tot}} = -\frac{1}{c}\partial_t\mathbf{B}_{\text{tot}}, \quad (12.16)$$

$$\operatorname{curl}\mathbf{H} = \frac{4\pi}{c}\mathbf{j}_{\text{ext}} + \frac{1}{c}\partial_t\mathbf{D}. \quad (12.17)$$

Comparing equation (12.14) and (12.6), one sees that the longitudinal component of \mathbf{D} equals the longitudinal component of external electric field. If one subtracts equation (12.14) from equation (12.1), one finds that the longitudinal component of \mathbf{P} is determined by ρ_{ind} ,

$$\operatorname{div}\mathbf{P} = -\rho_{\text{ind}}. \quad (12.18)$$

Equation (12.16) fixes the transverse component of \mathbf{E}_{tot} , but not the transverse components of \mathbf{D} and \mathbf{P} individually¹. In practice, one uses different choices for the partition of $\mathbf{E}_{\text{tot,trans}}$ into $\mathbf{D}_{\text{trans}}$ and $\mathbf{P}_{\text{trans}}$ allowing different interpretations of the auxiliary quantities:

¹Note that the longitudinal components of both \mathbf{H} and \mathbf{M} are not fixed, either. Here, we set $\operatorname{div}\mathbf{H} = 0$.

$\mathbf{D}_{\text{trans}}$	$c \text{curl} \mathbf{M}$	$\partial_t \mathbf{P}$
$\mathbf{E}_{\text{ext,trans}}$	$c \text{curl} \mathbf{M} + \partial_t \mathbf{P} = \mathbf{j}_{\text{ind,trans}}$	
$\mathbf{E}_{\text{tot,trans}}$	$\mathbf{j}_{\text{ind,trans}}$	0
$\mathbf{E}_{\text{tot,trans}} + \int_{-\infty}^t dt' \mathbf{j}_{\text{ind,trans}}(t')$	0	$\mathbf{j}_{\text{ind,trans}}$

Table 12.1: Different partitions of the transverse total electric field and the induced current.

i) $\mathbf{D}_{\text{trans}} = \mathbf{E}_{\text{ext,trans}}$:

In this case, \mathbf{D} is equal to the external electric field, $\mathbf{D} = \mathbf{E}_{\text{ext}}$. A comparison of equations (12.9) and (12.17) then shows that \mathbf{H} equals the external magnetic field, $\mathbf{H} = \mathbf{B}_{\text{ext}}$. Subtraction of equation (12.8) from equation (12.16) gives

$$\text{curl} \mathbf{P}_{\text{trans}} = \frac{1}{c} \partial_t \mathbf{M}, \quad (12.19)$$

and subtraction of equation (12.9) from equation (12.17) yields

$$\text{curl} \mathbf{M} = \frac{1}{c} \mathbf{j}_{\text{ind,trans}} - \frac{1}{c} \partial_t \mathbf{P}_{\text{trans}}. \quad (12.20)$$

This means that the transverse polarization and the magnetization are coupled.

ii) $\mathbf{D}_{\text{trans}} = \mathbf{E}_{\text{tot,trans}}$:

Now the transverse component of \mathbf{P} vanishes, $\mathbf{P}_{\text{trans}} = 0$. Repeating the subtraction procedure from the previous item, one finds

$$\text{curl} \mathbf{M} = \frac{1}{c} \mathbf{j}_{\text{ind,trans}}. \quad (12.21)$$

Compared to the previous case, \mathbf{M} is solely determined by the induced transverse current density, while the transverse polarization vanishes.

iii) $\partial_t \mathbf{D}_{\text{trans}} = 4\pi \mathbf{j}_{\text{ind,trans}} + \partial_t \mathbf{E}_{\text{tot,trans}}$:

It follows that

$$\partial_t \mathbf{P}_{\text{trans}} = \mathbf{j}_{\text{ind,trans}}. \quad (12.22)$$

As a direct consequence \mathbf{M} vanishes, $\mathbf{M} = 0$, which can be easily seen by subtraction of equation (12.9) from equation (12.17). The response of the system is then solely determined by \mathbf{P} .

Note that the physical fields are \mathbf{E}_{tot} and \mathbf{B}_{tot} , as they determine the Lorentz force. The partitions are summarized in Table 12.1.

As was done before, one can now eliminate the induced sources by expanding them in powers of the either the external, the total or the auxiliary fields. The expansion coefficients are called material parameters. Depending on the partition of \mathbf{E}_{tot} in $\mathbf{D}_{\text{trans}}$ and $\mathbf{P}_{\text{trans}}$, the material parameters can be different; they total fields, however, must be the same in all cases. Based on the choice of the partition and on the choice of the fields that are used for the expansion of \mathbf{P} and \mathbf{M} , equations (12.12) and (12.13) fix the material parameters.

In translationally invariant systems, all material parameters depend only on a wave vector \mathbf{k} and a frequency ω , as long as one works only in the linear regime. Starting with the case iii) of the partition of $\mathbf{E}_{\text{tot,trans}}$, one has

$$\mathbf{E}_{\text{tot}} = \mathbf{D} - \frac{4\pi}{i\omega} \mathbf{j}_{\text{ind}}. \quad (12.23)$$

Expressing \mathbf{j}_{ind} via the conductivity in terms of \mathbf{E}_{tot} , one can relate \mathbf{D} and \mathbf{E}_{tot} ,

$$\mathbf{D} = \left(\mathbf{1} + \frac{4\pi}{i\omega} \sigma \right) \mathbf{E}_{\text{tot}}. \quad (12.24)$$

Now one can introduce the dielectric function

$$\varepsilon = \mathbf{1} + \frac{4\pi}{i\omega} \sigma \quad (12.25)$$

and finds

$$\mathbf{D} = \varepsilon \mathbf{E}_{\text{tot}} \quad (12.26)$$

Therefore the whole response of the medium can be expressed in terms of dielectric functions. Splitting now the fields and the current densities into longitudinal and transverse parts,

$$\begin{pmatrix} \mathbf{j}_{\text{ind,long}} \\ \mathbf{j}_{\text{ind,trans}} \end{pmatrix} = \begin{pmatrix} \sigma_{\text{long,long}} & \sigma_{\text{long,trans}} \\ \sigma_{\text{trans,long}} & \sigma_{\text{trans,trans}} \end{pmatrix} \begin{pmatrix} \mathbf{E}_{\text{ext,long}} \\ \mathbf{E}_{\text{ext,trans}} \end{pmatrix}, \quad (12.27)$$

one sees that the dielectric function comprises in fact four different response functions.

In case ii) of the partition of $\mathbf{E}_{\text{tot,trans}}$, one can easily relate $\mathbf{E}_{\text{tot,long}}$ and \mathbf{D}_{long} in the same way as was done for the previous case,

$$\mathbf{D}_{\text{long}} = \varepsilon_{\text{long,long}} \mathbf{E}_{\text{tot,long}} + \frac{4\pi}{i\omega} \sigma_{\text{long,trans}} \mathbf{E}_{\text{tot,trans}} \quad (12.28)$$

with

$$\varepsilon_{\text{long,long}} = \mathbf{1} + \frac{4\pi}{i\omega} \sigma_{\text{long,long}}. \quad (12.29)$$

The transverse electric field in the second term in equation (12.28) can be expressed in terms of the magnetic field via the Maxwell equations,

$$\mathbf{E}_{\text{tot,trans}} = -\frac{\omega}{k^2 c} \mathcal{K} \mathbf{B}_{\text{tot}} \quad (12.30)$$

with

$$\mathcal{K}_{ij} = \epsilon_{ij\ell} k_\ell, \quad (12.31)$$

where $\epsilon_{ij\ell}$ is the Levi-Civita tensor. So one has

$$\mathbf{D}_{\text{long}} = \epsilon_{\text{long,long}} \mathbf{E}_{\text{tot,long}} + \tilde{\xi} \mathbf{B}_{\text{tot}} \quad (12.32)$$

with

$$\tilde{\xi} = \frac{4\pi i}{k^2 c} \sigma_{\text{long,trans}} \mathcal{K}. \quad (12.33)$$

The magnetization can be calculated by applying the curl on both sides of equation (12.21) and the performing a Fourier transform,

$$\mathbf{M} = -\frac{i}{k^2 c} \mathcal{K} \mathbf{j}_{\text{ind,trans}}. \quad (12.34)$$

Utilizing again the conductivity, expressing the transverse electric field in terms of the magnetic field and plugging everything into equation (12.34), one has

$$\mathbf{H} = \tilde{\zeta} \mathbf{E}_{\text{tot,long}} + \tilde{\mu} \mathbf{B}_{\text{tot}} \quad (12.35)$$

with

$$\tilde{\zeta} = \frac{4\pi i}{k^2 c} \mathcal{K} \sigma_{\text{trans,long}}, \quad (12.36)$$

$$\tilde{\mu} = \mathbb{1} - \frac{4\pi i \omega}{k^4 c^2} \mathcal{K} \sigma_{\text{trans,trans}} \mathcal{K}. \quad (12.37)$$

The relations between the auxiliary fields and the total fields are called constitutive relations. The previous calculations have shown one possible form of the constitutive relations:

$$\begin{pmatrix} \mathbf{D}_{\text{long}} \\ \mathbf{H} \end{pmatrix} = \begin{pmatrix} \epsilon_{\text{long,long}} & \tilde{\xi} \\ \tilde{\zeta} & \tilde{\mu} \end{pmatrix} \begin{pmatrix} \mathbf{E}_{\text{tot,long}} \\ \mathbf{B}_{\text{tot}} \end{pmatrix}. \quad (12.38)$$

Another form of the constitutive relations that is widely used reads

$$\begin{pmatrix} \mathbf{D}_{\text{long}} \\ \mathbf{B}_{\text{tot}} \end{pmatrix} = \begin{pmatrix} \epsilon & \xi \\ \zeta & \mu \end{pmatrix} \begin{pmatrix} \mathbf{E}_{\text{tot,long}} \\ \mathbf{H} \end{pmatrix}. \quad (12.39)$$

The choice of the set of constitutive relations is arbitrary, as one set can be transformed into another by solving a linear system of equations.

12.2 From microscopic to macroscopic Maxwell equations

We have seen in the previous chapter that the response of a molecular lattice to external fields can be calculated - at least in principle - analytically. These calculations have been based on solving the microscopic Maxwell equations, where the sources of all induced electromagnetic fields are all charge and current densities. The sum of the induced and the external fields defines the microscopic fields that are spatially highly fluctuating. However, for the calculation of the response within the dipole approximation, only the values of the microscopic fields at the positions of the dipoles were needed. These fields are denoted as the local fields. All fields are summarized in Table 12.2.

Field	description
external	fields that are created by sources outside the medium
microscopic	sum of the external fields and all internal fields in the medium at any point (total fields)
local	microscopic field at the positions of the dipoles
macroscopic	a spatial average of the microscopic field

Table 12.2: Summary of the different kinds of fields.

The aim of macroscopic electrodynamics is to find a (hydrodynamic) smooth description of the response of the medium to either external fields or total macroscopic fields whose spatial variations occur only on length scales that are much larger than the typical molecular length scales. A common approach is to average both the electric and magnetic dipole moments over regions whose size lies above the molecular length scales, but below the length scale of the variation of the external electromagnetic fields, yielding the macroscopic polarization $\bar{\mathbf{P}}$ and magnetization $\bar{\mathbf{M}}$ to be defined in Section 12.4. If these both are expanded in powers of the external fields,

$$\begin{pmatrix} \bar{P}_i \\ \bar{M}_i \end{pmatrix} = \sum_j \begin{pmatrix} \left. \frac{\partial \bar{P}_i}{\partial (E_{\text{ext}})_j} \right|_{\mathbf{E}_{\text{ext}}=0, \mathbf{B}_{\text{ext}}=0} & \left. \frac{\partial \bar{P}_i}{\partial (B_{\text{ext}})_j} \right|_{\mathbf{E}_{\text{ext}}=0, \mathbf{B}_{\text{ext}}=0} \\ \left. \frac{\partial \bar{M}_i}{\partial (E_{\text{ext}})_j} \right|_{\mathbf{E}_{\text{ext}}=0, \mathbf{B}_{\text{ext}}=0} & \left. \frac{\partial \bar{M}_i}{\partial (B_{\text{ext}})_j} \right|_{\mathbf{E}_{\text{ext}}=0, \mathbf{B}_{\text{ext}}=0} \end{pmatrix} \begin{pmatrix} E_{\text{ext},j} \\ B_{\text{ext},j} \end{pmatrix} \quad (12.40)$$

one can define the external macroscopic susceptibilities,

$$\begin{pmatrix} (\bar{\chi}_{EE})_{ij} & (\bar{\chi}_{EM})_{ij} \\ (\bar{\chi}_{ME})_{ij} & (\bar{\chi}_{MM})_{ij} \end{pmatrix} \equiv \begin{pmatrix} \left. \frac{\partial \bar{P}_i}{\partial (E_{\text{ext}})_j} \right|_{\mathbf{E}_{\text{ext}}=0, \mathbf{B}_{\text{ext}}=0} & \left. \frac{\partial \bar{P}_i}{\partial (B_{\text{ext}})_j} \right|_{\mathbf{E}_{\text{ext}}=0, \mathbf{B}_{\text{ext}}=0} \\ \left. \frac{\partial \bar{M}_i}{\partial (E_{\text{ext}})_j} \right|_{\mathbf{E}_{\text{ext}}=0, \mathbf{B}_{\text{ext}}=0} & \left. \frac{\partial \bar{M}_i}{\partial (B_{\text{ext}})_j} \right|_{\mathbf{E}_{\text{ext}}=0, \mathbf{B}_{\text{ext}}=0} \end{pmatrix}, \quad (12.41)$$

where it is assumed that the medium has no polarization or magnetization in the absence of external electromagnetic fields.

In order to obtain the macroscopic fields, the microscopic fields have to be averaged over the same types of regions that were used for the averaging of the dipole moments. In doing so, one eliminates the spatial microscopic fluctuations in the microscopic fields. An expansion of the polarization and the magnetization in powers of the total macroscopic electric and magnetic fields, $\bar{\mathbf{E}}$ and $\bar{\mathbf{H}}$ defines the (irreducible) macroscopic response properties. If one takes only the linear terms into account and assumes that the medium has no polarization or magnetization in the absence of external electromagnetic fields, the irreducible response functions are defined as

$$\begin{pmatrix} (\bar{\chi}_{EE})_{ij} & (\bar{\chi}_{EM})_{ij} \\ (\bar{\chi}_{ME})_{ij} & (\bar{\chi}_{MM})_{ij} \end{pmatrix} \equiv \begin{pmatrix} \left. \frac{\partial \bar{P}_i}{\partial E_j} \right|_{\bar{\mathbf{E}}=0, \bar{\mathbf{H}}=0} & \left. \frac{\partial \bar{P}_i}{\partial H_j} \right|_{\bar{\mathbf{E}}=0, \bar{\mathbf{H}}=0} \\ \left. \frac{\partial \bar{M}_i}{\partial E_j} \right|_{\bar{\mathbf{E}}=0, \bar{\mathbf{H}}=0} & \left. \frac{\partial \bar{M}_i}{\partial H_j} \right|_{\bar{\mathbf{E}}=0, \bar{\mathbf{H}}=0} \end{pmatrix}. \quad (12.42)$$

Finally, we are in the position to determine the macroscopic response functions appearing in equation (12.39) for single and double barred cases,

$$\begin{pmatrix} \varepsilon & \xi \\ \zeta & \mu \end{pmatrix} = \begin{pmatrix} \mathbb{1} + 4\pi\chi_{EE} & 4\pi\chi_{EM} \\ 4\pi\chi_{ME} & \mathbb{1} + 4\pi\chi_{MM} \end{pmatrix}. \quad (12.43)$$

There exist two possible sets of response functions, depending on whether the external or the macroscopic fields are known.

12.3 Averaging procedure

In the following, we denote the average of a function f by angular brackets,

$$\langle f(\mathbf{r}) \rangle := \int_{\mathcal{R}(\mathbf{r})} d^3\mathbf{r}' w(\mathbf{r} - \mathbf{r}') f(\mathbf{r}'), \quad (12.44)$$

where $w(\mathbf{r})$ is a weight function with the following properties:

- i) w is normalized.
- ii) w has a plateau around \mathbf{r} with a latitude L_{av} that is much larger than the typical atomic length scale, but still smaller than the wavelength of the external light field [86].

We denote the set of dipoles that lie within $\mathcal{R}(\mathbf{r})$ by $S(\mathbf{r})$,

$$S(\mathbf{r}) = \{i | \mathbf{R}_i \in \mathcal{R}(\mathbf{r})\}. \quad (12.45)$$

As a next step, we divide $\mathcal{R}(\mathbf{r})$ into subregions \mathcal{R}_i that are centered at the positions \mathbf{R}_i of the dipoles. We have depicted an example of such a partition in Figure 12.1.

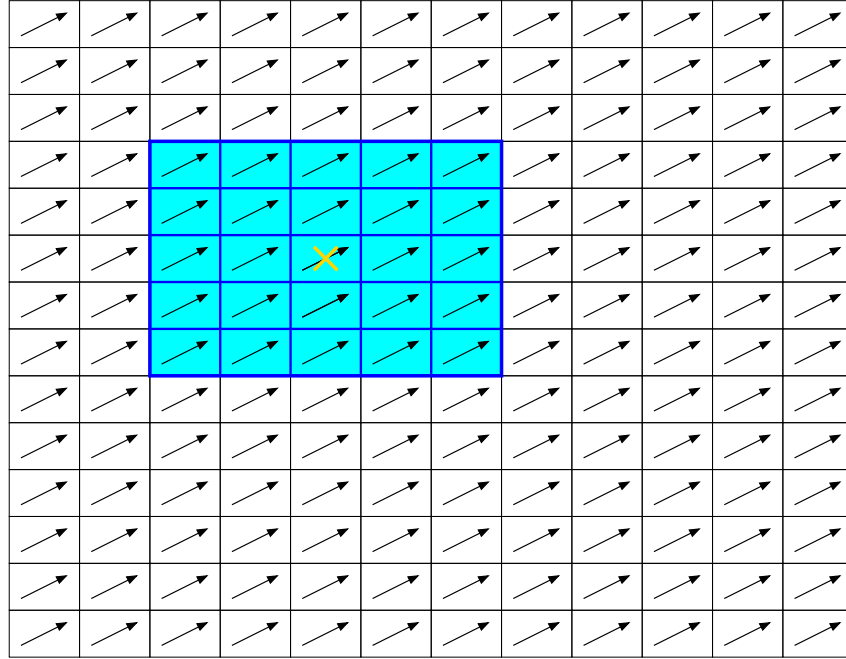


Figure 12.1: Partition of the averaging region into subregions. The yellow x denotes the position \mathbf{r} at which the averaged field is to be calculated. The blue region depicts the volume over which the averaging is performed.

The partitioning is done in such a way that the union of all regions yields the averaging region,

$$\mathcal{R}(\mathbf{r}) = \bigcup_{i \in S(\mathbf{r})} \mathcal{R}_i \quad (12.46)$$

and that the subregion reflects the symmetry of the surrounding dipoles. For a crystal lattice, for example, a natural choice for the subregion would be the unit cell.

We will assume for the rest of this work that averaging the microscopic density yields a macroscopic density n_{res} that is independent of the position,

$$\bar{n}_{\text{res}} = \left\langle \sum_j \delta(\mathbf{r} - \mathbf{R}_j) \right\rangle \quad (12.47)$$

Thus, the medium can be considered as homogeneous on a macroscopic level.

The medium can be classified according to its microscopic structure:

- i) Completely parallel alignment: In this case the resonators are aligned parallel over length scales that are much larger than the wavelength of the external fields. If L_C is of the order of the macroscopic system size, all resonators of the medium

can be considered as being in a parallel alignment. If one neglects the effect of the boundaries, the macroscopic response functions will be independent of the position inside the medium. This implies for the averaging that the microscopic response functions and therefore the induced dipole moments inside the averaging region are identical.

ii) Photonic crystals: Now, the spatial variations of the resonators occur on length scales that are comparable to the wavelength of the light field. Such media are called photonic crystals and are subject of current research, as photons in these media can acquire band gaps due to Bragg scattering.

iii) Random medium:

In this regime, one can think about the distribution of the resonators as being random like in a gas or a fluid. The response function of each single resonator can then be replaced by the average of the response function over all possible orientations denoted by a bar.

12.4 Polarization and magnetization

Using the average defined in the previous section, the macroscopic polarization and magnetization are given by,

$$\bar{\mathbf{P}}(\mathbf{r}) = \left\langle \sum_j \mathbf{p}_j \delta(\mathbf{r} - \mathbf{R}_j) \right\rangle, \quad (12.48)$$

$$\bar{\mathbf{M}}(\mathbf{r}) = \left\langle \sum_j \mathbf{m}_j \delta(\mathbf{r} - \mathbf{R}_j) \right\rangle, \quad (12.49)$$

where j labels the dipoles and \mathbf{R}_j their position. Utilizing the microscopic response functions,

$$\begin{pmatrix} \mathbf{p}_j \\ \mathbf{m}_j \end{pmatrix} = \begin{pmatrix} \alpha_j & \beta_{\text{EM},j} \\ \beta_{\text{ME},j} & \gamma_j \end{pmatrix} \begin{pmatrix} \mathbf{E}_{\text{ext}}(\mathbf{R}_j) \\ \mathbf{B}_{\text{ext}}(\mathbf{R}_j) \end{pmatrix}, \quad (12.50)$$

one can perform a gradient expansion of the external fields,

$$\begin{pmatrix} \mathbf{E}_{\text{ext}}(\mathbf{R}_j) \\ \mathbf{B}_{\text{ext}}(\mathbf{R}_j) \end{pmatrix} = \begin{pmatrix} \mathbf{E}_{\text{ext}}(\mathbf{r}) \\ \mathbf{B}_{\text{ext}}(\mathbf{r}) \end{pmatrix} + \sum_{\ell} (\mathbf{r} - \mathbf{R}_j)_{\ell} \frac{\partial}{\partial R_{\ell}} \begin{pmatrix} \mathbf{E}_{\text{ext}}(\mathbf{R}) \\ \mathbf{B}_{\text{ext}}(\mathbf{R}) \end{pmatrix} \Big|_{\mathbf{R}=\mathbf{r}} + \dots, \quad (12.51)$$

yielding,

$$\begin{pmatrix} \bar{\mathbf{P}}(\mathbf{r}) \\ \bar{\mathbf{M}}(\mathbf{r}) \end{pmatrix} = \left\langle \sum_j \begin{pmatrix} \alpha_j & \beta_{\text{EM},j} \\ \beta_{\text{ME},j} & \gamma_j \end{pmatrix} \delta(\mathbf{r} - \mathbf{R}_j) \right\rangle \begin{pmatrix} \mathbf{E}_{\text{ext}}(\mathbf{r}) \\ \mathbf{B}_{\text{ext}}(\mathbf{r}) \end{pmatrix}. \quad (12.52)$$

Here, it was also used that the spatial variations of the external fields occur on length scales that are much larger than L_{av} . For a parallel alignment of identical resonators, averaging simply gives,

$$\bar{\mathbf{P}}(\mathbf{r}) = \bar{n}_{\text{res}}\alpha\mathbf{E}_{\text{ext}}(\mathbf{r}) + \bar{n}_{\text{res}}\beta_{\text{EM}}\mathbf{B}_{\text{ext}}(\mathbf{r}), \quad (12.53)$$

$$\bar{\mathbf{M}}(\mathbf{r}) = \bar{n}_{\text{res}}\beta_{\text{ME}}\mathbf{E}_{\text{ext}}(\mathbf{r}) + \bar{n}_{\text{res}}\gamma\mathbf{B}_{\text{ext}}(\mathbf{r}). \quad (12.54)$$

In case of a random distribution of the orientations, one has

$$\bar{\mathbf{P}}(\mathbf{r}) = \bar{n}_{\text{res}}\bar{\alpha}\mathbf{E}_{\text{ext}}(\mathbf{r}) + \bar{n}_{\text{res}}\bar{\beta}_{\text{EM}}\mathbf{B}_{\text{ext}}(\mathbf{r}), \quad (12.55)$$

$$\bar{\mathbf{M}}(\mathbf{r}) = \bar{n}_{\text{res}}\bar{\beta}_{\text{ME}}\mathbf{E}_{\text{ext}}(\mathbf{r}) + \bar{n}_{\text{res}}\bar{\gamma}\mathbf{B}_{\text{ext}}(\mathbf{r}). \quad (12.56)$$

Note that the bar over the microscopic polarizabilities denotes their spherical average.

12.5 Macroscopic fields

Based on the partitioning introduced in Section 12.3, the averaged field is given as the sum of the contributions from each individual subregion (see Figure 12.1). Each contribution from a single subregion can be split into two parts, namely a contribution from the dipoles inside \mathfrak{J}_i and outside \mathfrak{D}_i of the subregion under consideration. If we denote the volume of $\mathcal{R}(\mathbf{r})$ by $V(\mathbf{r})$, we can write for the macroscopic fields

$$\begin{aligned} \begin{pmatrix} \bar{\mathbf{E}}(\mathbf{r}) \\ \bar{\mathbf{H}}(\mathbf{r}) \end{pmatrix} &= \begin{pmatrix} \langle \mathbf{E}_{\text{micro}}(\mathbf{r}) \rangle \\ \langle \mathbf{H}_{\text{macro}}(\mathbf{r}) \rangle \end{pmatrix} \\ &= \begin{pmatrix} \mathbf{E}_{\text{ext}}(\mathbf{r}) \\ \mathbf{B}_{\text{ext}}(\mathbf{r}) \end{pmatrix} + \sum_{i \in S(\mathbf{r})} \mathfrak{J}_i(\mathbf{r}) + \mathfrak{D}_i(\mathbf{r}), \\ &= \begin{pmatrix} \mathbf{E}_{\text{ext}}(\mathbf{r}) \\ \mathbf{B}_{\text{ext}}(\mathbf{r}) \end{pmatrix} + \sum_{i \in S(\mathbf{r})} \frac{1}{V(\mathbf{r})} \int_{\mathcal{R}_i} d^3\mathbf{r}' \left(\begin{pmatrix} \mathbf{E}_{\text{dip}}(\mathbf{r}', \mathbf{R}_i) \\ \mathbf{H}_{\text{dip}}(\mathbf{r}', \mathbf{R}_i) \end{pmatrix} + \sum_{j \neq i} \begin{pmatrix} \mathbf{E}_{\text{dip}}(\mathbf{r}', \mathbf{R}_j) \\ \mathbf{H}_{\text{dip}}(\mathbf{r}', \mathbf{R}_j) \end{pmatrix} \right). \end{aligned} \quad (12.57)$$

where we have assumed that the spatial fluctuations of the external fields are on a length scale that is much larger than the spatial extension of the averaging region.

Calculation of $\mathcal{I}_i(\mathbf{r})$

We now start with the calculation of \mathcal{I}_i for each individual subregion. For doing so, we need the explicit expressions of the microscopic near-fields,

$$\begin{pmatrix} \mathbf{E}_{\text{micro}}(\mathbf{r}) \\ \mathbf{H}_{\text{micro}}(\mathbf{r}) \end{pmatrix} = \begin{pmatrix} \mathbf{E}_{\text{ext}}(\mathbf{r}) \\ \mathbf{B}_{\text{ext}}(\mathbf{r}) \end{pmatrix} + \sum_i \left[\frac{3(\mathbf{r} - \mathbf{R}_i) \otimes (\mathbf{r} - \mathbf{R}_i)}{|\mathbf{x} - \mathbf{R}_i|^5} - \frac{\mathbb{1}}{|\mathbf{r} - \mathbf{R}_i|^3} \right] \begin{pmatrix} \mathbf{p}_i \\ \mathbf{m}_i \end{pmatrix}. \quad (12.58)$$

One easily observes that for the evaluation of \mathfrak{J}_i one has to be careful with the singularities of the fields inside of \mathcal{R}_i . We will assume in the following that only one dipole is located within $\mathcal{R}_i(\mathbf{r})$, but a generalization to several dipoles is straightforward. In order to analyze the behavior at the singular point \mathbf{R}_i , one constructs another region $\tilde{\mathcal{R}}_{i,u}$, where the parameter u can be used in order to shrink the original region $\tilde{\mathcal{R}}_{i,u=1} = \mathcal{R}_i$ to the singular point $\tilde{\mathcal{R}}_{i,u=0}(\mathbf{r}) = \{\mathbf{R}_i\}$. The explicit construction of $\tilde{\mathcal{R}}_{i,u}(\mathbf{r})$ reads

$$\tilde{\mathcal{R}}_{i,u} = \{\mathbf{R}_i + u(\mathbf{r}'' - \mathbf{R}_i(\mathbf{r})) | \mathbf{y} \in \mathcal{R}_i\}. \quad (12.59)$$

For convenience, we parameterize the integration variables as $\mathbf{r}' = \mathbf{R}_i + \boldsymbol{\xi}$. If we denote the shifted region by $\mathcal{R}'_i(\mathbf{r}) = \{\mathbf{r}'' - \mathbf{R}_i | \mathbf{r}'' \in \mathcal{R}_i\}$ and use the same notation for the shifted $\tilde{\mathcal{R}}_{i,u}(\mathbf{x})$, the integral reads

$$\mathfrak{J}_i = \int_{\mathcal{R}'_i \setminus O} d^3\boldsymbol{\xi} \begin{pmatrix} \mathbf{E}_{\text{dip}}(\boldsymbol{\xi}, O) \\ \mathbf{H}_{\text{dip}}(\boldsymbol{\xi}, O) \end{pmatrix} + \lim_{u \rightarrow 0} \int_{\tilde{\mathcal{R}}'_{i,u}} d^3\boldsymbol{\xi} \begin{pmatrix} \mathbf{E}_{\text{dip}}(\boldsymbol{\xi}, O) \\ \mathbf{H}_{\text{dip}}(\boldsymbol{\xi}, O) \end{pmatrix}, \quad (12.60)$$

where O is the origin. We now look at the contribution from the singularity and start with a rescaling of the integration variable $\boldsymbol{\xi} \rightarrow u\boldsymbol{\xi}$,

$$\mathfrak{J}_{i,\text{sing}} = \lim_{u \rightarrow 0} \int_{\mathcal{R}'_i} d^3\xi u^3 \begin{pmatrix} \mathbf{E}_{\text{dip}}(\boldsymbol{\xi}u, O) \\ \mathbf{H}_{\text{dip}}(\boldsymbol{\xi}u, O) \end{pmatrix}. \quad (12.61)$$

If one looks at the explicit expressions for the dipole fields, one can make two observations:

- i) The contribution from the transverse fields is zero in the limit $u \rightarrow 0$.
- ii) The longitudinal parts give rise to a non-vanishing contribution that is independent of u . However, it depends on the subregion chosen.

The integral then reads

$$\mathfrak{J}_{i,\text{sing}} = \int_{\mathcal{R}'_i} d^3\boldsymbol{\xi} \begin{pmatrix} -\text{grad} \frac{\boldsymbol{\xi} \cdot \mathbf{p}_i}{|\boldsymbol{\xi}|^3} \\ -\text{grad} \frac{\boldsymbol{\xi} \cdot \mathbf{m}_i}{|\boldsymbol{\xi}|^3} \end{pmatrix}. \quad (12.62)$$

As we want to use Stoke's integral theorem, we have to parameterize the boundary \mathcal{B}_i of \mathcal{R}'_i , $\mathcal{B}_i = \partial\mathcal{R}'_i$. If we assume in addition that \mathcal{R}'_i is convex, we can always find a parameterization in the following way,

$$\begin{aligned} \mathcal{B}_i = & \{\xi_i \hat{e}_i + \xi_j \hat{e}_j + k^+(\xi_i, \xi_j) \hat{e}_k | (\xi_i, \xi_j) \in A_k\} \cup \{\xi_i \hat{e}_i + \xi_j \hat{e}_j + k^-(u, v) \hat{e}_k | (\xi_i, \xi_j) \in A_k\}, \\ & \text{with } i, j, k = x, y, z \text{ and } i \neq j \neq k \text{ and } k^+(u, v) \geq k^-(u, v). \end{aligned} \quad (12.63)$$

So we finally have for the integral

$$\mathfrak{J}_{i,\text{sing}} = \begin{pmatrix} p_{i,1} \int_{A_x} d\xi_2 d\xi_3 \frac{x^-}{\sqrt{(x^-)^2 + \xi_2^2 + \xi_3^2}} - \frac{x^+}{\sqrt{(x^+)^2 + \xi_2^2 + \xi_3^2}} \\ p_{i,2} \int_{A_y} d\xi_1 d\xi_3 \frac{y^-}{\sqrt{\xi_1^2 + (y^-)^2 + \xi_3^2}} - \frac{y^+}{\sqrt{\xi_1^2 + (y^+)^2 + \xi_3^2}} \\ p_{i,3} \int_{A_z} d\xi_1 d\xi_2 \frac{z^-}{\sqrt{\xi_1^2 + \xi_2^2 + (z^-)^2}} - \frac{z^+}{\sqrt{\xi_1^2 + \xi_2^2 + (z^+)^2}} \\ m_{i,1} \int_{A_x} d\xi_2 d\xi_3 \frac{x^-}{\sqrt{(x^-)^2 + \xi_2^2 + \xi_3^2}} - \frac{x^+}{\sqrt{(x^+)^2 + \xi_2^2 + \xi_3^2}} \\ m_{i,2} \int_{A_y} d\xi_1 d\xi_3 \frac{y^-}{\sqrt{\xi_1^2 + (y^-)^2 + \xi_3^2}} - \frac{y^+}{\sqrt{\xi_1^2 + (y^+)^2 + \xi_3^2}} \\ m_{i,3} \int_{A_z} d\xi_1 d\xi_2 \frac{z^-}{\sqrt{\xi_1^2 + \xi_2^2 + (z^-)^2}} - \frac{z^+}{\sqrt{\xi_1^2 + \xi_2^2 + (z^+)^2}} \end{pmatrix}. \quad (12.64)$$

We define for each dipole a matrix \mathcal{F}_i containing local environmental form factors by

$$(\mathcal{F}_i)_{jk} = -\delta_{jk} \int_{A_j} d\xi_l d\xi_n \frac{j^-}{\sqrt{(j^-)^2 + \xi_l^2 + \xi_n^2}} - \frac{j^+}{\sqrt{(j^+)^2 + \xi_l^2 + \xi_n^2}} \quad (12.65)$$

with $j, k, l, n = x, y, z$ and $j \neq l \neq n$.

The desired integral has then the form

$$\mathfrak{J}_{i,\text{sing}} = - \begin{pmatrix} \mathcal{F}_i & 0 \\ 0 & \mathcal{F}_i \end{pmatrix} \begin{pmatrix} \mathbf{p}_i \\ \mathbf{m}_i \end{pmatrix}. \quad (12.66)$$

We make the following observations:

- i) Both electric and magnetic dipoles have the same environmental form factors.
- ii) Physically the form factors take the geometry of the surrounding dipoles into account.

We will give explicit expressions for form factors in Section 12.7.

The analysis of the integral over the region with the removed origin is now straightforward.

The contributions from the longitudinal parts of the fields cancel, so one finally has

$$\mathfrak{J}_i = - \begin{pmatrix} \mathcal{F}_i & 0 \\ 0 & \mathcal{F}_i \end{pmatrix} \begin{pmatrix} \mathbf{p}_i \\ \mathbf{m}_i \end{pmatrix} + i \int_{\mathcal{R}_i} d^3\xi \begin{pmatrix} \frac{\xi \times \mathbf{p}_i}{|\xi|^3} \\ \frac{\xi \times \mathbf{m}_i}{|\xi|^3} \end{pmatrix}. \quad (12.67)$$

In the following, we will neglect the contribution from the transverse fields, as they are suppressed by a factor of characteristic length scale of \mathcal{R}_i divided by the wavelength of the external light field.

Calculation of $\mathcal{O}_i(\mathbf{r})$

As a next step, we consider the contribution of the dipoles outside the region under consideration. We denote the set of dipoles we want to take into account by $O_i = S(\mathbf{R}_i) \setminus \{i\}$.

Note that not all dipoles under consideration $\in O_i$ belong to $S(\mathbf{r})$. This can be easily understood if one looks at the dipoles on the boundary of the averaging region. In the following we only consider the case of an orthorhombic lattice with lattice constants a , b , and c . We choose the origin of the coordinate system such that it coincides with the center of \mathcal{R}_i . We further assume that all dipole moments are equal. As a next step we organize the surrounding dipoles in shell structures around \mathcal{R}_i . We label each dipole by three numbers r_j ($j = 1, 2, 3$) that determine the relative position to the origin $\mathbf{r}_i = r_1 a \hat{e}_1 + r_2 b \hat{e}_2 + r_3 c \hat{e}_3$. The k -th shell is then defined as

$$\mathcal{S}_k = \{r_1, r_2, r_3 | \max(|r_1|, |r_2|, |r_3|) = k\}. \quad (12.68)$$

The shell structure is supposed to lead to a good convergence, as there might be cancellations from opposing dipoles. Using Mathematica, a direct calculation of the contributions from the first and the second shell shows that these vanish. The proof that the contributions from further shells will vanish follows from the result of the calculation based on the extinction theorem that is given in Appendix E. It should be noted that this cancellation does not take place anymore when the boundary of the sample is reached.

Finally, if one sums up all contributions, one finds

$$\begin{pmatrix} \bar{\mathbf{E}}(\mathbf{r}) \\ \bar{\mathbf{H}}(\mathbf{r}) \end{pmatrix} = \begin{pmatrix} \mathbf{E}_{\text{ext}}(\mathbf{r}) \\ \mathbf{B}_{\text{ext}}(\mathbf{r}) \end{pmatrix} - \sum_{i \in S(\mathbf{r})} \frac{1}{V(\mathbf{r})} \begin{pmatrix} \mathcal{F}_i & 0 \\ 0 & \mathcal{F}_i \end{pmatrix} \begin{pmatrix} \mathbf{p}_i \\ \mathbf{m}_i \end{pmatrix} \quad (12.69)$$

This expression can be further simplified, if all resonators are in a parallel alignment, as then all form factors are equal,

$$\begin{pmatrix} \bar{\mathbf{E}}_{\text{para}}(\mathbf{r}) \\ \bar{\mathbf{H}}_{\text{para}}(\mathbf{r}) \end{pmatrix} = \begin{pmatrix} \mathbf{E}_{\text{ext}}(\mathbf{r}) \\ \mathbf{B}_{\text{ext}}(\mathbf{r}) \end{pmatrix} - \begin{pmatrix} \mathcal{F} & 0 \\ 0 & \mathcal{F} \end{pmatrix} \begin{pmatrix} \mathbf{P}_{\text{para}}(\mathbf{r}) \\ \mathbf{M}_{\text{para}}(\mathbf{r}) \end{pmatrix}. \quad (12.70)$$

For random media, we employ the approximation that \mathcal{F}_i and the dipole moments are uncorrelated. This leads to an equation similar to equation (12.70), but with \mathcal{F} replaced by $\bar{\mathcal{F}}$. For the case of an orthorhombic lattice, one would choose for the calculation of \mathcal{F} an ellipsoidal environment.

The physical interpretation of equation (12.70) is that the total macroscopic fields differ from the external ones due to screening inside the medium. However, one should note at this point that the response of the resonators is solely determined by the local fields from a microscopic point of view. If one considers gases or liquids, the molecules do not rest at fixed positions, but translate and rotate. Thus it is reasonable to consider the response to the averaged fields in these cases, as the spatial average can then be regarded as equivalent to the thermal average.

12.6 Macroscopic response functions

We are now in the position to give explicit expressions for the macroscopic response functions. Starting with the external response functions, one sees by looking at equation (12.52) that these are simply the averages of the microscopic response functions:

$$\begin{pmatrix} \bar{\chi}_{EE} & \bar{\chi}_{EM} \\ \bar{\chi}_{ME} & \bar{\chi}_{MM} \end{pmatrix} = \left\langle \sum_j \begin{pmatrix} \alpha_j & \beta_{EM,j} \\ \beta_{ME,j} & \gamma_j \end{pmatrix} \delta(\mathbf{r} - \mathbf{R}_j) \right\rangle. \quad (12.71)$$

For a completely parallel alignment of the resonators, the expressions for the response functions are

$$\begin{pmatrix} \bar{\chi}_{EE} & \bar{\chi}_{EM} \\ \bar{\chi}_{ME} & \bar{\chi}_{MM} \end{pmatrix} = \bar{n}_{\text{res}} \begin{pmatrix} \alpha & \beta_{EM} \\ \beta_{ME} & \gamma \end{pmatrix}, \quad (12.72)$$

while for the random case, they are given by

$$\begin{pmatrix} \bar{\chi}_{EE} & \bar{\chi}_{EM} \\ \bar{\chi}_{ME} & \bar{\chi}_{MM} \end{pmatrix} = \bar{n}_{\text{res}} \begin{pmatrix} \bar{\alpha} & \bar{\beta}_{EM} \\ \bar{\beta}_{ME} & \bar{\gamma} \end{pmatrix}. \quad (12.73)$$

If one wants to know the response to the total macroscopic field, one first solves equation (12.69) for the external fields, plugs these into equation (12.52) and solves for the polarization and the magnetization in terms of the macroscopic fields. In the case of a parallel alignment of the resonators one obtains

$$\begin{pmatrix} \bar{\bar{\chi}}_{EE} & \bar{\bar{\chi}}_{EM} \\ \bar{\bar{\chi}}_{ME} & \bar{\bar{\chi}}_{MM} \end{pmatrix} = \left[\mathbb{1} - \bar{n}_{\text{res}} \begin{pmatrix} \mathcal{F} & 0 \\ 0 & \mathcal{F} \end{pmatrix} \begin{pmatrix} \alpha & \beta_{EM} \\ \beta_{ME} & \gamma \end{pmatrix} \right]^{-1} \bar{n}_{\text{res}} \begin{pmatrix} \alpha & \beta_{EM} \\ \beta_{ME} & \gamma \end{pmatrix}. \quad (12.74)$$

The corresponding expression for a random medium is

$$\begin{pmatrix} \bar{\bar{\chi}}_{EE} & \bar{\bar{\chi}}_{EM} \\ \bar{\bar{\chi}}_{ME} & \bar{\bar{\chi}}_{MM} \end{pmatrix} = \left[\mathbb{1} - \bar{n}_{\text{res}} \begin{pmatrix} \bar{\mathcal{F}} & 0 \\ 0 & \bar{\mathcal{F}} \end{pmatrix} \begin{pmatrix} \bar{\alpha} & \bar{\beta}_{EM} \\ \bar{\beta}_{ME} & \bar{\gamma} \end{pmatrix} \right]^{-1} \bar{n}_{\text{res}} \begin{pmatrix} \bar{\alpha} & \bar{\beta}_{EM} \\ \bar{\beta}_{ME} & \bar{\gamma} \end{pmatrix}. \quad (12.75)$$

12.7 Environmental form factors

In this section, we give of a little catalogue of environmental form factors for various systems. For fluids and gases usually the form factors for the sphere are used, for a crystal, however, a form factor corresponding to the unit cell has to be chosen.

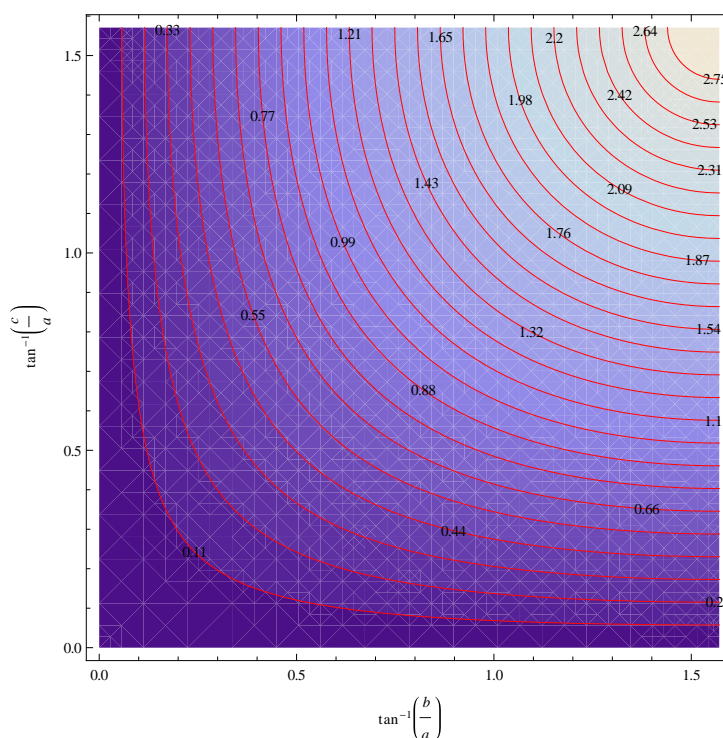
The environmental form factors for crystals with orthorombic unit cells are shown in figure 12.2.

If one considers a spherical geometry and take only into account the electric polarizability, one recovers the Clausius-Mossotti equation,

$$\chi_{EE, \text{macro}} = \left(\mathbb{1} - \frac{4\pi}{3} n_{\text{res}} \alpha \right)^{-1} n_{\text{res}} \alpha. \quad (12.76)$$

Geometry	direction	form factor in units of $4\pi/3$
Sphere	x	1
	y	1
	z	1
Cubic unit cell	x	1
	y	1
	z	1
Orthorombic unit cell	x	$\frac{6}{\pi} \arctan \left(\frac{b/a c/a}{\sqrt{1+(b/a)^2+(c/a)^2}} \right)$
	y	$\frac{6}{\pi} \arctan \left(\frac{a/b c/b}{\sqrt{1+(a/b)^2+(c/b)^2}} \right)$
	z	$\frac{6}{\pi} \arctan \left(\frac{a/c b/a}{\sqrt{1+(a/c)^2+(b/c)^2}} \right)$

Table 12.3: Environmental form factors

Figure 12.2: Environmental form factors in units of $4\pi/3$ for an orthorombic unit cell

The typical approach [44, 87] in order to derive this equation is based on the construction of an artificial spherical cavity around one dipole under consideration. The screening fields of all other dipoles inside the cavity are treated explicitly, while one uses a continuum ap-

proximation for the dipoles outside of the cavity. The construction of the cavity, however, seems rather artificial. For that reason the approach has been criticized in the literature [88, 89]. It has been proposed that the dipoles do not see their own fields, so these fields have to be removed making the difference between the local and the macroscopic field. Note that our approach proposed here recovers not only the Clausius Mossotti equation, but also gives a generalization to more general scenarios.

12.8 Macroscopic response functions of simple metamaterials

We now apply the results from the previous sections of this chapter to the calculation of external macroscopic response functions of metamaterials built from molecular SRRs. We first start with materials that solely consists of SRRs for a variety of different packings. We then proceed to media built from several different building blocks.

Our main focus shall be only on the first resonances throughout the whole section. We will neglect the electric response from fields parallel to the z -direction and consider only the magnetic response for the case that the field is parallel to the z -direction. Thus, we set ϵ_{zz} to one as well as μ_{xx} and μ_{yy} . All external microscopic polarizabilities used in this section are those obtained in Chapter 8 and include the interaction of each dipole with its neighbors.

12.8.1 Parallel SRRs

If all resonators are aligned in a parallel manner as shown in Figure 12.3, the macroscopic response functions read

$$\bar{\epsilon} = \mathbb{1} + 4\pi\bar{n}_{\text{res}}\alpha, \quad (12.77)$$

$$\bar{\mu} = \mathbb{1} + 4\pi\bar{n}_{\text{res}}\gamma, \quad (12.78)$$

$$\bar{\xi} = -\bar{\zeta}^T = 4\pi\bar{n}_{\text{res}}\beta_{\text{EM}}. \quad (12.79)$$

The macroscopic medium is therefore both anisotropic and bianisotropic.

12.8.2 Anti-parallel geometry

The twisted geometry is obtained by starting from a parallel alignment of the resonators. Within each plane the resonators remain in a parallel alignment, but the slits of the SRRs of two neighboring planes are rotated against each other by 180 degrees. The geometry

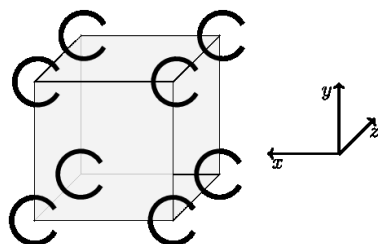


Figure 12.3: "Parallel alignment" of SRRs.

is depicted in Figure 12.4. We then have for the material parameters,

$$\bar{\epsilon} = \mathbb{1} + 4\pi\bar{n}_{\text{res}} \frac{\alpha_{yy} + \alpha_{zz}}{2} \text{diag}(1, 1, 0), \quad (12.80)$$

$$\bar{\mu} = \mathbb{1} + 4\pi\bar{n}_{\text{res}}\gamma, \quad (12.81)$$

while the bianisotropic coefficients vanish due to a direct cancellation which can be easily seen by summing β_{EM} for a ring and its twisted partner.

12.8.3 SRRs in plane with random slit position

The medium under consideration is built up from parallel planes of SRRs where the slits are not in a parallel alignment. If the z -axis is normal to the plane, averaging over all possible configurations yields

$$\bar{\alpha} = \frac{\alpha_{xx} + \alpha_{yy}}{2} \text{diag}(1, 1, 0). \quad (12.82)$$

The magnetic polarizability remains unchanged, while the averaged electromagnetic and magnetoelectric polarizabilities vanish. This means that such a medium exhibits no bianisotropy on a macroscopic level. The form of the macroscopic response functions is identical to the one obtained in the previous section. However, the microscopic polarizabilities are different.

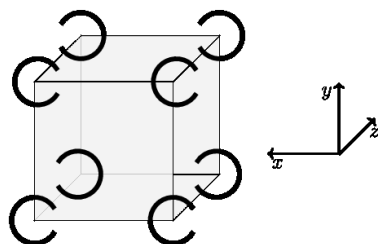


Figure 12.4: Anti-parallel alignment of SRRs.

12.8.4 Random SRR medium with completely arbitrary direction of slits

We now abandon the requirement that the rings must be aligned in planes as compared to the previous case. The medium once again exhibits no bianisotropy and the effective material parameters are

$$\bar{\epsilon} = \mathbb{1} + 4\pi\bar{n}_{\text{res}} \frac{\alpha_{xx} + \alpha_{yy}}{3} \mathbb{1}, \quad (12.83)$$

$$\bar{\mu} = \mathbb{1} + 4\pi\bar{n}_{\text{res}} \frac{\gamma_{zz}}{3} \mathbb{1}, \quad (12.84)$$

such that the medium is isotropic. In return, the effective oscillatory strength of the magnetic polarizability decreases by a factor of three.

12.8.5 Two-component medium

Finally, we consider a medium that consists of two different kinds of resonators, SRRs and resonators exhibiting only electric resonances. The spatial density and the response functions of the second type of resonators are distinguished from those belonging to the SRRs by a prime. If both types of resonators are aligned in parallel manner, the dielectric

function reads as follows

$$\bar{\epsilon} = \mathbf{1} + 4\pi\bar{n}_{\text{res}}\alpha + 4\pi\bar{n}'_{\text{res}}\alpha', \quad (12.85)$$

while one can use the expressions from Section 12.8.1 for the other response functions.

Chapter 13

Index of refraction

13.1 Index of refraction

We are aiming now at the calculation of the index of refraction in terms of the macroscopic parameters from the previous chapter¹. We will assume that the medium is extended over the whole space and that it is spatially homogeneous so that the macroscopic response functions are independent of the position. We want to study the propagation of electromagnetic waves, so we consider the Maxwell equations without external sources and look for non-trivial solutions. The equations read in Fourier space (\mathbf{k}, ω)

$$\begin{pmatrix} k\mathcal{K} & 0 \\ 0 & k\mathcal{K} \end{pmatrix} \begin{pmatrix} \mathbf{E} \\ \mathbf{H} \end{pmatrix} = \begin{pmatrix} k_0\mathbf{B} \\ -k_0\mathbf{D} \end{pmatrix}, \quad (13.1a)$$

$$\begin{pmatrix} \mathbf{k} \cdot \mathbf{D} \\ \mathbf{k} \cdot \mathbf{B} \end{pmatrix} = \begin{pmatrix} 0 \\ 0 \end{pmatrix}, \quad (13.1b)$$

where we have introduced the matrix \mathcal{K} with

$$\mathcal{K}_{ij} = \epsilon_{ijm} \hat{k}_m \quad (13.2)$$

and $k_0 = \omega/c$ and $|\hat{\mathbf{k}}| = 1$. The index of refraction is defined by

$$n^2 = \frac{k^2}{k_0^2}, \quad (13.3)$$

so one has

$$\mathbf{k} = k_0 n \hat{\mathbf{k}} \quad (13.4)$$

¹For simplicity we omit the bar on the external response functions.

One can rewrite the Maxwell equations,

$$\begin{pmatrix} n\mathcal{K} & 0 \\ 0 & n\mathcal{K} \end{pmatrix} \begin{pmatrix} \mathbf{E} \\ \mathbf{H} \end{pmatrix} = \begin{pmatrix} \mathbf{B} \\ -\mathbf{D} \end{pmatrix}. \quad (13.5)$$

We further need the constitutive relations

$$\begin{pmatrix} \mathbf{D}(\mathbf{x}) \\ \mathbf{B}(\mathbf{x}) \end{pmatrix} = \begin{pmatrix} \varepsilon & \xi \\ \zeta & \mu \end{pmatrix} \begin{pmatrix} \mathbf{E}(\mathbf{x}) \\ \mathbf{H}(\mathbf{x}) \end{pmatrix}, \quad (13.6)$$

enabling us to eliminate the \mathbf{D} - and \mathbf{B} -field. Solving now for the \mathbf{H} -field,

$$\mathbf{H} = n\mu^{-1}\mathcal{K}\mathbf{E} - \mu^{-1}\zeta\mathbf{E}, \quad (13.7)$$

we obtain a single equation, determining the \mathbf{E} -field,

$$(\mathbf{1} + n^2\epsilon^{-1}\mathcal{K}\mu^{-1}\mathcal{K} - \epsilon^{-1}\xi\mu^{-1}\zeta - n\epsilon^{-1}\mathcal{K}\mu^{-1}\zeta + n\epsilon^{-1}\xi\mu^{-1}\mathcal{K}) \mathbf{E} = 0. \quad (13.8)$$

In order to obtain non-trivial field configurations, the determinant of the matrix within the brackets has to vanish,

$$\det(\mathbf{1} + n^2\epsilon^{-1}\mathcal{K}\mu^{-1}\mathcal{K} - \epsilon^{-1}\xi\mu^{-1}\zeta - n\epsilon^{-1}\mathcal{K}\mu^{-1}\zeta + n\epsilon^{-1}\xi\mu^{-1}\mathcal{K}) \stackrel{!}{=} 0 \quad (13.9)$$

The propagation of electromagnetic waves in various media has been studied in great detail in the literature [90, 91].

13.2 Extinction theorem

The extinction theorem provides an alternative route to the calculation of the index of refraction, if the microscopic polarizabilities are known. One splits the whole space into two regions where the first region is a classical vacuum and the second region is filled with the material under consideration. One then considers an incident electromagnetic wave as an external field. The induced dipoles of the medium are treated within a continuum approximation, that is one averages the microscopic polarizabilities over the unit cell. In doing so, the local, microscopic, and macroscopic electromagnetic fields become equal. The Maxwell equations are then solved self-consistently by taking into account the full radiation fields of the smeared dipoles and choosing a plane Ansatz for the macroscopic fields. Inside the medium the radiation fields can be written as a sum of two contributions: The first one exactly extinguishes the incident wave, and the second one is the propagating wave with a modified wave vector. Relating the modified wave vector to the wave vector of the incident wave gives Snell's law of refraction. One also obtains an explicit expression

for the index of refraction in terms of the microscopic polarizabilities. The law of reflection is also a result of the calculation. Furthermore the Fresnel equations are obtained. Note that the calculation presented in appendix E also includes bianisotropy. The results obtained with the extinction theorem serve as a check for the expressions obtained with the medium theory. It has been found that both methods yield the same results.

13.3 Index of refraction of an SRR medium

13.3.1 Geometry of the molecular crystal

At first, we calculate the index of refraction for a medium that is solely composed of split ring resonators. We consider an orthorhombic unit cell and use three different parameterizations of the packing employing the lattice constants Δ_i with $i = x, y, z$. The different packing scenarios are displayed in Table 13.1 and explicit expressions for the spatial density n_{SRR} of the quantum SRRs are given.

13.3.2 Calculation of refractive index

If an electromagnetic field with a wave vector parallel to the x -axis and an electric field vector parallel to the y -axis is applied, the index of refraction for this specific type of light field is given by

$$n^2 = \epsilon_{yy}\mu_{zz} - \xi_{yz}\zeta_{zy}. \quad (13.10)$$

We will be only interested in the behavior near to the first resonance, so we neglect the term in the microscopic polarizabilities that give rise to higher resonances. Using the explicit expressions from section 8.4.3, one finally finds

$$n^2 = 1 + 4\pi n_{\text{SRR}}(\alpha_{yy} + \gamma_{zz}). \quad (13.11)$$

As the imaginary parts of α and γ are always positive, the imaginary part of the index of refraction will be positive. The decisive point is that the bianisotropic term $(4\pi n_{\text{SRR}})^2 \beta_{\text{EM},yz} \beta_{\text{ME},zy}$ cancels the term $(4\pi n_{\text{SRR}})^2 \alpha_{yy} \gamma_{zz}$ which would be responsible for n to become negative in the vicinity of the resonance. In order to suppress the impact of the bianisotropy, two possibilities lie at hand:

- i) One arranges the SRRs in such a way that the contributions to the radiation fields from the microscopic bianisotropic polarizabilities cancel. We have seen that this can be achieved by employing either an anti-parallel or a random configuration of the SRRs, as shown in Chapter 12.

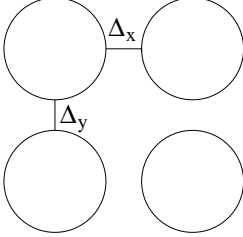
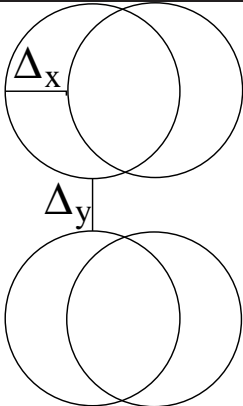
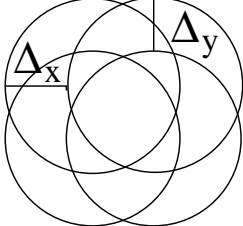
Packing	parametrization	n_{SRR}
P1		$1/[(2R + \Delta_x)(2R + \Delta_y)\Delta_z]$
P2		$1/[(2R + \Delta_x)\Delta_y\Delta_z]$
P3		$1/[\Delta_x\Delta_y\Delta_z]$

Table 13.1: Different types of packings, their parameterizations and the resulting spatial density.

- ii) One embeds the SRRs into a host medium that provides an electric resonance in the vicinity of the magnetic resonance of the SRRs.

If we choose the first possibility, the index of refraction reads,

$$n^2 = 1 + 4\pi n_{\text{SRR}}(\alpha_{yy} + \gamma_{zz}) + (4\pi n_{\text{SRR}})^2 \alpha_{yy} \gamma_{zz}. \quad (13.12)$$

We can achieve negative refraction if the real parts of both ϵ and μ are negative. The idea is now to calculate the minima of both ϵ and μ with the aim to find possible parameters that both become negative. We consider only the first resonance,

$$\epsilon_{yy} = 1 + 4\pi n_{\text{SRR}} \frac{f_\alpha}{\omega_0^2 - \omega^2 - 2i\eta\omega}, \quad (13.13a)$$

$$\mu_{zz} = 1 + 4\pi n_{\text{SRR}} \frac{f_\gamma}{\omega_0^2 - \omega^2 - 2i\eta\omega}, \quad (13.13b)$$

set the first derivative to zero and find the frequency of the minimum as $\omega_{\min} = \sqrt{\omega_0(\omega_0 + 2\eta)}$, provided that the oscillatory strengths are positive. We plug the minimum into the macroscopic response functions and perform a Taylor expansion for small η/ω_0 ,

$$\epsilon(\omega_{\min}) = 1 - 4\pi n_{\text{SRR}} \frac{f_\alpha}{4\omega_0\eta} \left(1 - \frac{\eta}{\omega_0}\right) + 4\pi i n_{\text{SRR}} \frac{f_\alpha}{\omega_0\eta} + \mathcal{O}(\eta/\omega_0), \quad (13.14a)$$

$$\mu(\omega_{\min}) = 1 - 4\pi n_{\text{SRR}} \frac{f_\gamma}{4\omega_0\eta} \left(1 - \frac{\eta}{\omega_0}\right) + 4\pi i n_{\text{SRR}} \frac{f_\gamma}{\omega_0\eta} + \mathcal{O}(\eta/\omega_0). \quad (13.14b)$$

Utilizing the explicit expression for the magnetic oscillator strength from Chapter 8, one sees that the magnetic permeability is apart from a constant numerical factor determined by only three dimensionless parameters: $L^3 n_{\text{SRR}}$, $(\omega_m L/c)^2$, and ω_0/η . The scaling of ω_0 with L^{-1} makes the first parameter independent of the L . The main task is now to find regions in the parameter space where the real part of magnetic permeability becomes negative. We first determine the geometry of the molecular crystal and derive then the desired condition.

13.3.3 Condition for negative permeability

Aiming at materials that exhibit a strong magnetic response, we utilize the straightforward expressions in order to determine the possible model parameters for which the minimum of the real part of the magnetic permeability becomes negative. One finds that the following condition must hold

$$n_{\text{SRR}} L^3 > \frac{225\pi^4}{256} \frac{1}{\alpha} \frac{c}{v_F} \frac{\eta}{\omega_{\text{pl}}(\pi/L)} \quad (13.15)$$

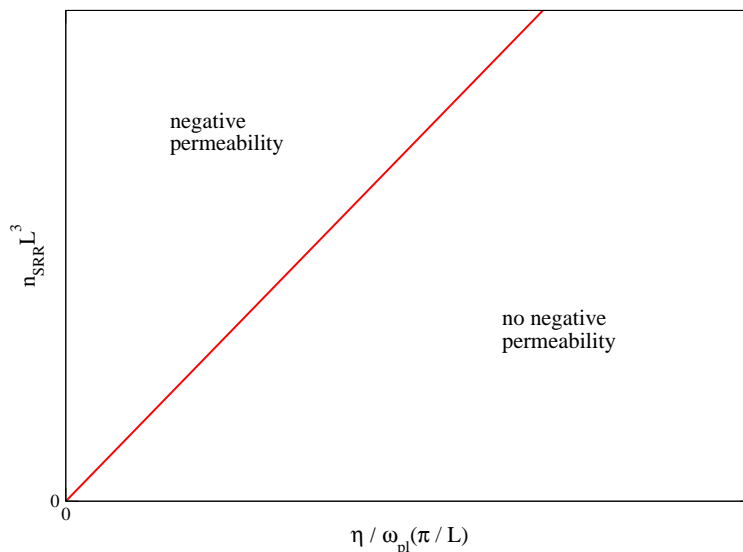


Figure 13.1: Division of the parameter space spanned by $n_{\text{SRR}}L^3$ and $\eta/\omega_{\text{pl}}(q_1)$ into two regions. The Fermi velocity changes the slope of the boundary line between the two regions.

Apart from the constant prefactors, three dimensionless quantities enter the condition (13.15): L^3n_{SRR} , v_{F}/c and $\eta/\omega_{\text{pl}}(q_1)$. The first quantity depends on the ratio of the system size L and the lattice constants of the molecular crystal, $L^3/(\Delta_x\Delta_y\Delta_z)$. The second quantity is completely determined by the electronic structure of the quantum ring. The third quantity is just the quality factor and describes the width of the resonance. Condition (13.15) can be utilized to divide the parameter space into two different regions: In one region the real part of the magnetic permeability becomes negative in the vicinity of the resonance, while this is not possible for the other region. Both regions are shown in Figure 13.1.

As a final step, the minimum length L_{min} of the π -system of organic molecules is calculated such that the real part of μ may become negative. Introducing a mean distance parameter Δ between the rings and setting $\Delta_x = \Delta_y = \Delta_z = \Delta$, one can solve for L_{min}/Δ and plot it against η/ω_0 , Figure 13.2.

The results shown in Figure 13.2 can be used in two different ways:

- i) If the packing is known, one can calculate L_{min} .
- ii) If one wants to obtain a resonance at a certain frequency, one can use the plasmon dispersion from equation (8.5) to determine the required chain length and then

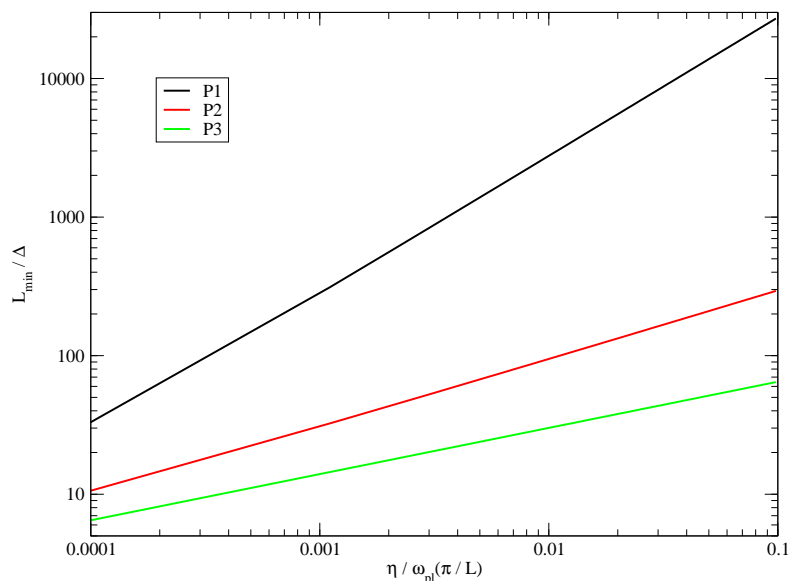


Figure 13.2: Minimum length that is required to obtain a negative permeability.

$\eta/\omega_{p1}(q_1)$	$L = 8a$			$L = 23a$		
	P1	P2	P3	P1	P2	P3
0.001	0.08	0.69	1.52	0.22	1.98	4.38
0.01	0.01	0.22	0.71	0.02	0.65	2.03

Table 13.2: Mean distance parameters in Bohr for the three different packings.

employ Figure 13.2 to find a packing such that the magnetic permeability may become negative.

Note that the negative permeability also means that the refractive index may become negative.

13.3.4 Designing optical metamaterials

We are now in the position to determine the packing parameters for a material exhibiting resonances in the visible regime. The building blocks consist of organic molecules with a single conjugated chain. We have found in Chapter 8 that such systems exhibit resonances in the visible regime for chain lengths between 8 and 23 carbon atoms. For these chain lengths, the lattice parameters of the molecular crystal are calculated such that the index of refraction may become negative. The results are summarized in Table 13.2.

As the mean distance between neighboring carbon atoms is roughly $2.66a_0$, all packing scenarios are unrealistic. This means that the quantum SRR geometry presented in this work is not suitable for designing optical metamaterials. Nevertheless, one can use the insight gained in this work to improve upon this issue. One introduces either several slits, so the length of each sub wire will mainly determine the resonance frequency, while the total size of the ring can be increased without redshifting the plasmon frequency. Such a strategy is not possible for three dimensional structures, as long as quantum effects are negligible, due to the fact that the electric restoring forces are independent from the system size. Alternatively, one can use multichannel systems, where the restoring forces are bigger owing to the higher dimensionality. Another possibility is to consider structures with a band gap resulting from Bragg scattering, so that the system size can be increased without decreasing the excitation energy.

Chapter 14

Summary and Outlook

In this work an analytical model allowing the calculation of plasmonic resonances in molecular nanostructures has been developed and all necessary equations have been derived. This model was compared to a numerically implemented discretized model. It has been found that the agreement between both models systematically improved when the system size of the nanostructure under consideration is increased. The observation has been made for various simple geometries, and therefore it is reasonable that the analytical model can also be applied to other geometries than the ones studied in this work. The reasons for the deviations have been identified as the neglect of finite size effects and reflection oscillations in the analytical model.

The analytical model was then applied to the calculation of polarizabilities of split ring geometries and for the first time a fully microscopic description of the response behavior of split ring resonators was given. The results were compared to the discretized model. Besides, a comparison with the circuit models that are widely used in the metamaterial community for describing the response of mesoscopic resonators to electromagnetic waves was made. It could be shown that both the resonance frequency and the oscillator strength are mainly determined by the shape of the induced charge density wave for the low-lying plasmonic resonances, making the density approach more favorable than the circuit models. Furthermore the quantum corrections to the response properties and the impact of band structure effects were analyzed and explicit expressions were given. Based on these results, the tunability of magnetic resonances for isolated resonators was discussed and first simple guide-lines for the construction of building blocks with desired optical properties were elaborated.

In the subsequent chapter the response of single molecules was studied by means of density functional theory calculations. The plasmonic resonances were identified and both their resonance frequencies and the oscillator strengths could be reproduced by utilizing the

analytical model using parameters from a ground state calculation.

The second part of this work dealt with the calculation of the macroscopic material parameters. For that purpose, the analytical model has been extended such that the interaction of the individual resonators with each other could be taken systematically into account. It was found that the bianisotropy plays a crucial role in the coupling of the resonators.

Then, two sets macroscopic response functions including the bianisotropic coefficients were defined and their applicability was discussed. A systematic method for calculating these response functions was presented and it was shown that this approach is a direct extension of the Clausius-Mossotti theory by introducing the concept of environmental form factors. The results were also applied to various metamaterials and the impact of the packing pattern of the buildings blocks on the macroscopic response functions was analyzed.

Finally, the index of refraction was calculated and conditions for negative refraction were given. The required minimum length of split ring resonators building a metamaterial with negative refraction was calculated. The possibility to achieve negative refraction in the optical regime using molecular split ring resonator was ruled out. However, the guidelines given before were extended such that molecular geometries can be developed that are suitable building blocks of metamaterials.

We want to conclude this work by giving some suggestions for viable candidates for negative refraction. One class of candidates are resonator geometries cut out of graphite or even graphene. Another class are SURMOFS (surface-attached crystalline and oriented metal-organic framework multilayers), where e.g., organic chains linked by metal atoms could be grown in a ring structure on a surface. A third candidate might be carbon nanotubes with a slit.

Zusammenfassung

Im Rahmen dieser Arbeit wurde ein analytisches Modell entwickelt, welches die mikroskopische Berechnung von plasmonischen Anregungen in molekularen Nanostrukturen ermöglicht, und alle dafür notwendigen Gleichungen hergeleitet. Das Modell wurde gegen eine numerische Implementierung eines diskretisierten Modells getestet und dabei stellte sich heraus, dass sich die Übereinstimmung zwischen beiden Modellen systematisch verbesserte, wenn die Systemgröße der betrachteten Nanostruktur vergrößert wurde. Diese Beobachtung konnte für mehrere einfache Geometrien gemacht werden, und daher ist es sinnvoll anzunehmen, dass sich das Modell auch auf andere Geometrien als diejenigen, die in dieser Arbeit untersucht worden sind, anwenden lässt. Die Abweichungen ergeben sich aus der Vernachlässigung der Effekte, die durch die endliche Struktur bedingt sind, sowie der Reflektions-Oszillationen. Mit dem analytischen Modell wurden dann die Polarisierbarkeiten von Splitringgeometrien berechnet und wiederum mit dem diskretisierten Modell verglichen. Außerdem wurde ein Vergleich mit den Schwingkreismodellen, die häufig im Bereich der Metamaterialien Anwendung finden, durchgeführt. Es konnte gezeigt werden, dass sowohl die Resonanzfrequenz als auch die Oszillatorstärke hauptsächlich durch die räumliche Struktur der induzierten Ladungsdichtewelle bestimmt werden. Zusätzlich wurden Quantenkorrekturen zu den Antworteigenschaften sowie der Einfluss der elektrischen Struktur untersucht. Basierend auf diesen Ergebnissen wurden Strategien erarbeitet, die elektromagnetischen Antworteigenschaften masszuschneiden.

Anschließend wurden die Antworteigenschaften von einzelnen Molekülen mittels Dichtefunktionalmethoden berechnet. Die plasmonischen Anregungen wurden identifiziert und sowohl ihre Resonanzfrequenzen als auch ihre Oszillatorstärken konnten mit dem analytischen Modell reproduziert werden, indem nur Parameter aus einer Grundzustandsrechnung verwendet wurden.

Der zweite Teil dieser Arbeit beschäftigte sich mit der Berechnung der makroskopischen Materialparameter. Für diesen Zweck wurde das analytische Modell so erweitert, dass die Wechselwirkungen der einzelnen Resonatoren untereinander systematisch berücksichtigt werden konnten. Dabei stellte sich heraus, dass die Bianisotropie eine zentrale Rolle bei der Kopplung der Resonatoren spielt. Anschließend wurden zwei Sätze an

makroskopischen Antwortfunktionen einschließlich der entsprechenden Bianisotropieeffizienten definiert und die Möglichkeiten ihrer Anwendbarkeit diskutiert. Es wurde eine systematische Methode für die Berechnung dieser Antwortfunktionen aufgezeigt und eine Erweiterung der Clausius-Mossotti-Theorie wurde erhalten. Dabei wurde ein neues Konzept eingeführt, nämlich die Berücksichtigung der Geometrie der Einheitszelle durch Umgebungsformfaktoren. Der entwickelte Formalismus wurde dann auf verschiedene Metamaterialien angewandt und der Einfluss der Kristallstruktur wurde untersucht.

Schließlich wurde der Brechungsindex berechnet und Bedingungen für das Auftreten von negativer Brechung wurden gegeben. Die Minimumlänge von Splitringresonatoren, die notwendig ist, um negative Brechung zu erzielen, wurde berechnet und ausgehend von den Ergebnissen konnte die Möglichkeit ausgeschlossen werden, ein Metamaterial aus Splitringresonatoren zu bauen, das im sichtbaren Frequenzbereich einen negativen Brechungsindex aufzeigt. Dennoch konnten die Erkenntnisse aus dieser Arbeit verwendet werden, um Vorschläge für Bausteine von Metamaterialien machen zu können.

Die Arbeit soll mit einigen möglichen Kandidaten für negative Brechung abgeschlossen werden: Eine Möglichkeit sind Resonatoren, die aus Graphit oder Graphen herausgeschnitten werden. Alternativ kommen auch SURMOFS (surface-attached crystalline and oriented metal-organic framework multilayers) in Frage. Dabei gilt das Interesse besonders organischen Ketten, die durch Metallatome verbunden sind und auf einer Oberfläche in einer Ringstruktur aufgebracht sind. Als dritte Möglichkeit kommen Kohlenstoffnanoröhrchen mit einem Schlitz in Frage.

Lebenslauf

Name	Stephan Bernadotte
Geburtstag	04.11.1980
Geburtsort	Konstanz
Eltern	Maritta Mahlbacher, geb. Berg Jan Bernadotte
Staatsangehörigkeit	deutsch
Familienstand	ledig

Schulbildung

1987-1991	Grundschule Sonnenhalde Konstanz
1991-2000	Heinrich-Suso-Gymnasium Konstanz
Juni 2000	Abitur (Note: 1,0)

Hochschulbildung

Okt. 2000	Beginn des Chemiestudiums an der TH Karlsruhe
Okt. 2003	Beginn des Physikstudiums an der TH Karlsruhe
Okt. 2004 - April 2005	Diplomarbeit in Chemie unter Anleitung von Prof. Dr. W. Klopper
Mai 2005	Diplom in Chemie (Note: 1,2)
August 2005 - August 2006	Diplomarbeit in Physik unter Anleitung von Prof. Dr. F. Klinkhamer
Sept. 2006	Diplom in Physik (Note: 1,2)
Oktober 2006	Beginn der Promotion unter Anleitung von Prof. Dr. W. Klopper und Prof. Dr. F. Evers
Okt. 2006 - Dez. 2006	Wissenschaftlicher Angestellter am Centrum für funktionelle Nanostrukturen
Jan. 2007 - Dez. 2010	Wissenschaftlicher Angestellter am Institut für Nanotechnologie
seit Jan. 2011	Wissenschaftlicher Angestellter am Centrum für funktionelle Nanostrukturen

Publikationsliste

- i) S. Bernadotte, F.R. Klinkhamer, *Classical spacetime foam models and photon propagation*, Phys. Rev. D **75**, 024028 (2007).
- ii) D. Bokhan, S. Bernadotte, S. Ten-no, *Implementation of the CCSD(T)(F12) method using numerical quadratures*, Chem. Phys. Lett. **469**, 214-218 (2009).
- iii) D. Bokhan, S. Bernadotte, S. Ten-no, *Explicitly correlated second-order Møller-Plesset perturbation theory for unrestricted Hartree-Fock reference functions with exact satisfaction of cusp conditions*, J. Chem. Phys. **131**, 084105 (2009).

Poster

S. Bernadotte, W. Klopper, F. Evers, *Ring Molecules as Basic Modules in Metamaterials?*
at KSOP Summer School 2008, August 20-21.

Danksagungen

- Ich möchte mich bei meinen Doktorvätern Wim Klopper und Ferdinand Evers für die Betreuung und Unterstützung herzlich bedanken.
- Ich danke Martin Wegener für fachliche Diskussionen.
- Ich danke Christoph Jacob für Unterstützung und Diskussionen.
- Ich bedanke mich bei den Systemadministratoren für ihre Hilfe bei technischen Problemen.
- Besonders danke ich Alexander Baldes und Angela Bihlmeier für die Schaffung einer tollen Arbeitsatmosphäre.
- Ich danke Ericka Barnes für die Hilfe bei der Korrektur der Arbeit und die zahlreichen Asia days.
- Ich danke Nils Middendorf für die Hilfe beim Hung-Gar-Training.
- Ich danke Tenno-Sensei für die Einladung nach Japan.
- Ich danke dem KHYS für die Ermöglichung des Forschungsaufenthaltes in Japan.
- Ich danke der Arbeitsgruppe Evers für wissenschaftliche Diskussionen bei den Gruppentreffen.
- Herzlicher Dank gebührt auch dem Untertan.

Bibliography

- [1] V. G. Veselago, Soviet Physics Uspekhi **10**, 509 (1968).
- [2] J. B. Pendry, A. J. Holden, D. J. Robbins, and W. J. Stewart, Microwave Theory and Techniques, IEEE Transactions on **47**, 2075 (1999).
- [3] G. Dolling *et al.*, Opt. Lett. **30**, 3198 (2005).
- [4] J. Yang, C. Sauvan, H. T. Liu, and P. Lalanne, Phys. Rev. Lett. **107**, 043903 (2011).
- [5] J. B. Pendry, Phys. Rev. Lett. **85**, 3966 (2000).
- [6] I. I. Smolyaninov, Y.-J. Hung, and C. C. Davis, Science **315**, 1699 (2007).
- [7] T. Ergin, N. Stenger, P. Brenner, J. B. Pendry, and M. Wegener, Science **328**, 337 (2010).
- [8] D. Schurig *et al.*, Science **314**, 977 (2006).
- [9] J. Valentine, J. Li, T. Zentgraf, G. Bartal, and X. Zhang, Nature Materials **8**, 568 (2009).
- [10] L. H. Gabrielli, J. Cardenas, C. B. Poitras, and M. Lipson, Nature Photonics **3**, 461 (2009).
- [11] V. M. Shalaev, Nature Photonics **1**, 41 (2007).
- [12] C. M. Soukoulis and M. Wegener, Nature Photonics **advance online publication** (2011).
- [13] J. Valentine *et al.*, Nature **455**, 376 (2008).
- [14] S. Tretyakov, Metamaterials **1**, 40 (2007).
- [15] J. Zhou *et al.*, Phys. Rev. Lett. **95**, 223902 (2005).
- [16] P. J. Burke, Nanotechnology, IEEE Transactions on **2**, 55 (2003).

- [17] D. L. John, L. C. Castro, and D. L. Pulfrey, *Journal of Applied Physics* **96**, 5180 (2004).
- [18] B. Kanté, S. N. Burokur, A. Sellier, A. de Lustrac, and J.-M. Lourtioz, *Phys. Rev. B* **79**, 075121 (2009).
- [19] N. Liu *et al.*, *Advanced Materials* **19**, 3628 (2007).
- [20] N. Liu and H. Giessen, *Angewandte Chemie International Edition* **49**, 9838 (2010).
- [21] H. Guo *et al.*, *Opt. Express* **15**, 12095 (2007).
- [22] A. Alu, ArXiv e-prints (2010), 1012.1351.
- [23] A. Chipouline, C. Simovski, and S. Tretyakov, ArXiv e-prints (2011), 1106.3835.
- [24] I. Tsukerman, ArXiv e-prints (2011), 1106.3227.
- [25] A. Pors, I. Tsukerman, and S. I. Bozhevolnyi, ArXiv e-prints (2011), 1104.2972.
- [26] C. J. F. Böttcher, *Theory of Electric Polarization* (Elsevier, New York, 1952).
- [27] P. Debye, *Polar Molecules* (Dover, New York, 1945).
- [28] J. H. V. Vleck, *Theory of Electric and Magnetic Susceptibilities* (Oxford University Press, 1932).
- [29] H. Fröhlich, *Theory of Dielectrics* (Oxford University Press, 1949).
- [30] S. Guenneau, A. Movchan, G. Pétursson, and S. A. Ramakrishna, *New Journal of Physics* **9**, 399 (2007).
- [31] M. Brun, S. Guenneau, and A. B. Movchan, **94**, 061903 (2009).
- [32] O. Hessel, *Nature* **455**, 299 (2008).
- [33] D. R. Smith, W. J. Padilla, D. C. Vier, S. C. Nemat-Nasser, and S. Schultz, *Phys. Rev. Lett.* **84**, 4184 (2000).
- [34] R. Marqués, F. Medina, and R. Rafii-El-Idrissi, *Phys. Rev. B* **65**, 144440 (2002).
- [35] K. Aydin, Z. Li, M. Hudlička, S. Tretyakov, and E. Ozbay, *New J. Phys.* **9**, 326 (2007).
- [36] C. R. Simovski and S. He, *Phys. Lett. A* **311**, 254 (2003).

- [37] S. Linden *et al.*, *Science* **306**, 1351 (2004).
- [38] X. Chen, B. Wu, J. Kong, and T. M. Grzegorzczuk, *Phys. Rev. E* **71**, 046610 (2005).
- [39] X. Chen, T. M. Grzegorzczuk, B.-I. B. Wu, J. Pacheco, and J. A. Kong, *Phys. Rev. E* **70**, 016608 (2004).
- [40] D. R. Smith, D. C. Vier, T. Koschny, and C. M. Soukoulis, *Phys. Rev. E* **71**, 036617 (2005).
- [41] J. Zhou, E. N. Economou, T. Koschny, and C. M. Soukoulis, *Opt. Lett.* **31**, 3620 (2006).
- [42] O. Sydoruk, E. Tatartschuk, E. Shamonina, and L. Solymar, *Journal of Applied Physics* **105**, 014903 (2009).
- [43] R. Marques and M. J. Freire, On the usefulness of split ring resonators for magnetic metamaterial design at infrared and optical frequencies, in *Electrotechnical Conference, 2006. MELECON 2006. IEEE Mediterranean*, pp. 222 –224, 2006.
- [44] J. D. Jackson, *Klassische Elektrodynamik* (Walter de Gruyter, 2002).
- [45] W. Brenig, *Statistical Theory of Heat - Nonequilibrium Phenomena* (Springer-Verlag, 1989).
- [46] M. W. Klein, C. Enkrich, M. Wegener, C. M. Soukoulis, and S. Linden, *Opt. Lett.* **31**, 1259 (2006).
- [47] R. A. Shelby, D. R. Smith, S. C. Nemat-Nasser, and S. Schultz, *Applied Physics Letters* **78**, 489 (2001).
- [48] E. Fick and G. Sauermann, *Quantenstatistik dynamischer Prozesse - Band 2* (Akademische Verlagsgesellschaft Geest und Portig K.-G., Leipzig, 1983).
- [49] D. Pines, *Elementary excitations in solids : lectures on protons, electrons, and plasmons*The advanced book program - Advanced book classics (Perseus Books, Reading, Mass., 1999).
- [50] G. D. Mahan, *Many-particle physics*Physics of solids and liquids, 3. ed. ed. (Kluwer Academic, Plenum Publ., New York [u.a.], 2000), Includes bibliographical references and index.
- [51] A. A. Abrikosov, L. P. Gorkov, and I. E. Dzalosinskij, *Methods of quantum field theory in statistical physics*, Rev. engl. ed. ed. (Dover Publ., New York, 1975).

- [52] I. Egri, *Physics Reports* **119**, 363 (1985).
- [53] J. Rogan and J. E. Inglesfield, *Journal of Physics C: Solid State Physics* **14**, 3585 (1981).
- [54] D. F. DuBois, *Annals of Physics* **7**, 174 (1959).
- [55] D. F. DuBois, *Annals of Physics* **8**, 24 (1959).
- [56] C. Ambrosch-Draxl, K. Hummer, S. Sagmeister, and P. Puschnig, *Chemical Physics* **325**, 3 (2006), *Electronic Processes in Organic Solids*.
- [57] M. L. Tiago and J. R. Chelikowsky, *Solid State Communications* **136**, 333 (2005).
- [58] Y. Noguchi and K. Ohno, *Phys. Rev. A* **81**, 045201 (2010).
- [59] T. Giamarchi, *Quantum physics in one dimension* International series of monographs on physics ; 121 (Clarendon Press, Oxford, 2004).
- [60] J. M. Ziman, *Electrons and phonons : the theory of transport phenomena in solids* The international series of monographs on physics, Repr. ed. (Clarendon Pr., Oxford, 1967), *Literaturangaben*.
- [61] T. Holstein, *Annals of Physics* **29**, 410 (1964).
- [62] J. Friedel, *Il Nuovo Cimento (1955-1965)* **7**, 287 (1958), 10.1007/BF02751483.
- [63] H. J. Monkhorst, *Phys. Rev. B* **20**, 1504 (1979).
- [64] N. W. Ashcroft and N. D. Mermin, *Solid State Physics* (Thomson, 1976).
- [65] I. Wolfram Research, *Mathematica*, Version 8.0 ed. (Wolfram Research, Inc., Champaign, Illinois, 2010).
- [66] A. L. Fetter and J. D. Walecka, *Quantum Theory of Many-Particle Systems* (Dover Publications, 2003).
- [67] K. Linghua, Y. Baorong, and H. Xiwei, *Plasma Science and Technology* **9**, 519 (2007).
- [68] W. J. Padilla, *Opt. Express* **15**, 1639 (2007).
- [69] TURBOMOLE V6.3 2011, a development of University of Karlsruhe and Forschungszentrum Karlsruhe GmbH, 1989-2007, TURBOMOLE GmbH, since 2007; available from <http://www.turbomole.com>.

- [70] P. A. M. Dirac, Proc. Royal Soc. (London) A **123**, 714 (1929).
- [71] J. C. Slater, Phys. Rev. **81**, 385 (1951).
- [72] A. D. Becke, Phys. Rev. A **38**, 3098 (1988).
- [73] S. Vosko, L. Wilk, and M. Nusair, Can. J. Phys. **58**, 1200 (1980).
- [74] J. P. Perdew, Phys. Rev. B **33**, 8822 (1986).
- [75] F. Weigend and R. Ahlrichs, Phys. Chem. Chem. Phys. **7** (2005).
- [76] J. P. Perdew and Y. Wang, Phys. Rev. B **45**, 13244 (1992).
- [77] J. Tao, J. P. Perdew, V. N. Staroverov, and G. E. Scuseria, Phys. Rev. Lett. **91**, 146401 (2003).
- [78] V. N. Staroverov, G. E. Scuseria, J. Tao, and J. P. Perdew, J. Chem. Phys. **119**, 12129 (2003).
- [79] C. Lee, W. Yang, and R. G. Parr, Phys. Rev. B **37**, 785 (1988).
- [80] A. D. Becke, J. Chem. Phys. **98**, 5648 (1993).
- [81] A. D. Becke, **98**, 1372 (1993).
- [82] J. W. Negele and H. Orland, *Quantum many-particle systems* Frontiers in physics ; 68, 4. print. ed. (Addison-Wesley, Redwood City, Calif. [u.a.], 1992).
- [83] P. Siemsen, R. C. Livingston, and F. Diederich, **39**, 2633 (2000).
- [84] F. Diederich, Chem. Commun. , 219 (2001).
- [85] M. Mayor and C. Didschies, Angewandte Chemie International Edition **42**, 3176 (2003).
- [86] G. Russakoff, American Journal of Physics **38**, 1188 (1970).
- [87] M. Born and E. Wolf, *Principles of Optics* (Cambridge University Press, 1998).
- [88] M. Ortuno and R. Chicon, American Journal of Physics **57**, 818 (1989).
- [89] J. H. Hannay, European Journal of Physics **4**, 141 (1983).
- [90] J. Kong, *Theory of Electromagnetic Waves* (John Wiley & Sons, 1975).

- [91] E. J. Post, *Formal Structure of Electromagnetism* (North Holland Publishing Company, Amsterdam, 1962).
- [92] F. London, *J. Phys. Radium* **8**, 397 (1937).
- [93] F. Schwabl, *Quantenmechanik* (Springer, 1998).
- [94] S. D. George, T. Petrenko, and F. Neese, *Inorganica Chimica Acta* **361**, 965 (2008), Protagonists in Chemistry: Professor Edward I Solomon.
- [95] R. G. Parr and W. Yang, *Density-functional theory of atoms and molecules* The international series of monographs on chemistry ; 16, 1. iss. paperback ed. (Oxford Univ. Pr. [u.a.], New York, 1994).
- [96] R. M. Dreizler and E. K. U. Gross, *Density functional theory : an approach to the quantum many-body problem* (Springer, Berlin, 1990).

Appendix A

Coupling of the SRR to the light field

A.1 Dependence on the origin

The external light fields acting on the ring are given by

$$\mathbf{E}_{\text{ext}}(\mathbf{r}, \omega) = \mathbf{E}_0(\omega) \exp(i\mathbf{k} \cdot \mathbf{r}), \quad (\text{A.1a})$$

$$\mathbf{B}_{\text{ext}}(\mathbf{r}, \omega) = \mathbf{B}_0(\omega) \exp(i\mathbf{k} \cdot \mathbf{r}), \quad (\text{A.1b})$$

where \mathbf{E}_0 and \mathbf{B}_0 are related via

$$\mathbf{B}_0 = \frac{1}{k} \mathbf{k} \times \mathbf{E}_0. \quad (\text{A.2})$$

If the wave length k^{-1} is much larger than the spatial extension of the ring, the dipole approximation is employed, i.e., one assumes that both the electric and the magnetic fields are spatially constant over the length scale of the molecule. Such constant fields, however, do not satisfy the Maxwell equations. From

$$\text{curl} \mathbf{E} = i\omega \mathbf{B}, \quad (\text{A.3})$$

it is clear that a spatially homogenous magnetic field demands an electric field that is linear in the coordinates. According to

$$\text{curl} \mathbf{B} = -i\omega \mathbf{E}, \quad (\text{A.4})$$

such a field requires a magnetic field that depends quadratically on the coordinates. If one would continue this process to all orders, one would end up with the plane wave solution. In order to describe a homogeneous electric and magnetic field, the plane wave electric field has to be expanded to first order in the wave vector around a point \mathbf{r}_0 ,

$$\mathbf{E}_{\text{ext}}(\mathbf{r}, \omega) = \mathbf{E}_0 + i[\mathbf{k} \cdot (\mathbf{r} - \mathbf{r}_0)] \mathbf{E}_0, \quad (\text{A.5})$$

where the first term on the RHS is just the homogeneous electric field and the second term gives rise to the homogeneous magnetic field according to equation (A.3). In contrast to the homogeneous magnetic field, the electric field is not translationally invariant. This already indicates that the results obtained with this electric field depend on the choice of \mathbf{r}_0 .

In order to determine the induced density, one first has to calculate the potential by integrating the electric field from one end of the wire to the point on the wire where the potential is to be calculated at. However, the potential depends on the choice of the expansion point and respectively of the origin. For the term describing the homogeneous electric field this imposes no problem, as a shift of the point changes the potential by a constant value. The term describing the magnetic field is not only changed by a constant when the origin is shifted, so the induced density depends on the origin. In order to understand what happens, we now turn to the derivation of the coupling Hamiltonian in the long wavelength limit. We will then see that the gradient expansion from above leads not only to a description of the coupling of to the magnetic field, but also to the gradient of the electric field.

The issue of the dependence on the origin appears also in quantum chemistry. A typical way to remove this problem is the usage of so called gauge including atomic orbitals [92].

A.2 The coupling Hamiltonian

We are now aiming at a systematic way to couple a quantum mechanical system to an external light field given as in equations (A.1a) and (A.1b). The coupling Hamiltonian in the Coulomb gauge reads

$$\hat{H}_{\text{coupl}} = \int_{\mathbb{R}^3} d^3\mathbf{r} \hat{\mathbf{j}} \cdot \mathbf{A}_{\text{ext}}(\mathbf{r}, \omega), \quad (\text{A.6})$$

where the external vector potential \mathbf{A}_{ext} leading to the fields given in equations (A.1a) and (A.1b) is given by

$$\mathbf{A}_{\text{ext}}(\mathbf{x}) = \frac{1}{i\omega} \mathbf{E}_0 \exp(i\mathbf{k} \cdot \mathbf{x}). \quad (\text{A.7})$$

Performing a gradient expansion around the origin, we arrive at

$$\hat{H}_{\text{coupl}} = \frac{1}{i\omega} \int d^3\mathbf{x} \hat{\mathbf{j}}(\mathbf{x}) \cdot \mathbf{E}_0 [1 + i\mathbf{k} \cdot \mathbf{x} + \mathcal{O}(kL)], \quad (\text{A.8})$$

where L denotes the typical length scale of the molecular system under consideration. The evaluation of the integrals can be found in textbooks [44, 93], so one ends up with

the following Hamiltonian:

$$\hat{H}_{\text{coupl}} = -\hat{\mathbf{p}} \cdot \mathbf{E}_0 - \hat{\mathbf{m}} \cdot \mathbf{B}_0 - \frac{1}{6}i \sum_{i,j} E_{0,i} \hat{Q}_{ij} k_j, \quad (\text{A.9})$$

where we have introduced the operators of the electric dipole moment $\hat{\mathbf{p}}$,

$$\hat{\mathbf{p}} = \int d^3\mathbf{r} \mathbf{r} \hat{\rho}(\mathbf{r}) \quad (\text{A.10})$$

the magnetic moment,

$$\hat{\mathbf{m}} = \int d^3\mathbf{r} \mathbf{r} \times \hat{j}(\mathbf{r}), \quad (\text{A.11})$$

and the electric quadrupole moment,

$$\hat{Q}_{ij} = \int d^3\mathbf{r} (3r_i r_j - \delta_{ij} r^2) \hat{\rho}(\mathbf{r}). \quad (\text{A.12})$$

A direct calculation shows that a shift of the origin yields only higher order terms $\mathcal{O}((L/\lambda)^2)$, as the lower order terms cancel. By a proper choice of the origin, it is possible to minimize the quadrupole coupling terms. A similar strategy is also applied in the literature [94], but there the minimization is done for the oscillatory strengths.

For the SRRs considered in this thesis, the quadrupole term can be made to vanish as shown in the next section. The choice of the origin has not only an impact on the description of the coupling of the external fields to the SRR, but also on the radiation fields, as they will then be determined completely by the electric and magnetic dipole moments.

A.3 Choice of origin

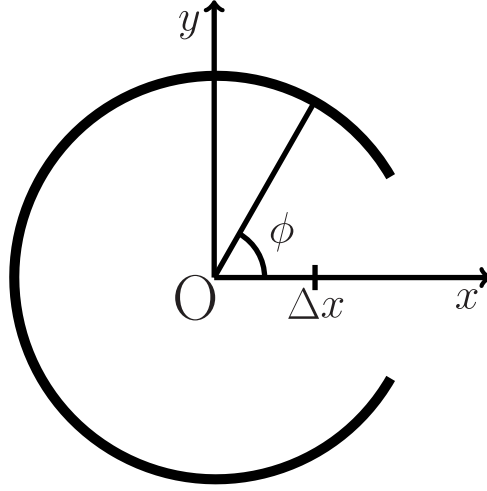
We use that the density profile of a plasmon with m nodes is given by

$$\pi_m(\phi) = \frac{1}{\sqrt{(\pi - \phi_0)R}} \cos\left(\frac{\phi - \phi_0}{\pi - \phi_0} m \frac{\pi}{2}\right) \delta(r - R) \delta(z). \quad (\text{A.13})$$

For plasmons with an odd number of nodes, only Q_{12} and Q_{21} are non-vanishing which can be easily checked by means of group theory,

$$Q_{xy} = -\frac{24(\pi - \phi_0)^2 \cos(2\phi_0)}{((n+4)\pi - 4\phi_0)(\pi(n-4) + 4\phi_0)} R^2. \quad (\text{A.14})$$

The only choice for the origin maintaining the symmetries of the single SRR is along the x -axis as depicted in Figure A.1.

Figure A.1: Shift of the origin O by Δx .

If we shift the origin by Δx , the quadrupole moment in the shifted coordinate system indicated by a prime reads

$$Q'_{xy} = Q_{xy} - 3p_y \Delta x, \quad (\text{A.15})$$

where p_2 denotes y -component of the electric dipole moment,

$$p_y = -\frac{8(\pi - \phi_0)^2 \cos(\phi_0)}{-4\phi_0^2 + 8\pi\phi_0 + (m^2 - 4)\pi^2} R. \quad (\text{A.16})$$

Now one can determine the position of the origin leading to a vanishing quadrupole moment

$$\Delta x = \frac{Q_{xy}}{3p_y} = \frac{((m+2)\pi - 2\phi_0)(\pi(m-2) + 2\phi_0) \cos(2\phi_0) \sec(\phi_0)}{((n+4)\pi - 4\phi_0)(\pi(n-4) + 4\phi_0)} R. \quad (\text{A.17})$$

A.4 External potentials

The spatially constant electric field is given as the gradient of the following scalar potential $\Phi_{\text{ext,el}}$,

$$\Phi_{\text{ext,el}}(\mathbf{r}, \omega) = -\mathbf{E}_0(\omega) \cdot \mathbf{r}. \quad (\text{A.18})$$

The explicit expression on the ring reads

$$\Phi_{\text{ext,el}}(\phi, \omega) = -R (E_{\text{ext},1}(\omega) \cos \phi + E_{\text{ext},2}(\omega) \sin \phi). \quad (\text{A.19})$$

For the magnetic response, we consider a centrosymmetric electric field giving rise to a spatially constant magnetic field,

$$E_{\text{CS}}(\phi, \omega) = i \frac{\omega R}{2c} B_{\text{ext}}(\omega) \hat{e}_\phi \quad (\text{A.20})$$

and shift the origin as determined in section A.3,

$$E_{\text{CS,shifted}}(\phi, \omega) = i \frac{\omega R}{2c} B_{\text{ext}}(\omega) \left(\hat{e}_\phi - \frac{\Delta x}{R} \underbrace{\hat{e}_y}_{=\cos \phi \hat{e}_\phi} \right), \quad (\text{A.21})$$

The potential is then given by

$$\begin{aligned} \Phi_{\text{ext,mag}}(\phi, t) &= -R \int_0^\phi d\phi' E_{\text{CS,shifted}}(\phi') \hat{e}_{\phi'} \\ &= -i \frac{\omega R^2}{2c} B_{\text{ext}}(\omega) \left(\phi - \frac{\Delta x}{R} \sin \phi \right). \end{aligned} \quad (\text{A.22})$$

The induced density as a response to both potentials is then given by

$$\delta\rho(\phi, \omega) = \int d\phi' \chi_{\text{ext}}(\phi, \phi') (\Phi_{\text{ext,el}}(\phi', \omega) + \Phi_{\text{ext,mag}}(\phi', \omega)). \quad (\text{A.23})$$

Appendix B

Calculation of the polarizabilities

B.1 Calculation of the electromagnetic moments

We now derive all expressions that are needed in order to calculate the electromagnetic moments if the induced charge density of the molecular SRR is known. The electric dipole moment is given by

$$\mathbf{p}(\omega) = \int d^3\mathbf{r} \delta\rho(\phi, \omega) \delta(r - R) \delta(z) \mathbf{r}. \quad (\text{B.1})$$

Performing the r - and z -integration, one obtains,

$$\mathbf{p}(\omega) = R \int_{\phi_0}^{2\pi - \phi_0} d\phi R \rho(\phi, \omega) \begin{pmatrix} \cos \phi \\ \sin \phi \\ 0 \end{pmatrix}. \quad (\text{B.2})$$

The expression for the magnetic moment in terms of the induced current density reads

$$\mathbf{m}(\omega) = -\frac{1}{2c} \int d^3\mathbf{r} \mathbf{r} \times \delta\mathbf{j}_{\text{trans}}(\mathbf{r}, \omega). \quad (\text{B.3})$$

The transverse current density can be calculated from the current density by employing equation (4.38). Performing a multipole expansion of the induced density and performing the spatial integral, one finds that the contribution of the longitudinal current density to the magnetic moment is proportional to Q_{xy} . The idea now for the calculation of the magnetic moment is to utilize equation (B.3) with the total current density instead of the transverse one and then to shift the origin such that Q_{xy} vanishes.

Using now the continuity equation on polar coordinates

$$\frac{1}{R} \partial_\phi \delta I_\phi(\omega, \phi) = i\omega \delta\rho(\phi, \omega), \quad (\text{B.4})$$

we can express the induced current $\delta I(\phi, \omega)$ in terms of $\delta\rho(\phi, \omega)$,

$$\delta I_\phi(\phi, \omega) = i\omega \int_{\phi_0}^{\phi} d\phi' R \delta\rho(\phi', \omega), \quad (\text{B.5})$$

and so we have for the current density

$$\delta \mathbf{j}(\phi, \omega) = i\omega \int_{\phi_0}^{\phi} d\phi' R \delta\rho(\phi', \omega) \delta(r - R) \delta(z). \quad (\text{B.6})$$

Plugging this into the expression for the magnetic moment, one has

$$\mathbf{m}(\omega) = -\frac{1}{2c} i\omega R \int_{\phi_0}^{2\pi-\phi_0} d\phi R \int d\phi' R \delta\rho(\phi', \omega) \hat{e}_z. \quad (\text{B.7})$$

With help of a step function Θ ,

$$\mathbf{m}(\omega) = -\frac{1}{2c} i\omega R \int_{\phi_0}^{2\pi-\phi_0} d\phi R \int d\phi' R \Theta(\phi - \phi') \delta\rho(\phi', \omega) \hat{e}_z, \quad (\text{B.8})$$

we can perform the ϕ -integration. Relabeling ϕ' by ϕ , we have

$$\mathbf{m}(\omega) = \frac{1}{2c} i\omega R^2 \int_{\phi_0}^{2\pi-\phi_0} d\phi \phi \delta\rho(\phi, \omega) \hat{e}_z. \quad (\text{B.9})$$

So far we have used the center of the ring as the coordinate origin. Shifting the origin to the position we obtained in Section A.3, we obtain the final result

$$\mathbf{m}(\omega) = \frac{1}{2c} i\omega R^2 \int_{\phi_0}^{2\pi-\phi_0} d\phi \left(\phi - \frac{\Delta x}{R} \sin(\phi) \right) \delta\rho(\phi, \omega) \hat{e}_z. \quad (\text{B.10})$$

B.2 Explicit expressions for the polarizabilities

Calculating $\delta\rho(\phi, \omega)$ with the help of equation (A.23) and determining the electromagnetic moments by employing equations (B.2) and (B.10), we obtain the expressions for all polarizabilities by making a comparison to equation (8.13),

$$\alpha(\omega) = - \int d\phi R \int d\phi' R \begin{pmatrix} -eR \cos \phi \\ -eR \sin \phi \\ 0 \end{pmatrix} \chi(\phi, \phi', \omega) \begin{pmatrix} -eR \cos \phi' & -eR \sin \phi' & 0 \end{pmatrix}, \quad (\text{B.11})$$

$$\beta_{\text{EM}}(\omega) = - \int d\phi R \int d\phi' R \begin{pmatrix} -eR \cos \phi \\ -eR \sin \phi \\ 0 \end{pmatrix} \chi(\phi, \phi', \omega) \begin{pmatrix} 0 & 0 & -\frac{e}{2c} i\omega R^2 \left(\phi' - \frac{\Delta x}{R} \sin \phi' \right) \end{pmatrix}, \quad (\text{B.12})$$

$$\beta_{\text{ME}}(\omega) = - \int d\phi R \int d\phi' R \begin{pmatrix} 0 \\ 0 \\ \frac{e}{2c} i\omega R^2 \left(\phi - \frac{\Delta x}{R} \sin(\phi) \right) \end{pmatrix} \chi(\phi, \phi', \omega) \begin{pmatrix} -eR \cos \phi' & -eR \sin \phi' & 0 \end{pmatrix}, \quad (\text{B.13})$$

$$\gamma(\omega) = - \int d\phi R \int d\phi' R \begin{pmatrix} 0 \\ 0 \\ \frac{e}{2c} i\omega R^2 \left(\phi - \frac{\Delta x}{R} \sin(\phi) \right) \end{pmatrix} \chi(\phi, \phi', \omega) \begin{pmatrix} 0 & 0 & -\frac{e}{2c} i\omega R^2 \left(\phi' - \frac{\Delta x}{R} \sin \phi' \right) \end{pmatrix}. \quad (\text{B.14})$$

Appendix C

Basics of (TD)DFT

C.1 DFT

Solving the Schrödinger equation of an interacting many-particle system leads to a wave function that depends on the coordinates of all particles. The power of density functional theory is the fact that the ground state energy and other observables are completely determined, once the ground state density ρ_0 is given. Hohenberg and Kohn have shown that (i) the energy is a unique functional of ρ_0 , $E[\rho_0]$ and that (ii) the true ground state density minimizes this functional. The electronic energy of molecules in the Born-Oppenheimer approximation comprises the kinetic energy of the electrons ($T[\rho_0]$), their mutual Coulomb interaction $V_{ee}[\rho_0]$, and the coupling to external fields like the electric fields of the nuclei or the applied static electric fields ($V_{\text{ext}}[\rho_0]$). The bottleneck of pure DFT is the representation of the kinetic energy in terms of the density. For that reason, Kohn and Sham introduced a non-interacting reference system whose single-particle states $|\phi_i\rangle$ yield the correct ground state density. The kinetic energy can then be calculated in terms of the single-particle orbitals,

$$T_{\text{KS}} = \sum_i \langle \phi_i | -\frac{1}{2m} \Delta | \phi_i \rangle. \quad (\text{C.1})$$

If one separates the Hartree term $J[\rho_0]$ from the electronic interaction energy, the energy functional can be recast into the following form,

$$E[\rho_0] = T_{\text{KS}}[\rho_0] + J[\rho_0] + \underbrace{T[\rho_0] - T_{\text{KS}}[\rho_0] + V_{ee}[\rho_0] - J[\rho_0]}_{\equiv E_{\text{xc}}[\rho_0]} + V_{\text{ext}}[\rho_0], \quad (\text{C.2})$$

where the exchange correlation energy E_{xc} has been introduced. Minimizing the energy with respect to the Kohn Sham orbitals and keeping the numbers of particles fixed by introducing a chemical potential leads to effective single-particle equations, the Kohn

Sham equations that have to be solved in a self-consistent manner as in the case of Hartree-Fock. However, the exact exchange correlation energy is not known, so one has to use approximations. A catalogue of the resulting functionals can be found in [95, 96].

C.2 TDDFT

In the main task of time-dependent density functional theory is the calculation of the density-density correlation function. The irreducible correlation function is defined via

$$\chi_{\text{irr}}(\mathbf{r}, \mathbf{r}', \omega) = \chi_{\text{KS}}(\mathbf{r}, \mathbf{r}', \omega) + \int d^3\mathbf{r}'' \int d^3\mathbf{r}''' \chi_{\text{KS}}(\mathbf{r}, \mathbf{r}'', \omega) f_{\text{xc}}(\mathbf{r}'', \mathbf{r}''', \omega) \chi_{\text{irr}}(\mathbf{r}''', \mathbf{r}', \omega), \quad (\text{C.3})$$

where χ_{KS} is the correlation function of the non-interacting Kohn-Sham system and f_{xc} is the exchange correlation kernel which is the Fourier transform of the second derivative of the exchange correlation energy with respect to the density. One usually employs the adiabatic approximation, i.e., one neglects the frequency dependency of f_{xc} . The full response function is determined from the irreducible one in the same way as in Chapter 4.

Appendix D

Identification of the plasmonic modes from TDDFT calculations

In this appendix we show how to identify plasmonic resonances by looking at a sample output of the `escf` program. We consider the two lowest excitations that transform like b_u . The relevant data for the analysis are the excitation energies in eV and the dominant contributions of the single particle excitations.

1 singlet b_u excitation

Total energy:	-774.6492297177836
Excitation energy:	0.7471414181640997E-01
Excitation energy / eV:	2.033076112467895
Excitation energy / nm:	609.8357225591878
Excitation energy / cm^{-1} :	16397.85868322400
Oscillator strength:	
velocity representation:	3.456598514634738
length representation:	3.708739168103826

mixed representation: 3.580440760044131

Rotatory strength:

velocity representation: 0.0000000000000000

velocity rep. / $10^{(-40)}\text{erg}\cdot\text{cm}^3$: 0.0000000000000000

length representation: 0.0000000000000000

length rep. / $10^{(-40)}\text{erg}\cdot\text{cm}^3$: 0.0000000000000000

Dominant contributions:

occ. orbital	energy / eV	virt. orbital	energy / eV	coeff. ² *100
5 bg	-4.46	6 au	-3.33	96.7

2 singlet bu excitation

Total energy: -774.6239524808460

Excitation energy: 0.9999137875405113E-01

Excitation energy / eV: 2.720905020861006

Excitation energy / nm: 455.6728112737820

Excitation energy / $\text{cm}^{(-1)}$: 21945.57092522920

Oscillator strength:

velocity representation: 0.3387124752823621E-01

```

length representation:          0.3647043486873625E-01
mixed representation:          0.3514670048486292E-01

```

Rotatory strength:

```

velocity representation:       0.0000000000000000
velocity rep. / 10(-40)erg*cm3: 0.0000000000000000
length representation:         0.0000000000000000
length rep. / 10(-40)erg*cm3: 0.0000000000000000

```

Dominant contributions:

occ. orbital	energy / eV	virt. orbital	energy / eV	coeff. ² *100
4 bg	-5.96	6 au	-3.33	68.0
5 bg	-4.46	7 au	-1.63	25.0

First, we calculate the energy of the contributing single particle excitations. For the first excitation one has only one dominant contribution and the single-particle excitation energy is 1.13 eV. We then compare this energy to the excitation energy. The large difference between 2.03 and 1.13 eV must be due to restoring forces. So the excitation must be a plasmon. This is also suggested by the high value of the oscillator strength. The single-particle excitation energies for the second excitation are 2.63 eV and 2.83 eV. The values are close to 2.72 eV, so we identify the excitation as RSPE.

Appendix E

Extinction theorem

In this section, we intend to derive the index of refraction based on a completely microscopic calculation. We assume that the medium lies in the half-space below the xy -plane and the upper part is the vacuum. We consider then an incident electromagnetic wave and calculate the fields as a response of the medium. Inside the medium, the incident field will give rise to two electromagnetic waves. The first one will extinct the incident wave whereas the other one travels with a modified dispersion relation. One further obtains Snell's law of refraction and the Fresnel equations for transmission. Outside of the medium, a reflected wave results from the radiation fields of the medium and the law of reflection is found.

We start from the Maxwell equations without external sources,

$$\begin{pmatrix} \text{curl} & 0 \\ 0 & \text{curl} \end{pmatrix} \begin{pmatrix} E \\ H \end{pmatrix} = \begin{pmatrix} -\frac{1}{c}\partial_t B \\ \frac{1}{c}\partial_t D \end{pmatrix} \quad (\text{E.1})$$

and

$$\begin{pmatrix} \mathbf{D} \\ \mathbf{B} \end{pmatrix} = \begin{pmatrix} \mathbf{E} \\ \mathbf{H} \end{pmatrix} + 4\pi \begin{pmatrix} \mathbf{P} \\ \mathbf{M} \end{pmatrix}. \quad (\text{E.2})$$

Applying the curl on both sides of equation (E.1) and using equation (E.2), one finds

$$\begin{pmatrix} \square & 0 \\ 0 & \square \end{pmatrix} \begin{pmatrix} \mathbf{D} \\ \mathbf{B} \end{pmatrix} = 4\pi \begin{pmatrix} \text{curl curl} & -i\frac{1}{c}\partial_t \text{curl} \\ i\frac{1}{c}\partial_t \text{curl} & \text{curl curl} \end{pmatrix} \begin{pmatrix} \mathbf{P} \\ \mathbf{M} \end{pmatrix}. \quad (\text{E.3})$$

or after Fourier transformation to frequency space

$$\begin{pmatrix} \square & 0 \\ 0 & \square \end{pmatrix} \begin{pmatrix} \mathbf{D} \\ \mathbf{B} \end{pmatrix} = 4\pi \begin{pmatrix} \text{curl curl} & ik_0 \text{curl} \\ -ik_0 \text{curl} & \text{curl curl} \end{pmatrix} \begin{pmatrix} \mathbf{P} \\ \mathbf{M} \end{pmatrix}, \quad (\text{E.4})$$

where we have used $k_0 = \omega/c$. Apart from solutions of the homogeneous equation, one finally has

$$\begin{pmatrix} \mathbf{D}(\mathbf{r}) \\ \mathbf{B}(\mathbf{r}) \end{pmatrix} = \int_{\mathbb{R}^3} d^3\mathbf{r}' G(\mathbf{r}, \mathbf{r}') 4\pi \begin{pmatrix} \text{curl curl} & ik_0 \text{curl}' \\ -ik_0 \text{curl}' & \text{curl}' \text{curl}' \end{pmatrix} \begin{pmatrix} \mathbf{P} \\ \mathbf{M} \end{pmatrix}, \quad (\text{E.5})$$

where we have employed the retarded Green's function $G(\mathbf{r}, \mathbf{r}')$,

$$G(\mathbf{r}, \mathbf{r}') = \frac{\exp(ik_0|\mathbf{r} - \mathbf{r}'|)}{|\mathbf{r} - \mathbf{r}'|}. \quad (\text{E.6})$$

We divide the space into a region without medium $\mathcal{R}_W = \{\mathbf{r} | \mathbf{r} \in \mathbb{R}^3 \wedge r_3 < 0\}$ and a region containing the medium $\mathcal{R}_M = \{\mathbf{r} | \mathbf{r} \in \mathbb{R}^3 \wedge r_3 > 0\}$ and assume that the medium consists of electric and magnetic dipoles with the same dipole moments \mathbf{p} and \mathbf{m} at positions \mathbf{R}_i , so that the polarization P and the magnetization M are given by

$$\begin{pmatrix} \mathbf{P}(\mathbf{r}) \\ \mathbf{M}(\mathbf{r}) \end{pmatrix} = \sum_i \begin{pmatrix} \mathbf{p} \delta(\mathbf{r} - \mathbf{R}_i) \\ \mathbf{m} \delta(\mathbf{r} - \mathbf{R}_i) \end{pmatrix}. \quad (\text{E.7})$$

Again we introduce a convex neighborhood of each dipole $\mathcal{U}_{u,i}$ and construct the punctured manifold

$$\mathcal{M} = \mathcal{R}_M \setminus \bigcup_i \mathcal{U}_{u,i}. \quad (\text{E.8})$$

If now the incident fields \mathbf{E}_{inc} and \mathbf{B}_{inc} propagate from the vacuum inside the medium, they will induce electric and magnetic dipoles. Their strength and direction is determined by the microscopic polarizabilities

$$\begin{pmatrix} p \\ m \end{pmatrix} = \begin{pmatrix} \alpha & \beta \\ -\beta^T & \gamma \end{pmatrix} \begin{pmatrix} \mathbf{E}_{\text{loc}} \\ \mathbf{H}_{\text{loc}} \end{pmatrix} \quad (\text{E.9})$$

and the local fields E_{loc} and H_{loc} at the position of the dipole. These fields are the sum of the incident fields and the radiation fields of all other dipoles. When the contribution from all other dipoles is treated within a continuum approximation, we replace the sum over all individual dipoles by an integral over the punctured manifold times the spatial density n_{dip} of the dipoles:

$$\begin{aligned} \begin{pmatrix} \mathbf{E}_{\text{loc}}(\mathbf{r}) \\ \mathbf{H}_{\text{loc}}(\mathbf{r}) \end{pmatrix} &= \begin{pmatrix} \mathbf{E}_{\text{inc}}(\mathbf{r}) \\ \mathbf{H}_{\text{inc}}(\mathbf{r}) \end{pmatrix} + n_{\text{dip}} \int_{\mathcal{M}} d^3\mathbf{r}' G(\mathbf{r}, \mathbf{r}') \\ &\quad \begin{pmatrix} \text{curl}' \text{curl}' \alpha - ik_0 \text{curl}' \beta^T & \text{curl}' \text{curl}' \beta + ik_0 \text{curl}' \gamma \\ -\text{curl}' \text{curl}' \beta^T - ik_0 \text{curl}' \alpha & \text{curl}' \text{curl}' \gamma - ik_0 \text{curl}' \beta \end{pmatrix} \begin{pmatrix} E_{\text{loc}}(\mathbf{r}') \\ H_{\text{loc}}(\mathbf{r}') \end{pmatrix} \\ &\quad - \underbrace{4\pi n_{\text{dip}} \begin{pmatrix} \alpha & \beta \\ -\beta^T & \gamma \end{pmatrix} \begin{pmatrix} E_{\text{loc}}(\mathbf{r}) \\ H_{\text{loc}}(\mathbf{r}) \end{pmatrix}}_{\text{due to equation (E.2)}}. \end{aligned} \quad (\text{E.10})$$

One finds

$$\begin{aligned} \begin{pmatrix} \mathbf{E}_{\text{loc}}(\mathbf{r}) \\ \mathbf{H}_{\text{loc}}(\mathbf{r}) \end{pmatrix} &= \begin{pmatrix} \mathbf{E}_{\text{inc}}(\mathbf{r}) \\ \mathbf{H}_{\text{inc}}(\mathbf{r}) \end{pmatrix} + n_{\text{dip}} \int_{\mathcal{R}_M} d^3\mathbf{r}' G(\mathbf{r}, \mathbf{r}') \\ &\quad \begin{pmatrix} \text{curl}' \text{curl}' \alpha - ik_0 \text{curl}' \beta^T & \text{curl}' \text{curl}' \beta + ik_0 \text{curl}' \gamma \\ -\text{curl}' \text{curl}' \beta^T - ik_0 \text{curl}' \alpha & \text{curl}' \text{curl}' \gamma - ik_0 \text{curl}' \beta \end{pmatrix} \begin{pmatrix} E_{\text{loc}}(\mathbf{r}') \\ H_{\text{loc}}(\mathbf{r}') \end{pmatrix} \cdot \quad (\text{E.11}) \\ &\quad - n_{\text{dip}} \begin{pmatrix} 4\pi\mathbb{1} + \mathcal{F}_U & 0 \\ 0 & 4\pi\mathbb{1} + \mathcal{F}_U \end{pmatrix} \begin{pmatrix} \alpha & \beta \\ -\beta^T & \gamma \end{pmatrix} \begin{pmatrix} E_{\text{loc}}(\mathbf{r}) \\ H_{\text{loc}}(\mathbf{r}) \end{pmatrix} \end{aligned}$$

We now perform partial integrations and use

$$\frac{\partial}{\partial r_i} G(\mathbf{r}, \mathbf{r}') = -\frac{\partial}{\partial r'_i} G(\mathbf{r}, \mathbf{r}'), \quad (\text{E.12})$$

then we can take all derivatives in front of the integral

$$\begin{aligned} \begin{pmatrix} \mathbf{E}_{\text{loc}}(\mathbf{r}) \\ \mathbf{H}_{\text{loc}}(\mathbf{r}) \end{pmatrix} &= \begin{pmatrix} \mathbf{E}_{\text{inc}}(\mathbf{r}) \\ \mathbf{H}_{\text{inc}}(\mathbf{r}) \end{pmatrix} + n_{\text{dip}} \begin{pmatrix} \text{curl} \text{curl} \alpha - ik_0 \text{curl} \beta^T & \text{curl} \text{curl} \beta + ik_0 \text{curl} \gamma \\ -\text{curl} \text{curl} \beta^T - ik_0 \text{curl} \alpha & \text{curl} \text{curl} \gamma - ik_0 \text{curl} \beta \end{pmatrix} \\ &\quad \int_{\mathcal{R}_M} d^3\mathbf{r}' G(\mathbf{r}, \mathbf{r}') \begin{pmatrix} E_{\text{loc}}(\mathbf{r}') \\ H_{\text{loc}}(\mathbf{r}') \end{pmatrix} \quad (\text{E.13}) \\ &\quad - n_{\text{dip}} \begin{pmatrix} 4\pi\mathbb{1} + \mathcal{F}_U & 0 \\ 0 & 4\pi\mathbb{1} + \mathcal{F}_U \end{pmatrix} \begin{pmatrix} \alpha & \beta \\ -\beta^T & \gamma \end{pmatrix} \begin{pmatrix} E_{\text{loc}}(\mathbf{r}) \\ H_{\text{loc}}(\mathbf{r}) \end{pmatrix}. \end{aligned}$$

For the incident field, we choose a plane wave satisfying the Maxwell equations *in vacuo* with \mathbf{k}_{inc} as a wave vector and $k_{\text{inc}} = k_0$,

$$\begin{pmatrix} \mathbf{E}_{\text{inc}}(\mathbf{r}) \\ \mathbf{H}_{\text{inc}}(\mathbf{r}) \end{pmatrix} = \begin{pmatrix} \mathbf{E}_{\text{inc}}^{(0)} \\ \mathbf{H}_{\text{inc}}^{(0)} \end{pmatrix} \exp(i\mathbf{k}_{\text{inc}} \cdot \mathbf{r}), \quad (\text{E.14})$$

and make the following plane wave *Ansatz* for the local fields:

$$\begin{pmatrix} \mathbf{E}_{\text{loc}}(\mathbf{r}) \\ \mathbf{H}_{\text{loc}}(\mathbf{r}) \end{pmatrix} = \begin{pmatrix} \mathbf{E}_{\text{loc}}^{(0)} \\ \mathbf{H}_{\text{loc}}^{(0)} \end{pmatrix} \exp(i\mathbf{k}_{\text{trans}} \cdot \mathbf{r}), \quad (\text{E.15})$$

where $\mathbf{k}_{\text{trans}}$ denotes the wave vector of the transmitted wave. We further need the following integral

$$\int_{\mathcal{R}_M} d^3\mathbf{r}' G(\mathbf{r}, \mathbf{r}') \exp(i\mathbf{k}_{\text{trans}} \cdot \mathbf{r}') = \begin{cases} 2\pi \frac{\exp(i[k_{\text{trans},1}r_1 + k_{\text{trans},2}r_2 + qr_3])}{q(q - k_{\text{trans},3})} + 4\pi \frac{\exp(i\mathbf{k}_{\text{trans}} \cdot \mathbf{r})}{k_{\text{trans}}^2 - k_0^2} & r_3 > 0 \\ -2\pi \frac{\exp(i[k_{\text{trans},1}r_1 + k_{\text{trans},2}r_2 - qr_3])}{q(q + k_{\text{trans},3})} & r_3 < 0 \end{cases} \quad (\text{E.16})$$

with

$$q^2 \equiv k_0^2 - k_{\text{trans},1}^2 - k_{\text{trans},2}^2. \quad (\text{E.17})$$

For later convenience we define the following wave vectors

$$\mathbf{k}_{\text{ext}} \equiv \begin{pmatrix} k_{\text{trans},1} \\ k_{\text{trans},2} \\ q \end{pmatrix}, \quad \mathbf{k}_{\text{refl}} \equiv \begin{pmatrix} k_{\text{trans},1} \\ k_{\text{trans},2} \\ -q \end{pmatrix}. \quad (\text{E.18})$$

We introduce the matrix $\mathcal{K}_{\text{type}}$,

$$\mathcal{K}_{ij} \equiv \epsilon_{ijm} k_{\text{type},m} \quad (\text{E.19})$$

and $\mathcal{T}_{\text{type}}$,

$$\mathcal{T}_{\text{type}} \equiv - \begin{pmatrix} \mathcal{K}_{\text{type}}^2 \alpha + k_0 \mathcal{K}_{\text{type}} \beta^{\text{T}} & -\mathcal{K}_{\text{type}} \beta - k_0 \mathcal{K}_{\text{type}} \gamma \\ -\mathcal{K}_{\text{type}}^2 \beta^{\text{T}} - k_0 \mathcal{K}_{\text{type}} \alpha & \mathcal{K}_{\text{type}}^2 \gamma - k_0 \mathcal{K}_{\text{type}} \beta \end{pmatrix}. \quad (\text{E.20})$$

The final equations for $r_3 > 0$ then read

$$\begin{aligned} \begin{pmatrix} 0 \\ 0 \end{pmatrix} &= \underbrace{\begin{pmatrix} \mathbf{E}_{\text{inc}}^{(0)} \\ \mathbf{B}_{\text{inc}}^{(0)} \end{pmatrix} \exp(\mathbf{i}\mathbf{k}_{\text{inc}} \cdot \mathbf{r})}_I + \underbrace{\frac{2\pi n_{\text{dip}}}{q(q - k_{\text{trans},3})} \mathcal{T}_{\text{ext}} \begin{pmatrix} \mathbf{E}_{\text{loc}}^{(0)} \\ \mathbf{H}_{\text{loc}}^{(0)} \end{pmatrix} \exp(\mathbf{i}\mathbf{k}_{\text{ext}} \cdot \mathbf{r})}_{II} \\ &- \left\{ \underbrace{\left[\begin{pmatrix} \mathbb{1} & 0 \\ 0 & \mathbb{1} \end{pmatrix} + n_{\text{dip}} \begin{pmatrix} \mathcal{F}_U & 0 \\ 0 & \mathcal{F}_U \end{pmatrix} \begin{pmatrix} \alpha & \beta \\ -\beta^{\text{T}} & \gamma \end{pmatrix} \right]}_{\Sigma_{\text{CM}}} + \frac{4\pi n_{\text{dip}}}{k_{\text{trans}}^2 - k_0^2} \mathcal{T}_{\text{trans}} \right. \\ &\left. + 4\pi n_{\text{dip}} \begin{pmatrix} \alpha & \beta \\ -\beta^{\text{T}} & \gamma \end{pmatrix} \right\} \begin{pmatrix} \mathbf{E}_{\text{trans}}^{(0)} \\ \mathbf{H}_{\text{trans}}^{(0)} \end{pmatrix} \exp(\mathbf{i}\mathbf{k}_{\text{trans}} \cdot \mathbf{r}), \end{aligned} \quad (\text{E.21})$$

where we have introduced the matrix Σ_{CM} .

- i) For the sum of term I and II to cancel, the exponents must be equal for all values of \mathbf{r} inside the medium, so we have

$$k_{\text{trans},1} = k_{\text{inc},r}, \quad k_{\text{trans},2} = k_{\text{inc},2}, \quad q = k_{\text{inc},3}. \quad (\text{E.22})$$

- ii) The field strengths of local fields may be determined from the fields strength of the incident fields,

$$\begin{pmatrix} \mathbf{E}_{\text{inc}}^{(0)} \\ \mathbf{H}_{\text{inc}}^{(0)} \end{pmatrix} = \frac{2\pi n_{\text{dip}}}{k_{\text{inc},3}(k_{\text{inc},3} - k_{\text{trans},3})} \mathcal{T}_{\text{ext}} \begin{pmatrix} \mathbf{E}_{\text{loc}}^{(0)} \\ \mathbf{H}_{\text{loc}}^{(0)} \end{pmatrix}. \quad (\text{E.23})$$

According to Clausius-Mossotti theory, the local fields and the macroscopic fields are related via

$$\begin{pmatrix} \mathbf{E}_{\text{loc}}^{(0)} \\ \mathbf{H}_{\text{loc}}^{(0)} \end{pmatrix} = \Sigma_{\text{CM}}^{-1} \begin{pmatrix} \mathbf{E}_{\text{macr}}^{(0)} \\ \mathbf{H}_{\text{macr}}^{(0)} \end{pmatrix}, \quad (\text{E.24})$$

so the macroscopic fields can be expressed in terms of the incident ones,

$$\begin{pmatrix} \mathbf{E}_{\text{inc}}^{(0)} \\ \mathbf{H}_{\text{inc}}^{(0)} \end{pmatrix} = \frac{2\pi n_{\text{dip}}}{k_{\text{inc},3}(k_{\text{inc},3} - k_{\text{trans},3})} \mathcal{T}_{\text{ext}} \Sigma_{\text{CM}}^{-1} \begin{pmatrix} \mathbf{E}_{\text{macr}}^{(0)} \\ \mathbf{H}_{\text{macr}}^{(0)} \end{pmatrix}. \quad (\text{E.25})$$

The equation expresses on the one hand the extinction of the incident wave by another one that is produced by the radiating dipoles. On the other hand we can read off all transmission coefficients, appearing in the Fresnel equations of transmission.

iii) Defining the index of refraction as

$$n^2 = \frac{k_{\text{trans}}^2}{k_0^2}, \quad (\text{E.26})$$

one easily sees

$$\frac{\cos \theta_{\text{inc}}}{\cos \theta_{\text{trans}}} = n \quad (\text{E.27})$$

which is just Snell's law.

iv) The remaining terms of equation (E.21) impose the condition, the the local fields must be eigenvectors of the matrix within the curly bracket with eigenvalue zero:

$$\det \left\{ \Sigma_{\text{CM}} + \frac{4\pi n_{\text{dip}}}{k_{\text{trans}}^2 - k_0^2} \mathcal{T}_{\text{trans}} + 4\pi n_{\text{dip}} \begin{pmatrix} \alpha & \beta \\ -\beta^{\text{T}} & \gamma \end{pmatrix} \right\} \stackrel{!}{=} 0. \quad (\text{E.28})$$

This equation determines the dispersion relations of the photonic dispersion relation by solving for k_0 in terms of $\mathbf{k}_{\text{trans}}$.

Outside of the medium, one observes in addition to the incident wave a reflected one,

$$\begin{pmatrix} \mathbf{E}_{\text{refl}}^{(0)} \\ \mathbf{H}_{\text{refl}}^{(0)} \end{pmatrix} \exp(\mathbf{i}\mathbf{k}_{\text{refl}} \cdot \mathbf{r}) = \frac{2\pi n_{\text{dip}}}{q(q + k_{\text{trans},3})} \mathcal{T}_{\text{refl}} \begin{pmatrix} \mathbf{E}_{\text{local}}^{(0)} \\ \mathbf{H}_{\text{loc}}^{(0)} \end{pmatrix} \exp(\mathbf{i}\mathbf{k}_{\text{refl}} \cdot \mathbf{r}). \quad (\text{E.29})$$

We can make two observations:

i) Using the definition of the environmental form factors, one sees

$$\theta_{\text{refl}} = \pi - \theta_{\text{inc}}, \quad (\text{E.30})$$

which is the law of reflection.

- ii) We can also express the amplitudes of the reflected wave in terms of the amplitudes of the wave within the medium,

$$\begin{pmatrix} \mathbf{E}_{\text{refl}}^{(0)} \\ \mathbf{H}_{\text{refl}}^{(0)} \end{pmatrix} = \frac{2\pi n_{\text{dip}}}{k_{\text{inc},3}} (k_{\text{inc},3} + k_{\text{trans},3}) \mathcal{T}_{\text{refl}} \Sigma_{\text{CM}} \begin{pmatrix} \mathbf{E}_{\text{macr}}^{(0)} \\ \mathbf{H}_{\text{macr}}^{(0)} \end{pmatrix}. \quad (\text{E.31})$$

We can read off the transmission coefficients, appearing in the Fresnel equations of reflection.